Characterization and modelling of porous automotive engine encapsulation materials for external acoustics

Alexandre Wilkinson

Par **Alexandre WILKINSON**

Characterization and modelling of porous automotive engine encapsulation materials for external acoustics

Thèse présentée
pour l'obtention du grade
de Docteur de l'UTC

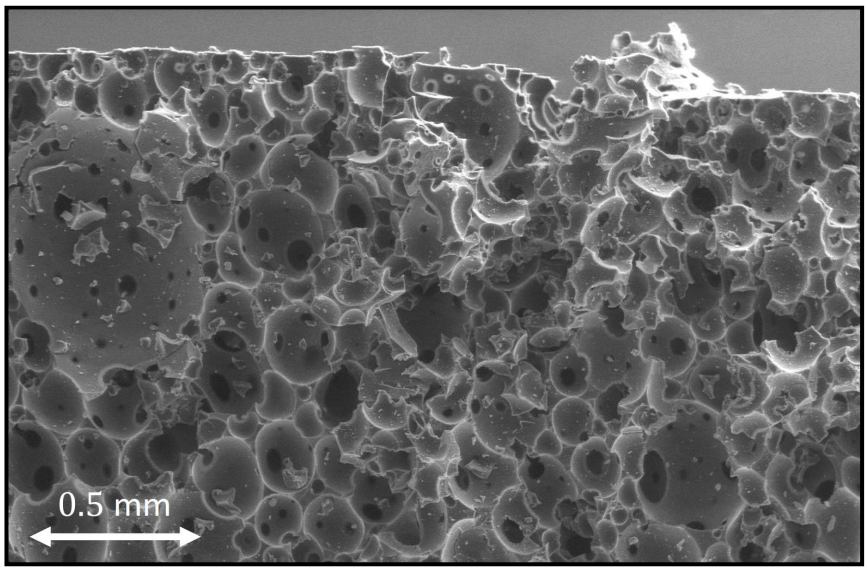

Soutenue le 24 avril 2024
Spécialité : Acoustique et Vibrations : Unité de recherche en Mécanique - Laboratoire Roberval (FRE UTC - CNRS 2012)
D2806

Characterization and modelling of porous automotive engine encapsulation materials for external acoustics

Thesis submitted for the degree of Doctor

Spécialité : Acoustique et Vibrations

Par **Alexandre Wilkinson**

Soutenue le 24 avril 2024

Laboratoire Roberval, Université de technologie de Compiègne
Centre de recherche Royallieu - CS 60319 - 60203 Compiègne CEDEX, France

Thesis supervisors

Nicolas DAUCHEZ	Professor	UTC, Compiègne
Mohamed RACHIK	PhD	UTC, Compiègne

Manuscript reviewers

Olivier DOUTRES	Professor	ETS, Montréal
Gaël CHEVALLIER	Professor	UFC, Besançon

Defence committee

Philippe LECLAIRE	Professor	ISAT, Nevers
Lucie ROULEAU	PhD	CNAM, Paris
Jean-Daniel CHAZOT	PhD	UTC, Compiègne

Invited committee

Stéphane JOB	PhD	ISAE-Supméca, Saint-Ouen
Arnaud DUVAL	Eng.	Trèves Group, Reims

Abstract

The encapsulation of car engines by porous screens is a technology that reduces the noise they radiate into their environment. Currently, their use relies mostly on their ability to absorb sound when placed inside the engine compartment, at a distance from the engine, but a new configuration that positions them directly in contact with the engine offers several advantages. Notably, this allows a reduction in mass and raw materials needed, but significantly alters their acoustic behaviour. In particular, the engine temperature, applied preload, and the amount of contact between the engine and the screen influence the acoustic behaviour of the system. This thesis aims to characterize the porous encapsulation materials and study their acoustic behaviour in their new configuration, in contact with a radiating surface representing the engine. This work is part of an industrial project called SEMPAE (Simulation of engine encapsulation for external acoustics, from 2020 to 2024), which is a collaboration between Trèves Group, an automotive equipment supplier, Renault Group, an automotive manufacturer, ESI Group, a software publisher, and the Roberval research laboratory at UTC.

First, various encapsulation materials, including polymer foams and fibrous materials, are characterized to obtain their properties that serve as input for poroelastic models. Various characterization methods are compared and applied. Special attention is given to the characterization of mechanical properties, for which there are still many uncertainties.

Next, the stiffness of melamine foam compressed against a rigid surface is studied. Its relaxation over time is observed and modelled, highlighting the complex rheology of porous materials. Its nonlinearity as a function of strain is accounted for, revealing the interaction between the intrinsic nonlinearity of the material and the shape nonlinearity of a sample with a pyramidal geometry. Since the compression stiffness of an asperity made from a porous material can be modelled, the contact stiffness of a porous material with a rough surface can be predicted.

Finally, the reduction of the acoustic power radiated by a plate covered with a screen consisting of a porous layer and a heavy sheet is studied. The mass-spring behaviour of the screen significantly reduces the radiated power beyond the resonance of the system. Experimental results reveal that by reducing the contact ratio between the screen and the plate, the resonance is shifted towards lower frequencies, which improves the acoustic insulation of the covering. Partial contact is created experimentally by cutting grooves into the screens, and is modelled using the parallel transfer matrix method.

Résumé

L'encapsulage de moteurs automobiles par des écrans poreux est une solution technologique qui sert à réduire le bruit qu'ils rayonnent dans l'environnement. L'utilisation actuelle de ces écrans repose principalement sur leur capacité à absorber le son lorsqu'ils sont placés à distance du moteur dans son compartiment, mais une nouvelle configuration qui les place directement au contact du moteur apporte plusieurs avantages. Ceci permet notamment un gain de masse et de matière première, mais modifie significativement leur comportement acoustique. En particulier, la température du moteur, la précontrainte appliquée, et la proportion de contact entre le moteur et l'écran pilotent le comportement acoustique du système. Cette thèse a pour objectif de caractériser les matériaux poreux d'encapsulage et d'étudier leur comportement acoustique dans leur nouvelle configuration au contact d'une surface rayonnante représentant le moteur. Ce travail s'inscrit dans un projet industriel appelé SEMPAE (Simulation de l'Encapsulage Moteur Pour l'Acoustique Externe, de 2020 à 2024), mené en collaboration entre le groupe Trèves, équipementier automobile, le groupe Renault, constructeur automobile, le groupe ESI, éditeur de logiciel, et le laboratoire de recherche Roberval de l'UTC.

Dans un premier temps, plusieurs matériaux d'encapsulage, dont des mousses polymères et des matériaux fibreux, sont caractérisés pour obtenir leurs propriétés et alimenter une modélisation poroélastique. Les diverses méthodes de caractérisation sont comparées entre elles et appliquées. Une attention particulière est portée à la caractérisation des propriétés mécaniques, pour lesquelles il reste à ce jour beaucoup d'incertitudes.

Ensuite, la raideur d'une mousse en mélamine comprimée par une surface rigide est étudiée. Sa relaxation au cours du temps est observée et modélisée, mettant en lumière la rhéologie complexe des matériaux poreux. Sa non-linéarité en fonction de la déformation est prise en compte, permettant de comprendre l'interaction entre la non-linéarité intrinsèque du matériau et la non-linéarité due à la forme d'un échantillon à géométrie pyramidale. Puisque la raideur de compression d'une aspérité composée d'un matériau poreux peut être modélisée, la raideur de contact d'un matériau poreux à surface rugueuse peut être prédite.

La dernière partie porte sur la réduction de la puissance acoustique rayonnée par une plaque recouverte d'un écran constitué d'une couche poreuse et d'une masse lourde. Le comportement masse-ressort de l'écran permet une réduction significative de la puissance rayonnée au-delà de la résonance du système. L'expérience montre qu'en réduisant la surface de contact entre l'écran et la plaque, la résonance se déplace vers les basses fréquences, améliorant donc l'isolation acoustique de l'écran. Le contact partiel est créé expérimentalement en rainurant les écrans et peut être modélisé par la méthode des matrices de transfert en parallèle.

Acknowledgements

I would like to thank everyone who accompanied me, directly and indirectly, along this journey. Thank you to my supervisors Nicolas Dauchez and Mohamed Rachik for giving me the opportunity to pursue a PhD under their direction, allowing me to benefit from their expertise. I also extend my gratitude to collaborators within the SEMPAE project for being helpful and available to answer my queries. These include Laurent Polac from Renault Group, Marc Anciant from ESI Group, and Lei Lei, Arnaud Duval and Guillaume Crignon from Trèves Group. Thank you to those who took the time to build this project. Furthermore, thank you to Nicolas Dauchez, Trèves Group and UTeam for granting me the extra time I needed to complete my work.

Thank you to Caroline Zimmerman, Valérie Duquenne, and Nathalie Barrast of the Roberval laboratory, for helping with the administrative workload required in a project of this kind.

Thank you to the people who had a hand in the organization of the JJCAB 2021 conference at the UTC in Compiègne. This includes the members of the SFA (french acoustics association), Fatiha Benrezzak, Jean-Michel Ville, and the members of the GVB group. I am also grateful to Zoheir Aboura's for his financial support of the event.

I also extend my deep gratitude to the people I worked with at the Roberval laboratory, who helped me see my experiments through. Thank you to Isabelle Velluet, Islam Ramadan, Loïc Escher, Yorick Buot de l'Épine and Kamal Naoui for sharing their experimental expertise and helping me carry out my experiments. Thank you to Islam Ramadan for his work on the development of the QMA measurement bench that I used throughout my work. Thank you to Philippe Pouille for taking the time and making his equipment available to experiment with materials they were not designed to be used with. I am also grateful to Thomas Boutin for taking the time to look for realistic solutions to problems which might not have had any, and for letting me work in his commendably tidy workshop.

Thank you to the permanent staff of the Roberval laboratory, and notably the acoustics and vibrations team. Thank you in particular to Jean-Daniel Chazot for sharing and explaining some codes and toolboxes created before my arrival. I also thank Stéphane Job and Jean-Philippe Crété from the ISAE-Supméca Quartz laboratory for collaborating on an article. I had many helpful and thorough discussions with Stéphane Job which I found enlightening. Thank you to Philippe Leclaire and Ludovic Cauvin for taking the time to participate in my yearly PhD progress review and giving their input on my work. I also thank Matelys members, notably François-Xavier Bécot, Fabien Marchetti, Luc Jaouen and Fabien Chevillotte for interesting conversations during several conferences.

Thank you to the other PhD students and interns of the Roberval laboratory for their good humour. Thank you in particular to Grégoire Markey, Simon Rampnoux, Camille Leblanc, Christophe Langlois, Alexandre Berthet, Luca Nicola Quaroni, Gabriel Gaucherand, Najib Bin Fazail, Stanislas Teillet, Carlos García, Thomas Poupon, Matthieu Duroyon, Apolline Brisson, Yackine Tadjou, Silouane de Reboul, Youcef Medelfef, and all the others I crossed during my time here. The real PhD was the friends I made along the way.

Thank you Kevin for your energy. Thank you to Ridley for the stews and the constant encouragement.

At last, thank you to my parents for supporting me in (nearly) every decision I take, and to Anthony for their motivating words.

Abbreviations

PBN	Pass-By Noise
SPL	Sound Pressure Level
TL	Transmission Loss
IL	Insertion Loss
ABIL	AirBorne Insertion Loss
SBIL	Solid-Borne Insertion Loss
TMM	Transfer Matrix Method
PTMM	Parallel Transfer Matrix Method
FEM	Finite Elements Method
RVE	Representative Volume Element
PUC	Periodic Unit Cell
DBM	Delany-Bazley-Miki model
JCA	Johnson-Champoux-Allard model
JCAL	Johnson-Champoux-Allard-Lafarge model
JCAPL	Johnson-Champoux-Allard-Pride-Lafarge model
FSI	Frame Stiffness Influence criterion
TTS	Time-Temperature Superposition
WLF	William-Landel-Ferry law
SEM	Scanning Electron Microscope
CI	Confidence Interval

Symbols

Constants and air properties

T_0	Ambient temperature: $T_0 = 18°\text{C} = 291.2$ K
P_0	Atmospheric pressure: $P_0 = 101.3$ kPa
R	Ideal gas constant: $R = 8.314\ \text{J}\,\text{K}^{-1}\,\text{mol}^{-1}$
$R_{specific}$	Specific gas constant of dry air: $R_{specific} = 287.0\ \text{J}\,\text{K}^{-1}\,\text{mol}^{-1}$
Pr	Prandtl number: $\text{Pr} = \frac{\mu_0 c_p}{\kappa_0} = 0.7107$
c_p	Specific heat at constant pressure: $c_p = 1002.3\ \text{J}\,\text{kg}^{-1}\,\text{K}^{-1}$
c_v	Specific heat at constant volume: $c_v = c_p - R_{specific} = 715.3\ \text{J}\,\text{kg}^{-1}\,\text{K}^{-1}$
γ_0	Heat capacity ratio of air: $\gamma = \frac{c_p}{c_v} = 1.401$
ρ_0	Air density: $\rho_0 = \frac{P_0}{RT} = 1.212\ \text{kg}\,\text{m}^{-3}$
c_0	Speed of sound in air: $c_0 = \sqrt{\frac{K_0}{\rho_0}} = \sqrt{\gamma_0 RT} = 342.2\ \text{m}\,\text{s}^{-1}$
K_0	Isostatic bulk modulus in air: $K_0 = \gamma_0 P_0 = \rho_0 c_0^2 = 1.42 \times 10^5$ Pa
Z_0	Characteristic impedance of air: $Z_0 = \rho_0 c_0 = 414.9\ \text{kg}\,\text{s}^{-1}\,\text{m}^{-2}$
μ_0	Dynamic viscosity: $\mu_0 = 1.84 \times 10^{-5}\text{kgm}^{-1}\,\text{s}^{-1}$ or $\text{N}\,\text{s}\,\text{m}^{-2}$

ν_0	Kinematic viscosity of air: $\nu_0 = \frac{\mu_0}{\rho_0} = 1.518 \times 10^{-5}\ \mathrm{m^2\,s^{-1}}$
κ_0	Thermal conductivity of air: $\kappa_0 = 0.256\ \mathrm{W\,m^{-1}K^{-1}}$
δ_0	Thickness of a fluid's viscous boundary layer, which is frequency-dependant: $\delta_0 = \sqrt{\frac{2\mu_0}{\omega\rho_0}}$ (m)
δ_0'	Thickness of a fluid's thermal boundary layer which is frequency-dependant: $\delta_0' = \frac{\delta_0}{\sqrt{\mathrm{Pr}}} = \sqrt{\frac{2K_0}{\omega\rho_0 c_p}}$.

General symbols

∇	Gradient operator
$\nabla\cdot$	Divergence operator
∇^2	Laplacian operator
N	Number of terms used in a model
i, j	Indices, when used as subscripts
j	Imaginary number ($j^2 = -1$)
f	Frequency (Hz)
ω	Angular frequency ($\mathrm{rad\,s^{-1}}$)
A	Amplitude of a periodic signal or wave
θ	Angle (°, rad)
p	Pressure of a wave propagating in a fluid (Pa)
v	Velocity of a wave propagating in a fluid ($\mathrm{m\,s^{-1}}$)
u	Displacement of a wave propagating in a fluid (m)
k	Wavenumber inside a fluid ($\mathrm{m^{-1}}$)
c	Wave velocity inside a fluid ($\mathrm{m\,s^{-1}}$)
K	Bulk modulus of a fluid (Pa)
ρ	Density of a fluid ($\mathrm{kg\,m^{-3}}$)
$Y(t)$	Heaviside step function
J	Cost function in an optimization problem
β	Set of several parameters used in a minimization problem

Transfer Matrix dimensions

α	Absorption coefficient (-)
α_d	Diffuse field absorption coefficient (-)
R	Reflection coefficient of a system (-)
T	Transmission coefficient of a system (-)
Z_s	Surface impedance at the surface of a system ($\mathrm{kg\,s^{-1}\,m^{-2}}$)
v_n	Normal velocity of a wave at the surface of a system ($\mathrm{m\,s^{-1}}$)
Z_t	Transfer impedance at the surface of a system ($\mathrm{kg\,s^{-1}\,m^{-2}}$)
v_p	Velocity of a radiating surface ($\mathrm{m\,s^{-1}}$)
σ_r	Radiation efficiency of a system (-)

$\{V\}$	State vector inside a medium in TMM
$[T_i]$	Transfer matrix relating the state vector at the start and at the end of a medium
$[I_{ij}]$	Interface matrix relating the state vectors between two media, corresponding to the medium downstream from the propagation
$[J_{ij}]$	Interface matrix relating the state vectors between two media, corresponding to the medium upstream of the propagation
$[D]$	Matrix representing the complete TMM system, without boundary conditions
$[D']$	Matrix representing the complete TMM system, with boundary conditions

Transport parameters and equivalent fluid properties

$\tilde{\rho}_{eq}$	Equivalent density of a fluid occupying the volume of the pores of a porous medium ($\mathrm{kg\,m^{-3}}$)
$\tilde{K}_{eq}$	Equivalent bulk modulus of a fluid occupying the volume of the pores of a porous medium (Pa)
$\tilde{\rho}_f$	Equivalent density of a fluid occupies the entire volume of a biphasic porous medium ($\mathrm{kg\,m^{-3}}$)
$\tilde{K}_f$	Equivalent bulk modulus of a fluid occupies the entire volume of a biphasic porous medium (Pa)
$\tilde{c}_{eq}$	Equivalent wave velocity in an equiavlent fluid ($\mathrm{m\,s^{-1}}$)
$\tilde{k}_{eq}$	Equivalent spatial wavenumber in an equiavlent fluid ($\mathrm{m^{-1}}$)
$\tilde{Z}_{eq}$	Equivalent impedance of an equiavlent fluid ($\mathrm{kg\,s^{-1}\,m^{-2}}$)
$\tilde{\alpha}_\omega$	Dynamic tortuosity of an equivalent fluid (-)
ϕ	Open porosity (-)
α_∞	High frequency limit of the tortuosity, or geometric tortuosity (-)
σ	Viscous airflow resistivity ($\mathrm{N\,s\,m^{-4}}$)
q_0	Viscous airflow permeability ($\mathrm{m^2}$)
R	Airflow resistance ($\mathrm{N\,s\,m^{-3}}$)
Λ	Viscous characteristic length (m)
Λ'	Thermal characteristic length (m)
q'_0	Static thermal permeability ($\mathrm{m^2}$)
α_0	Static viscous tortuosity (-)
α'_0	Static thermal tortuosity (-)
M	Viscous shape factor of the pores (-)
r	Porous material pore radius (m)
σ_s	Average pore radius when assuming a log-normal size distribution (m)
$\bar{s}$	Pore radius standard deviation when assuming a log-normal size distribution (m)
f_0	Transition frequency between low frequency and high frequency viscous effects, based on pore dimensions (Hz)
f'_0	Transition frequency between low frequency and high frequency thermal effects, based on pore dimensions (Hz)

f_v	Transition frequency between low frequency and high frequency viscous effects, independently of pore dimensions (Hz)
f_t	Transition frequency between low frequency and high frequency thermal effects, independently of pore dimensions (Hz)

General mechanical properties

E	Young's modulus (Pa)
$\tilde{E}$	Complex and frequency dependant modulus (Pa)
E'	Storage modulus (Pa)
E''	Loss modulus (Pa)
$\tilde{G}$, $\tilde{N}$	Complex and frequency dependant shear modulus (Pa)
G'	Shear storage modulus (Pa)
G''	Shear loss modulus (Pa)
E^*	Effective elastic modulus (Pa)
φ	Loss angle, or phase lag, between stress and strain (rad, °)
η	Loss factor (-)
τ	Material exponential decay relaxation time (s)
ν, $\tilde{\nu}$	Poisson ratio (-)
f_r	Quarter-wavelength frequency inside a poroelastic layer (Hz)
J_{el}	Elastic volume ratio (-)
E_{sec}	Secant modulus, defined as the ratio of stress over strain (Pa)
E_{tan}	Tangent modulus, defined as the derivative of stress with respect to strain (Pa)
E_s	Energy absorption efficiency (-)

Viscoelasticity parameters

E_i	Modulus of index i in the rheological representation of a viscoelastic model (Pa)
η_i	Viscosity of index i in the rheological representation of a viscoelastic model (-)
τ_i	Relaxation time of index i in the rheological representation of a viscoelastic model (s)
T_g	Glass transition tempearature of a medium (K, °C)
a_T	Frequency multiplication coefficient when performing TTS
T_R	Reference temperature when performing TTS (K, °C)
T_0	Target temperature to which to shift frequency-dependant data when performing TTS, or measurement temperature (K, °C)
C_1, C_2	WLF coefficients
E_a	Material activation energy for flow ($\mathrm{J\,mol^{-1}}$)
E_d	Energy dissipated by a viscoelastic material during a cyclical loading period (J)
a	Ageing parameter of the ageing model (-)
r	Rejuvenation parameter of the ageing model (-)
f	Fluidity term of the ageing model ($\mathrm{s^{-1}}$)

α_i, μ_i, ν_i	Hyperfoam parameters of index $i \geq 1$ (-, Pa, -)

Biot properties

ρ_1	Material skeleton density, also known as the true bulk density, equal to the porous material density *in vacuo* ($\mathrm{kg\,m^{-3}}$)
ρ_s	Density of the solid phase of the material ($\mathrm{kg\,m^{-3}}$)
$\tilde{\rho}_{limp}$	Equivalent fluid density when using the limp approximation ($\mathrm{kg\,m^{-3}}$)
$\tilde{\rho}_t$	Apparent density of the fluid phase with the limp hypothesis ($\mathrm{kg\,m^{-3}}$)
v_x^s	Velocity of the compression wave in the solid phase of a poroelastic medium ($\mathrm{m\,s^{-1}}$)
v_y^s	Velocity of the shear wave in the solid phase of a poroelastic medium ($\mathrm{m\,s^{-1}}$)
v_x^f	Velocity of the compression wave in the fluid phase of a poroelastic medium ($\mathrm{m\,s^{-1}}$)
σ_x^s	Stress of the compression wave in the solid phase of a poroelastic medium (Pa)
$\sigma_x y^s$	Stress of the shear wave in the solid phase of a poroelastic medium (Pa)
σ_x^f	Stress of the compression wave in the fluid phase of a poroelastic medium (Pa)
$\boldsymbol{\sigma}^t$	Total stress tensor in a biphasic porous medium
$\boldsymbol{\sigma}^f$	Stress tensor in the fluid phase of a biphasic porous medium
$\boldsymbol{\sigma}^s$	Stress tensor in the solid phase of a biphasic porous medium
ε^f	Strain tensor inside the fluid phase
ε^s	Strain tensor inside the solid phase
u^f	Displacement vector in the fluid phase (m)
u^s	Displacement vector in the solid phase (m)
$[\tilde{H}_E]$	Elasticity matrix of the skeleton
$[\tilde{H}_R]$	Elasticity matrix of the fluid
$[\tilde{H}_Q]$	Strain coupling matrix between the solid and fluid phases
$\tilde{K}_b$	Bulk modulus of the porous material (Pa)
$\tilde{K}_s$	Bulk modulus of material constituting the skeleton (Pa)
$\tilde{K}_c$	Bulk modulus of the skeleton *in vacuo* (Pa)
ρ_{12}	Apparent density caused by the added inertia due to the material tortuosity ($\mathrm{kg\,m^{-3}}$)
ρ_{11}	Apparent density of the solid phase of the material ($\mathrm{kg\,m^{-3}}$)
ρ_{22}	Apparent density of the fluid phase of the material ($\mathrm{kg\,m^{-3}}$)
δ_1, δ_2	Wavenumbers of the compression waves 1 and 2 ($\mathrm{m^{-1}}$)
δ_3	Wavenumber of the shear wave 3 ($\mathrm{m^{-1}}$)
ξ_1, ξ_2	Velocity ratio of the fluid over the velocity of the frame for the Biot compression waves 1 and 2 (sometimes written μ_1 and μ_2 in the literature) (-)
ξ_3	Velocity ratio of the fluid over the velocity of the frame for the Biot shear wave 3 (sometimes written μ_3 in the literature) (-)

Material dimensions

h	Material sample height or width (m)
S	Sample cross-section area (m^2)
D	Diameter of a cylindrical sample, and diameter of the impedance tube (m)
l	Porous cell strut length (m)
w	Porous cell strut width (m)
t	Porous cell strut average thickness (m)
h_0	Porous material cell height (m)
S_{pyr}	Pyramid cross-section area throughout its height (m^2)
w	Length of the side of the cross-section area of a pyramid throughout its height
w_0	Length of the side of the flat surface area at the tip of a pyramid
R_{asp}	Curvature radius of spherical asperities in the Greenwood-Williamson surface roughness model (m)
N_{asp}	Number of asperities on a rough surface in the Greenwood-Williamson surface roughness model
m_s	Surface mass density of a heavy layer($kg\,m^{-2}$)

Characterization bench and measurement setup related properties

L	Length of the impedance tube (m)
s	Spacing between the two microphones placed upstream from a sample in an impedance tube (m)
H_{ij}	Transfer function between microphones i and j (-)
V_{sample}	Total volume of a porous sample (m^3)
V_f	Fluid phase volume of a porous sample (m^3)
V_s	Solid phase volume of a porous sample (m^3)
V_t	Volume of a porosity measurement tank (m^3)
M_n	Slope of the squared refractive index of a porous medium as a function of $f^{-\frac{1}{2}}$
D_p	Penetration depth of an acoustic wave inside a porous material (wave amplitude divided by a factor 20) (m)
m	Slope of $\Sigma = \frac{\phi}{\rho_0}\left[\mathrm{Re}(\tilde{\rho}_{eq}) + \mathrm{Im}(\tilde{\rho}_{eq})\right]$ as a funcion of $\omega^{-3/2}$
f_{min}, ω_{min}	Minimum frequency / angular frequency required to perform a high-frequency asymptotic approximation on $\Sigma = \frac{\phi}{\rho_0}\left[\mathrm{Re}(\tilde{\rho}_{eq}) + \mathrm{Im}(\tilde{\rho}_{eq})\right]$ (Hz, $rad\,s^{-1}$)
Q	Volumetric flow rate of a fluid ($m^3\,s^{-1}$)
ΔP	Difference in air pressure upstream and downstream from a porous sample obstructing a flow (Pa)
ΔP_c	Difference in air pressure upstream and downstream from a calibrated airflow resistance sample obstructing a flow (Pa)
R_c	Airflow resistance of a calibrated airflow resistance sample obstructing a flow ($N\,s\,m^{-3}$)
$H(\nu)$	Function relating a sample's stiffness to its shape, its modulus and its Poisson ratio (-)

s	Sample shape factor, equal to the ratio of its diameter over its height (-)
S_p	Surface area of a radiating surface (m^2)
Π_{vib}	Vibrational power of a plate (W)
Π_{rad}	Radiated acoustic power (W)
Π_{inj}	Injected power into a system (W)
$vibIL$	Insertion Loss at constant vibrational power
F	Measured force (N)
δ	Compression distance of a sample (m)
δ_{err}	Error on the compression distance of a sample stemming from the wrong determination of its height (m)

Time convention $e^{-j\omega t}$ is used.
Variables written with the tilde diacritic ˜ are complex and frequency dependant.
Tensors are written in boldface.
Some numerical values have been hidden from the published version of this document for confidentiality reasons.

Contents

Preamble

Context

Vehicle noise constitutes a significant source of annoyance in densely populated urban areas. In the Île-de-France region in France, which encompasses Paris, a 2021 survey [1] revealed that road noise represents the biggest source of annoyance for 47 % of residents, followed by pedestrian behaviour for 20 % of the population. When residents are at home, it becomes the predominant source of annoyance for 30 % of people, followed by neighbourhood noises for 25 % of people. Exposure to excessive noise levels is harmful to human health, and is associated with greater risks of developing cardio-metabolic diseases such cardiac disorders, diabetes, hypertension, and heart attacks. According to the noise observatory Bruitparif, residents of the Île-de-France region lose 7 months of healthy life due to noise pollution from transportation, which leads to stress, hypertension, sleep disorders, and cardiovascular issues [2]. Furthermore, noise was identified as the second most harmful environmental factor after air pollution by the OMS [3], and causes 12 000 premature deaths every year in Europe, while exposing around 20 % of its population to harmful levels.

Consequently, the economic toll associated with noise pollution is substantial. In France, the cost of noise to society was estimated at 147.1 billion euros [4]. This cost incorporates non-merchant aspects, such as the impact on individuals such as annoyance, sleep deprivation, psychological illnesses, and learning difficulties. It also incorporates merchant costs, which include productivity loss, indemnities, hospitalizations, medicine, real estate depreciation, and costs of noise fighting programmes. A breakdown of these costs is shown in Figure 1.

Many standardization organizations and governing bodies have instituted regulations addressing the sound levels of vehicles, such as ISO standards, SAE standards, and others [5]. The United Nations Economic Commission for Europe (UNECE) has established European regulation 51, concerning the Pass-By Noise (PBN) of four-wheeled vehicles, as a measure to combat against excessive road traffic noise. Over time, this regulation has been revised, leading to a reduction of the maximum allowed pass-by noise level from 82 dBA in 1970 to 68 dBA in 2024 [6, 7], as illustrated in Figure 2. In practical terms, this is equivalent to a single car in 1970 being allowed the noise level of thirty cars in 2024. Furthermore, this regulation was recently reviewed to improve the urban soundscape by changing the measurement procedure and reducing the allowed PBN from 72 dBA in 2016 to 68 dBA in 2024. The new regulation, denoted as 51.3, supersedes its predecessor 51.2, by modifying the PBN measurement protocol and reducing the maximum allowed level. As a consequence, the automotive industry is consistently seeking innovative and efficient ways to diminish the acoustic emissions of their vehicles.

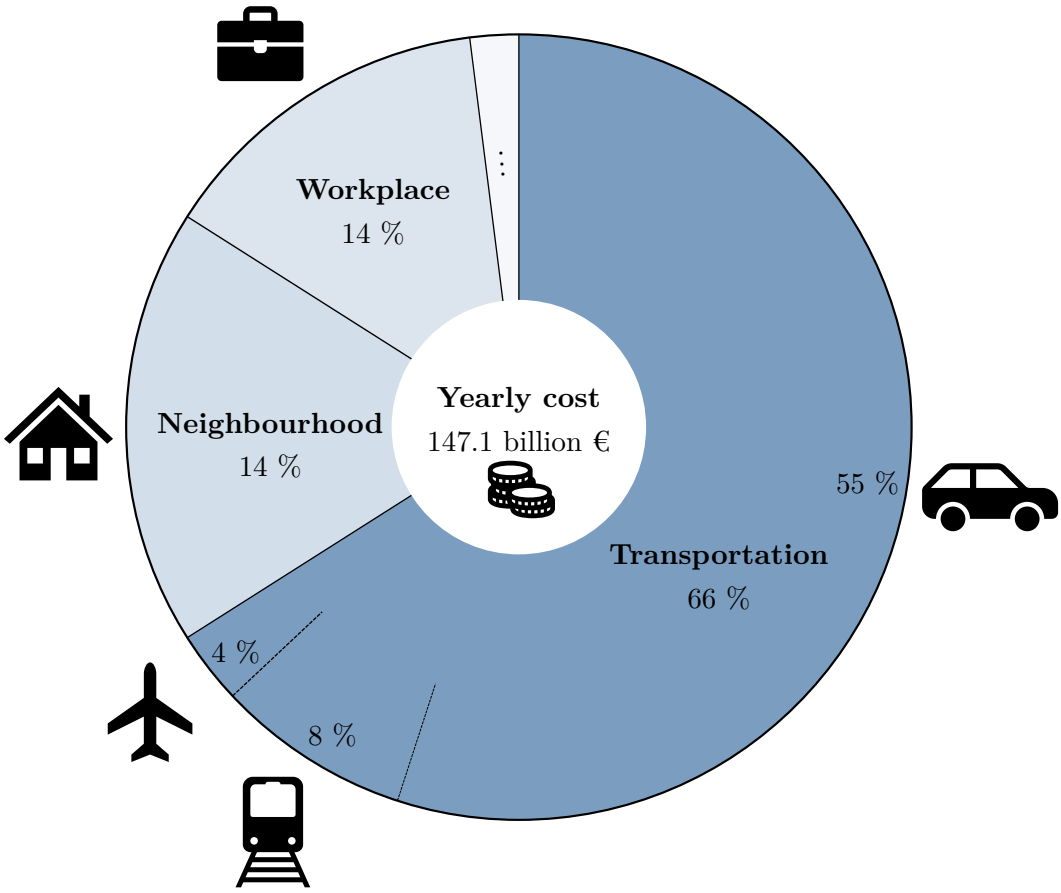

Figure 1. Yearly cost of noise to society in France, from reference [4].

Engine encapsulation

Cars contain several noise sources that can be addressed to reduce their overall noise radiation. Tyre noise is a major source of noise, especially as a car's speed increases. It can be radiated outwards from the vibration of the tyre sidewalls, or be transmitted into the cabin through solid-borne propagation. Reducing tyre noise is a challenging task because it often has adverse effects on fuel consumption and driving safety. Exhaust noise is another significant source of noise, yet thanks to advancements in exhaust silencers, it is quite well controlled in modern vehicles. Aerodynamic noises become predominant as a car's speed increases, and present a major difficulty to be controlled. Finally, engine noise is predominant at low car speeds, and serves as the focal point of this research project. Some car noise sources are illustrated in Figure 3, and the contribution of different noises for varying car speeds is shown in Figure 4. Generally, it is accepted that tyre rolling noise is the predominant noise source in pass-by noise tests, representing the majority of the radiated noise. Consequently, due to the ongoing difficulty of reducing tyre rolling noise, strong constrains are placed on reducing the other noise sources. Altogether, it is important to keep in mind that due to the masking effect of sound, each of these noise sources should be targeted independently to achieve an overall reduction of the noise level.

The reduction of combustion engine noise can be achieved through encapsulation with poroelastic materials. These materials have many practical applications thanks to their high porosity, flexibility, and damping, and are used as a passive solution in many industries, including the construction, aeronautic, and automotive industries. They have demonstrated their efficacy in shock absorption in packaging [10, 11] and impact damping [12, 13], possibly associated with a structure [14, 15]. Further, as components of multilayer panels, they contribute significantly to vibration reduction [16] and

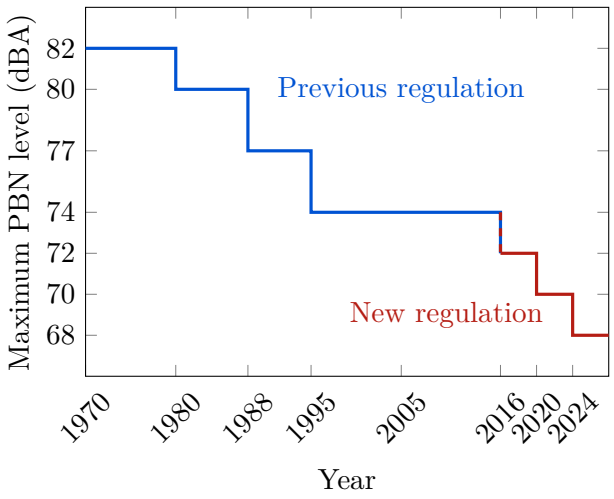

Figure 2. Regulated maximum allowed PBN over time in Europe.

Figure 3. Noise sources on a car.

acoustic insulation [17, 18, 19, 20, 21]. Porous screens are also used to provide radiation attenuation of vibroacoustic sources [22, 23, 24, 25].

The ECoBEx project, acronym for "Optimized screens for external noise" (or "ÉCrans optimisés pour le Bruit Extérieur"), and run from 2014 to 2017, demonstrated the effectiveness of porous screens in reducing the noise radiated by engines [26]. Porous screens have two main acoustic roles in engine encapsulation. First, they absorb the energy of impinging sound waves thanks to their internal dissipation properties. Second, they create an insulation barrier between the acoustic source and the outside environment, by taking advantage of the mass or of the spring-mass-like behaviour. For high cover rates of the porous screens around the acoustic source (above 50 % approximately [27]), it much more advantageous to exploit the insulating behaviour of the screens rather than their absorbing properties. The ECoBEx project studied the case of thermocompressed screens of varying thickness placed around the engine bay, such as hood liners and dashboard insulators, which leveraged the absorption performance of these porous screens. A thermocompressed porous hood liner and dashboard insulator are pictured in Figure 5.

An alternative setup to the solutions proposed by the ECoBEx project involves placing the porous screens in direct contact with the engine, which offers several advantages. First, the reduced surface area to cover reduces the required volume of screens, which reduces manufacturing costs and primary goods consumption. Second, the reduced volume of the screens contributes to weight reduction and positively impacts fuel consumption. Third, positioning the screens closer to the acoustic source and the ability to achieve very high cover rates of the engine reduce the risks of acoustic leaks. Some examples of porous encapsulation screens are presented in Figure 6. These screens are mounted around various parts of the engine and have the ability to follow their geometry closely, resulting in

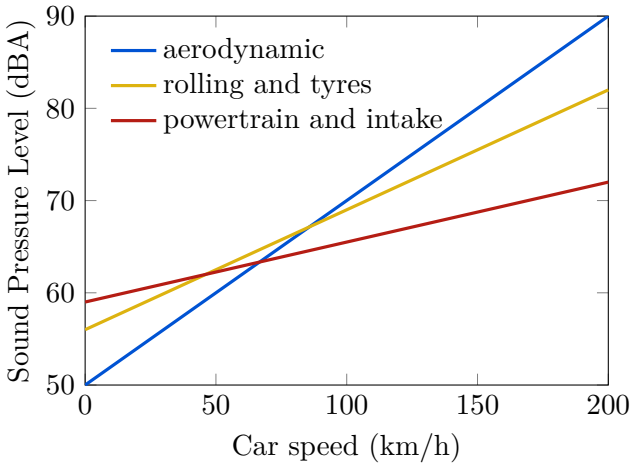

Figure 4. SPL of different car noise sources as a function of car speed [8, 9].

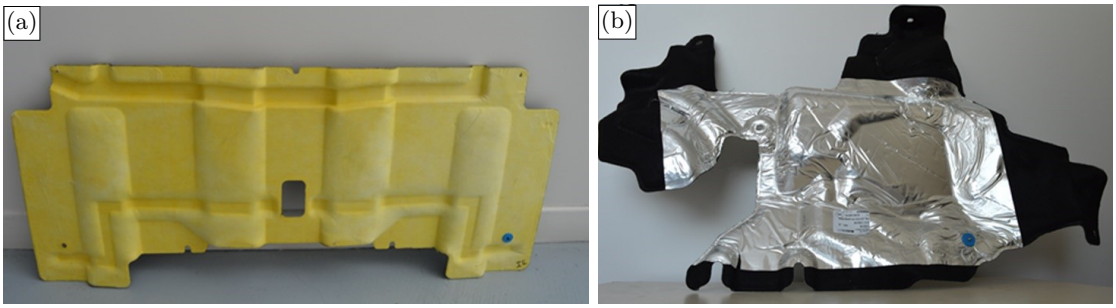

Figure 5. ECoBEx poroelastic screens used for automotive applications, from reference [26]. (a) A hood liner, and (a) a dashboard insulator.

high contact areas. They are often held in place by tuckers, which are solid pieces that clip onto the engine and compress the porous screens in place.

This new configuration offers several advantages, however it also changes the acoustic behaviour of the screens. Instead of being driven by their absorption capabilities, the screens' behaviour is now driven by their acoustic insulating capabilities, where a mass-spring behaviour can be taken advantage of. Furthermore, the acoustic behaviour of the screens is significantly altered by the direct transmission of solid-borne engine vibrational waves. The SEMPAE project, acronym for "Simulation of engine encapsulation for exterior acoustics" (or "Simulation d'Encapsulage Moteur Pour l'Acoustique Externe"), focuses on studying and enhancing engine encapsulation technology for encapsulation materials placed directly in contact with the engine. This project was run from 2020 to 2024, and its ultimate goal is to produce a numerical prediction of the pass-by noise level contribution of a car engine encapsulated by porous screens. As a note, although this project was conceived mostly to treat combustion engine noise, acoustic encapsulation is also applited to electric vehicle motors, due to higher frequency tonal electric noise and mechanical noise sources from the gear motor.

Figure 6. Possible encapsulation components of a car engine using poroelastic screens [28].

Framework of the SEMPAE project

The SEMPAE project is a collaboration between three companies, Renault Group, ESI Group, and Trèves Group, and the Roberval research laboratory. Renault Group is a leading car manufacturer with expertise in measuring and characterizing the acoustic radiation of bare and encapsulated engine components. Additionally, they are equipped to perform standardized PBN measurements on real vehicles. Trèves Group is an automotive supplier specializing in manufacturing underbody, boot, engine and car interior trim porous materials, including encapsulation screens. Furthermore, as head coordinator of the SEMPAE project, they provided the technical specifications for the experimental and numerical investigations. They measured the sound radiation of a real engine casing part to evaluate the impact of the screens, and correlated the findings with a full numerical model of the experimental setup. ESI Group is a software publisher specializing in mechanical, acoustic, and crash test numerical simulations. Their objective was to numerically predict the radiated noise of the encapsulated engine. However, they withdrew from the project midway, and the numerical modelling was resumed by Trèves Group. As a result, part of the thesis work was redirected to a more academic investigation about compression of porous material with asperities in collaboration with colleagues from the ISAE-Supméca Quartz laboratory.

Finally, the Université de technologie de Compiègne (UTC) Roberval research laboratory performs numerical and experimental multi-physics work, with proficiency in acoustics, vibrations, material behaviour and computational mechanics. The PhD work presented in this dissertation was hosted by the Roberval laboratory, and its research was focused on characterizing and modelling of the encapsulation materials. The objectives of this thesis were to synthesize and challenge porous characterization methods to apply them to the encapsulation materials, and to identify the modelling approaches that best capture material behaviour. The initial project organization is illustrated in Figure 7.

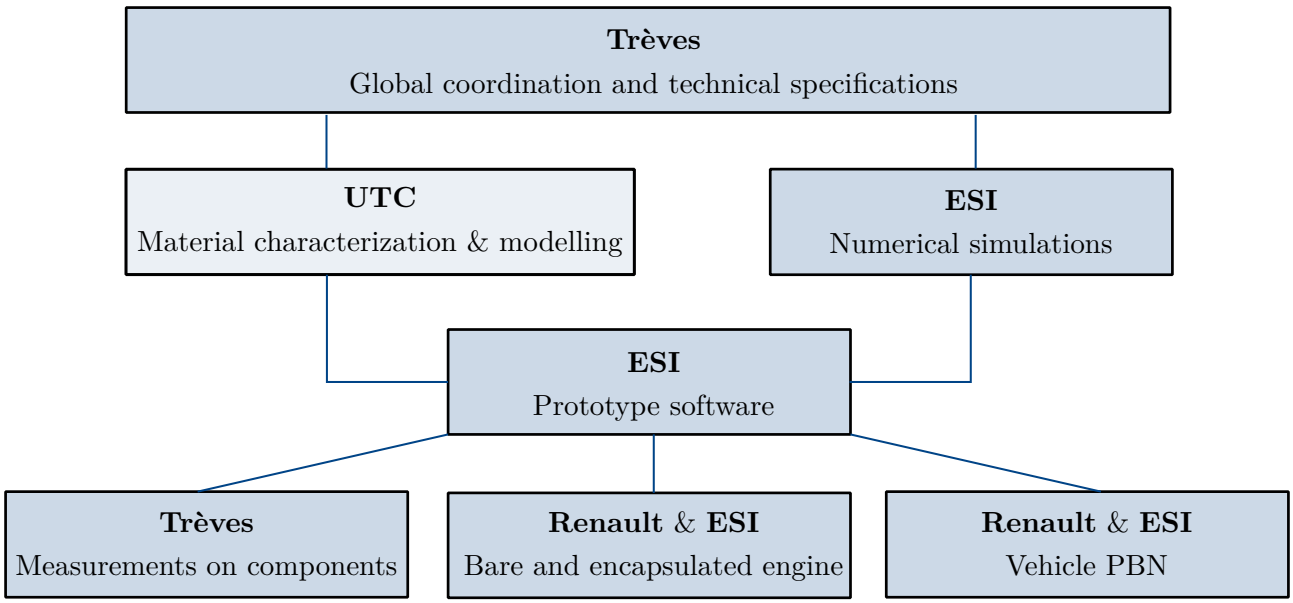

Figure 7. Diagram of the initial organization of the SEMPAE project.

Objectives of the thesis and structure of the document

The focus of PhD research conducted within the SEMPAE project centred on the characterization and the modelling of engine encapsulation materials placed in contact with the engine. While many methods are available to characterize porous materials, the absence of robust methods for certain properties, notably mechanical properties, poses a challenge, and the characterization of some encapsulation materials can be particularly tricky, because of their inhomogeneity and high resistivity for example. Moreover, the placement of the porous screens in contact with the engine raises questions about their behaviour. For instance, the mechanical preload applied onto the material also affects its mechanical properties and the amount of contact it has with the engine, which is crucial in determining the acoustic insulation efficiency. This partial contact can arise due to the complex engine geometry and to the uneven surface of the encapsulation material. These are some of the subjects that needed to be explored to meet the objectives of the SEMPAE project.

This document is structured as follows. First, an overview of the state of the art of porous materials modelling is given in Chapter 1. Next, porous material characterization methods are investigated and applied to encapsulation materials in Chapter 2, in order to determine the capabilities and limits of existing methods and the conditions for obtaining the best results on real non-ideal materials. Equivalent fluid transport parameters as well as mechanical parameters are obtained. Then, the partial contact due to the compression of macroscopic asperities of a rough porous surface, as well as material nonlinearity and relaxation, are studied in detail in Chapter 3. This sheds light on the influence of the static preload on the material's mechanical behaviour, notably for small displacements where the roughness asperities are compressed before the bulk material behaviour. Finally, the reduction of the noise level of a radiating plate covered by a porous screen with partial contact is investigated in Chapter 4. Conclusions and perspectives are given at the end of this document in the General conclusion.

Chapter 1. State of the art of porous media modelling

1 | Introduction

Porous media have a complex microstructure which gives them interesting characteristics. Due to this biphasic nature, composed in part of a solid phase, and in part of a fluid phase saturating the material's pores, simplifying assumptions about the way waves propagate within them are made to model their behaviour. In this chapter, a bibliography of models and methods used to predict the acoustic behaviour of porous media is presented. These bibliographical elements and methods are commonly used when studying porous materials.

Predicting the acoustic behaviour of a porous medium is done using the biphasic Biot model, which accounts for waves propagating in its solid and fluid phases, and is presented in Section 2. The Biot model couples the behaviour of these two distinct phases which each contribute to dissipating energy through damping. The solid phase can thus be modelled using a viscoelastic model, as explained in Section 3, and the fluid phase using an equivalent fluid model, as presented in Section 4. To quickly predict the acoustic behaviour of one-dimensional arrays of porous layers by incorporating the Biot model, a simple solution called the transfer matrix method is presented in Section 5, and is used to showcase the differences between the existing models in Section 6. Finally, a common method to experimentally measure the behaviour of porous materials is presented using an impedance tube is presented in Section 7.

2 | Wave propagation in poroelastic media

2.1 | Biphasic nature of porous media

A porous material consists of two phases: a solid phase, also known as the skeleton or the frame, and a fluid phase filling the pores, composed of air in our case. These are shown in Figure 1.1(a). Among porous materials, we can distinguish foams with a polymer skeleton, such as polyurethane foam and melamine foam for instance, fibrous materials composed of tangled fibres, such as glass wool, rock wool, and biomaterials, and granular materials consisting of particles in contact, such as sand and powders.

The propagation of an impinging acoustic wave through a porous media results in viscous and thermal energy dissipation effects. A first source of dissipation is the skeleton's viscoelastic behaviour which mechanically dissipates energy during loading-unloading cycles, which is the strongest around the skeleton's resonance frequencies [29]. Another source of dissipation is the viscosity of the fluid moving inside the pores rubbing against the skeleton. The final source of dissipation is the thermal gradient created by the pressure wave exchanging thermal energy with the skeleton. The dissipative behaviour of porous materials combined with their light weight and flexibility makes them highly attractive for many applications.

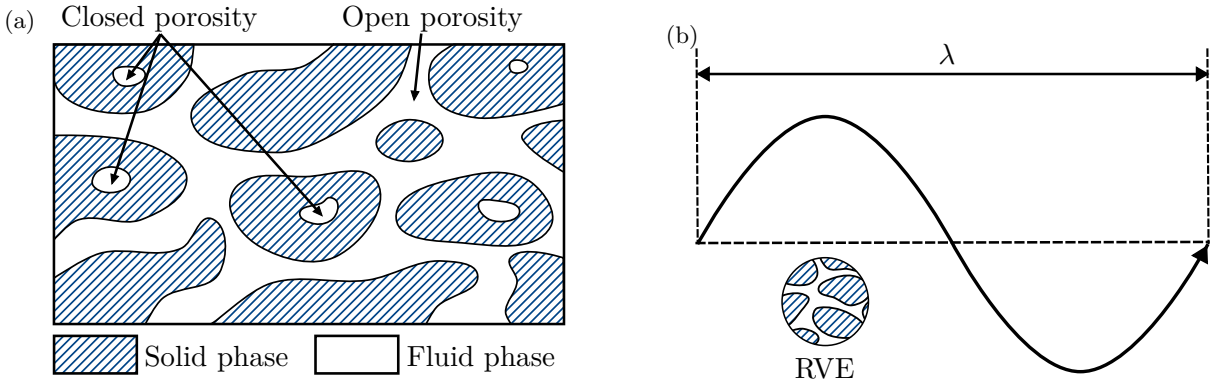

Figure 1.1. (a) Representation of the biphasic nature of a porous material. (b) The Representative Volume Element (RVE) must be much smaller than the wavelength.

The propagation of waves through a porous medium can be modelled at varying levels of complexity, from modelling only the acoustic wave in the fluid phase to accounting for the multiple waves propagating through the fluid and the skeleton. The hypothesis of material homogeneity is commonly assumed for their modelling. This is done by estimating the Representative Volume Element (RVE) of the material, which is the smallest volume in which the material properties can be considered homogeneous and representative of the entire medium. The homogeneity hypothesis postulates that the wavelength of the waves is much larger than the RVE, for both the skeleton and the fluid filling the pores, as shown in Figure 1.1(b). This allows the homogenization principle to be applied. It is also required that the RVE be statistically representative of the material as a whole. For example, Nguyen et al. [30] find that this is valid when the RVE contains more than approximately 10 pore diameters. Models used in this work to model porous materials presented below are based on this homogenization hypothesis.

2.2 | Poroelastic Biot-Allard Model

2.2.1 | Origins and base formulation

The question of acoustic wave propagation in porous media was studied by Beranek in 1947 [31] and Zwikker and Kosten in 1949 [32]. The models they proposed were limited in material types, frequency range and geometry. Then, Biot proposed a model in 1956 [33, 34, 35], which was initially developed for geological applications and oil prospection. It caused some controversy when it was published, first because the theory of homogenization had not been invented yet [36], and second because the slow compression wave it predicted had been too difficult to measure in low and high frequencies until 1980 [37]. Lakes [38] examines the validity of classical elasticity when applied to porous media, finding that Cosserat elasticity may give better predictions. Biot's theory was then applied to acoustics by Allard in 1993 [39] by integrating the work done by Johnson [40], Champoux and Allard [41], and Lafarge [42] into the Biot model, into what is sometimes called the Biot-Allard theory.

The Biot model considers the biphasic medium as the superposition of two coupled media occupying the volume, which are the viscoelastic solid and the fluid phases. The observation scale is considered much larger relative to the RVE, so the observed dimensions are statistically averaged over the RVE, a condition required for the stress-strain relations to be valid [43]. The Biot model relies on continuous media mechanics formalism with a small strains hypothesis and a linear stress-strain relationship.

The Biot model expresses the total stress tensor $\boldsymbol{\sigma}^t$ as the sum of the stress tensor in the fluid $\boldsymbol{\sigma}^f$ and the skeleton $\boldsymbol{\sigma}^s$:

$$\boldsymbol{\sigma}^t = \boldsymbol{\sigma}^f + \boldsymbol{\sigma}^s. \tag{1.1}$$

The fluid stress tensor $\boldsymbol{\sigma}^f$ contains only compressive pressures and is related to the fluid pressure p, whereas the skeleton stress tensor $\boldsymbol{\sigma}^s$ contains shear and compressive stresses. They are given by

$$\boldsymbol{\sigma}^f = \begin{bmatrix} -\phi p & 0 & 0 \\ 0 & -\phi p & 0 \\ 0 & 0 & -\phi p \end{bmatrix}, \quad \boldsymbol{\sigma}^s = \begin{bmatrix} \sigma^s_{11} & \sigma^s_{12} & \sigma^s_{13} \\ \sigma^s_{21} & \sigma^s_{22} & \sigma^s_{23} \\ \sigma^s_{31} & \sigma^s_{32} & \sigma^s_{33} \end{bmatrix}. \tag{1.2}$$

The porosity ϕ represents the ratio of fluid volume to the total porous material volume [44]:

$$\phi = \frac{V_{air}}{V_t}. \tag{1.3}$$

In the fluid and the skeleton, the compressive strain ε_{ii} and shear strain ε_{ij} are related to the displacement u by

$$\varepsilon_{ii} = \frac{\partial u_i}{\partial x_i}, \quad \varepsilon_{ij} = \frac{1}{2}\left(\frac{\partial u_i}{\partial x_j} + \frac{\partial u_j}{\partial x_j}\right). \tag{1.4}$$

Because the stress tensors are symmetric, they can be written using Voigt notation:

$$\{\sigma^s\} = (\sigma^s_{11}, \sigma^s_{22}, \sigma^s_{33}, \sigma^s_{12}, \sigma^s_{23}, \sigma^s_{31})^T, \quad \{\sigma^f\} = (-\phi p, \ -\phi p, \ -\phi p, 0, 0, 0)^T. \tag{1.5}$$

Voigt notation is also used for strain tensor representation

$$\{\varepsilon^s\} = \begin{Bmatrix} \varepsilon^s_{11} \\ \varepsilon^s_{22} \\ \varepsilon^s_{33} \\ 2\varepsilon^s_{12} \\ 2\varepsilon^s_{23} \\ 2\varepsilon^s_{31} \end{Bmatrix} = \begin{bmatrix} \frac{\partial}{\partial x_1} & 0 & 0 \\ 0 & \frac{\partial}{\partial x_2} & 0 \\ 0 & 0 & \frac{\partial}{\partial x_3} \\ \frac{\partial}{\partial x_2} & \frac{\partial}{\partial x_1} & 0 \\ 0 & \frac{\partial}{\partial x_3} & \frac{\partial}{\partial x_2} \\ \frac{\partial}{\partial x_3} & 0 & \frac{\partial}{\partial x_1} \end{bmatrix} \begin{Bmatrix} u^s_1 \\ u^s_2 \\ u^s_3 \end{Bmatrix}, \quad \{\varepsilon^f\} = \begin{Bmatrix} \varepsilon^s_{11} \\ \varepsilon^s_{22} \\ \varepsilon^s_{33} \\ 2\varepsilon^s_{12} \\ 2\varepsilon^s_{23} \\ 2\varepsilon^s_{31} \end{Bmatrix} = \begin{bmatrix} \frac{\partial}{\partial x_1} & 0 & 0 \\ 0 & \frac{\partial}{\partial x_2} & 0 \\ 0 & 0 & \frac{\partial}{\partial x_3} \\ \frac{\partial}{\partial x_2} & \frac{\partial}{\partial x_1} & 0 \\ 0 & \frac{\partial}{\partial x_3} & \frac{\partial}{\partial x_2} \\ \frac{\partial}{\partial x_3} & 0 & \frac{\partial}{\partial x_1} \end{bmatrix} \begin{Bmatrix} u^f_1 \\ u^f_2 \\ u^f_3 \end{Bmatrix}. \tag{1.6}$$

Next, the stress-strain relationship in Biot's theory is given as:

$$\begin{cases} \{\sigma^s\} = [\tilde{H}_E]\{\varepsilon^s\} + [\tilde{H}_Q]\{\varepsilon^f\} \\ \{\sigma^f\} = [\tilde{H}_Q]\{\varepsilon^s\} + [\tilde{H}_R]\{\varepsilon^f\}, \end{cases} \tag{1.7}$$

where $[\tilde{H}_E]$ is the elasticity matrix of the skeleton, $[\tilde{H}_R]$ the elasticity matrix of the fluid and $[\tilde{H}_Q]$ is strain coupling matrix between the phases. When the material is isotropic, they are expressed as

$$[\tilde{H}_R] = \begin{bmatrix} \tilde{R} & \tilde{R} & \tilde{R} & 0 & 0 & 0 \\ \tilde{R} & \tilde{R} & \tilde{R} & 0 & 0 & 0 \\ \tilde{R} & \tilde{R} & \tilde{R} & 0 & 0 & 0 \\ 0 & 0 & 0 & 0 & 0 & 0 \\ 0 & 0 & 0 & 0 & 0 & 0 \\ 0 & 0 & 0 & 0 & 0 & 0 \end{bmatrix}, \quad [\tilde{H}_Q] = \begin{bmatrix} \tilde{Q} & \tilde{Q} & \tilde{Q} & 0 & 0 & 0 \\ \tilde{Q} & \tilde{Q} & \tilde{Q} & 0 & 0 & 0 \\ \tilde{Q} & \tilde{Q} & \tilde{Q} & 0 & 0 & 0 \\ 0 & 0 & 0 & 0 & 0 & 0 \\ 0 & 0 & 0 & 0 & 0 & 0 \\ 0 & 0 & 0 & 0 & 0 & 0 \end{bmatrix}. \tag{1.8}$$

Biot performed two thought experiments ("gedanken" experiments) to find expressions for the elastic coefficient $\tilde{R}$ and the coupling coefficient $\tilde{Q}$. When the bulk modulus of the porous material $\tilde{K}_b$ is

much smaller than the bulk modulus of the elastic material of the skeleton $\tilde{K}_s$, $\tilde{R}$ and $\tilde{Q}$ are given as

$$\tilde{R} = \phi^2 \tilde{K}_{eq}, \tag{1.9}$$

$$\tilde{Q} = (1-\phi)\phi \tilde{K}_{eq}, \tag{1.10}$$

where $\tilde{K}_{eq}$ is the fluid phase's equivalent bulk modulus, which is complex and frequency dependant representing its dissipative properties. Next, the elasticity matrix of the skeleton $[\tilde{H}_E]$ is

$$[\tilde{H}_E] = \begin{bmatrix} \tilde{P} & \tilde{A} & \tilde{A} & 0 & 0 & 0 \\ \tilde{A} & \tilde{P} & \tilde{A} & 0 & 0 & 0 \\ \tilde{A} & \tilde{A} & \tilde{P} & 0 & 0 & 0 \\ 0 & 0 & 0 & \tilde{N} & 0 & 0 \\ 0 & 0 & 0 & 0 & \tilde{N} & 0 \\ 0 & 0 & 0 & 0 & 0 & \tilde{N} \end{bmatrix} = \begin{bmatrix} \tilde{A} & \tilde{A} & \tilde{A} & 0 & 0 & 0 \\ \tilde{A} & \tilde{A} & \tilde{A} & 0 & 0 & 0 \\ \tilde{A} & \tilde{A} & \tilde{A} & 0 & 0 & 0 \\ 0 & 0 & 0 & 0 & 0 & 0 \\ 0 & 0 & 0 & 0 & 0 & 0 \\ 0 & 0 & 0 & 0 & 0 & 0 \end{bmatrix} + \begin{bmatrix} 2\tilde{N} & 0 & 0 & 0 & 0 & 0 \\ 0 & 2\tilde{N} & 0 & 0 & 0 & 0 \\ 0 & 0 & 2\tilde{N} & 0 & 0 & 0 \\ 0 & 0 & 0 & \tilde{N} & 0 & 0 \\ 0 & 0 & 0 & 0 & \tilde{N} & 0 \\ 0 & 0 & 0 & 0 & 0 & \tilde{N}, \end{bmatrix} \tag{1.11}$$

where the elastic coefficient $\tilde{P}$ is related to $\tilde{A}$ and $\tilde{N}$ by

$$\tilde{P} = \tilde{A} + 2\tilde{N}. \tag{1.12}$$

By performing a third thought experiment, Biot shows that $\tilde{N}$ corresponds to the shear modulus $\tilde{G}$ of the solid phase, also sometimes called the second Lamé coefficient μ in the literature:

$$\tilde{N} = \frac{\tilde{E}}{2(1+\nu)}. \tag{1.13}$$

It is related to the bulk modulus by $\tilde{K}_b = \frac{2\tilde{N}(1+\nu)}{3(1-2\nu)}$. $\tilde{A}$ corresponds to the first Lamé coefficient, also written λ in the literature:

$$\tilde{A} = \frac{\nu \tilde{E}}{(1+\nu)(1-2\nu)} + \frac{\tilde{Q}^2}{\tilde{R}}. \tag{1.14}$$

In these expressions, ν is the Poisson ratio and $\tilde{E}$ is the elastic Young's modulus, which can be complex and frequency dependant. By using Lagrange's equation and by introducing a viscous dissipation function, Biot finds the following equation of motion

$$\begin{cases} \nabla \cdot \tilde{\boldsymbol{\sigma}}^s = \rho_{11} \frac{\partial^2 \{u^s\}}{\partial t^2} + \rho_{12} \frac{\partial^2 \{u^f\}}{\partial t^2} + \tilde{b} \left(\frac{\partial \{u^s\}}{\partial t} - \frac{\partial \{u^f\}}{\partial t} \right) \\ \nabla \cdot \tilde{\boldsymbol{\sigma}}^f = \rho_{12} \frac{\partial^2 \{u^s\}}{\partial t^2} + \rho_{22} \frac{\partial^2 \{u^f\}}{\partial t^2} + \tilde{b} \left(\frac{\partial \{u^f\}}{\partial t} - \frac{\partial \{u^s\}}{\partial t} \right) \end{cases}, \tag{1.15}$$

where $\nabla\cdot$ is the divergence and t is the time variable. The apparent density ρ_{12} is the added inertia due to tortuosity, and ρ_{11} and ρ_{22} are the apparent densities of the solid and fluid phases of the material.

$$\rho_{12} = -\phi \rho_0 (\alpha_\infty - 1), \tag{1.16}$$

$$\rho_{11} = \rho_1 - \rho_{12}, \tag{1.17}$$

$$\rho_{22} = \phi \rho_0 - \rho_{12}, \tag{1.18}$$

where ρ_0 is the density of the surrounding fluid and ρ_1 is the bulk density of the porous material *in vacuo*, also known as the true bulk density:

$$\rho_1 = (1-\phi)\rho_s, \tag{1.19}$$

where ρ_s is the density of solid phase of the material.

Finally, by combining the equations of motion with the stress-strain relationship, the Biot model equations are found:

$$\begin{cases} -\omega^2\tilde{\rho}_{11}\{u^s\} - \omega^2\tilde{\rho}_{12}\{u^f\} = \tilde{N}\nabla^2\{u^s\} + (\tilde{P}-\tilde{N})\nabla^2\cdot\{u^s\} + \tilde{Q}\nabla^2\cdot\{u^f\} \\ -\omega^2\tilde{\rho}_{12}\{u^s\} - \omega^2\tilde{\rho}_{22}\{u^f\} = \tilde{Q}\nabla^2\cdot\{u^s\} + \tilde{R}\nabla^2\cdot\{u^f\}. \end{cases} \tag{1.20}$$

The apparent Biot densities are enriched with the viscous dissipative effects through the coefficient $\tilde{b}$, yielding the inertial coefficients $\tilde{\rho}_{11}$ for the solid phase, $\tilde{\rho}_{22}$ for the fluid phase, and $\tilde{\rho}_{12}$ for the coupling:

$$\tilde{\rho}_{11} = \rho_{11} - j\frac{\tilde{b}}{\omega}, \tag{1.21}$$

$$\tilde{\rho}_{22} = \rho_{22} - j\frac{\tilde{b}}{\omega}, \tag{1.22}$$

$$\tilde{\rho}_{12} = \rho_{12} + j\frac{\tilde{b}}{\omega}, \tag{1.23}$$

Additionally, the viscous damping coefficient $\tilde{b}$, which was initially chosen as a real constant by Biot, can be given a frequency dependant expression using an equivalent fluid model that represents the dissipation inside the fluid phase. For example, using the parameters of the JCA motionless skeleton equivalent fluid model described in Section 4.3.3, $\tilde{b}$ can be expressed as

$$\tilde{b} = \phi^2\sigma\sqrt{1 + j\omega\frac{M}{2}\frac{\alpha_\infty\rho_f}{\phi\sigma}}, \tag{1.24}$$

where the shape factor M is given by

$$M = \frac{8\alpha_\infty\mu}{\sigma\phi\Lambda^2}. \tag{1.79}$$

α_∞ is the high frequency limit of the tortuosity, σ is the airflow resistivity, and Λ is the viscous characteristic length described in Section 4.2. The ratio of the velocity of the fluid over that of the frame for the compression waves, ξ_1 and ξ_2, and the for the shear wave, ξ_3, are

$$\xi_1 = \frac{\tilde{P}\delta_1^2 - \tilde{\rho}_{11}\omega^2}{\tilde{\rho}_{12}\omega^2 - \tilde{Q}\delta_1^2}, \tag{1.25}$$

$$\xi_2 = \frac{\tilde{P}\delta_2^2 - \tilde{\rho}_{11}\omega^2}{\tilde{\rho}_{12}\omega^2 - \tilde{Q}\delta_2^2}, \tag{1.26}$$

$$\xi_3 = \frac{N\delta_3^2 - \omega^2\tilde{\rho}_{11}}{\omega^2\tilde{\rho}_{22}}. \tag{1.27}$$

The complex wavenumbers of the two compression waves δ_1 and δ_2, and the wavenumbers of the shear wave δ_3 are

$$\delta_1 = \sqrt{\frac{\omega^2}{2(\tilde{P}\tilde{R}-\tilde{Q}^2)}\left(\tilde{P}\tilde{\rho}_{22} + \tilde{R}\tilde{\rho}_{11} - 2\tilde{Q}\tilde{\rho}_{12} - \sqrt{\xi}\right)}, \tag{1.28}$$

$$\delta_2 = \sqrt{\frac{\omega^2}{2(\tilde{P}\tilde{R}-\tilde{Q}^2)}\left(\tilde{P}\tilde{\rho}_{22} + \tilde{R}\tilde{\rho}_{11} - 2\tilde{Q}\tilde{\rho}_{12} + \sqrt{\xi}\right)}, \tag{1.29}$$

$$\delta_3 = \sqrt{\frac{\omega^2}{\tilde{N}}\frac{\tilde{\rho}_{11}\tilde{\rho}_{22} - \tilde{\rho}_{12}^2}{\tilde{\rho}_{22}}}, \tag{1.30}$$

where

$$\xi = \left(\left(\tilde{P}\tilde{\rho}_{22} + \tilde{R}\tilde{\rho}_{11} - 2\tilde{Q}\tilde{\rho}_{12} \right)^2 - 4 \left(\tilde{P}\tilde{R} - \tilde{Q}^2 \right) \left(\tilde{\rho}_{11}\tilde{\rho}_{22} - \tilde{\rho}_{12}^2 \right) \right). \tag{1.31}$$

As a result of Equation 1.20, the Biot model describes three coupled waves propagating within a homogenized biphasic medium: two compression waves, one which propagates mostly in the skeleton and one which propagates mostly in the fluid, and a shear wave. For normal incidence waves, no shear wave propagates in the medium.

2.2.2 | Different formulations

Different formulations of the Biot model exist. The formulation in Equation 1.20 starts with the solid and fluid phase stress tensors $\boldsymbol{\sigma}^s$ and $\boldsymbol{\sigma}^f$ to obtain a state vector containing the three solid phase displacements $\{u^s\}$ and three fluid phase displacements $\{u^f\}$. Biot suggested a new formulation in 1962 [45] starting from the total stress tensor $\boldsymbol{\sigma}^t$ and the fluid pressure p to obtain a state vector containing $\{u^s\}$ and $\{w\} = \phi \left(\{u^f\} - \{u^s\} \right)$. A formulation by Dazel et al. [46] obtains a state vector containing the total displacement $\{u^t\}$ and the skeleton displacement $\{u^s\}$, resulting in simplified equations without any further assumptions.

Another commonly used formulation consists in using a state vector containing the solid phase displacement $\{u^s\}$ and the fluid pressure p [47, 48]. As a result of this formulation, only four degrees of freedom are used instead of six, which is advantageous for accelerating FEM computations [49]. This formulation gives the following equations:

$$\begin{cases} \nabla \cdot \hat{\boldsymbol{\sigma}}(\{u^s\}) + \omega^2 \tilde{\rho} \{u^s\} + \tilde{\gamma} \nabla p = 0 \\ \nabla^2 p + \omega^2 \frac{\tilde{\rho}_{22}}{\tilde{R}} p - \omega^2 \tilde{\gamma} \frac{\tilde{\rho}_{22}}{\phi^2} \nabla \cdot \{u^s\} = 0, \end{cases} \tag{1.32}$$

where the fluid phase equivalent properties $\tilde{\rho}_{eq}$ and $\tilde{K}_{eq}$ are related to $\tilde{\rho}_{22}$ and $\tilde{R}$ by

$$\tilde{\rho}_{22} = \phi^2 \tilde{\rho}_{eq}, \tag{1.33}$$

$$\tilde{R} = \phi^2 \tilde{K}_{eq}. \tag{1.34}$$

$\hat{\boldsymbol{\sigma}}$ is the stress tensor of the skeleton in vacuum, and

$$\tilde{\gamma} = \phi \left(\frac{\tilde{\rho}_{12}}{\tilde{\rho}_{22}} - \frac{\tilde{R}}{\tilde{Q}} \right), \tag{1.35}$$

$$\tilde{\rho} = \tilde{\rho}_{11} - \frac{\tilde{\rho}_{12}^2}{\tilde{\rho}_{22}}. \tag{1.36}$$

The implementation of the Biot model in a FEM model can be quite expensive numerically. [19, 50, 51, 52] discuss FEM meshing criteria needed for numerical convergence, finding that up to 12 elements per the smallest wavelength are required. The implementation of the Biot model using the Transfer Matrix Method (TMM) is described by Brouard et al. [53], and is explained in Section 5.2.

2.2.3 | Material parameters used by the Biot model and anisotropy

The Biot model incorporates an equivalent fluid model for the fluid phase and viscoelastic properties for the solid phase. The equivalent fluid model is contained inside the fluid's complex and frequency dependant density $\tilde{\rho}_{eq}$ and bulk modulus $\tilde{K}_{eq}$. The mechanical viscoelastic parameters needed are presented here.

The Young's modulus $\tilde{E}$ (Pa) is required, which is complex and frequency-dependant: $\tilde{E} = E' + jE'' = E'(1 + j\eta)$. E' is called the storage modulus and E'' is called the loss modulus. The shear modulus $\tilde{G}$ is also complex and frequency dependant: $\tilde{G} = G' + jG'' = G'(1 + j\eta)$. Second, the loss factor η (-) is the ratio of the loss modulus over the storage modulus: $\eta = \frac{G''}{G'} = \frac{E''}{E'} = \tan\varphi$, where φ is the loss angle, or phase lag, between stress and strain, with $0 < \varphi < \pi/2$. The Poisson ratio ν (-) which relates the Young's modulus and the shear modulus is also complex and frequency dependant: $\tilde{\nu} = \nu' + j\nu''$. It is often close to $\nu = 0$ for fibrous media, and closer to 0.44 for polymer foams due to their microstructure [54, 55, 56], while it is close to 0.3 for the polymer material itself.

A summary of Poisson ratio values for a wide range of materials can be found in [57]. In reality, its value depends on material microstructure, nonlinearity, time-dependent relaxation, inhomogeneous strain field, and amplitude and frequency of excitation (or strain rate) undergone by the material. For example, numerical computations of the Young's modulus on cellular structures find that they are nearly incompressible ($\nu \approx 0.5$) at small strains [54], however the cell struts begin to buckle as the strain increases which modifies the Poisson effect. Mott and Roland [58] show that, in classical elasticity, most materials contain ν in the range of 0.2 to 0.5, which includes pure elements, engineering alloys, polymers, and ceramics, whereas it can take any value between -1 and 0.5 for porous materials due to their unique microstructure. Porous materials' auxetic behaviour ($\nu < 0$) has often been reported, as in [59, 60, 61, 62] for example. Some compression measurements at large deformations appear to reveal an auxetic behaviour for a melamine foam for example, shown in Figure 1.2. Nonetheless, a constant real value of ν is often used for simplicity's sake, and because it is consistent with real observations of porous materials subjected to small strains.

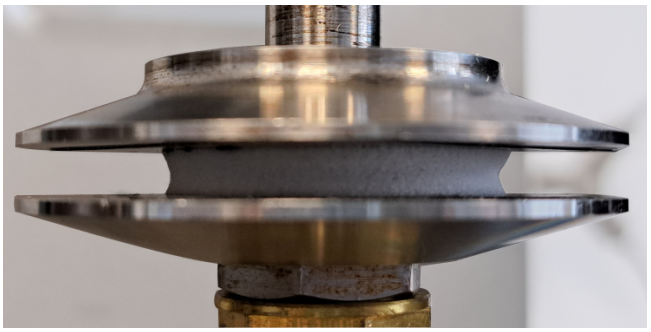

Figure 1.2. Cylindrical sample of melamine foam compressed to 80 % strain.

When the material is anisotropic, the number of independent emchanical parameters increases with the degree of anisotropy. When the material is isotropic, there are two independent parameters: $\tilde{E}$ and $\tilde{\nu}$, related by $\tilde{G} = \frac{\tilde{E}}{2(1+\tilde{\nu})}$. When the material is assumed transversely isotropic around axis x_3, 5 parameters are necessary: $\tilde{E}_1 = \tilde{E}_2$, $\tilde{E}_3$, $\tilde{\nu}_{12}$, $\tilde{\nu}_{13} = \tilde{\nu}_{23}$, and $\tilde{G}_{13} = \tilde{G}_{23}$. This is typical of polymer foams due to the polymerization foaming process and the effect of gravity [63, 64, 65], where the pores are elongated and the stiffness is higher in the growth direction. It is also often the case for fibrous materials which are created by layering fibres in the horizontal plane such as glass wool [66, 67, 68, 69, 70]. When the material is assumed orthotropic, as studied for example in references [63, 68, 71, 72, 73, 74], 9 parameters are required: $\tilde{E}_1$, $\tilde{E}_2$, $\tilde{E}_3$, $\tilde{\nu}_1$, $\tilde{\nu}_2$, $\tilde{\nu}_3$, $\tilde{G}_{23}$, $\tilde{G}_{13}$, and $\tilde{G}_{12}$.

2.3 | Limp approximation model

The limp model can be used to account for the inertia of the solid phase of the porous material while completely neglecting its stiffness, which simplifies the Biot model into an equivalent fluid model. In 1947, Beranek suggests a model for soft blankets where the bulk modulus of the frame is much smaller than the bulk modulus of the fluid [31]. In 1981, Ingard compares the limp hypothesis to rigid skeleton model [75]. Other limp models have been proposed by Ingard [76], Katragadda et al. [77] and Panneton [78].

The limp hypothesis consists in neglecting the stiffness of the frame. This is possible when the bulk modulus of the frame *in vacuo* $\tilde{K}_c$ is much smaller than the bulk modulus of the fluid in the pores $\tilde{K}_{eq}$. By setting $\hat{\boldsymbol{\sigma}} \approx 0$ in Equation 1.32, the system of equation of the (u, p) Biot formulation can be simplified to [39, 78]

$$\Delta p + \frac{\tilde{\rho}_{limp}}{\tilde{K}_{eq}} \omega^2 p = 0, \tag{1.37}$$

where the limp equivalent density $\tilde{\rho}_{limp}$ is

$$\tilde{\rho}_{limp} = \frac{\tilde{\rho}\tilde{\rho}_{eq}}{\tilde{\rho} + \tilde{\rho}_{eq}\tilde{\gamma}^2}. \tag{1.38}$$

When the bulk modulus of the frame K_b is much smaller than the bulk modulus of its constitutive material, the limp equivalent density can be approximated by [78, 79]

$$\tilde{\rho}_{limp} \approx \frac{\rho_t \tilde{\rho}_{eq} - \rho_0^2}{\rho_t + \tilde{\rho}_{eq} - 2\rho_0}, \tag{1.39}$$

when the bulk modulus of the frame $\tilde{K}_b$ is much smaller than the bulk modulus of the elastic material of the frame $\tilde{K}_s$, which is often the case for porous materials. $\rho_t = \rho_1 + \phi\rho_0$ is the apparent density of the equivalent fluid limp medium.

In other words, the limp hypothesis turns the poroelastic model into an equivalent fluid model, where the relative movement between the fluid and solid phases affects the dissipated energy, especially in low frequencies. When compared to a motionless equivalent fluid notation, the limp hypothesis brings differences mostly at low frequencies, since they have different low-frequency asymptotes. For high material density, the limp modulus resembles the rigid frame modulus.

Beranek in 1947 [31] suggests that the limp approximation is valid when the bulk modulus of the frame in vacuum $\tilde{K}_c = 2\tilde{N}\frac{1-\nu}{1-2\nu}$ is much smaller than the bulk modulus of the fluid in the pores $\tilde{K}_{eq}$:

$$\left| \frac{\tilde{K}_c}{\phi \tilde{K}_{eq}} \right| < 0.05. \tag{1.40}$$

Alternatively, Doutres in 2007 proposes a Frame Stiffness Influence (FSI) criterion [70] to assess the validity of the limp hypothesis:

$$FSI = \frac{\tilde{\rho}_{limp}}{\tilde{\rho}_c} \frac{\tilde{K}_c}{\phi \tilde{K}_{eq}}, \tag{1.41}$$

where $\tilde{\rho}_c = \rho_1 - \frac{\tilde{\rho}_{12}}{\phi}$. The FSI is frequency dependant, and so its limit for using the limp model is set to 0.2, which is less strict than Beranek's criterion. In air, by saying $\tilde{K}_{eq} \approx P_0$, the FSI simplifies to

$$FSI < 0.2 \Leftrightarrow \left| \tilde{K}_c \right| < 20 \text{ kPa}, \tag{1.42}$$

The limp model is well-suited when the material exhibits rigid body motion or when the skeleton

deforms with negligible stiffness. For example, some glass wools are well represented by this model. It is also well adapted to applications where the skeleton is prone to moving, such as transmission loss measurements with an air gap or when the material is placed on a vibrating structure. The validity of the limp model depends on the material parameters, but also on the setup and the frequency range of interest. For example, Ingard [76] shows that the prediction of the absorption of a porous layer against a rigid wall using the limp approximation is inaccurate in low frequencies, below the resonance frequency of the skeleton. On the other hand, Göransson [47, 80] finds the limp model is adapted to aircraft double wall transmission problems in the frequency range of interest.

3 | Viscoelastic models

3.1 | Typical viscoelastic behaviour

Poroelastic materials have a behaviour that is typically considered as viscoelastic, which is a combination of an elastic and a viscous component. The elastic component is responsible for a stress which is instantaneous and proportional to the strain undergone by the material. This can be likened to a spring's behaviour. The viscous component is responsible for a stress which is proportional to the strain rate undergone by the material, and can be likened to a dashpot's behaviour.

The viscous component causes energy dissipation within the material as it is deformed. Viscoelastic models are useful for describing a wide range of materials, including polymers such as rubbers and plastics, some high temperature metals, some viscous fluids such as some paints or inks, bituminous materials, and poroelastic materials. A viscoelastic material is often represented using a rheological model, which is an assembly of springs E_i and dashpots η_i. These relate the strain ε and the stress σ within the material. A review of viscoelastic models can be found in references [81, 82, 83, 84]. The resulting complex and frequency-dependant modulus $\tilde{E}$ represents this viscoelastic behaviour. An example of a typical E' and η as a function of frequency is given in Figure 1.3.

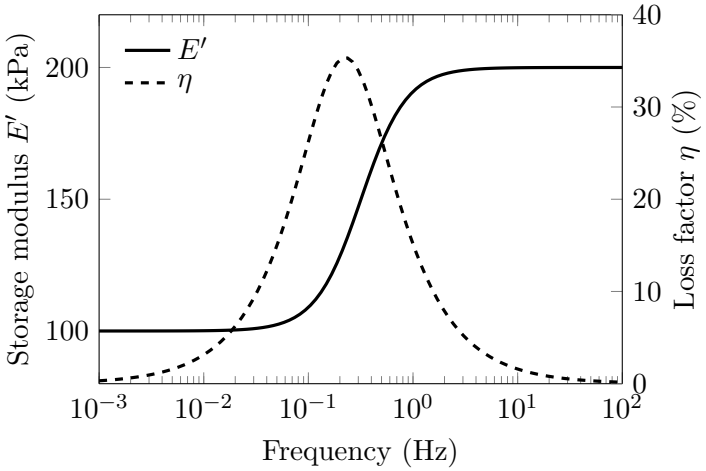

Figure 1.3. Typical storage modulus E' and loss factor η as a function of frequency for a simple viscoelastic material described by a Zener model.

An example of a typical response of a viscoelastic material shown in Figure 1.3. The modulus E' which increases monotonically from a low frequency asymptote to a high frequency asymptote, and during the rapid transition zone, the loss factor η exhibits a peak of high dissipation. This can be explained by a glass transition within the material, where the structure of the material rearranges itself from a viscous rubbery state to a brittle glassy state. It is related to the glass transition temperature T_g of the material. This transition occurs at a specific frequency range that depends on the composition

and the temperature of the material. At different temperatures, this frequency range is shifted, due to a time-temperature equivalence, explained further below in Section 3.4.

The stress-strain curves resulting from viscoelastic models during cyclic loading do not always follow the same path during loading $\dot{\varepsilon} > 0$ and unloading $\dot{\varepsilon} < 0$. This, the energy dissipated over a cycle is of a cyclical loading of period $2\pi/\omega$ and of amplitude A is [83, 85]

$$E_d = \int_0^{2\pi/\omega} \sigma\dot{\varepsilon}dt = \int_0^{2\pi/\omega} \tilde{E}'\varepsilon\dot{\varepsilon}dt = \pi A^2\eta E' = \pi A^2 E''. \tag{1.43}$$

3.2 | Common rheological models: Maxwell and Kelvin-Voigt

The simplest rheological models are the Maxwell model [86], which is a spring and a dashpot in series, and the Kelvin-Voigt model, which is a spring and a dashpot in parallel. They are represented on Figure 1.4.

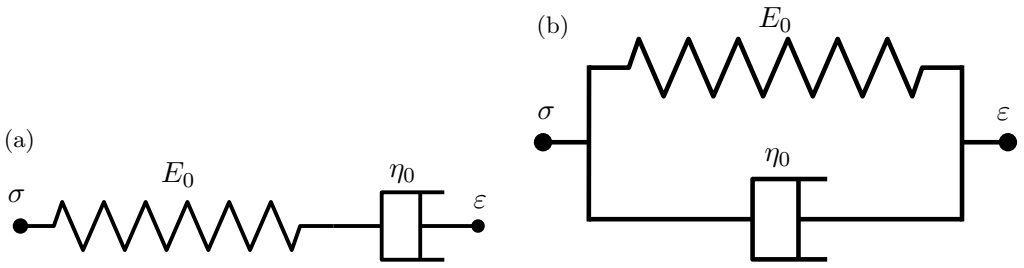

Figure 1.4. Schematic representation of the springs and dashpots in (a) a Maxwell and (b) a Kelvin-Voigt models.

The Maxwell representation is well adapted for representing the stress relaxation of fluid-like materials, due to an irreversible strain component and a stress which tends to zero at long durations in the absence of strain. The Maxwell model relates the stress and strain as

$$\frac{\dot{\sigma}}{E_0} + \frac{\sigma}{\eta_0} = \dot{\varepsilon}. \tag{1.44}$$

Stress relaxation refers to the evolution of the stress σ when the strain ε is kept constant. However, it does not capture strain creep, which refers to the evolution of the strain ε when the stress σ is kept constant. In contrast, the Kelvin-Voigt model is well adapted for representing strain creep but not stress relaxation, and represents solid-like materials because its deformation is entirely reversible. It relates the stress and strain as

$$\sigma = E_0\varepsilon + \eta_0\dot{\varepsilon}. \tag{1.45}$$

The dynamic modulus $\tilde{E}$ for the Maxwell and for the Kelvin-Voigt models respectively are

$$\tilde{E} = \frac{E_0\eta_0^2\omega^2 + j\omega E_0^2\eta_0}{\eta_0^2\omega^2 + E_0^2}, \tag{1.46}$$

$$\tilde{E} = E_0\left(1 + j\omega\frac{E_0}{\eta_0}\right). \tag{1.47}$$

To characterize the stress response of a viscoelastic material or strain, the relaxation function $H(t)$ can be used, which is the stress response of the material subjected to a strain Heaviside step defined by

$$Y(t) = \begin{cases} 1 & \text{if } t \geq 0, \\ 0 & \text{if } t < 0. \end{cases} \tag{1.48}$$

For a Maxwell representation, the relaxation function is

$$H(t) = E_0 \, \mathrm{e}^{-\frac{E_0}{\eta_0} t} \, Y(t). \tag{1.49}$$

Alternatively, for rheological models that have no instantaneous elasticity, such as the Kelvin-Voigt model, the creep function $C(t)$ is used instead of the relaxation function, which is the strain response to a stress Heaviside step $Y(t)$. For a Kelvin-Voigt representation, the creep function is

$$C(t) = \frac{1}{E_0} \left(1 - \mathrm{e}^{-\frac{E_0}{\eta_0} t} \right) Y(t). \tag{1.50}$$

As can be seen from the relaxation function in Equation 1.49 and the creep function in Equation 1.50, the stress and strain decay of these models is exponential. The characteristic relaxation time τ_0 of the decay is

$$\tau_0 = \frac{E_0}{\eta_0}. \tag{1.51}$$

The material time-dependant response can be formulated by applying the Boltzmann superposition principle, which stipulates that the stress caused by the sum of several strains over time is equal to the sum of the stresses caused by each strain [81]. Consequently, the stress response $\sigma(t)$ in response to an arbitrary time dependant strain $\varepsilon(t)$ is

$$\sigma(t) = H(0)\varepsilon(t) + \int_{-\infty}^{t} \varepsilon(\tau) \, \dot{H}(t - \tau) d\tau. \tag{1.52}$$

3.3 | More advanced rheological models: Zener and generalized Maxwell

To describe more complex material behaviours, there are some more advanced rheological models. One that is often used is the Zener model, also called Standard Linear Solid model, which adds a long term spring E_0 in parallel to a Maxwell model. Its rheological representation is shown in Figure 1.5. This has the advantage of representing the relaxation like a Maxwell model, with a non-zero stress asymptote as time goes to infinity, as well as the creep behaviour of the Kelvin-Voigt model. Its stress decay corresponds to the stress decay of a Maxwell model offset by the long term stiffness E_0, which is more accurate for modelling many materials. The Zener model's relaxation function is given by

$$H(t) = \left(E_0 + E_1 \mathrm{e}^{-\frac{E_1}{\eta_1} t} \right) Y(t). \tag{1.53}$$

The dynamic modulus $\tilde{E}$ for the Zener model is

$$\tilde{E} = E_0 + E_1 \frac{\omega^2 \tau_1^2}{1 + \omega^2 \tau_1^2} + j E_1 \frac{\omega \tau_1}{1 + \omega^2 \tau_1^2}. \tag{1.54}$$

Another commonly used model is the generalized Maxwell model [87, 88]. This representation contains a static spring E_0 in series with N Maxwell models. Its stress decay corresponds to the sum of the decay of the N Maxwell models offset by the long term stiffness E_0. Hence, it is capable of representing the effective behaviour of complex materials with multiple relaxation times. Its rheological representation is shown in Figure 1.5(a), and its relaxation function is given by

$$H(t) = \left(E_0 + \sum_{i=1}^{N} E_i \mathrm{e}^{-\frac{E_i}{\eta_i} t} \right) Y(t). \tag{1.55}$$

The dynamic modulus $\tilde{E}$ for the generalized Maxwell model can be represented as a Prony series as

$$\tilde{E} = E_0 + \sum_{i=1}^{N} E_i \frac{\omega^2 \tau_i^2}{1 + \omega^2 \tau_i^2} + jE_i \frac{\omega \tau_i}{1 + \omega^2 \tau_i^2}. \tag{1.56}$$

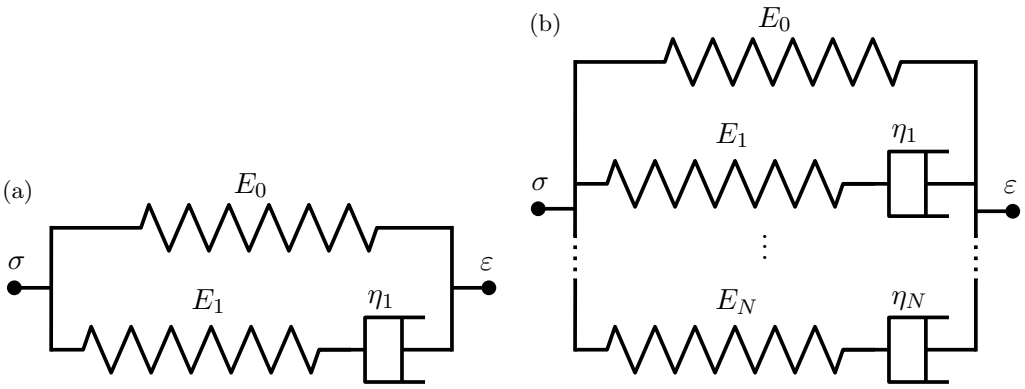

Figure 1.5. Schematic representation of the springs and dashpots for the (a) Zener and the (b) Generalized Maxwell models.

3.4 | Time-temperature superposition principle

A characteristic feature of viscoelastic materials is that they exhibit a time-temperature equivalence. This means that an increase in temperature causes the material to behave according to its lower frequency behaviour, and a decrease in temperature causes it to behave according to its higher frequency behaviour. Equivalently, a shift in the frequency of the material's behaviour is equivalent to keeping the frequency the same but shifting its temperature. Applying this principle allows the creation of a master curve, spanning a large frequency range at a given temperature. Sperling [89] offers a review of polymer viscoelasticity for sound and vibration energy absorption, and their time-temperature equivalence principle. The creation process of a master curve is shown on Figure 1.6.

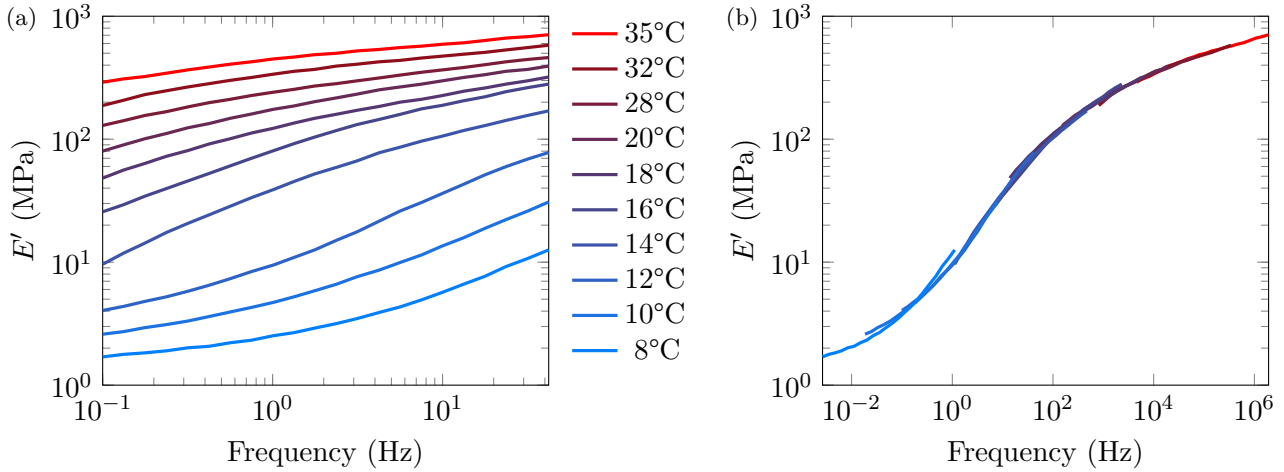

Figure 1.6. Illustration of the time-temperature principle. (a) The storage modulus E' is measured over the same frequency range at temperatures between 8°C and 35°C. (a) The frequency of each curve is translated relative to the reference temperature $T_{ref} = 12$°C to obtain a obtain master curve.

Two commonly used time-temperature superposition are the Arrhenius [90, 91] and the William-

Landel-Ferry (WLF) [92] laws. This equivalence can be exploited to predict the material behaviour over a different range of temperatures, or to extend the frequency range of material characterization when measurement range is limited for example. The WLF law relates the temperature and frequency dependence of the modulus $\tilde{E}$ through

$$\log_{10}(a_T) = \frac{-C_1 (T_0 - T_R)}{C_2 + (T_0 - T_R)}, \tag{1.57}$$

where a_T is the coefficient by which to multiply the frequencies of the modulus at reference temperature T_R to obtain its new frequencies abscissa at temperature T_0, and C_1 and C_2 are material-specific coefficients. The WLF equation is valid for temperatures T_0 close to and greater than T_g: $T_g < T_0 < T_g + 100$ K. Any temperature can be used for T_R, although William, Landel and Ferry [92] recommend using $T_R \approx T_g + 50$ K.

Alternatively, the Arrhenius law computes a_T through

$$\log_{10}(a_T) = \frac{E_a}{2.303R}\left(\frac{1}{T_0} - \frac{1}{T_R}\right), \tag{1.58}$$

where E_a is the material's activation energy for flow, and R is the ideal gas constant. Arrhenius' equation is valid in the glassy region, for temperatures $T_0 < T_g$.

4 | Motionless skeleton equivalent fluid models

4.1 | General case of an equivalent fluid

The simplest way of modelling a porous medium is the equivalent fluid approach, with an equivalent bulk modulus $\tilde{K}_{eq}$ and an equivalent density $\tilde{\rho}_{eq}$. The *tilde* diacritic denotes complex and frequency dependant quantities, representing the energy dissipation of the acoustic wave traversing the medium. In 1949, Zwikker and Kosten [32] were the first to represent the propagation of sound in a porous medium as an equivalent fluid by considering pores as straight cylinders. Several equivalent fluid models were developed over the years with increasing complexity, able to capture more physical phenomena.

Reducing the porous medium to an equivalent fluid requires the hypothesis of a rigid skeleton, which means that the frame has no displacement and no deformation, except for the limp model which takes into account the skeleton displacement when it has no stiffness. Rigid skeleton equivalent fluid models are not suitable when the skeleton deforms or exhibits rigid body motion. No waves propagating through the skeleton are modelled for equivalent fluid representations. The only compression wave propagating in the medium behaves according to the Helmholtz equation:

$$\frac{1}{\omega^2 \tilde{\rho}_{eq}} \Delta p + \frac{1}{\tilde{K}_{eq}} p = 0. \tag{1.59}$$

The skeleton can be assumed decoupled from the fluid and immobile beyond the decoupling frequency f_d [32]:

$$f_d = \frac{1}{2\pi} \frac{\sigma \phi^2}{\rho_1}. \tag{1.60}$$

Above the frequency, the visco-inertial coupling between the solid and fluid phases is low enough that the acoustic wave propagating in the fluid does not generate a wave in the skeleton.

The fluid properties of the equivalent fluid also have complex values, and are related to $\tilde{K}_{eq}$ and $\tilde{\rho}_{eq}$. The wave velocity $\tilde{c}_{eq}$ is given by

$$\tilde{c}_{eq} = \sqrt{\frac{\tilde{K}_{eq}}{\tilde{\rho}_{eq}}}. \tag{1.61}$$

The wavenumber $\tilde{k}_{eq}$ is written as

$$\tilde{k}_{eq} = \frac{\omega}{\tilde{c}_{eq}}. \tag{1.62}$$

The equivalent characteristic impedance of the medium $\tilde{Z}_{eq}$ is expressed as

$$\tilde{Z}_{eq} = \tilde{\rho}_{eq}\tilde{c}_{eq} = \sqrt{\tilde{\rho}_{eq}\tilde{K}_{eq}}. \tag{1.63}$$

For time notation $e^{-j\omega t}$, $\frac{\mathrm{Im}(\tilde{k}_{eq})}{\mathrm{Re}(\tilde{k}_{eq})} > 0$, otherwise $\frac{\mathrm{Im}(\tilde{k}_{eq})}{\mathrm{Re}(\tilde{k}_{eq})} < 0$, which guarantees that the wave amplitude to decrease as it propagates.

4.2 | Transport parameters of equivalent fluid models

4.2.1 | The porosity ϕ

The porosity represents the ratio of fluid volume to the total volume of the material

$$\phi = \frac{V_{air}}{V_t}. \tag{1.3}$$

The open porosity refers to the volume of fluid inside the porous material that is accessible to the ambient fluid. The open porosity is usually used to model porous materials. In contrast, air bubbles trapped inside hermetic pockets within the material are referred to as the closed porosity.

4.2.2 | The airflow resistivity σ

The air flow resistivity σ is a parameter describing viscous phenomena at low frequency, expressed in $\mathrm{N\,s\,m^{-4}}$. The air flow resistivity corresponds to the airflow resistance R ($\mathrm{N\,s\,m^{-3}}$) of a material per unit length. The resistance of a sample of thickness h (m) obstructing an airflow is related to the pressure difference upstream and downstream from the sample:

$$R = \frac{\Delta P}{Q} = \sigma h, \tag{1.64}$$

where S is the cross-section area of the specimen ($\mathrm{m^2}$), Q is the volumetric flow rate ($\mathrm{m^3\,s^{-1}}$), and $\Delta P = P_2 - P_1$ is the pressure difference upstream and downstream of the sample, as shown in Figure 1.7. The resistivity is the resistance per unit length:

$$\sigma = \frac{\Delta P S}{Q h}, \tag{1.65}$$

which comes from Darcy's law [93]

$$\sigma\phi\vec{v} = -\vec{\nabla}p, \tag{1.66}$$

where $\vec{\nabla}p$ is the pressure gradient inside the material and $\vec{v}$ is the fluid velocity. The airflow resistivity is a low-frequency viscous parameter, which can be expressed independently of the saturating fluid through the static viscous permeability q_0 ($\mathrm{m^2}$) :

$$q_0 = \frac{\mu_0}{\sigma}, \tag{1.67}$$

where μ_0 is the viscosity of the surrounding air.

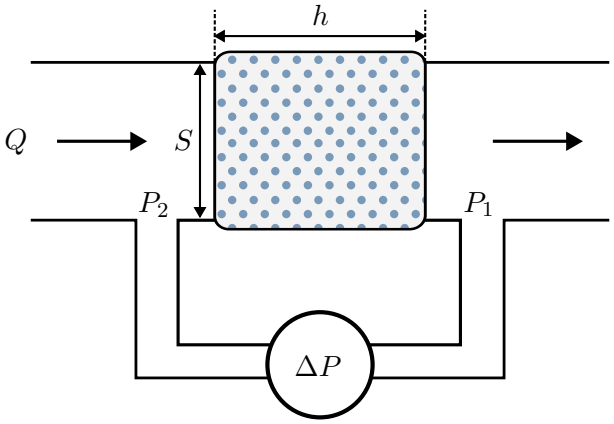

Figure 1.7. Schematic of the air flow resistivity.

For cylindrical pores of radius r and inclined at an angle θ (see Figure 1.9), σ can be expressed as [40]

$$\sigma = \frac{8\mu_0}{\phi r^2 \cos^2\theta}. \tag{1.68}$$

Material airflow resistivity can depend on the direction of measurement. For fibrous materials where the fibres are stacked in the horizontal plane, the airflow resistivity is usually greater in the direction normal to the fibres. Further, for polymer foams that are created through a foaming process, the direction of growth creates an anisotropy in the cell structure which causes a different air airflow resistivity in different directions.

4.2.3 | The high-frequency limit of the dynamic viscous tortuosity α_∞

The dynamic tortuosity $\tilde{\alpha}_\omega$ (-) is a complex frequency dependant parameter, which indicates the viscous energy dissipation between the fluid and the structure, as well as the inertial effects caused by the complex path taken by the sound waves inside the porous medium. It can be seen as an added inertia to the fluid inside the porous medium, giving access to an effective density $\tilde{\rho}_{eq}$ [39]

$$\tilde{\rho}_{eq} = \tilde{\alpha}_\omega \rho_0. \tag{1.69}$$

Viscous dissipations are strongest within the viscous skin limit δ_0 from the surfaces of the pores, shown in Figure 1.8. This viscous skin depth δ_0 approaches 0 at high frequencies:

$$\delta_0 = \sqrt{\frac{2\mu_0}{\omega\rho_0}} \to 0 \text{ when } \omega \to \infty. \tag{1.70}$$

At high frequencies, for a viscous skin layer that tends to 0, the dynamic tortuosity $\tilde{\alpha}_\omega$ tends to the geometric tortuosity α_∞ [40]

$$\tilde{\alpha}_\infty = \lim_{\omega\to\infty} \tilde{\alpha}_\omega \sim \alpha_\infty. \tag{1.71}$$

α_∞ is called the high frequency limit of the tortuosity, or simply the geometric tortuosity or tortuosity, and is computed exactly as [40]

$$\alpha_\infty = \frac{\frac{1}{V}\int_V v^2 dV}{\left(\frac{1}{V}\int_V \vec{v}\, dV\right)^2}, \tag{1.72}$$

where $\vec{v}$ is the velocity of inviscid fluid particles at high frequency, and V is the homogenization volume. The viscous tortuosity α_∞ is a geometric parameter that indicates the added length travelled

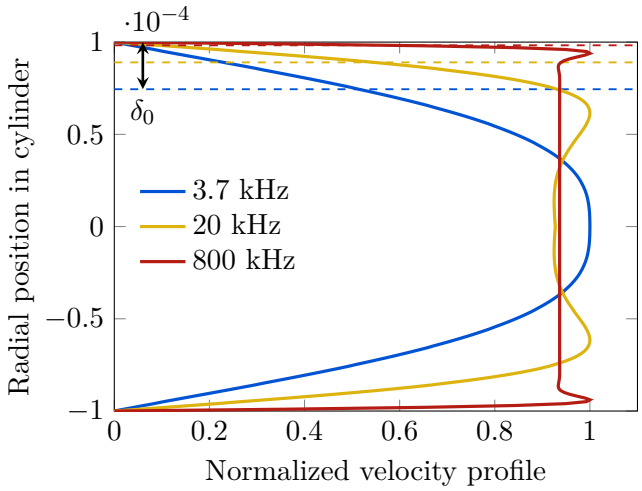

Figure 1.8. Velocity profile of a fluid inside a cylinder of radius $R = 100$ µm for different frequencies, and corresponding viscous skin depth δ_0.

by waves propagating through the porous medium, due to obstacles and a winding path. It corresponds to the squared ratio of the tortuous path length $L_{tortuous}$ over that of a straight path $L_{straight}$:

$$\alpha_\infty = \left(\frac{L_{tortuous}}{L_{straight}} \right)^2 . \tag{1.73}$$

In the general case, the tortuosity must always verify $\alpha_\infty \geq 1$. For fibrous material, the tortuosity can be approximated from the porosity as $\alpha_\infty \approx \phi^{-1}$ [94]. For a model with straight non-inclined cylindrical pores, tortuosity is $\alpha_\infty = 1$. For cylindrical pores inclined at an angle θ, the tortuosity becomes $\alpha_\infty = \frac{1}{(\cos\theta)^2}$. Some simplified cylindrical pore geometries and their tortuosity are presented in Figure 1.9.

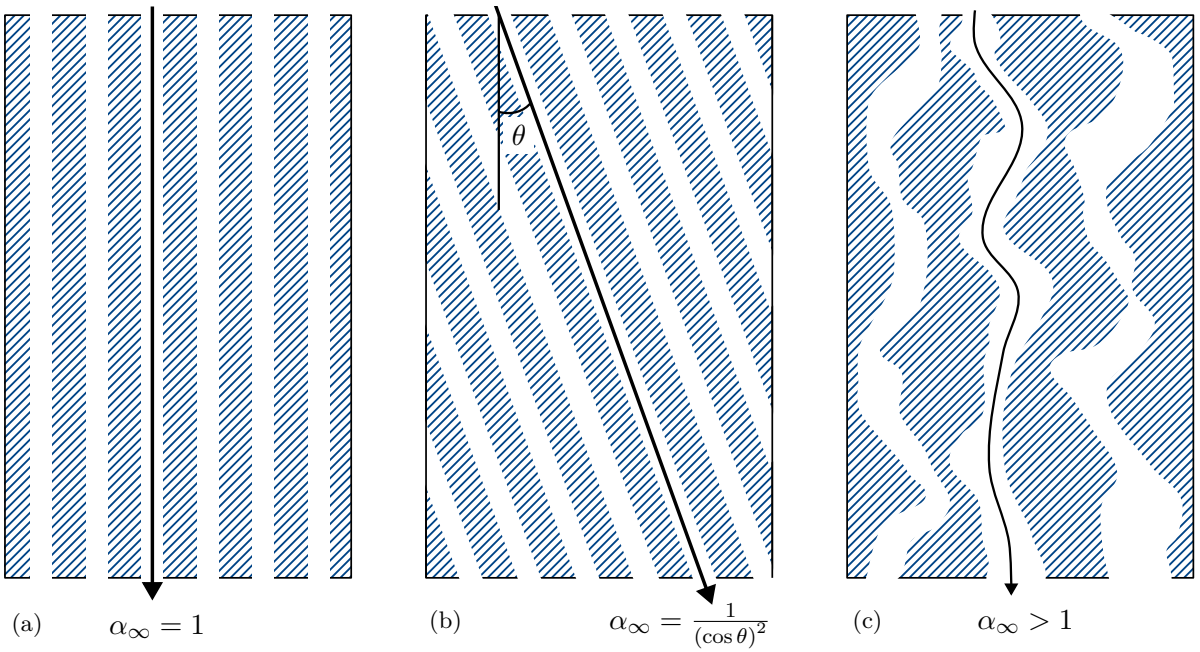

Figure 1.9. Different pore models and their corresponding tortuosity, for (b) straight cylindrical pores, (a) inclined cylindrical pores, and (c) randomly shaped pores.

4.2.4 | The viscous and thermal characteristic lengths Λ and Λ'

The viscous characteristic length Λ (m) is a viscous parameter at high frequencies. It is connected to viscous effects at high frequencies in the dynamic tortuosity $\tilde{\alpha}_\omega$:

$$\lim_{\omega\to\infty} \tilde{\alpha}_\omega = \alpha_\infty \left(1 + (1+j)\frac{\delta_0}{\Lambda}\right). \tag{1.74}$$

It represents twice the volume-to-surface ratio of the pores, weighted by local fluid velocity [40, 95]

$$\Lambda = 2\frac{\int_V |v|^2 \, dV}{\int_S |v|^2 \, dS}, \tag{1.75}$$

where V is the homogenization volume and S is the surface area of the walls of the pores.

The thermal characteristic length Λ' is a thermal parameter at high frequencies and corresponds to twice the volume-to-surface ratio of the pores, without velocity weighting [41]:

$$\Lambda' = 2\frac{\int_V dV}{\int_S dS}. \tag{1.76}$$

Λ' can also be written

$$\Lambda' = \frac{2\phi}{S_{contact}}, \tag{1.77}$$

where $S_{contact}$ is the contact area between the fluid and the skeleton phases per unit volume. In practice, Λ is close to the radius of the smallest pores, because this is where the viscous boundary layer most affects flow velocity, and Λ' is close to the radius of the largest pores, as shown in Figure 1.10. By definition, the inequality $\Lambda' > \Lambda$ is always satisfied.

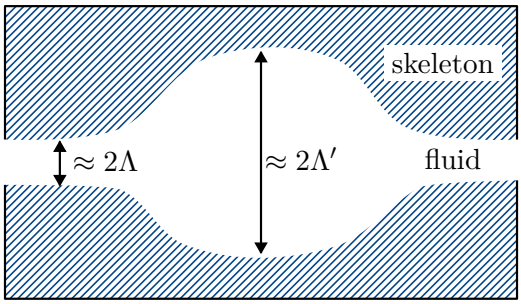

Figure 1.10. Λ can be assimilated to the radius of the smallest pores, Λ' to the radius of the largest pores.

Λ can also be expressed as [39, 95]

$$\Lambda = \sqrt{\frac{8\mu_0\alpha_\infty}{\sigma\phi}}\frac{1}{c}, \tag{1.78}$$

where $c \approx 1$. Additionally, simplified expressions of Λ and Λ' can be found by making an assumption of cylindrical pores with radius r [40]. In this case, the shape factor M is equal to 1:

$$M = \frac{8\alpha_\infty\mu}{\phi\Lambda^2\sigma} = 1. \tag{1.79}$$

Thus, the simplified expressions of the characteristic lengths are

$$\Lambda^2 = \frac{8\mu}{\phi\sigma}, \tag{1.80}$$

$$\Lambda = \Lambda' = r. \tag{1.81}$$

For fibrous media where fibres are perpendicular to the flow direction, $2\Lambda \approx \Lambda'$ [39].

4.2.5 | The thermal permeability q_0'

The thermal permeability is an indicator of thermal exchanges between the solid and fluid phases at low frequencies. It is obtained as a thermal analogy of the viscous permeability q_0. For cylindrical pores, the expression of q_0' can be simplified to

$$q_0' = \frac{\phi \Lambda'^2}{8}. \tag{1.82}$$

4.3 | Common models

Commonly used motionless skeleton equivalent fluid models are presented in this section in order of chronology and increasing complexity.

4.3.1 | Delany-Bazley model

The empirical Delany-Bazley model, published in 1970, provides an estimation of the wavenumber $\tilde{k}_{eq}$ and the characteristic impedance $\tilde{Z}_{eq}$ of materials as a function of frequency [96]. This empirical model was established from a dataset of measurements on highly porous ($\phi \sim 1$) fibrous materials to fit empirical coefficients. The model assumes that the porous material contains inclined cylindrical pores and requires only one parameter, the resistivity σ, and writes

$$\tilde{Z}_{eq} = \rho_0 c_0 \left(1 + 0.051 X^{-0.75} - j0.087 X^{-0.73}\right), \tag{1.83}$$

$$\tilde{k}_{eq} = \frac{2\pi f}{c_0} \left(1 + 0.175 X^{-0.59} - j0.086 X^{-0.70}\right), \tag{1.84}$$

where $X = \frac{f}{\sigma}$ must be within the range 0.01 to 1, corresponding to the domain where the model has been validated. This model is easy to use as it requires only one parameter, but it lacks a physical basis as it may yield negative values for the real part of the surface impedance at low frequencies. Several authors have suggested different coefficients for $\tilde{Z}_{eq}$ and $\tilde{k}_{eq}$, such as [97] and [98].

4.3.2 | Delany-Bazley-Miki model

The Delany-Bazley-Miki model, published by Miki in 1990, improves upon the Delany-Bazley model with new coefficients obtained from the same measurement dataset as Delany and Bazley [98]. This model is preferable to the previous one as it is valid over a slightly broader frequency range, and addresses the issue of negative values for the real part of the surface impedance:

$$\tilde{Z}_{eq} = \rho_0 c_0 \left(1 + 0.070 X^{-0.632} - j0.107 X^{-0.632}\right), \tag{1.85}$$

$$\tilde{k}_{eq} = \frac{2\pi f}{c_0} \left(1 + 0.109 X^{-0.618} - j0.160 X^{-0.618}\right), \tag{1.86}$$

where, once again, $X = \frac{f}{\sigma}$ is within the range 0.01 to 1.

4.3.3 | JCA model

Following Zwikker's work which dealt with straight cylindrical pores, Johnson, Koplik and Dashen developed a semi-phenomenological model which can compute the equivalent density $\tilde{\rho}_{eq}$ for pores of arbitrary cross-sections, published in 1987 [40]. This formulation accounts for the visco-inertial effects in the medium by using four material parameters.

The model is based on equations that establish the asymptotic behaviour of the material's equivalent quantities at low and high frequencies, and links them by the simplest possible function. It does so by relating the equivalent density of the fluid inside the pores to the density of the air through a dynamic tortuosity $\tilde{\alpha}_\omega$ (see Equation 1.69). Johnson's equivalent density is calculated as

$$\tilde{\rho}_{eq}(\omega) = \frac{\rho_0 \alpha_\infty}{\phi}\left(1 + \frac{\phi\sigma}{j\omega\alpha_\infty\rho_0}\sqrt{1 + j\omega\frac{4\alpha_\infty^2\mu_0\rho_0}{\sigma^2\Lambda^2\phi^2}}\right). \tag{1.87}$$

Its low and high frequency asymptotes are:

$$\lim_{\omega\to 0}\tilde{\rho}_{eq} = \rho_0\alpha_\infty\left(1 + \frac{2\alpha_\infty\mu_0}{\Lambda^2\phi\sigma}\right), \tag{1.88}$$

$$\lim_{\omega\to\infty}\tilde{\rho}_{eq} = \rho_0\alpha_\infty\left(1 + (1+j)\frac{\delta_0}{\Lambda}\right). \tag{1.89}$$

In 1991, Champoux and Allard proposed a model to include thermal dissipation effects in the equivalent density K_{eq} by introducing Λ' similarly as Λ had been proposed for viscous effects [41]. The thermal dissipation effects come from the energy exchange between the fluid and the frame resulting from the temperature gradient induced by the acoustic pressure wave. The resulting equivalent bulk modulus is

$$\tilde{K}_{eq}(\omega) = \frac{\gamma_0 P_0}{\phi}\left(\gamma_0 - (\gamma_0 - 1)\left(1 + \frac{8\kappa_0}{j\omega\Lambda'^2 c_p\rho_0}\sqrt{1 + j\omega\frac{\Lambda'^2 c_p\rho_0}{16\kappa_0}}\right)^{-1}\right)^{-1}. \tag{1.90}$$

Its low and high frequency asymptotes are

$$\lim_{f\to\infty}\tilde{K}_{eq} = \gamma P_0, \text{ and } \lim_{f\to 0}\tilde{K}_{eq} = P_0. \tag{1.91}$$

The resulting Johnson-Champoux-Allard (JCA) model is composed of an equivalent density $\tilde{\rho}_{eq}$ and an equivalent bulk modulus $\tilde{K}_{eq}$. Note that these equations are considered inside the fluid homogenized to take up the entire volume of the porous material, not just the volume saturating the pores of the medium. Consequently, the equivalent fluid parameters taking up the whole volume of the porous material can be obtained by multiplying $\tilde{\rho}_{eq}$ and $\tilde{K}_{eq}$ by the porosity ϕ, and are noted $\tilde{\rho}_f$ and $\tilde{K}_f$

$$\phi\tilde{\rho}_{eq} = \tilde{\rho}_f, \quad \phi\tilde{K}_{eq} = \tilde{K}_f. \tag{1.92}$$

The JCA model is inaccurate, notably at low frequencies. First, the limit of the bulk modulus $\tilde{K}_{eq}$ as the frequency approaches 0 depends on the thermal characteristic length Λ', which is a high-frequency parameter. This is due to the simplified expression of the thermal characteristic length q'_0, a low-frequency thermal parameter, which is assigned the value $q'_0 = \frac{\phi\Lambda'^2}{8}$ which corresponds to an assumption of cylindrical pores. The significance of the thermal characteristic length is addressed in the JCAL model by Lafarge in 1997 Lafarge et al. [99], as explained below in Section 4.3.4. Second, the limit of the real part of the equivalent density $\tilde{\rho}_{eq}$ as the frequency tends to 0 is inaccurate. For example, for cylindrical pores, the low-frequency limit of $\mathrm{Re}(\tilde{\rho}_{eq})$ is $1.25\,\rho_0$ instead of $1.33\,\rho_0$ [39].

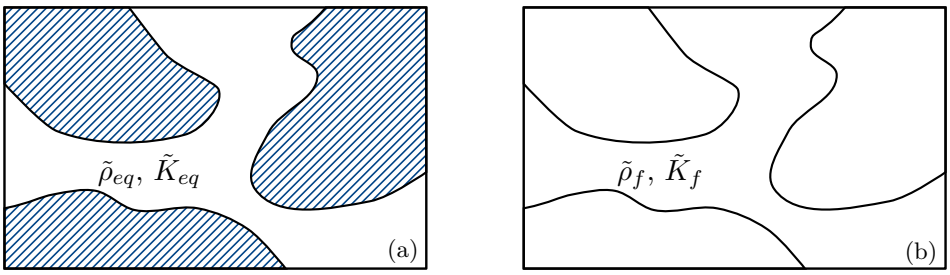

Figure 1.11. (a) Porosity not integrated ($\tilde{\rho}_{eq}$ and $\tilde{K}_{eq}$), and (b) porosity integrated ($\tilde{\rho}_f$ and $\tilde{K}_f$).

Further, it should not depend on the high frequency parameter Λ. This is improved in the Pride model, explained below in Section 4.3.5.

4.3.4 | JCAL model

Due to the absence of a low frequency thermal parameter the JCA model equations, Lafarge [99] introduces the thermal permeability q_0'. It was suggested by performing an analogy with the viscous permeability described previously by Johnson et al. [40]. The thermal permeability improves the model's behaviour at low frequencies. In the JCA model, q_0' was expressed as $q_0' = \frac{\phi\Lambda'^2}{8}$, corresponding to an assumption of cylindrical pores. In the JCAL model, this parameter is independent of the others and the new bulk modulus is expressed as

$$\tilde{K}_{eq}(\omega) = \frac{\gamma_0 P_0}{\phi}\left(\gamma_0 - (\gamma_0 - 1)\left(1 + \frac{\phi\kappa_0}{j\omega q_0' c_p \rho_0}\sqrt{1 + j\omega\frac{4q_0'^2 c_p\rho_0}{\kappa_0\Lambda'^2\phi^2}}\right)^{-1}\right)^{-1}. \tag{1.90}$$

4.3.5 | Pride-Lafarge model JCAPL

The JCA model was modified by Pride in 1993 [100], and then corrected by Lafarge the same year [42], to improve its accuracy and take into account possible pore constrictions. The viscous effects are introduced into the dynamic tortuosity [42, 100]:

$$\tilde{\alpha}_\omega = \alpha_\infty\left(1 + \frac{1}{j\tilde{\omega}}\tilde{F}(\omega)\right), \tag{1.93}$$

and the thermal effects are introduced into the bulk modulus [99]:

$$\tilde{K}_{eq} = \gamma_0 P_0\left(\gamma_0 - (\gamma_0 - 1)\left(1 + \frac{1}{j\tilde{\omega}'}\tilde{F}'(\omega)\right)^{-1}\right)^{-1}, \tag{1.94}$$

The analogy between viscous and thermal effects allows equivalent parameters to be expressed for both phenomena. The geometric functions $\tilde{F}$ and $\tilde{F}'$ are defined as

$$\tilde{F} = 1 - b + b\sqrt{1 + \frac{M}{2b^2}j\tilde{\omega}}, \quad \tilde{F}' = 1 - b' + b'\sqrt{1 + \frac{M'}{2b'^2}j\tilde{\omega}'}, \tag{1.95}$$

with

$$\tilde{\omega} = \frac{\omega\rho_0 q_0\alpha_\infty}{\mu_0\phi}, \quad \tilde{\omega}' = \frac{\omega\rho_0 c_p q_0'}{\kappa_0\phi}, \tag{1.96}$$

the viscous and thermal shape factors are written as

$$M = \frac{8q_0\alpha_\infty}{\phi\Lambda^2}, \quad M' = \frac{8q_0'}{\phi\Lambda'^2}, \tag{1.97}$$

and the geometric terms b and b' (sometimes called P or β in the literature) are written as

$$b = \frac{M}{4\left(\frac{\alpha_0}{\alpha_\infty} - 1\right)}, \quad b' = \frac{M'}{4\left(\alpha_0' - 1\right)}. \tag{1.98}$$

α_0 and α_0' (-) are two new material parameters called the static viscous tortuosity and static thermal tortuosity. Lafarge [101] proposes the following simplified expression for the dynamic tortuosity using b:

$$\tilde{\alpha}_\omega = \alpha_\infty + \frac{\sigma\phi}{j\omega\rho_0}\left(1 - b + b\left(1 + \left(\frac{2\alpha_\infty\mu_0}{b\phi\Lambda\sigma}\right)^2 \frac{j\omega\rho_0}{\mu}\right)^{1/2}\right). \tag{1.99}$$

The static viscous tortuosity α_0 and the static thermal tortuosity α_0' are the two additional terms in the Pride-Lafarge model compared to the JCAL model, which allow it to be accurate at low frequencies. However, even though the new parameters introduced improve the model's quality, they are not well known, and their experimental determination is not easy [102], meaning this model is rarely used in practice. The only existing methods to estimate these new parameters are micro-macro numerical simulation methods [103, 104, 105, 106]. The Johnson model of $\tilde{K}_{eq}$ (Equation 1.90) can be obtained from the Pride-Lafarge model by setting a value of 1 to the geometric term b [39]. The JCA and JCAL models can also be obtained from the Pride-Lafarge model by setting the values of M, b, M' and b' to 1 [107].

4.3.6 | Simplification of models to limit the number of parameters

Various models have added more and more parameters to describe the internal behaviour of porous materials, however recent efforts have been made to clarify how many of these parameters are really necessary and sufficient. Horoshenkov et al. [108] show that there is a clear dependence between Λ and Λ', since both are related to pore dimensions. For non-uniform cylindrical pores with a log-normal size distribution, of average radius $\bar{s}$ with a standard deviation σ_s which are 2 new parameters, the JCAL transport parameters can be expressed as [108, 109, 110]

$$\alpha_\infty = \mathrm{e}^{(\sigma_s \log 2)}, \tag{1.100}$$

$$\sigma = \frac{8\mu_0\alpha_\infty}{\bar{s}^2\phi}\mathrm{e}^{6(\sigma_s\log 2)^2}, \tag{1.101}$$

$$\Lambda = \bar{s}\mathrm{e}^{-5/2\,(\sigma_s\log 2)^2}, \tag{1.102}$$

$$\Lambda' = \bar{s}\mathrm{e}^{3/2\,(\sigma_s\log 2)^2}, \tag{1.103}$$

$$q_0' = \frac{\bar{s}^2\phi}{8\alpha_\infty}\mathrm{e}^{6(\sigma_s\log 2)^2}. \tag{1.104}$$

In short, only 3 directly measurable parameters ϕ, $\bar{s}$ and σ_s are required instead of 6 for the JCAL model.

5 | Modelling wave propagation in porous medium layers

The propagation of acoustic plane waves of pressure p inside an isotropic medium of arbitrary wavenumber k is governed by the Helmholtz wave equation [32]:

$$\Delta p + k^2 p = 0, \tag{1.59}$$

where the spatial wave number $k^2 = \frac{\omega^2}{c^2}$ and $c^2 = \frac{K}{\rho}$. The time and space dependence of the propagating acoustic wave of pressure p, displacement u, and the velocity v in a one dimensional space are

$$p(x,t) = A\mathrm{e}^{j(kx-\omega t)}, \tag{1.105}$$

$$u(x,t) = j\frac{Ak}{\rho\omega^2}\mathrm{e}^{j(kx-\omega t)}, \tag{1.106}$$

$$v(x,t) = \frac{Ak}{\rho\omega}\mathrm{e}^{j(kx-\omega t)}, \tag{1.107}$$

where A is the amplitude of the pressure wave. The pressure p and velocity v are related by

$$v(x,t) = \frac{1}{Z}p(x,t), \tag{1.108}$$

where Z is the characteristic acoustic impedance of the medium:

$$Z = \sqrt{\rho K} = \rho c. \tag{1.109}$$

In the case of air, $k = k_0$, $\rho = \rho_0$, $c = c_0$, and $Z = Z_0$. In the case of a dissipative equivalent fluid, $k = \tilde{k}_{eq}$, $\rho = \tilde{\rho}_{eq}$, $c = \tilde{c}_{eq}$, and $Z = \tilde{Z}_{eq}$ are complex numbers denoting dissipation inside the medium.

5.1 | Absorption and transmission problems

When a plane acoustic wave impinges on a layer, part of the acoustic wave energy is reflected at the surface of the layer, part is transmitted through the layer, and part is dissipated by the layer. The sum of the reflected, transmitted and absorbed energy are equal to the impinging wave's energy.

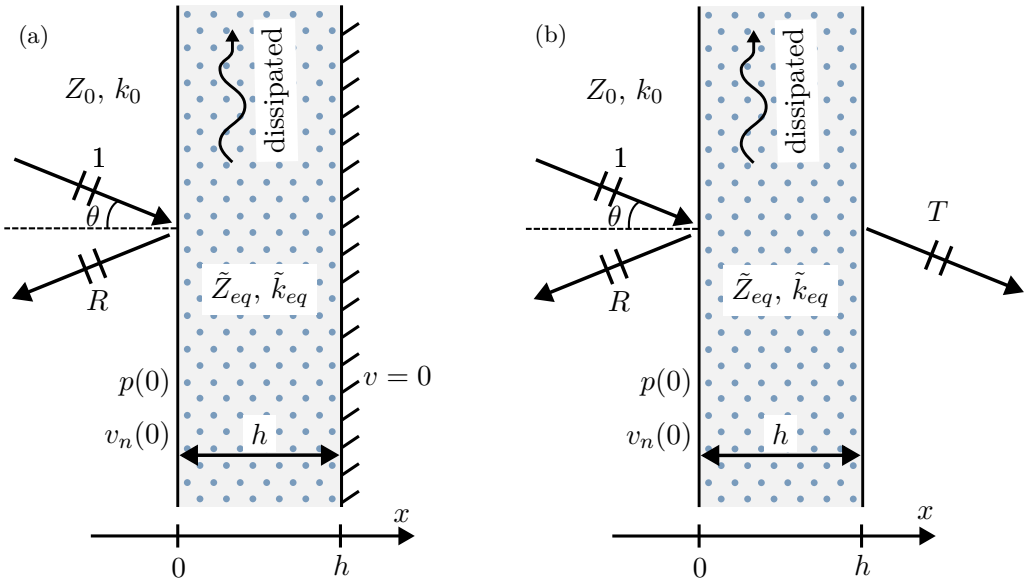

Figure 1.12. Illustration of a plane acoustic wave impinging onto a porous layer. (a) Absorption problem, (b) transmission problem.

The impinging wave arrives at an incidence angle θ relative to the surface normal. The reflection coefficient R is the amplitude of the reflected wave p_0^- over the amplitude of the incident wave p_0^+ at the surface of the layer. It can be written [39]

$$R = \frac{Z_s \cos\theta - Z_0}{Z_s \cos\theta + Z_0}, \tag{1.110}$$

where Z_s is the surface impedance, the ratio of pressure to velocity at the material surface:

$$Z_s = \frac{p(0)}{v_n(0)} = \frac{1}{\cos\theta} Z_0 \frac{1+R}{1-R}. \tag{1.111}$$

For example, for a rigid-backed porous layer of thickness h, with characteristic impedance $\tilde{Z}_{eq}$, wavenumber $\tilde{k}_{eq}$, and porosity ϕ, as shown in Figure 1.12(a), its surface impedance Z_s is given by

$$Z_s = -j \frac{\tilde{Z}_{eq}}{\phi \cos\theta} \cot\left(\tilde{k}_{eq} h\right). \tag{1.112}$$

The absorption coefficient α (-) is often used to characterize how effective a layer is at absorbing, *i.e.* not reflecting, sound waves. It is defined as

$$\alpha = 1 - |R|^2 . \tag{1.113}$$

In diffuse field incidence, the diffuse field absorption coefficient α_d is computed as

$$\alpha_d = \frac{\int_{\theta_{min}}^{\theta_{max}} \alpha(\theta) \cos\theta \sin\theta \, \mathrm{d}\theta}{\int_{\theta_{min}}^{\theta_{max}} \cos\theta \sin\theta \, \mathrm{d}\theta}, \tag{1.114}$$

where $\theta_{min} = 0°$ and $\theta_{max} < 90°$.

Moreover, for a transmission problem, where the wave propagates into a semi-infinite fluid beyond the layer, as shown in Figure 1.12(b), the transmission coefficient T represents the amplitude of the wave transmitted beyond the layer over the amplitude of the incident wave. The Transmission Loss TL (dB) is computed as

$$TL = 10 \log \left| \frac{1}{T^2} \right|. \tag{1.115}$$

The radiation efficiency factor σ_r of a multilayer placed on a vibrating surface of vibrational power Π_{vib} corresponds to ratio of the radiated acoustic power Π_{rad} over the vibrational power Π_{vib}. The vibrational power Π_{vib} is also equal to the radiated acoustic power of a piston with the same vibrational energy, which has a velocity v_p and surface area S_p. It is written

$$\sigma_r = \frac{\Pi_{rad}}{\Pi_{vib}} = \frac{\Pi_{rad}}{\frac{1}{2}\rho_0 c_0 S_p |v_p|^2}. \tag{1.116}$$

When computing the radiation efficiency of a multilayer backed by a vibrating rigid wall, Doutres et al. [24] show that using a transfer impedance Z_t which accounts for the velocity v_p of the backing is more accurate than using the surface impedance Z_s. The transfer impedance is given as

$$Z_t = \frac{p_0}{v_p - v_0}. \tag{1.117}$$

The radiation efficiency is then expressed as [111]

$$\sigma_r = \left| \frac{Z_t}{Z_t + Z_0} \right|^2 . \tag{1.118}$$

In the case of a rigid motionless wall backing, $v_p = 0$, which incurs $Z_t = Z_s$.

5.2 | Transfer Matrix Method

The Transfer Matrix Method (TMM) is based on plane wave propagation inside laterally infinite layers, as shown in Figure 1.13. It relies on describing the evolution of a state vector V, containing pressure p and velocity v information for example, throughout each layer and each interface of a multilayer system. This method allows for the calculation of wave propagation through any number of superimposed media [39, 53, 112].

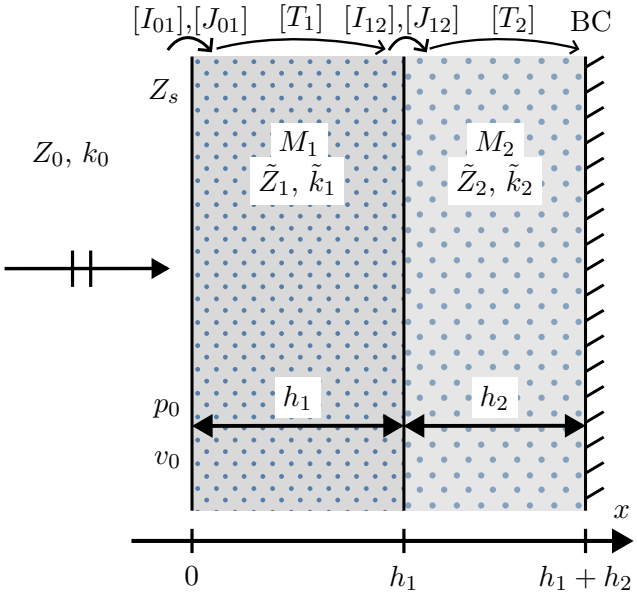

Figure 1.13. Diagram showing the methodology of the Transfer Matrix Method (TMM).

Within the ith layer M_i, the transfer matrix $[T_i]$ relates state vector V between the start and the end of the layer by

$$V(M_{i,start}) = [T_i]V(M_{i,end}). \tag{1.119}$$

For a fluid or an equivalent fluid the state vector containing the pressure and velocity variables is

$$V(M_i) = \begin{Bmatrix} p(M_i) \\ v_x(M_i) \end{Bmatrix}, \tag{1.120}$$

and $[T]$ is given by

$$[T] = \begin{bmatrix} \cos(k_x h) & \frac{j\omega\rho}{k_x}\sin(k_x h) \\ \frac{jk_x}{\omega\rho}\sin(k_x h) & \cos(k_x h) \end{bmatrix}, \tag{1.121}$$

where k_x is the wavenumber of the medium k projected in the direction x that the layers are stacked in:

$$k_x = k\cos\theta. \tag{1.122}$$

For a biphasic poroelastic Biot medium, there are six degrees of freedom in the general case, though this can be simplified to four degrees of freedom in normal incidence since there is no shear wave in the skeleton, or when using the (u, p) formulation. Consequently, in the general case, the state vector is

$$V = \begin{pmatrix} v_y^s & v_x^s & v_x^f & \sigma_x^s & \sigma_{xy}^s & \sigma_x^f \end{pmatrix}^T. \tag{1.123}$$

The transfer matrix $[T]$ is a six by six matrix, whose first three columns are

$$[T](:,1:3) = \begin{bmatrix} \omega k_y \cos(k_{1x}x_3) & -j\omega k_y \sin(k_{1x}x_3) & \omega k_y \cos(k_{2x}x_3) \\ -j\omega k_{1x} \sin(k_{1x}x_3) & \omega k_{1x} \cos(k_{1x}x_3) & -j\omega k_{2x} \sin(k_{2x}x_3) \\ -j\omega k_{1x}\xi_1 \sin(k_{1x}x_3) & \omega \xi_1 k_{1x} \cos(k_{1x}x_3) & -j\omega k_{2x}\xi_2 \sin(k_{2x}x_3) \\ -D_1 \cos(k_{1x}x_3) & jD_1 \sin(k_{1x}x_3) & -D_2 \cos(k_{2x}x_3) \\ j2Nk_yk_{1x} \sin(k_{1x}x_3) & -2Nk_yk_{1x} \cos(k_{1x}x_3) & j2Nk_yk_{2x} \sin(k_{2x}x_3) \\ -E_1 \cos(k_{1x}x_3) & jE_1 \sin(k_{1x}x_3) & -E_2 \cos(k_{2x}x_3) \end{bmatrix}, \tag{1.124}$$

and the last three columns of $[T]$ are

$$[T](:,4:6) = \begin{bmatrix} -j\omega k_y \sin(k_{2x}x_3) & j\omega k_{3x} \sin(k_{3x}x_3) & -\omega k_{3x} \cos(k_{3x}x_3) \\ \omega k_{2x} \cos(k_{2x}x_3) & \omega k_y \cos(k_{3x}x_3) & -j\omega k_y \sin(k_{3x}x_3) \\ \omega \xi_2 k_{2x} \cos(k_{2x}x_3) & \omega k_y \xi_3 \cos(k_{3x}x_3) & -j\omega k_y \xi_3 \sin(k_{3x}x_3) \\ jD_2 \sin(k_{2x}x_3) & j2Nk_{3x}k_y \sin(k_{3x}x_3) & -2Nk_{3x}k_y \cos(k_{3x}x_3) \\ -2Nk_yk_{2x} \cos(k_{2x}x_3) & N\left((k_{3x}^2 - k_y^2\right) \cos(k_{3x}x_3) & -jN\left(k_{3x}^2 - k_y^2\right) \sin(k_{3x}x_3) \\ jE_2 \sin(k_{2x}x_3) & 0 & 0 \end{bmatrix}. \tag{1.125}$$

where, for $i = 1, 2$:

$$D_i = (P + Q\mu_i)(k_y^2 + k_{i3}^2) - 2Nk_y^2, \tag{1.126}$$

$$E_i = (R\mu_i + Q)(k_y^2 + k_{i3}^2). \tag{1.127}$$

The x component of the wavenumbers of the two compression waves k_{1x} and k_{2x}, and of the shear wave k_{3x}, are

$$k_{ix} = \left(\delta_i^2 - k_y^2\right)^{1/2}, \tag{1.128}$$

where the square root $()^{1/2}$ symbol denotes the square root that yields a positive real part, and k_y is the transverse y component of the wavenumber for each wave:

$$k_y = k \sin\theta. \tag{1.129}$$

At the interface between the ith and the $(i+1)$th layer, the interface matrix $[I_{i\,i+1}]$ relates the state vector before and after the interface by

$$[I_{i\,i+1}]V(M_{i,end}) + [J_{i\,i+1}]V(M_{i+1,start}) = 0. \tag{1.130}$$

The matrix $[I]$ depends on the two connected media. Some common examples of interfaces matrices are given below:

- Between two fluids

$$[I_{i\,i+1}] = \begin{bmatrix} 1 & 0 \\ 0 & \frac{\phi_i}{\phi_{i+1}} \end{bmatrix}, \quad [J_{i\,i+1}] = -\begin{bmatrix} 1 & 0 \\ 0 & 1 \end{bmatrix}. \tag{1.131}$$

- Between two fluids connected by an impermeable interface of surface density m_s

$$[I_{i\,i+1}] = \begin{bmatrix} 1 & -j\omega m_s \phi_i \\ 0 & \phi_i \end{bmatrix}, \quad [J_{i\,i+1}] = -\begin{bmatrix} 1 & 0 \\ 0 & \phi_{i+1} \end{bmatrix}. \tag{1.132}$$

- Between a fluid and a biphasic poroelastic Biot layer

$$[I_{i\,i+1}] = \begin{bmatrix} 0 & -\phi_i \\ 1-\phi_{i+1} & 0 \\ 0 & 0 \\ \phi_{i+1} & 0 \end{bmatrix}, \quad [J_{i\,i+1}] = \begin{bmatrix} 0 & 1-\phi_{i+1} & \phi_{i+1} & 0 & 0 & 0 \\ 0 & 0 & 0 & 1 & 0 & 0 \\ 0 & 0 & 0 & 0 & 1 & 0 \\ 0 & 0 & 0 & 0 & 0 & 1 \end{bmatrix}. \tag{1.133}$$

- Between two biphasic Biot layers

$$[I_{i\,i+1}] = \begin{bmatrix} 1 & 0 & 0 & 0 & 0 & 0 \\ 0 & 1 & 0 & 0 & 0 & 0 \\ 0 & -\phi_i & \phi_i & 0 & 0 & 0 \\ 0 & 0 & 0 & 1 & 0 & 1 \\ 0 & 0 & 0 & 0 & 1 & 0 \\ 0 & 0 & 0 & 0 & 0 & \frac{1}{\phi_i} \end{bmatrix}, \quad [J_{i\,i+1}] = -\begin{bmatrix} 1 & 0 & 0 & 0 & 0 & 0 \\ 0 & 1 & 0 & 0 & 0 & 0 \\ 0 & -\phi_{i+1} & \phi_{i+1} & 0 & 0 & 0 \\ 0 & 0 & 0 & 1 & 0 & 1 \\ 0 & 0 & 0 & 0 & 1 & 0 \\ 0 & 0 & 0 & 0 & 0 & \frac{1}{\phi_{i+1}} \end{bmatrix}. \tag{1.134}$$

Furthermore, when the acoustic wave impinges on an interface at angle θ, the wave is refracted at a different angle depending on the frequency and the media's refractive indices $n_{r,i}$ according to Snell's law:

$$n_{r,1}\sin(\theta_1) = n_{r,2}\sin(\theta_2). \tag{1.135}$$

The overall system can be solved by assembling all matrices relating $V(M_0)$ to $V(M_N)$. In the case where the last layer is a(n equivalent) fluid medium, this can be written simply as

$$V(M_0) = \begin{bmatrix} a & b \\ c & d \end{bmatrix} V(M_N). \tag{1.136}$$

If there is a rigid wall boundary condition behind the materials, then $v_x(M_N) = 0$, and

$$\begin{Bmatrix} p(M_1) \\ v_x(M_1) \end{Bmatrix} = \begin{bmatrix} a & b \\ c & d \end{bmatrix} \begin{Bmatrix} p(M_i) \\ 0 \end{Bmatrix} = \begin{Bmatrix} a\,p(M_i) \\ c\,p(M_i) \end{Bmatrix}. \tag{1.137}$$

In this case, the surface impedance Z_s of the multilayer system is expressed simply as

$$Z_s = \frac{p(M_1)}{v_x(M_1)} = \frac{a\,p(M_i)}{c\,p(M_i)} = \frac{a}{c}. \tag{1.138}$$

The system of equations is then written as

$$[D]\{V\} = \begin{bmatrix} [I_{01}] & [J_{01}][T_1] & [0] & \dots & [0] & [0] \\ [0] & [I_{12}] & [J_{12}][T_2] & \dots & [0] & [0] \\ \vdots & \vdots & \vdots & & \vdots & \vdots \\ [0] & [0] & [0] & \dots & [I_{N-1\,N}] & [J_{N-1\,N}][T_N] \end{bmatrix} \begin{Bmatrix} V(M_0) \\ V(M_1) \\ \vdots \\ V(M_N) \end{Bmatrix} = \begin{Bmatrix} 0 \\ 0 \\ \vdots \\ 0 \end{Bmatrix}. \quad (1.139)$$

To solve the system of equations, the boundary conditions must be added. First, the surface impedance Z_s of the multilayer can be added to $[D]$ as

$$p(M_0) - Z_s v_n(M_0) = 0. \quad (1.140)$$

Next, if the multilayer ends with a fluid, there is still one equation missing, and if the multilayer ends with a biphasic medium, there are still three equations missing. In the case of a rigid backing, when the last layer is a fluid, the velocity of the fluid is equal to 0:

$$v_x(M_N) = 0. \quad (1.141)$$

Or in the case of a rigid backed biphasic medium, the velocities of the frame-borne waves and of the velocity of the fluid are equal to 0:

$$v_x^s(M_N) = 0, \quad (1.142)$$

$$v_y^s(M_N) = 0, \quad (1.143)$$

$$v_x^f(M_N) = 0. \quad (1.144)$$

In the case of a free-field semi-infinite fluid of impedance Z_0 behind the multilayer, the impedance of the wave must equal Z_0. This corresponds to adding a fluid medium at the end of the multilayer, connected to the Nth layer by an interface matrix $[I_{N\,N+1}]$ and $[J_{N\,N+1}]$, and then setting

$$p(M_{N+1}) = Z_0 v_x(M_{N+1}) \quad (1.145)$$

When adding the boundary conditions equations to $[D]$, a new matrix $[D']$ is obtained. The surface impedance can be computed easily as the determinant of $[D']$ without its first column over the determinant of $[D']$ without its second column:

$$Z_s = -\frac{\det[D'(:, 2:\text{end})]}{\det[D'(:, [1, 3:\text{end}])]}. \quad (1.146)$$

The reflection coefficient R is computed from Equation 1.110. When the multilayer is backed by a semi-infinite fluid, the transmission coefficient T is computed from [39]

$$T = (1+R)\frac{\det[D'(:, [1:\text{end}-1,\ \text{end}])]}{\det[D'(:, 2:\text{end})]}. \quad (1.147)$$

To compute the radiation efficiency σ_r, the rigid backing is given a velocity v_p. When the last layer is a fluid or an equivalent fluid, its velocity is

$$v_x(M_N) = v_p. \quad (1.148)$$

When the last layer is a biphasic medium, the velocity of the frame and the velocity of the fluid are

equal to v_p, and the shear velocity of the frame is set to 0 assuming only normal displacement:

$$v_x^s\left(M_N\right) = v_p, \tag{1.149}$$

$$v_y^s\left(M_N\right) = 0, \tag{1.150}$$

$$v_x^f\left(M_N\right) = v_p. \tag{1.151}$$

Solving the system for p_0 and v_0 allows the computation of the transfer impedance Z_t from Equation 1.117. The final result for σ_r is independent of the value of v_p.

The TMM is limited in higher frequencies, or for large layer thicknesses, because it becomes unstable. Dazel later suggested a more stable TMM implementation of the Biot model in 2007 [46], and in 2013 suggests a more general formulation using a proxy "information vector" to bypass this problem [113]. Moreover, since the TMM uses a plane wave approximation, it is also less accurate for very low frequencies [114].

6 | Comparison of models

6.1 | Summary of parameters used by different models

The various parameters required for different behaviour models are summarized in Table 1.1.

Table 1.1. Quantities used by different behaviour models.

	Transport parameters							**Skeleton parameters**			
	σ	ϕ	α_∞	Λ	Λ'	q_0'	α_0	α_0'	ρ_1	E	η	ν
	Nsm^{-4}	-	-	m	m	m^2	-	-	$\mathrm{kg/m}^3$	Pa	-	-
DBM	■	■	■	■	■	■	■	■				
JCA		■	■	■	■	■						
JCAL		■	■	■	■	■	■					
JCAPL		■	■	■	■	■	■	■				
limp									■			
Biot									■	■	■	■

6.2 | Rigid skeleton versus limp

The difference between the limp and the motionless skeleton equivalent fluid behaviours is predominant in low frequencies. At low frequencies, for the limp behaviour, the imaginary part of the density $\tilde{\rho}_{limp}$ tends to $-\infty$, whereas for the rigid skeleton behaviour it tends to 0. This is shown in Figure 1.14.

6.3 | Parameter zones of influence

Some of the parameters in Table 1.1 are low frequency parameters and some are high frequency parameters, whereas some have an influence everywhere. When computing an acoustic indicator, such as the absorption coefficient α for a rigid backed layer of porous material, the sensitivity Δ of the absorption coefficient α to any parameter β can be computed as

$$\Delta\alpha(\beta) = \frac{\partial\alpha}{\partial\beta}. \tag{1.152}$$

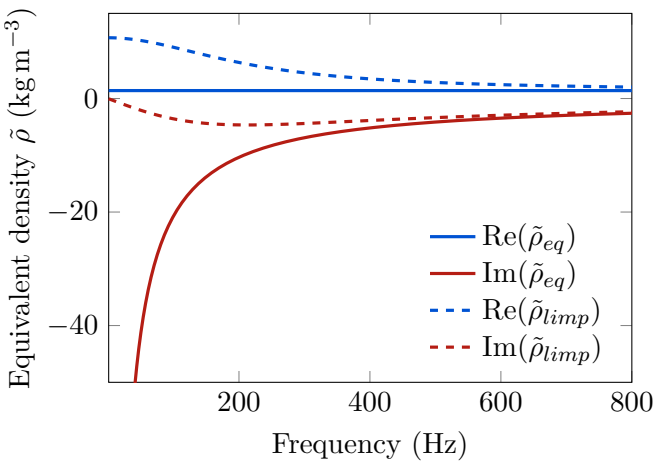

Figure 1.14. Real and imaginary parts of the equivalent fluid for rigid skeleton model (JCAL) and limp model, computed for a melamine foam material.

At low frequency ($f \sim 0$), the absorption coefficient gets close to 0, so this sensitivity can be normalized by the value of α to bring out the sensitivity of parameters in low frequencies. Further, the different parameters are expressed in different orders of magnitude (σ is in the order of 10^4 N s m^{-4}, and q_0' is in the order of 10^{-9} m^2). To correct for this, the sensitivity can also be normalized by the value of β, to express the sensitivity to a relative change in the parameter. The normalized sensitivity is then

$$\Delta_n \alpha(\beta) = \frac{\beta}{\alpha} \frac{\partial \alpha}{\partial \beta}. \tag{1.153}$$

The sensitivity of the absorption coefficient of a rigid-backed layer of melamine foam to transport and mechanical properties is shown in Figure 1.15. The results are computed numerically using symbolic expressions in Matlab. In regard to the transport parameters in Figure 1.15, this reveals how σ and q_0' dictate the low-frequency limit of the behaviour. α_∞, Λ and Λ' are more high-frequency parameters. The porosity ϕ influences all frequencies. Interestingly, at the quarter-wavelength resonance frequency of the skeleton f_r, the influence of α_∞ and of viscous parameters σ and Λ drops, whereas the influence of ϕ and of thermal parameters Λ' and q_0' increases. In regard to the mechanical parameters in Figure 1.15(d), their influence is limited to the quarter-wavelength resonance frequency of the skeleton f_r and its harmonics. The influence of the loss factor η is relatively small, especially compared to the influence of the Poisson ratio ν for instance, which could be because it is quite small, at $\eta = 4$ %. The storage modulus E' and the Poisson ratio ν have a very strong effect near the resonance frequency since they shift the resonance frequency, causing the peak with a high dynamic range to translate left and right.

It is worth noting that the transition between low and high frequencies is not very clear. The transition for viscous and thermal effects can be estimated using the viscous and thermal skin depths and the radius of the pores r. The viscous skin depth δ_0 corresponds to the penetration depth of rotational viscous movements, whereas the thermal skin depth $\delta_0' = \frac{\delta_0}{\sqrt{\mathrm{Pr}}}$ is the penetration depth of isothermal movement. These depths are thinner at higher frequencies. For a pore of characteristic radius r, the transition between low and high frequencies can be set when the viscous and thermal skins are equal to $r/2$, that is to say for frequencies f_0 and f_0' [42]

$$f_0 = \frac{1}{2\pi} \frac{8\mu_0}{\rho_0 r^2}, \quad f_0' = \frac{1}{2\pi} \frac{8\kappa_0}{\rho_0 c_p r^2}. \tag{1.154}$$

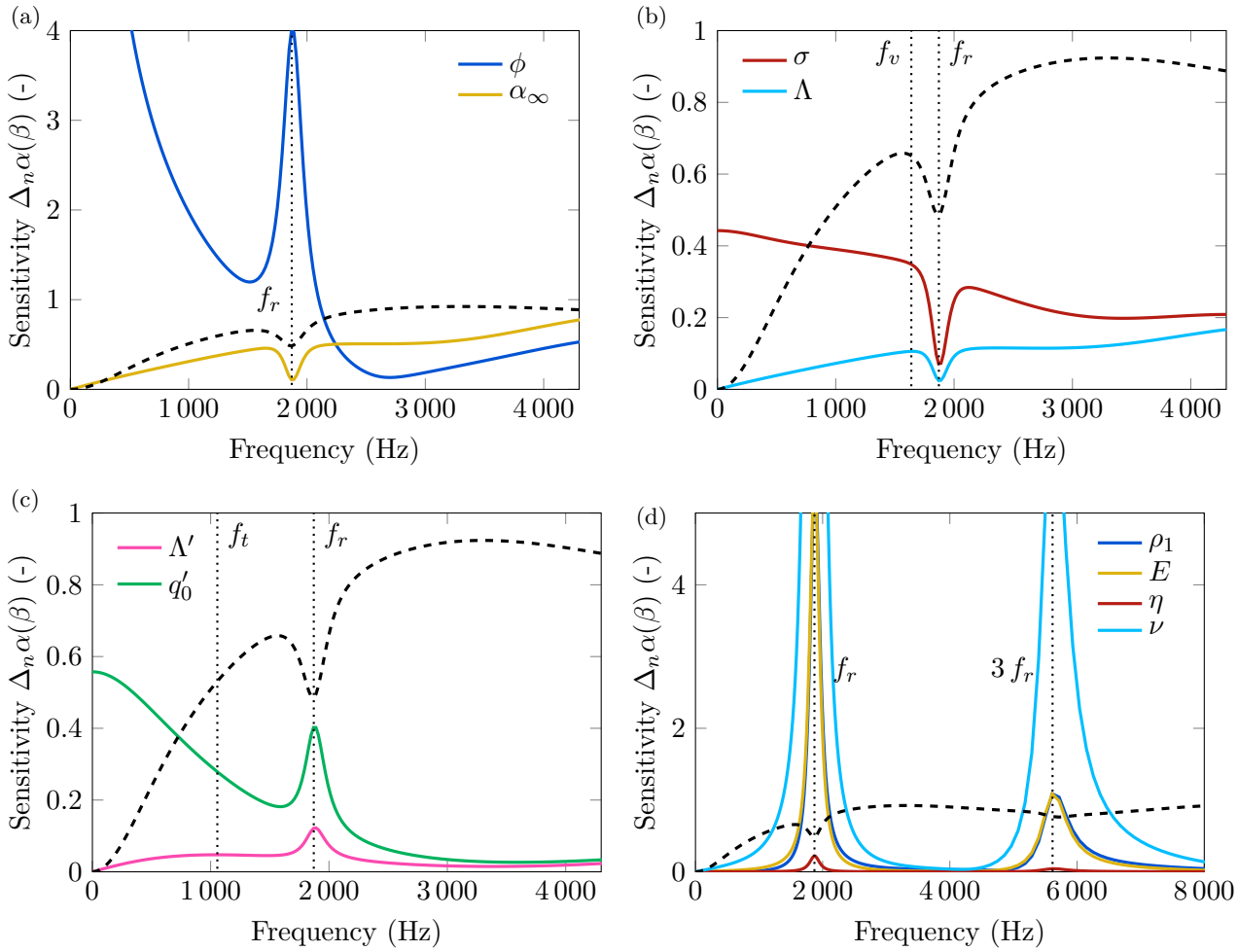

Figure 1.15. Normalized sensitivity Δ_n of the absorption coefficient α to (a) ϕ and α_∞, (b) viscous transport parameters σ and Λ, (c) thermal transport parameters Λ' and q'_0, and (d) mechanical material parameters using a Biot JCAL model. The black dashed line represents the absorption coefficient α.

Additionally, the low and high frequency behaviours can be identified independently of the pore dimensions from the characteristic frequencies f_v for viscous effects [115] and f_t for thermal effects [116]

$$f_v = \frac{1}{2\pi}\frac{\phi\sigma}{\rho_0\alpha_\infty}, \quad f_t = \frac{1}{2\pi}\frac{\phi\mu_0}{q'_0\rho_0\mathrm{Pr}}. \tag{1.155}$$

For a melamine foam, the characteristic frequencies are $f_v = 1\,684$ Hz and $f_t = 1\,057$ Hz, as illustrated in Figure 1.15(b) and Figure 1.15(c).

6.4 | Comparison of Absorption Coefficients

The absorption coefficient for several rigid-backed materials are plotted in Figure 1.16, using properties from Table 1.2 and TMM. These properties are representative of a stiff melamine foam, a dense polyurethane (PU) foam, and a glass wool. The absorption coefficient for the melamine in Figure 1.16(a) using the DBM, JCA, JCAL, limp and Biot models reveal the differences between the models. The DBM model is quite different from the other models. The difference between the JCA model ($q'_0 = 9.0\,10^{-9}$ m^2 with cylindrical pores hypothesis) and the JCAL model ($q'_0 = 3.0\,10^{-9}$ m^2) is notable. The limp and Biot models are computed using the JCAL model. The difference between the JCAL and limp models is quite small. The Biot model adds a significant resonance around 1880 Hz

which is not present in the other models. The FSI criterion is computed for several materials, averaged between 1 Hz and 800 Hz and shown in Table 1.2. The FSI of the melamine is 0.87, which is higher than the limit of 0.2. This explains the difference between the limp and the Biot representations.

The predictions from the JCAL, limp and Biot models are also represented for a dense polyurethane foam, called PU250, in Figure 1.16(b) and the glass wool in Figure 1.16(c). In both cases, the JCAL model is quite different from the limp and Biot models, especially in low frequencies. For the PU250, the Biot and limp models are quite different, whereas for the glass wool they are very close. This is because the FSI of the PU250 is 1.7, which makes it unadapted to the limp representation. Conversely, the FSI of the glass wool is $7.7\,10^{-3}$ which makes the limp representation sufficient in capturing its behaviour.

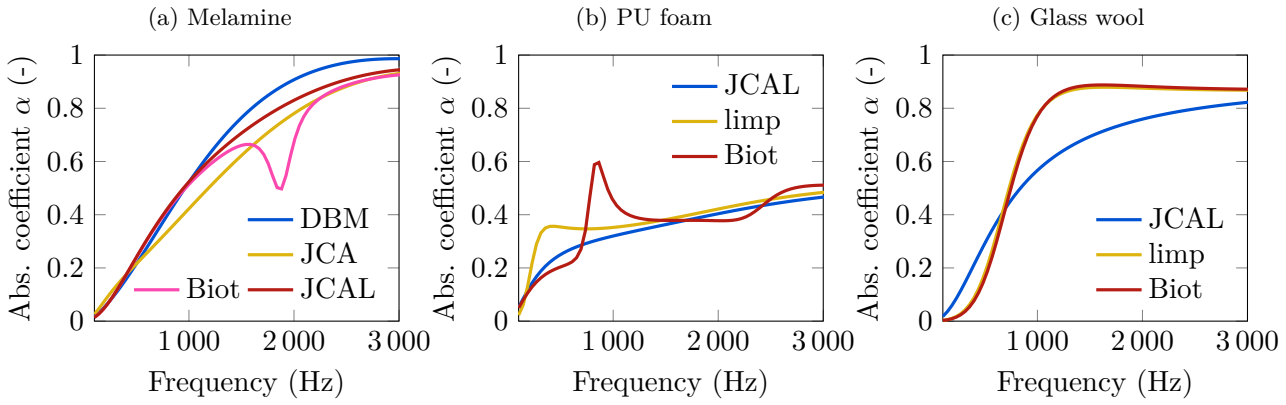

Figure 1.16. Absorption coefficient α using different models for (a) melamine, (b) PU250, (c) glass wool.

Table 1.2. Material properties and validity of the FSI for the materials whose absorption coefficient is plotted in Figure 1.16.

	h	σ	ϕ	α_∞	Λ	Λ'	q_0'	ρ_1	E	η	ν	FSI
	mm	$\mathrm{kNsm^{-4}}$	-	-	µm	µm	$10^{-9}\mathrm{m^2}$	$\mathrm{kg\,m^{-3}}$	kPa	%	-	-
Melamine	29.1	13.8	0.94	1.01	135.8	277.4	3.0	9.58	140	4	0.44	0.87
PU	20.9	[redacted]	0.79	2.45	17.9	170.2	16.2	242.5	300	18	0.44	1.70
Glass wool	20.0	105.0	0.95	1.00	35.1	105.3	1.31	17.0	1.4	3	0.0	0.008

7 | Impedance tube measurements

7.1 | Impedance tube properties and limits

Acoustic measurements in an impedance tube are often used to measure a material's behaviour. This relies on measuring the absorption coefficient α, the equivalent density $\tilde{\rho}_{eq}$ and bulk modulus $\tilde{K}_{eq}$ of a sample using two or three microphones for instance. The setup requirements are given by standard protocols [117, 118]. The setup of an impedance tube and its dimensions are indicated on the schematic representation in Figure 1.17.

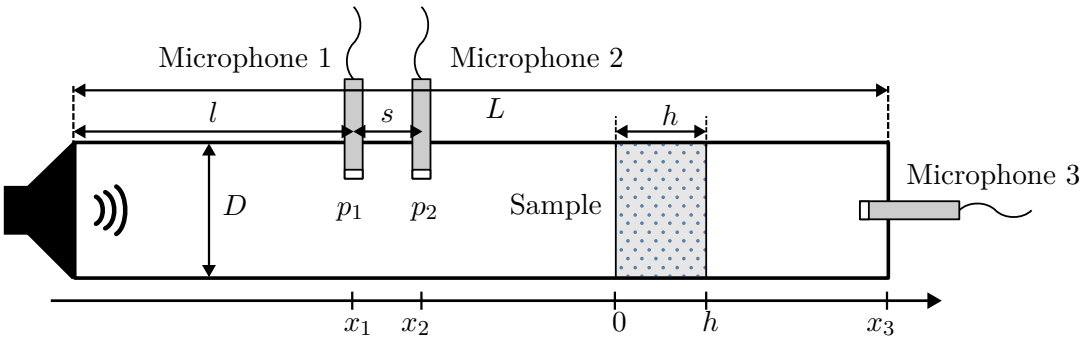

Figure 1.17. Measurement principle with a tube with 3 microphones.

The impedance tube measurements assume a plane wave hypothesis within the duct, which is valid below the propagation frequency of the first transverse mode. For a cylindrical duct of diameter D, this frequency is

$$f_{max,1} < \frac{1.84}{\pi D} c_0 \approx 0.586 \frac{c_0}{D}, \tag{1.156}$$

Moreover, there should be at most half a wavelength between two microphones to avoid indeterminate results:

$$f_{max,2} = 0.45 \frac{c_0}{s}. \tag{1.157}$$

To separate the incident and reflected waves, two microphones are required. If the microphones are too close, it becomes impossible to distinguish between their measured pressures for long wavelengths, *i.e.* for low frequencies. An empirical rule states that the distance s between the microphones should be at least a certain percentage of the longest wavelength, for instance 1.5 % [119]:

$$f_{min,1} = 0.015 \frac{c_0}{s}, \tag{1.158}$$

Further, the tube must be longer than half a wavelength to obtain a standing wave [120]:

$$f_{min,2} = 0.5 \frac{c_0}{L}, \tag{1.159}$$

The length of the tube L is recommended to be at least three times the diameter in [118]:

$$L > 3D, \tag{1.160}$$

though in practice it is better to have a length greater than 10 or 15 diameters [121]. Moreover, it is recommended to place the microphones at a distance l from the speaker that is at least three times the diameter of the tube, so that non-planar evanescent waves have disappeared:

$$l > 3D, \tag{1.161}$$

They should also be placed at least half a diameter (for non-structured materials) or two diameters (for asymmetrical material samples) away from the sample due the proximity distortion to the acoustic fields:

$$|x_2| > 2D. \tag{1.162}$$

7.2 | Two microphone method (reflection)

Let there be a sample in the impedance tube of reflection coefficient R. Upstream from the sample in the tube, at a distance $x < 0$ from the sample, the acoustic wave corresponds to the superposition of a forward wave and a backward propagating waves, written with a normalized amplitude:

$$p(x) = \mathrm{e}^{jk_0 x} + R\mathrm{e}^{-jk_0 x}. \tag{1.163}$$

By using 2 microphones at positions x_1 and $x_2 = x_1 + s$, the forward and backward waves can be separated by calculating the transfer function between the two microphones H_{12}

$$H_{12} = \frac{p_2}{p_1} = \frac{\mathrm{e}^{jk_0 x_2} + R\mathrm{e}^{-jk_0 x_2}}{\mathrm{e}^{jk_0 x_1} + R\mathrm{e}^{-jk_0 x_1}}. \tag{1.164}$$

The reflection coefficient is then expressed as

$$R = \frac{\mathrm{e}^{jk_0 s} - H_{12}}{H_{12} - \mathrm{e}^{jk_0 s}} \mathrm{e}^{j2k_0 x_1}. \tag{1.165}$$

The absorption coefficient α and the surface impedance Z_s of the sample can be deduced:

$$\alpha = 1 - |R|^2, \tag{1.113}$$

$$Z_s = Z_0 \frac{1+R}{1-R}. \tag{1.111}$$

7.3 | 3 microphone method (reflection and transmission)

To access the transmission behaviour and the intrinsic properties of the sample, it is necessary to add a new measurement. This can be done with 2 microphones and 2 cavities [122], 3 microphones with one downstream from the sample [123], or 4 microphones with two downstream from the sample [124, 125]. Salissou [102] then Doutres et al. [126] propose more easily implemented 3 microphone methods. A three-microphone and two cavity method is used here [126, 127].

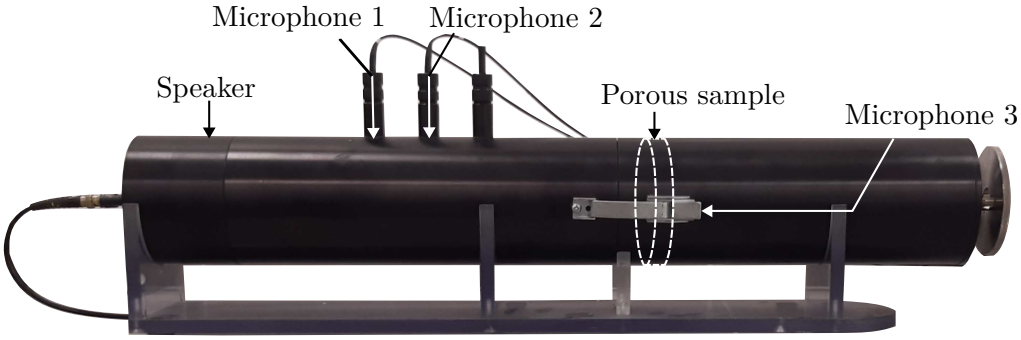

Figure 1.18. 100 mm diameter impedance tube used for acoustic measurements.

The measurement process is performed for two different cavity sizes in the case of asymmetric samples, which have different behaviours in different directions. The cavity represents the depth of the air gap $(x_3 - h)$ behind the sample. The measurement can be simplified to a single cavity if the sample is symmetric. The third microphone is placed at the end of the duct, flush with the rigid ending of the tube, at position x_3. The first measurement involves a cavity of depth $x_3^{(1)}$, and the second one involves a cavity of depth $x_3^{(2)}$. Upstream in the tube (*i.e.* $x < 0$), for each cavity configuration $i = 1, 2$, the pressure and velocity are given by

$$p^{(i)}(x) = \mathrm{e}^{jk_0x} + R^{(i)}\mathrm{e}^{-jk_0x}, \tag{1.166}$$

$$v^{(i)}(x) = \frac{1}{Z_s^{(i)}}\left(\mathrm{e}^{jk_0x} + R^{(i)}\mathrm{e}^{-jk_0x}\right). \tag{1.167}$$

Downstream in the tube ($x > h$)

$$p^{(i)}(x) = 2A^{(i)}\mathrm{e}^{jk_0x_3^{(i)}}\cos\left(-k_0\left(x - x_3^{(i)}\right)\right), \tag{1.168}$$

$$v^{(i)}(x) = -j2\frac{A^{(i)}}{Z_s^{(i)}}\mathrm{e}^{jk_0x_3^{(i)}}\sin\left(-k_0\left(x - x_3^{(i)}\right)\right), \tag{1.169}$$

where $A^{(i)}$ is the amplitude of the acoustic wave downstream from the sample computed from the transfer function H_{13}

$$H_{13}^{(i)} = \frac{p_3}{p_1} = \frac{2A^{(i)}\mathrm{e}^{jk_0x_3^{(i)}}}{\mathrm{e}^{jk_0x_1} + R^{(i)}\mathrm{e}^{-jk_0x_1}}, \tag{1.170}$$

therefore,

$$A^{(i)} = H_{13}^{(i)}\frac{\mathrm{e}^{jk_0x_1} + R^{(i)}\mathrm{e}^{-jk_0x_1}}{2\mathrm{e}^{jk_0x_3^{(i)}}}. \tag{1.171}$$

On either side of the sample, pressure and velocity are related by the transfer matrix $[T]$ of the sample:

$$\begin{Bmatrix} p(0) \\ v(0) \end{Bmatrix} = [T]\begin{Bmatrix} p(h) \\ v(h) \end{Bmatrix} = \begin{bmatrix} T_{11} & T_{12} \\ T_{21} & T_{22} \end{bmatrix}\begin{Bmatrix} p(h) \\ v(h) \end{Bmatrix}, \tag{1.172}$$

with

$$[T] = \frac{1}{p^{(1)}(h)v^{(2)}(h) - p^{(2)}(0)v^{(1)}(h)}\begin{bmatrix} p^{(1)}(0)v^{(2)}(h) - p^{(2)}(0)v^{(1)}(h) & p^{(2)}(0)p^{(1)}(h) - p^{(1)}(0)p^{(2)}(h) \\ v^{(1)}(0)v^{(2)}(h) - v^{(2)}(0)v^{(1)}(h) & p^{(2)}(h)v^{(2)}(0) - p^{(2)}(h)v^{(1)}(0) \end{bmatrix}, \tag{1.173}$$

where

$$p^{(i)}(0) = -j2\mathrm{e}^{k_0x_2}\frac{H_{12}^{(i)}\sin(k_0x_1) - \sin(k_0x_2)}{H_{12}^{(i)}\mathrm{e}^{jk_0s} - 1}, \tag{1.174}$$

$$v^{(i)}(0) = \frac{j2\mathrm{e}^{jk_0x_2}}{Z_s^{(i)}}\frac{H_{12}^{(i)}\cos(k_0x_1) - \cos(k_0x_2)}{H_{12}^{(i)}\mathrm{e}^{jk_0s} - 1}, \tag{1.175}$$

$$p^{(i)}(h) = -j2\mathrm{e}^{jk_0x_2}\frac{H_{12}^{(i)}\sin(k_0s)\cos\left(-k_0x_3^{(i)}\right)}{H_{12}^{(i)}\mathrm{e}^{jk_0s} - 1}, \tag{1.176}$$

$$v^{(i)}(h) = \frac{j2\mathrm{e}^{jk_0x_2}}{Z_s^{(i)}}\frac{H_{13}^{(i)}\sin(k_0s)\sin\left(-k_0x_3^{(i)}\right)}{H_{12}^{(i)}\mathrm{e}^{jk_0s} - 1}. \tag{1.177}$$

If the material sample is symmetric, *i.e.* its acoustic behaviour is identical in both mounting directions in the tube, then the reciprocity and uniformity of the solution lead to

$$\det([T]) = T_{11}T_{22} - T_{21}T_{12} = 1. \tag{1.178}$$

In this case, the measurement with a single cavity configuration $i = 1$ is sufficient, so $[T]$ can be simplified with $T_{11} = T_{22}$ to

$$[T] = \frac{1}{p^{(1)}(0)v^{(2)}(h) + v^{(1)}(0)p^{(1)}(h)} \begin{bmatrix} p^{(1)}(h)v^{(1)}(h) + p^{(1)}(0)v^{(1)}(0) & p^{(1)}(0)^2 - p^{(1)}(h)^2 \\ v^{(1)}(0)^2 - v^{(1)}(h)^2 & p^{(1)}(h)v^{(1)}(h) + p^{(1)}(0)v^{(1)}(0) \end{bmatrix}. \tag{1.179}$$

The absorption coefficient α of the sample is found from the transfer matrix $[T]$ as [128]

$$\alpha = 1 - \left| \frac{T_{11} - T_{21}Z_0}{T_{11} + T_{21}Z_0} \right|^2, \tag{1.180}$$

and the normal incidence sound transmission loss TL (in dB) is calculated as

$$TL = 20 \log_{10} \left(\frac{1}{2} \left| T_{11} + T_{22} + \frac{T_{12}}{Z_0} + T_{21}Z_0 \right| \right). \tag{1.181}$$

All in all, the equivalent properties $\tilde{K}_{eq}$ and $\tilde{\rho}_{eq}$ of the material are related to the transfer matrix $[T]$

$$[T] = \begin{bmatrix} \cos\left(\tilde{k}_{eq}h\right) & j \sin\left(\tilde{k}_{eq}h\right) Z_0 \\ \frac{j \sin\left(\tilde{k}_{eq}h\right)}{Z_0} & \cos\left(\tilde{k}_{eq}h\right) \end{bmatrix}, \tag{1.182}$$

therefore

$$\tilde{k}_{eq} = \frac{1}{h} \cos^{-1} \left(\frac{1 + R}{\mathrm{e}^{-jk_0x_2} + R\mathrm{e}^{jk_0x_2}} H_{32} \right), \tag{1.183}$$

$$\tilde{Z}_{eq} = -jZ_0 \tan\left(\tilde{k}_{eq}h\right). \tag{1.184}$$

In accordance with Equation 1.62 and Equation 1.63, the material's equivalent properties are then obtained as

$$\tilde{\rho}_{eq} = \frac{\tilde{Z}_{eq}\tilde{k}_{eq}}{\omega}, \tag{1.185}$$

$$\tilde{K}_{eq} = \frac{\tilde{Z}_{eq}^2}{\tilde{\rho}_{eq}}. \tag{1.186}$$

It should be noted that there is a singularity when $\cos\left(k_0x_3^{(1)}\right) \sin\left(k_0x_3^{(2)}\right) = \cos\left(k_0x_3^{(2)}\right) \sin\left(k_0x_3^{(1)}\right)$, in which case $[T]$ is not determined. As a consequence, it is necessary for the difference between the two cavity depths to satisfy

$$\left| x_3^{(1)} - x_3^{(2)} \right| < \frac{\pi}{k_0} \approx \frac{172}{f_{\max}}, \tag{1.187}$$

where $f_{\max}$ is given in Equation 1.156. Moreover, microphones are calibrated in amplitude using a pistonphone, as well as in phase with one another using the microphone swapping technique described in [117, 125].

It can be noted that the reproducibility of impedance tube measurements can vary depending on the laboratory, the method used and the material, according to the round-robin study in [129]. This study shows that impedance tube results depend on sample preparation, number of samples used, chosen sample size, mounting conditions, excitation signal, and method used to merge data from tubes of different diameters. When all laboratories are given the same set of samples, and therefore material inhomogeneity is eliminated, there is still a poor reproducibility of results due to sample mounting conditions, especially for resistive materials and granular materials with a rigid frame [130].

8 | Conclusion

Due to their biphasic nature, the modelling of porous materials can be done at different levels of complexity, depending on their internal structure and their usage conditions. When the material's skeleton is immobile, an equivalent fluid model is enough to represent the dissipative propagation in the fluid. Equivalent fluid models are quite easy to implement as they only require two complex and frequency dependant values, for instance an equivalent density $\tilde{\rho}_{eq}$ and an equivalent bulk modulus $\tilde{K}_{eq}$. The JCAL model provides a good compromise between modelling accuracy and simplicity, and, consequently, it is used as the equivalent fluid model of choice throughout this work. The characterization of the JCAL parameters is explored in the next chapter.

When the skeleton exhibits a rigid body movement, or when it moves but has a negligible stiffness, a limp model is well adapted to represent the extra dissipation caused by the added movement of the solid phase. This model differs mostly from the immobile rigid skeleton models at low frequencies.

When the material skeleton moves and transmits solid-borne waves, a full poroelastic Biot model is required. This model requires more parameters, is more complicated to implement due to increased degrees of freedom over an equivalent fluid model, however it gives the most accurate representation of porous behaviours in configurations where solid-borne waves cannot be neglected. The Biot model uses an equivalent fluid model, representing the dissipation within the fluid phase, as well as complex and frequency dependant viscoelastic mechanical properties, representing the dissipation within the solid phase.

The mechanical parameters can be estimated using different viscoelastic models, which represent their frequency dependence, as well as their temperature dependence through the time-temperature equivalence principle. The Transfer Matrix Method (TMM) is a simple way of implementing these models to predict the behaviour of a multilayer. Using these models to predict the behaviour of a porous medium requires the knowledge of material properties. In the next chapter, the methods used to characterize the materials and obtain these properties are described and applied.

Chapter 2. Experimental characterization of poroelastic materials

1 | Introduction

In this chapter, characterization methods for porous materials are presented and applied to materials studied within the SEMPAE project. There are two main objectives of this chapter. The first is to give an extensive review of characterization methods and assess their validity when applied to real, non-ideal materials used in the industry. For example, some materials are difficult to characterize due to their high mechanical stiffness, high airflow resistivity, high inhomogeneity, high variability, or low thickness. This will shed light on their practical limitations and how they can be overcome. The second objective is to accurately obtain the properties of the materials used for acoustic applications within the SEMPAE project, in order to model their behaviour and optimize their implementation. As such, various characterization methods are presented, their pros and cons are given, and they are compared to each other. Some of these methods are applied to characterize six studied materials.

The six studied materials are described in Section 2, to explain how they are made, what makes them unusual and why they can be difficult to characterize. The direct measurement methods for the transport parameters are presented Section 3. Inverse methods for the transport parameters are presented in Section 4, which include numerical iterative global optimization methods in Section 4.1, micro-macro approaches in Section 4.2, and the analytic indirect method in Section 4.3. At last, the direct mechanical characterization of porous materials is presented in Section 5, with a focus on the quasi-static method. This experimental method has many uncertainties caused by external factors and measurement conditions, such as preload, relaxation, and material surface roughness, which are analysed. In the end, the final material properties are given by combining the results from various methods in Section 6, and their computed absorption coefficient is compared to absorption coefficient measurements for validation.

2 | Materials studied and sample preparation

This section presents the six materials studied in this chapter, their manufacturing processes, and their features which make them unique and difficult to characterize. They are shown in Figure 2.1. The melamine foam in Figure 2.1(a) is chosen because it is often studied in the literature, and it is easy to cut into various shapes which is exploited in the following chapters. The other materials are tied to the SEMPAE project and are manufactured by Trèves Group. The Polyfiber material in Figure 2.1(d) and the polyurethane foams in Figure 2.1(b)-(c) are under-hood materials used for engine encapsulation, while the Greenflocks material in Figure 2.1(e) is a passenger compartment trim material.

(a) Melamine (b) PU60 (c) PU250 (d) Polyfiber (e) Greenflocks

Figure 2.1. Images of encapsulating materials. All cylindrical samples have a diameter of 44.5 mm.

2.1 | Materials description

Melamine foam

The melamine foam shown in Figure 2.1(a) is a standard polymer foam that is often studied in literature. It is a lightweight and highly porous foam with a rigid skeleton. It is easy to manufacture and cut into various shapes, making it ideal for prototyping and testing. For instance, melamine foam can easily be given a geometric pattern on its surface through a convolution process, where sheets are passed through rollers with the desired pattern and cut by a blade. Convoluted melamine foam, also called corrugated foam, with pyramidal and spherical patterns on their surface are shown in Figure 2.2. Nonetheless, melamine is fragile as its skeleton is sensitive to plastic damage and long-term stress. This material is not used in car trims, although it is still exploited in this work to create architected geometries in Chapter 3 and Chapter 4 thanks to its ease of cutting. Additionally, it is often studied in the literature and its properties are well known. For these reasons, it is studied in addition to the other SEMPAE materials.

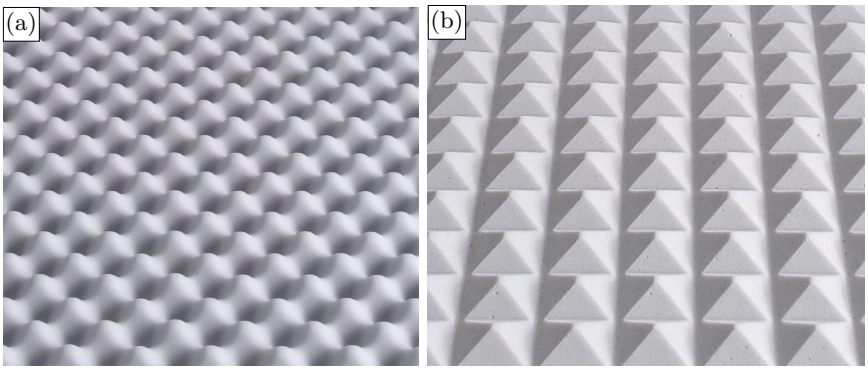

Figure 2.2. Convoluted foam in the shape of (a) spheres and (b) pyramids.

Polyurethane foams

Polyurethane foams of density 60 $\mathrm{kg\,m^{-3}}$ (PU60) and 250 $\mathrm{kg\,m^{-3}}$ (PU250), shown in Figure 2.1(b) and Figure 2.1(c) respectively are used in acoustic screens applications. Thanks to its low stiffness, the PU60 is often used as a soft spring in combination with another denser material, such as dual layer PU60 and PU250 in Figure 2.3(a) or dual layer PU60 and Polyfiber in Figure 2.3(b). Polyurethane foam is created by mixing polyols, isocyanates, and some additives into a mould. The mixture takes a few minutes to react and creates a porous network due to CO_2 gas creation. The density of the material can be adjusted by the amount of reactants injected, and the porosity can be controlled by the amount of water used. The ratio of isocyanates to polyols also determines the rigidity of the foam.

The reactants enter the mould through one or several injection points. Often, the mould is laid horizontally with the injection points above the cavity, as shown in Figure 2.4(a). An image of the

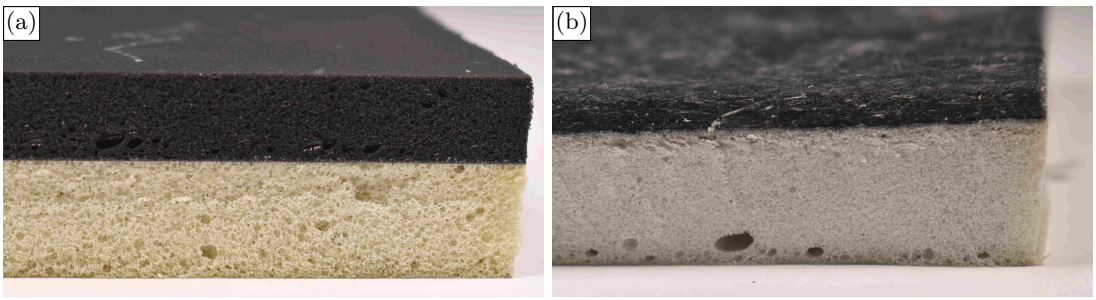

Figure 2.3. Bi-layer materials with (a) PU60 and PU250, and (b) PU60 and Polyfiber.

mould is shown in Figure 2.4(b). The moulds are filled at ambient pressure and vents let the excess gas escape. The mould is also heated and sprayed with wax, to facilitate foam demoulding without sticking. This causes the foam to have a smooth layer on its surface with closed pores. It is possible to create complex geometries with this technique, however it can be difficult to fill the corners of the mould, resulting in less dense regions in the final porous screen.

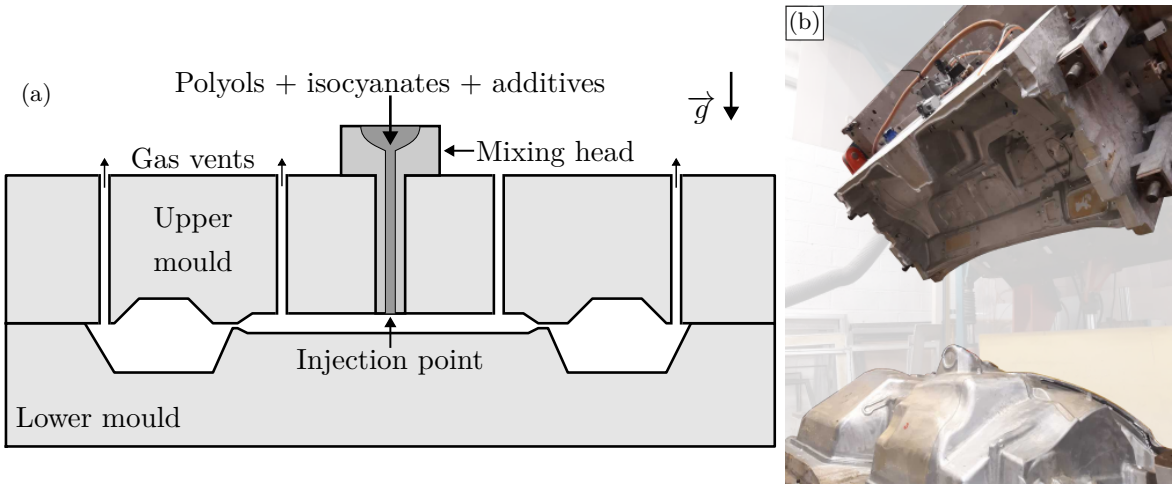

Figure 2.4. (a) Diagram and (b) image of a mould for creating a polyurethane foam screens.

Images of the microstructure of the PU60 and PU250 foams are shown in Figure 2.5. Their cells have visibly different geometries due to their different densities. The PU60 is less dense and more porous than the PU250, and their networks are connected by mostly open pores, meaning that there are no membranes closing off the openings connecting the pores. Foams with no such membranes are called reticulated foams. Further, their pores resemble Kelvin cells, also called tetrakaidecahedra [131].

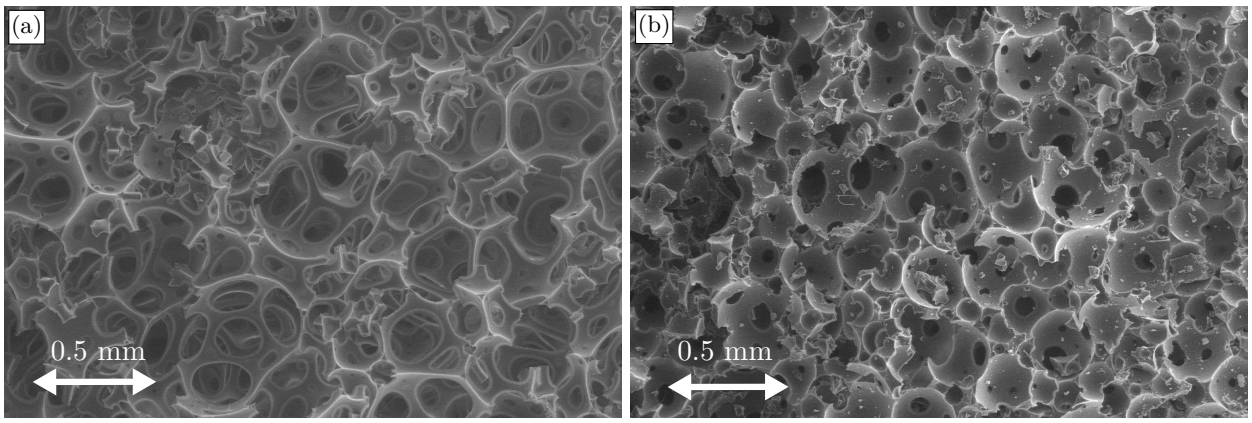

Figure 2.5. Microscopic view of a cross-section of (a) PU60 and (b) PU250 foams under SEM.

Polyfiber

Next, the Polyfiber, shown in Figure 2.1(d), is a stiff fibrous material made from polypropylene, glass fibre, and polyethylene terephthalate. It is highly resistive and thin (only 4.6 mm thick), meaning it can be used as a resistive film on a multilayer to create a mass-spring behaviour. It is sometimes used in conjunction with PU60, which is foamed directly on the Polyfiber, to create a bi-layer sheet used as an acoustic screen, shown in Figure 2.3.

Greenflocks

Finally, the Greenflocks shown in Figure 2.1(e) is a soft material used in car interior trims, and it is made from recycled polyurethane mattress flocks mixed with a binder. The recycled polyurethane mattresses are disinfected, shredded, and then mixed with CoPET bi-component fibres, as shown in Figure 2.6(a). The result is then airlay carded, thermofixed, calendared, die cut into slabs and then thermoformed to give them their final shape [132, 133]. Greenflocks sheets compressed to nominal thicknesses of 20 mm and 25 mm were studied. The Greenflocks material is highly porous, lightweight and soft. It is very heterogeneous due to its manufacturing process, as flocks from different origins are mixed together. The size of these flocks varies, but they are in the order of magnitude of the centimetre. Consequently, relative to the usual size of studied samples, this inhomogeneity is not always negligible. Moreover, the flocks can cause empty areas within the material where the airflow is unrestricted, and also result in a rough and uneven surface, visible in Figure 2.6(b).

2.2 | Sample preparation

Material samples adapted to the characterization setups must be created from the manufactured materials sheets. As the first step in the characterization process, sample preparation has a trickle-down effect on results, so it must be performed precautiously. The large material sheets obtained after manufacturing have dimensions indicated in Table 2.1. The characterization setups often require cylindrical samples of diameters 29 mm, 44.5 mm, or 100 mm. It is also possible to use cubic geometries for certain applications, though this is less common and is not used in this work.

The measurement of the thickness h of the materials is done with a caliper on several samples and on different locations on each sample. Measured samples are compressed between the caliper jaws, and the caliper jaws are opened until the sample falls under the effect of gravity, which yields the sample's thickness. Results vary due to measurement error and material inhomogeneity. The 95 % confidence interval on the measured thickness indicated in Table 2.1 is quite large for the Polyfiber,

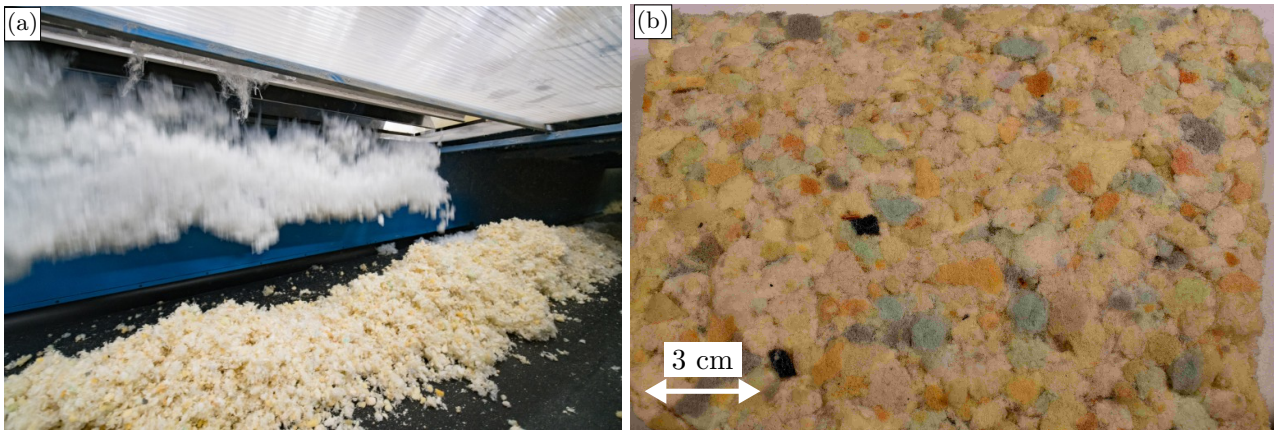

Figure 2.6. (a) Greenflocks manufacturing process, where the CoPET bi-component fibres (white) are mixed with the recycled PU mattress flocks (yellow). Photo courtesy of Trèves Group. (b) Greenflocks sheet with an uneven surface due to flocks inhomogeneity.

due to its low thickness, and for the Greenflocks material, due to its inhomogeneity.

Table 2.1. Thickness and approximate lateral dimensions of foam sheets. The 95 % relative confidence interval is given. For the melamine, it is computed for 29.1 mm thick samples.

Sheet dimensions	h (mm)	CI (±%)	Lateral dimensions (mm)
Melamine	18.9, 29.1, 47.7	0.4	1000 × 500
PU60	20.1	1.5	800 × 500
PU250	21.6	1.7	800 × 500
Polyfiber	4.6	8.2	1100 × 950
Greenflocks 20 mm	20.6	2.5	1000 × 800
Greenflocks 25 mm	24.9	4.6	1000 × 800

Several cutting methods exist, as presented and compared in Table 2.2. It is challenging to create samples with the perfect desired geometry, since for every cutting method, the efforts applied by the cutting agent to the porous sheet deform it significantly. It is common to obtain misshapen, skewed or ripped samples as a result of cutting, as shown in Figure 2.7. Samples could be frozen to ease the cutting process, however due to the low glass transition temperature of the polyurethane foams studied, they are not much easier to cut or shatter when frozen. The sample cut with the water jet method in Figure 2.7(b) has a visibly concave generatrix. The sample cut with a hole saw in Figure 2.7(a) seems more uniform, even though there are still cutting imperfections near the top and bottom for instance. Consequently, the hole saw method is used in this work.

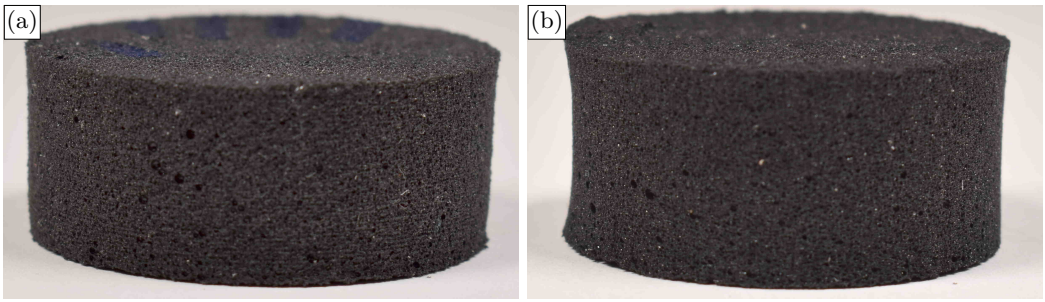

Figure 2.7. Comparison between cylindrical PU250 samples cut with (b) a hole saw and (a) a waterjet.

Table 2.2. Comparison of sample cutting methods.

Punch cutting	Method	A circular punch cutter is placed on the material sheet, and a normal force is applied to cut the samples.
	Pros	Easy and quick to perform. Does not require much equipment.
	Cons	Does not work well on dense materials. Applies a compressive force which deforms the material. Can lack precision in the cut.
Hole saw	Method	A hole saw mounted on a column drill is lowered into the material. A dry lubricant can help reduce friction.
	Pros	The rotation facilitates cutting and reduces compressive forces on the material. The process is quick.
	Cons	The saw's rotation generates torque that can deform the samples. Samples obtained are not perfectly cylindrical, with a variable diameter throughout their height and an oblique axis. Requires expensive, well-maintained, and sharpened hole saws. A powerful column drill is required for dense materials.
Waterjet	Method	A high-pressure water jet cuts cylinders in the sheet.
	Pros	Precise cutting shape.
	Cons	Requires expensive, heavy and voluminous equipment. The material is deformed under the water jet's load. The water jet loses precision for increased thickness, causing shape defects.

Furthermore, the PU60 and PU250 materials have a skin characterized by closed pores on their surface, which results from the wax used in the manufacturing process for demoulding. This skin is very thin and located on both sides of the samples. It has a higher air resistivity and lower porosity than the core of the materials, and therefore acts like a resistive screen. Indeed, airflow resistivity measurements have revealed that these resistive skins represent up to 91 % of the total resistivity of the entire sample. Consequently, in order to characterize the homogeneous and uniform cores of the materials, the samples studied in this work are without skin. It can be noted that these skins are present in the real final products, and can be modelled as simple thin resistive layers when necessary.

The resistive skins can be removed by manual abrasion using sandpaper. This works for the less-dense PU60, but it is too time-consuming and damaging for the PU250. Alternatively, the resistive skin can be removed by milling for the PU250. This results in flat and parallel opposite faces with a uniformly removed resistive skin. Images of PU60 and PU250 samples with and without resistive skin are shown in Figure 2.8 and Figure 2.9. Close-up SEM images of the cross-sections of these materials in Figure 2.8(c) and Figure 2.9(c) reveal the contrast between the core of the material and the surface skin. Subsequently, the PU60 is manually abraded and the PU250 is machined before characterization.

Moreover, it can be noted that the PU250 contains abnormally large pores close to the side facing up in the mould. These macropores are shown for different milling depths in Figure 2.10(a), and are shown in the SEM image in Figure 2.10(b). They decrease in size and number deeper into the material. The macropores are not considered in the characterization and modelling of these materials, and the PU250 foam is machined to a depth of 2 mm before characterization to limit influence of these macropores.

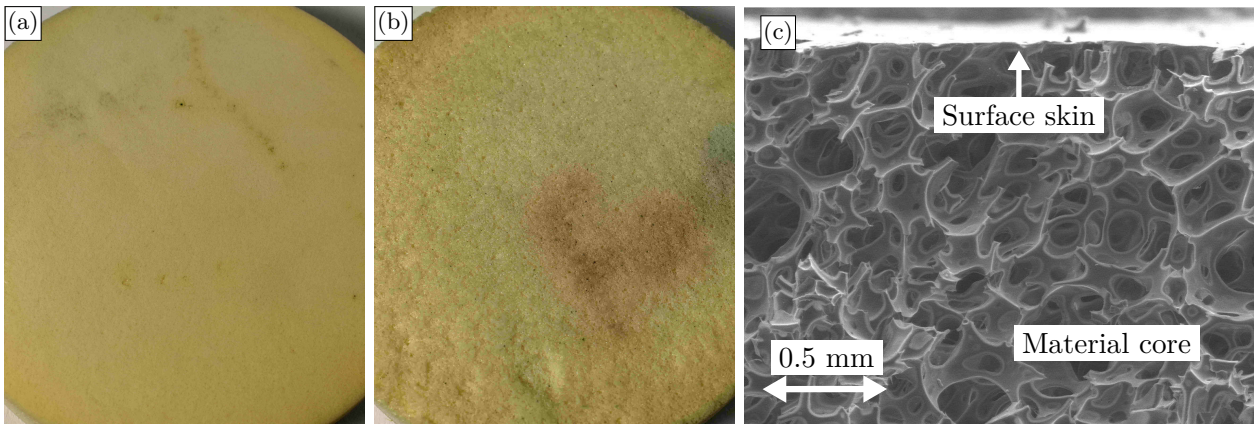

Figure 2.8. PU60 foam (a) with and (b) without resistive skin, removed by manual abrasion. (c) SEM image of a PU60 slice near its surface, with its skin still intact.

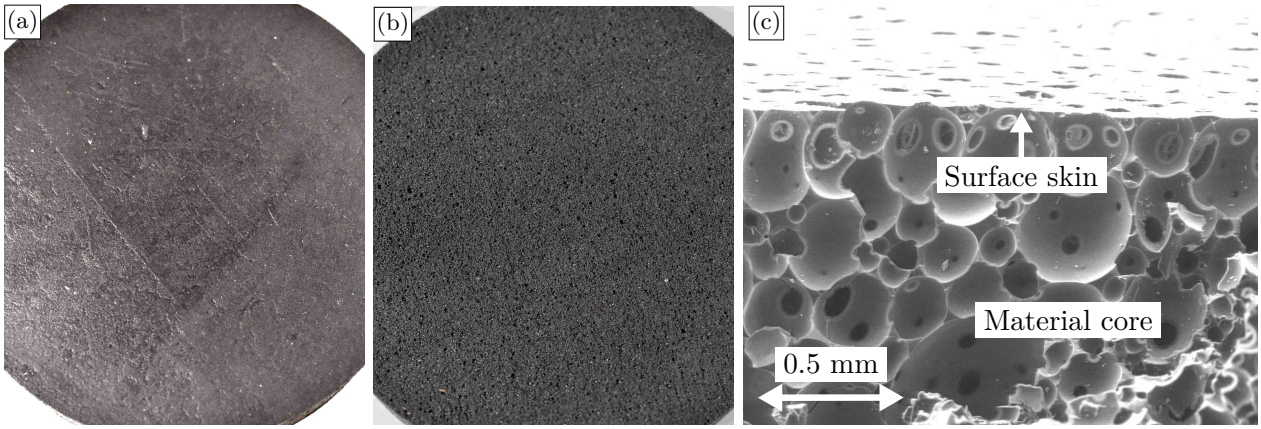

Figure 2.9. PU250 foam (a) with and (b) without resistive skin, removed by milling. (c) SEM image of a PU250 slice near its surface, with its skin still intact.

3 | Direct measurement of transport parameters

Methods to directly measure the transport parameters are discussed in this section. Transport parameters are related to the fluid saturating the pores of the porous material. The six transport parameters used by the JCAL model, described in Section 4.3.4, are the porosity ϕ (-), the tortuosity α_∞ (-), the resistivity σ (Nsm^{-4}), the viscous and thermal characteristic lengths Λ' (m) and Λ (m), and the thermal permeability q_0' (m^2). Throughout this chapter, the 95 % confidence interval (CI) is given alongside results where possible. This confidence interval is computed ideally from the results of four to six different samples, depending on measurement requirements and conditions.

3.1 | Porosity

3.1.1 | Measurement methods

The open porosity ϕ can be measured in many ways. As the closed porosity is not considered for acoustic modelling, only the open porosity is discussed. Traditionally, an air pycnometer could be used [134] to measure the porosity of any material. Mercury porosimetry is another common method, which involves saturating the porous sample with mercury, increasing the pressure and measuring the volume variation as the mercury is forced into the gaps of the pores [135, 136, 137]. Some more recent methods for porous acoustic materials were developed, such as Panneton and Gros' [138] method based on the measurement of the material's mass in air and in a vacuum, using Archimede's principle to

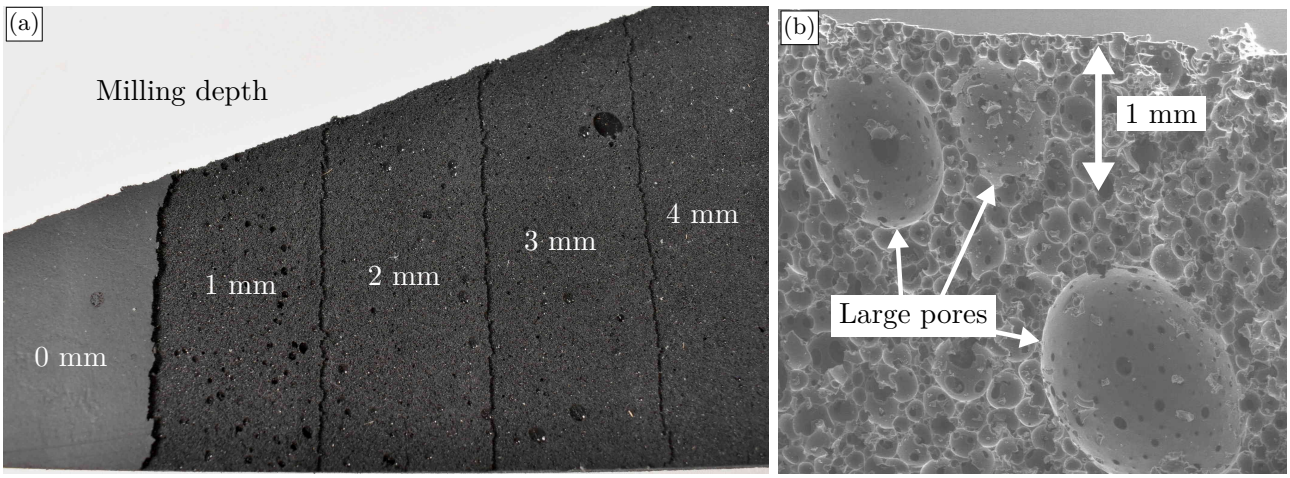

Figure 2.10. (a) PU250 sample milled at different depths on the side facing up during the moulding, revealing macropores near the surface. (b) Cross-sectional view of a PU250 sample under SEM. Macro-pores are visible on the left.

relate the difference in mass to the porosity. The porosity can also be computed from the measurement of the reflected and transmitted waves through a porous sample, as described by Groby et al. [139], at the same time as the tortuosity α_∞ and characteristic lengths Λ and Λ'. A method for measuring it from the low frequency ultrasound waves reflection coefficient of a sample (40 kHz) was proposed by Parmentier et al. [140], however this method requires *a priori* knowledge of α_∞ and Λ, which can be impractical. Jaouen and Bécot [141] suggest a method adapted to perforated screens based on standing wave tube measurements.

Two other commonly used methods to measure the porosity are presented in detail here. The first is a volume variation method which originated in the 1940s [32, 44, 142]. This method was then modified in 1991 by Champoux et al. [143] to avoid using liquids to measure a volume variation, and a variant by Leclaire et al. [144] relies on comparing the pressure with that of an empty reference chamber. This method involves placing the porous material in a tank which undergoes a volume variation, shown in Figure 2.11. The resulting pressure variation is measured, and using Boyle-Mariotte's law which states that the pressure P times the volume V of an ideal gas at iso-temperature is constant, the volumes and pressures before and after the variation are related by

$$P_0(V_f + V_{ext}) = (P_0 + \Delta P)(V_f + V_{ext} + \Delta V), \tag{2.1}$$

where V_{ext} is the fluid volume in the tank and outside the porous material, and V_f is the volume of the fluid phase. ΔP is the pressure change caused by the volume change ΔV. The porosity is then derived from the measurement through

$$\phi = \frac{V_f}{V_{sample}}, \quad V_f = \frac{P_0 V_{ext} - (P_0 + \Delta P)\,(V_{ext} + \Delta V)}{\Delta P}, \tag{2.2}$$

where $V_{sample} = V_s + V_f$ is the total volume taken by the sample, with V_s the volume of the solid phase.

The Boyle-Mariotte law is only valid at constant temperature, making the method highly temperature sensitive. Champoux et al. [143] suggests placing a massive brass cylinder around the sample holder as a heat sink, and wrapping the tank in an insulating material to limit the sensitivity to external temperature variations. Each sample measurement can take about twenty minutes to allow the temperature to stabilize after the pressure variation. This method works best for materials with low porosity.

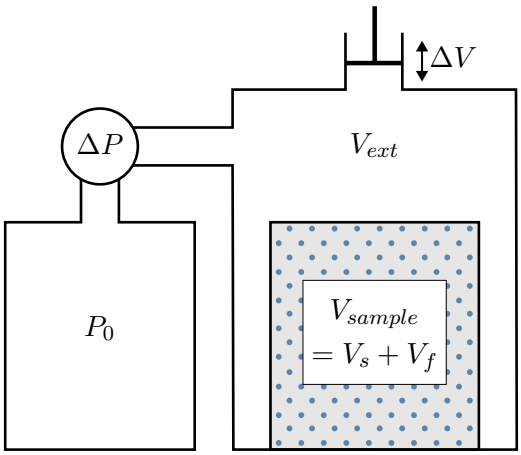

Figure 2.11. Porosity measurement bench of the volume variation method proposed by Beranek [44].

The second method presented in detail for measuring the porosity is the pressure-mass method by Salissou and Panneton [145], which will be applied to the materials studied in this project. In this method, the pressure within a tank and its mass are measured with and without the sample inside, in vacuum and under pressure of a heavy gas (such as argon). The four configurations are shown in Figure 2.12(b). The pressures P_i and masses M_i in these configurations, combined with the ideal gas law $PV = nRT$ are related to the material's porosity:

$$\phi = 1 - \frac{V_f}{V_{sample}} = 1 - \frac{RT_0}{V_{sample}} \left(\frac{M_2 - M_1}{P_2 - P_1} - \frac{M_4 - M_3}{P_4 - P_3} \right). \tag{2.3}$$

This method also provides access to the bulk density of the material *in vacuo* ρ_1:

$$\rho_1 = \frac{1}{V_{sample}} \left(M_3 - M_1 + \frac{1}{RT_0} \left((P_1 - P_3) V_t + P_3 V_s \right) \right), \tag{2.4}$$

$$V_s = RT_0 \left(\frac{M_2 - M_1}{P_2 - P_1} - \frac{M_4 - M_3}{P_4 - P_3} \right), \quad V_t = RT_0 \frac{M_2 - M_1}{P_2 - P_1}, \tag{2.5}$$

with V_t is the total volume of the tank.

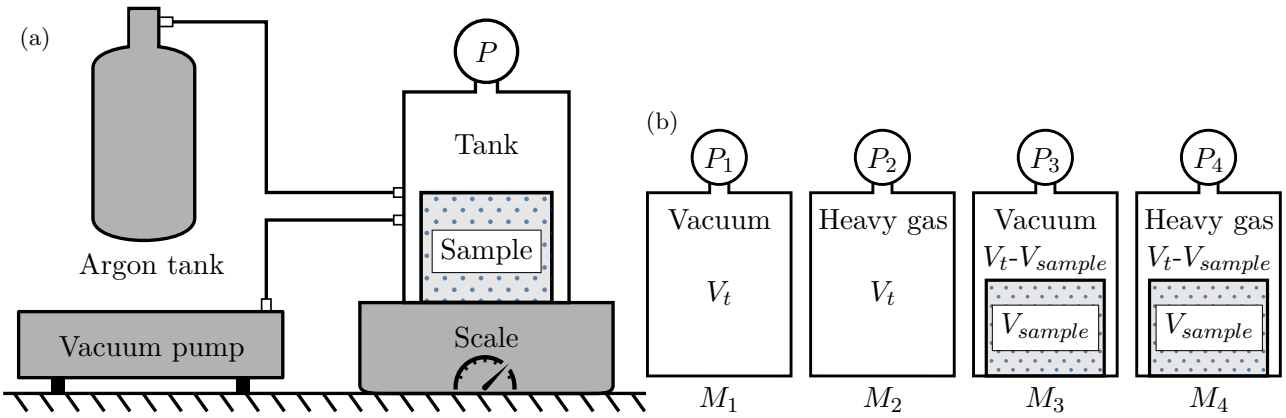

Figure 2.12. Porosity measurement with the pressure-mass method. (a) Diagram of the setup, (b) configurations of recorded mass and pressure.

The uncertainties tied to this method mainly come from the mass and pressure measurement errors. To minimize the measurement error, the tank should be filled with as big a volume of the measured porous material as possible to maximize the mass variation. The measurement uncertainty

due to the pressure and mass readings is highest for materials with low porosity and small volume [145]. Further, when recording the pressure variation in the tank, it is important to ensure that the temperature remains constant. Consequently, each measurement takes upwards of 5 minutes.

3.1.2 | Application and results

The pressure-mass method [145] is used to perform porosity measurements, using an Open Porosity/Density Meter Model PHI by Mecanum shown in Figure 2.13. This method is reliable and can be performed without any particular difficulty on the studied materials. The porosity of the melamine is measured at $\phi = 0.94$, which is slightly lower than what can be found in the literature, which is closer to $\phi = 0.99$ [146, 147, 148, 149]. To minimize the uncertainty, the tank must be filled as much as possible for the highly porous materials which is difficult to obtain a large volume for thin materials such as the Polyfiber, which has a height of $h = 4.6$ mm while the tank is 125 mm tall, which means many samples are required. Further, the macroporosity near the surface of the PU250 foam, shown in Figure 2.9, contributes to its overall porosity because the materials are considered homogeneous. The final results for the porosity ϕ and the density ρ_1 are presented in Table 2.3, and the narrow 95 % confidence interval found for the results attests to the reliability of this measurement procedure.

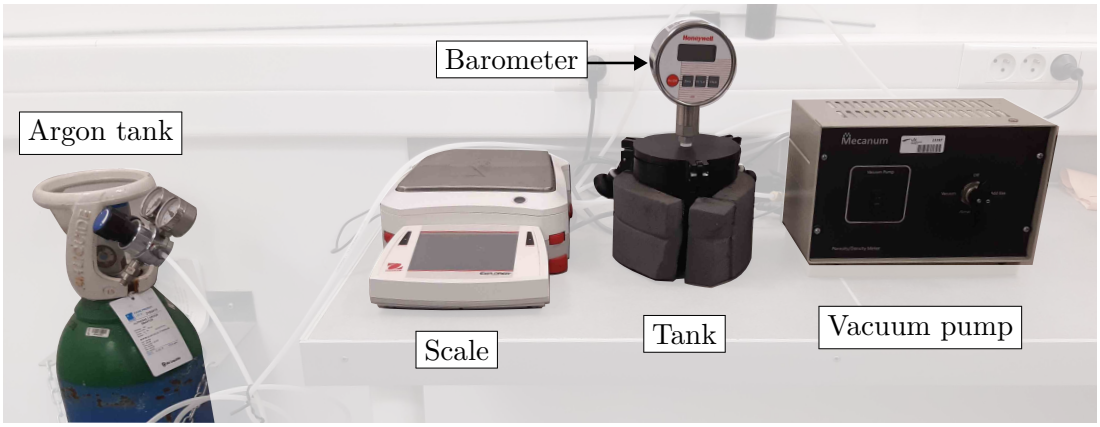

Figure 2.13. Open Porosity/Density Meter Model PHI 2011 by Mecanum.

Table 2.3. Measured porosity ϕ and *in vacuo* density ρ_1 for the studied foams. The relative 95 % Confidence Interval (CI) is given.

Porosity	ϕ (-)	CI (±%)	ρ_1 (kg m^{-3})	CI (±%)
Melamine	0.94	1.45	9.58	0.82
PU60	0.94	0.84	54.8	0.18
PU250	0.79	1.00	242.5	0.008
Polyfiber	0.99	0.59	275.5	-
Greenflocks 20 mm	0.94	1.90	65.6	3.70
Greenflocks 25 mm	0.95	0.22	55.3	7.31

3.2 | Tortuosity

3.2.1 | Measurement methods

The tortuosity α_∞ can be measured directly with several methods. A first method consists in saturating the porous material with a conductive fluid, and computing the tortuosity from [150, 151]

$$\alpha_\infty = \phi \frac{r_s}{r_f}, \tag{2.6}$$

where r_s is the resistivity of the material skeleton and r_f is the resistivity of the saturating fluid. The porosity ϕ is required for this method. Another method described by Groby et al. [139] consists in computing the tortuosity from the simultaneous measurement of the reflected and transmitted wave through a porous sample. Alternatively, ultrasonic wave measurement methods exist, using either a transmission or a reflection setup, which are described in detail in the following.

The transmission method [152, 153, 154] consists in placing an ultrasonic transmitter and receiver face to face. The measurement bench is shown in Figure 2.15(b). The transmitter emits a pulse that is measured by the receiver. Then, a porous sample is placed between the transmitter and the receiver, and the pulse is emitted again. The time lag Δt in the reception of the pulse induced by the presence of the material is recorded, as schematized in Figure 2.14. The time lag Δt is frequency dependant, and its high frequency asymptote is related to the tortuosity and the refractive index n_r, which is written

$$n_r(f) = 1 + c_0 \frac{\Delta t(f)}{h}. \tag{2.7}$$

The high frequency asymptote of n_r^2 can be written

$$n_r^2(f) = \alpha_\infty + \frac{M_n}{\sqrt{f}} \xrightarrow[f\to\infty]{} \alpha_\infty. \tag{2.8}$$

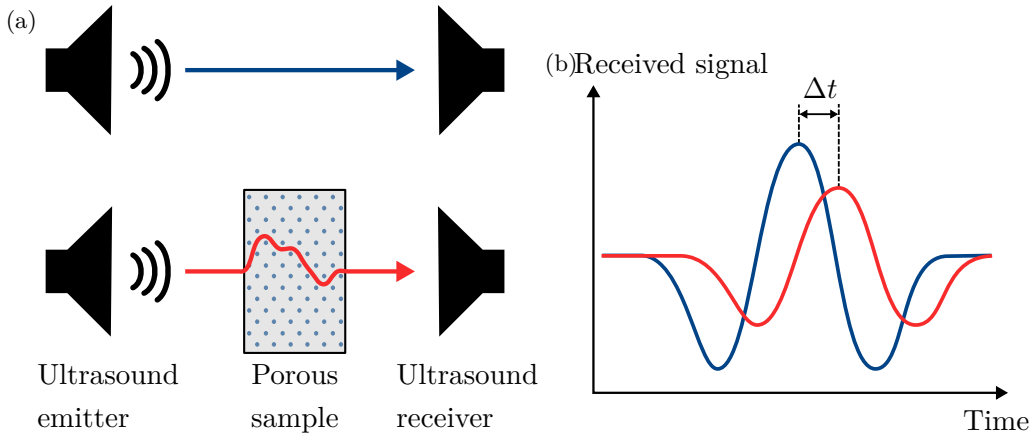

Figure 2.14. Tortuosity measurement principle by transmission. (a) Configuration of the ultrasound emitter and receiver, (b) received signal with and without sample.

In other words, Equation 2.8 describes a line with y-intercept α_∞ and slope M_n, as a function of $f^{-1/2}$. α_∞ is therefore found from a linear regression of n_r^2 when $f \to \infty$, as shown in Figure 2.15(a). Additionally, M_n can be related to the viscous and thermal characteristic lengths Λ and Λ', which is explained in Section 3.4. For this transmission method to work well, the waves must pass through and exit the sample for the ultrasound receiver to pick up the emitted wave. It is therefore recommended having a sample at most half as thick as the penetration depth of the acoustic wave D_p, which is the distance from which the acoustic wave is nearly completely dissipated [155]. D_p can be computed as

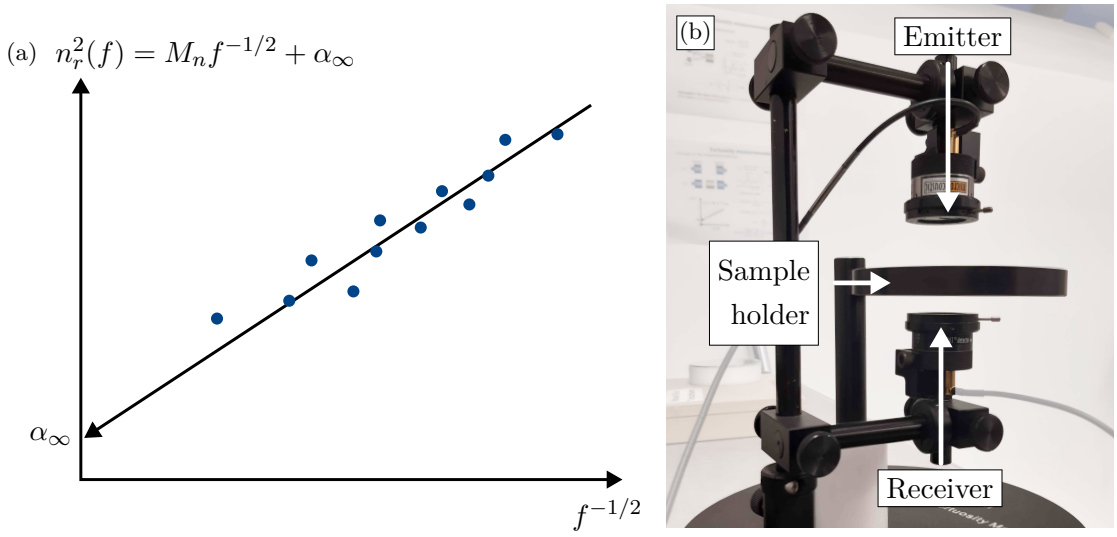

Figure 2.15. Tortuosity measurement with reflection setup. (a) How the linear regression on the refractive index n_r^2 leads to tortuosity, (b) measurement bench with the emitter and the receiver.

the distance where the acoustic wave's amplitude is divided by a factor 20 (*i.e.* −26 dB). Using only the airflow resistivity σ, the simple equivalent fluid Delany-Bazley-Miki model [98] can be used :

$$D_p(f) = \frac{\ln(20)}{0.160} \frac{c_0}{2\pi f} \left(\frac{f}{\sigma}\right)^{0.618}. \tag{2.9}$$

When materials are too thick and dissipative to use the transmission method, the alternative reflection method [156] can be used. It consists in sending an oblique ultrasonic wave onto the material's surface and measuring its reflection coefficient, obtained relative to a perfectly reflective surface. The reflection coefficient $r(\omega, \theta)$ is calculated for different incident angles θ, and the tortuosity α_∞ is computed from

$$\alpha_\infty = \frac{z^2}{2}\left(1 + \sqrt{\left(1 - \left(\frac{2}{z}\sin(\theta)\right)^2\right)}\right), \tag{2.10}$$

where $z = \frac{1+r(\omega,\theta)}{1-r(\omega,\theta)} \frac{\phi}{\cos\theta}$, and the porosity ϕ must be known beforehand. This principle is shown in Figure 2.16, and the measurement setup is shown in Figure 2.17.

The reflection coefficient can be computed for different incident angles θ and frequencies f. Ideally, all angles θ return the same tortuosity value, but this is not the case in practice. It has been observed during measurements that unusually high tortuosity values are obtained for angles greater than approximately 60°. For most materials, it is appropriate to use angles between 20° and 45° at frequencies between 80 kHz and 120 kHz [157]. This method requires materials to behave with a motionless skeleton, which is often true in this frequency range. However, some materials may require higher frequencies for satisfactory results. Further, it is recommended to take measurements for at least four different angles to obtain statistical data on the results. For both the transmission and reflection tortuosity measurement methods, the error on the sample thickness propagates proportionally to the computed tortuosity value. Overall, the transmission method is more reliable than the reflection method when it is applicable.

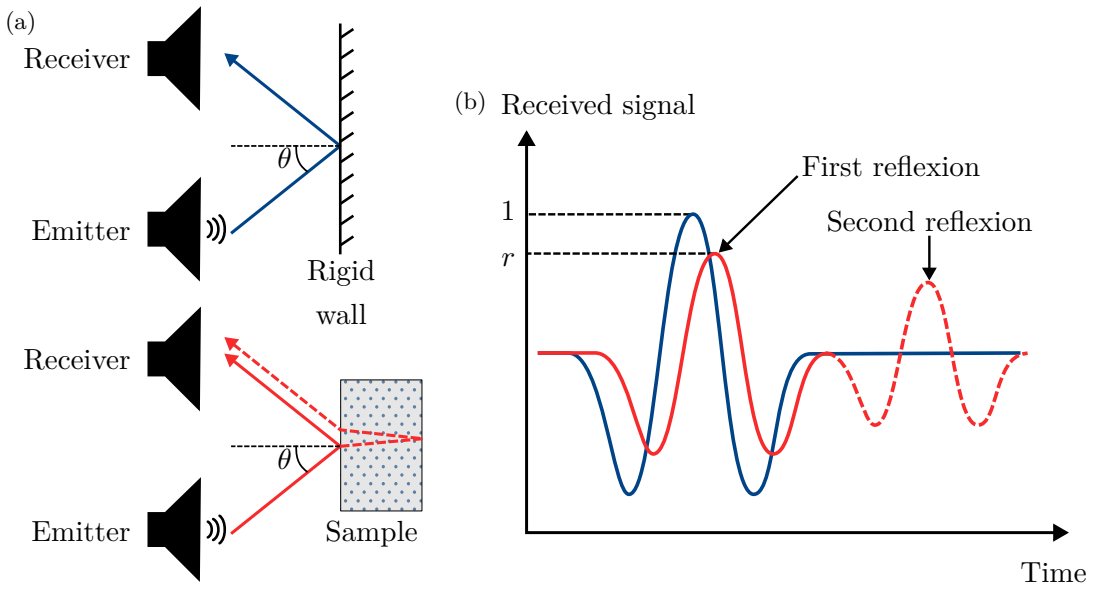

Figure 2.16. Tortuosity measurement by reflection. (a) Measurement configurations with the ultrasound emitter and receiver, (b) received signals.

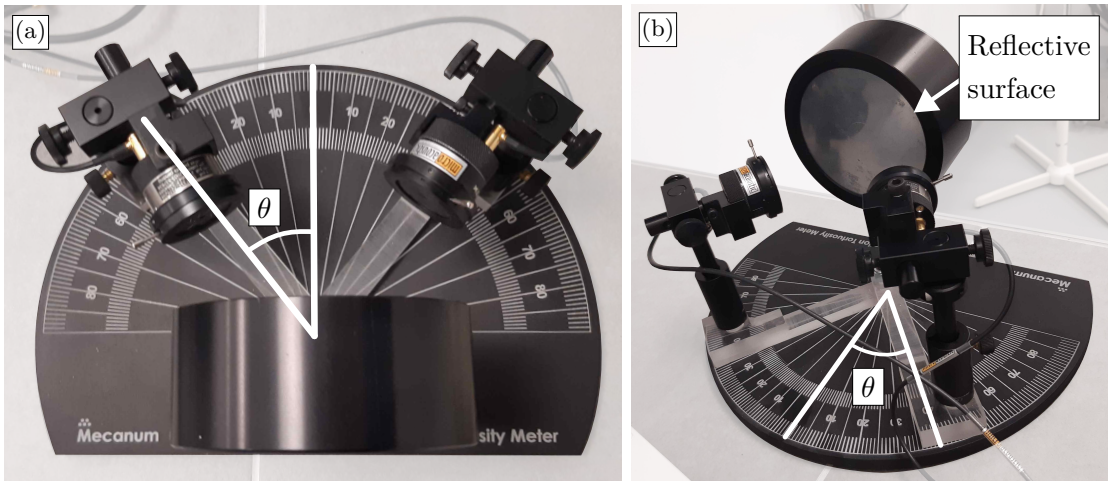

Figure 2.17. Tortuosity measurement experimental setup with the reflection method. (a) Top view, (b) side view.

3.2.2 | Application and results

Both transmission and reflection methods are applied with Mecanum's TOR Transmission and TOR Reflection tortuosity meters. Ultrasonic waves can be sent between 60 kHz and 180 kHz. Material ultrasonic wave penetration depths D_p at 180 kHz are presented in Table 2.4. Ideally D_p must exceed double the thickness of the material to apply the transmission method, which means that the PU250, and the PU60 and Polyfiber to a lesser extent, are not suitable for the transmission method. For these materials, it is preferable to perform the reflection measurement.

The measurement results for the tortuosity are presented in Table 2.5. The tortuosity of the melamine foam is very close 1, which is coherent with values found in the literature [146, 147, 148, 149]. The confidence interval indicates how reliable each method is for each material. For example, the transmission method is not well adapted to the PU250 (tortuosity confidence interval of ±48.14) but works better through reflection (tortuosity confidence interval of ±1.02). This is because the PU250 material is too opaque for the ultrasound waves to pass through it, as found in Table 2.4. The

Table 2.4. Acoustic wave penetration depth D_p of ultrasonic waves in materials and their thickness. Values in italics indicate penetration depths that are too small compared to the thickness of each material. The applicability of the transmission method is indicated in the final column.

Penetration depth	D_p at 180 kHz (mm)	Thickness (mm)	Transmission usable?
Melamine	28.5	19.0	✓
PU60	*20.6*	20.1	Uncertain ∼
PU250	*1.2*	20.2	×
Polyfiber	*4.9*	4.6	Uncertain ∼
Greenflocks 20 mm	24.6	20.6	✓
Greenflocks 25 mm	31.5	24.9	✓

tortuosity of the PU60 foam is 1.25, which can be considered quite high for an open cell foam. This indicates that the size of the cell openings are smaller, relative to the cell size, and the cell struts are thicker than for a melamine foam for example. The Polyfiber has a low standard deviation for both transmission and reflection, but the result obtained from the transmission method seems too high for this fibrous material (3.11 ± 0.53). Therefore, the reflection method (1.49 ± 0.12) is preferred for the Polyfiber. The Greenflocks was not characterized with the tortuosity meter, but its tortuosity was estimated at 1.03 for the GF 20 mm and at 1.01 for the GF 25 mm by the manufacturer Trèves Group using an inverse method.

Table 2.5. Geometric tortuosity α_∞ (-) obtained through transmission and reflection methods. The values in italics are subject to caution, due to large confidence intervals or insufficient penetration depth D_p of the ultrasound waves.

Tortuosity α_∞ (-)	Transmission	CI (±)	Reflection	CI (±)	Inverse method
Melamine	1.01	0.02	-	-	-
PU60	*1.58*	3.18	1.25	0.20	-
PU250	*14.20*	48.14	2.45	1.02	-
Polyfiber	*3.11*	0.53	1.49	0.12	-
Greenflocks 20 mm	-	-	-	-	1.03
Greenflocks 25 mm	-	-	-	-	1.01

3.3 | Airflow resistivity

3.3.1 | Measurement methods

The airflow resistivity σ is measured as the pressure difference across a sample of thickness h when an air flow is applied:

$$\sigma = \frac{\Delta P S}{Q h}, \tag{1.64}$$

where S is the sample cross-section area, Q is the volumetric flow rate crossing the sample, and ΔP is the pressure difference upstream and downstream from the sample. Measurement methods applied to porous acoustic materials are described by ISO standard 9053 [158, 159] and ASTM standard C 522 [160]. Methods using either static laminar airflow or alternating airflow exist. A static laminar airflow is used here, with a measurement principle illustrated in Figure 2.18. By using a calibrated resistance

R_c that causes a pressure drop ΔP_c

$$Q = \frac{\Delta P_c}{R_c}, \tag{2.11}$$

the resistivity of the sample is computed as [161, 162]

$$\sigma = R_c \frac{\Delta P S}{\Delta P_c h}. \tag{2.12}$$

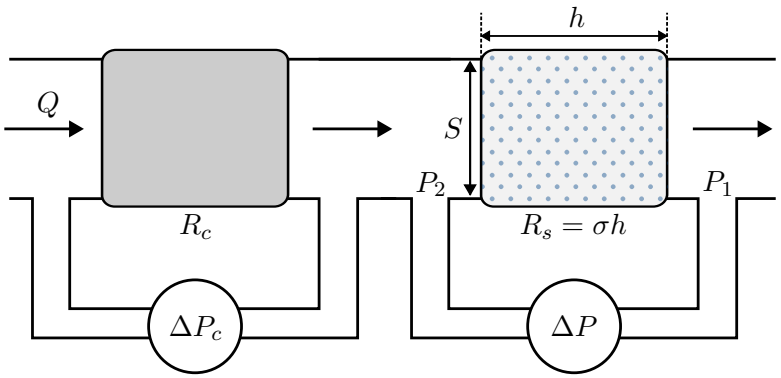

Figure 2.18. Principle of resistivity measurement with a calibrated resistance R_c.

Any error on the sample thickness propagates proportionally to the resistivity result. Further, samples are considered homogeneous and isotropic for this measurement, so an equivalent resistivity is computed for inhomogeneous materials, but this anisotropy can be evaluated by measuring the airflow resistivity in different directions. Since the air viscosity increases with temperature [163], the airflow resistivity also increases with temperature [164]. Schiavi et al. [165] show that this effect is very small in practice at ambient temperatures (approximately 0-30°C), though at much higher temperatures (approximately 800°C) its effect is more important [166].

3.3.2 | Application and results

Resistivity measurements are performed with a Mecanum Static Airflow Resistivity Meter Model SIG2011 resistivity meter, shown in Figure 2.19. The samples are mounted inside a cylindrical sample holder. The measurement error is high for samples with low resistivity, due to the relative reading error on the pressure ΔP. Furthermore, samples that are too resistive can saturate the pressure sensors. Nonetheless, airflow resistances of up to at least 500 000 $\mathrm{Nsm^{-3}}$ can be measured. Samples of varying diameter and thickness can be chosen to improve measurement accuracy accordingly.

This setup is sensitive to sample mounting conditions in the sample holder, because air leaks around the sample can drastically reduce the measured resistivity, especially for resistive materials. In addition, highly inhomogeneous materials like the Greenflocks may contain intrinsic airflow pathway leaks that are challenging to control. An example of an air leak around a sample is shown in Figure 2.20(a). To reduce the effect of air leaks around the sample, the sample contour can be sealed with vacuum grease, however this permanently penetrates inside the samples and makes them unusable for subsequent measurements. Alternatively, the sample edge can be surrounded with a thin resistive strip. A fabric strip is placed around the samples in this work to prevent leaks, shown in Figure 2.20(b).

The measurement results with this method are presented in Table 2.6. The resistivity of the melamine foam is found at 13 838 $\mathrm{Nsm^{-4}}$, which is close to values which can be found in the literature which are between 9 000 $\mathrm{Nsm^{-4}}$ and 15 000 $\mathrm{Nsm^{-4}}$ [146, 147, 148, 149]. The resistivity measured with this method can vary significantly from one sample to another depending on their mounting. The

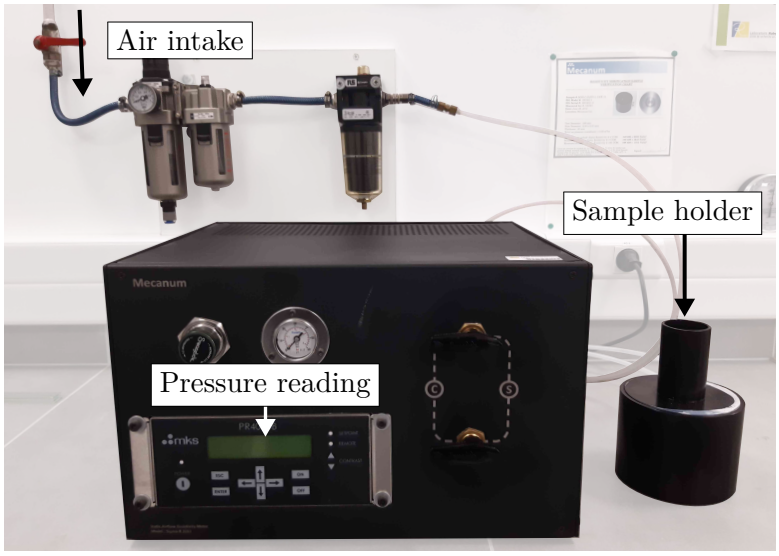

Figure 2.19. Resistivity measurement bench.

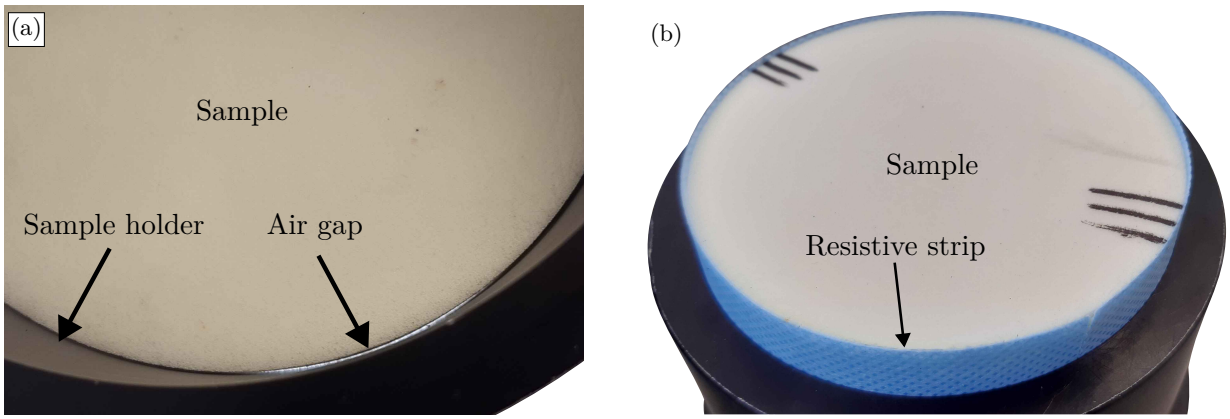

Figure 2.20. (a) PU60 foam sample mounted in the sample holder with a leak along its contour, (b) strip used to surround the sample to prevent the leak.

largest confidence interval is ±37.6 % for the PU250. This foam is highly resistive, so any air leak is likely to greatly modify the measured resistivity. In contrast, the Greenflocks 25 mm has a very low resistivity and is very inhomogeneous, which causes a large relative confidence interval of ±22.5 %. The confidence interval for other materials is less than 17.8 %, indicating fairly reliable and exploitable measurements.

3.4 | Characteristic lengths Λ and Λ'

The viscous and thermal characteristic lengths Λ and Λ' are difficult to measure directly. Consequently, no direct measurements of these parameters are performed on the six studied materials. Groby et al. [139] suggest a method to compute them from the reflected and transmitted waves sent onto a porous sample. Alternatively, the thermal characteristic length Λ' can be obtained by BET adsorption measurements, as described by Lemarinier et al. [167]. It is written

$$\Lambda' = \frac{2\phi}{S_{contact}}, \tag{2.13}$$

where $S_{contact}$ is the contact area between the fluid and the frame per fluid unit volume. The characteristic lengths are also related to the equivalent length L_{eq} of the path taken by a wave to cross the

Table 2.6. Measured airflow resistivity values for different materials. The absolute and relative 95 % confidence intervals are indicated.

Resistivity	σ (Nsm^{-4})	CI (±%)	CI (±Nsm^{-4})
Melamine	13 838	3.9	539
PU60	[redacted]	17.8	[redacted]
PU250	[redacted]	37.6	[redacted]
Polyfiber	228 728	11.6	26 344
Greenflocks 20 mm	[redacted]	15.3	[redacted]
Greenflocks 25 mm	[redacted]	22.5	[redacted]

material, so they can be retrieved from the ultrasonic transmission measurements described for the tortuosity in Section 3.2.1. The slope M_n of the squared refraction index n_r^2 as a function of $f^{-1/2}$ is related to Λ and Λ' through [39, 152, 153, 154]

$$L_{eq} = \frac{h}{c_0 M_n}\sqrt{\frac{\alpha_\infty \nu_0}{2}} = \left(\frac{1}{\Lambda} + \frac{\gamma_0 - 1}{\Lambda'\sqrt{\mathrm{Pr}}}\right)^{-1}. \tag{2.14}$$

Combined with the BET measurement for Λ', both characteristic lengths can be retrieved, as performed by Brown et al. [168]. Otherwise, by performing this measurement in two different fluids (for example, in air and helium), it is possible to obtain Λ and Λ' from the slopes M_n of the measurements, as proposed by Leclaire et al. [153, 154]. This experimental setup requires immersing the tortuosity-meter measurement bench in a gas different from air, which can be more difficult to implement in practice.

4 | Inverse methods for transport parameters

Some material parameters are difficult or impossible to measure directly, such as the thermal characteristic length Λ' and the thermal permeability q_0'. In this case, inverse methods can be used to infer their values through the material's behaviour. Iterative global optimization algorithms, presented in Section 4.1, rely on a least squares method for parameter calibration, and make assumptions about a model accuracy at representing an experimentally observed behaviour. Micro-macro approaches, presented in Section 4.2, make use of the micro-geometry of materials to compute macroscopic properties, and make assumptions about the geometric structure of the materials. Finally, the so-called indirect method, presented in Section 4.3, relies on analytically flipping measurement results to deduce material properties. This method makes strong assumptions about the material's motionless skeleton behaviour over a given frequency range. These three inverse methods are presented and applied to the six studied materials, with a focus on the transport parameters.

4.1 | Iterative inverse methods

The principle of iterative global optimization inverse methods and some commonly used algorithms are presented in this section.

4.1.1 | General methodology

Iterative global inverse characterization methods rely on fitting a set of sought parameters through an iterative optimization algorithm. The material properties are guessed by matching the modelled behaviour of a porous material to its measured behaviour. These methods can theoretically be applied to any measurement of a material's behaviour, as long as its parameters contribute significantly to the investigated response. The quality of a set of parameters β used as input parameters in the model is evaluated by a cost function J, which has to be minimized. This cost function can be the RMS difference between the computed and measured curves for instance. At each iteration of the algorithm, the parameter set β is adjusted to minimize J. Between iteration steps i and $i+1$, the set of parameters β_i is altered based on a set of rules determined by the algorithm used. The principle of this iterative process is presented in Figure 2.21.

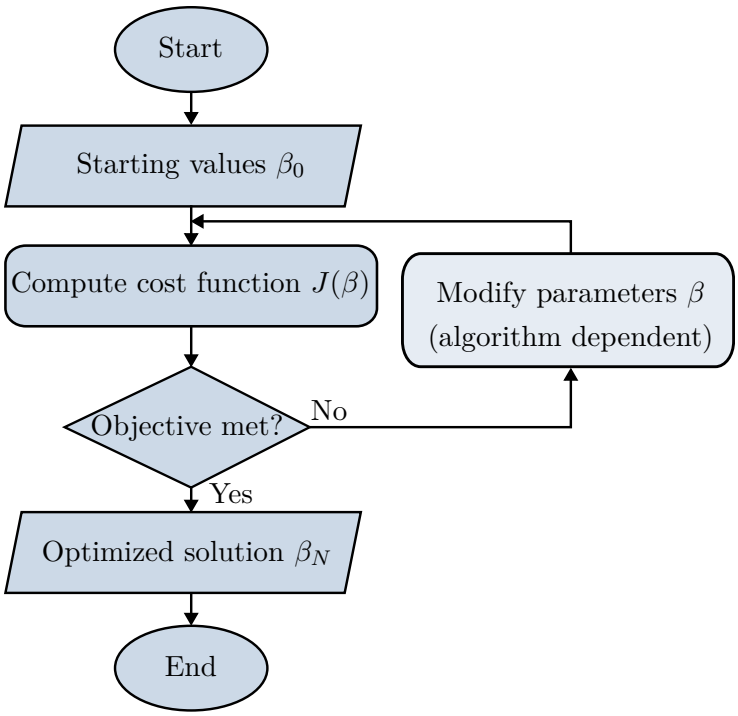

Figure 2.21. Principle of an optimization problem to be solved for inverse methods.

Iterative global inverse methods have been applied in many ways to porous materials, as shown in the review by Bonfiglio and Pompoli [169]. Some applications are tailored towards mechanical parameters [149, 170, 171] or damping properties [85, 172]. Terroir et al. [173] suggest a method for fully anisotropic equivalent fluid materials. The application of inverse methods to impedance tube measurements was suggested by Atalla et al. [174, 175] for coupling parameters, and by Sellen [176] for mechanical parameters.

4.1.2 | Common minimization algorithms

Several algorithms exist to solve minimization problems. Some common algorithms are presented here with their pros and cons. First, gradient search algorithms are a deterministic method which relies on computing the gradient of the cost function J with respect to the parameters β to find the direction in which β should evolve to reduce it. Gradient-based algorithms are fast but require a smooth gradient, which is not always guaranteed. Moreover, gradient methods have the drawback of often converging to a local minimum without efficiently searching for the global minimum in the parameter space. A local minimum is achieved by a set of parameters β that locally minimizes the cost function J, in opposition to the global minimum, which minimizes J over the entire parameter space.

Next, nonlinear best fit algorithms, such as the Nelder-Mead simplex algorithm [177] or the interior-point algorithm [178], are deterministic algorithms. These algorithms follow a set of rules, to modify the set parameters β to converge to a minimum. These deterministic algorithm also often run the risk of converging to local minima. Since these are deterministic algorithms that always converge to the same result for a given initial guess β_0, performing the minimization from different starting conditions, known as multi-start, can help find the global minimum.

Then, there are are heuristic probabilistic algorithms. Atalla [174] explores a differential evolution algorithm which proves to be an effective global search algorithm. There are also genetic algorithms are probabilistic algorithms based on the modification of populations of sets of parameters β. The sets of parameters are modified through selection, crossover, and mutation steps, mimicking genetic mutation and natural survival to heuristically select the best sets of parameters. Genetic algorithms contain several hyperparameters (crossover rate, mutation rate, etc.), and finding the right hyperparameters is time-consuming and tricky, requiring expertise and experience. They may require numerous iterations if poorly configured. Moreover, they often need to be combined with a local solver to finalize the convergence to a local minimum with a tighter tolerance.

Finally, the optimization process can be driven by a Bayesian process, which is a probabilistic method. The minimization results in a probability density function of the parameters β rather than a single value. This method makes use of the probabilistic nature of the experiments through the measurement uncertainty. On top of this, the Bayesian method incorporates an *a priori* distribution on the values of β, which allows the user to give information about the likely values of β based on experience and prior knowledge, which can help accelerate its convergence. Its application to a porous material in an impedance tube is described in [148, 179, 180].

4.1.3 | Practical considerations

Even though minimization inverse methods can theoretically fit any number of parameters, the more parameters there are and the less constrained they are, the more difficult it can be for the iterative process to converge. Consequently, placing constraints on parameter values is preferable to restrict the search range and accelerate the convergence. On top of this, parameters which are already known through direct measurements should be excluded from the minimization. When the inverse process is performed using impedance tube measurements, the high sensitivity of the measurements to the sample mounting conditions in the tube, caused by the preload which shifts the frame resonance, makes obtaining their true values from the minimization process unreliable. After all, even if measurements are performed perfectly, the numerical minimization process may not always converge properly, causing unreliable results.

Further, the parameters resulting from the optimization only have physical significance if the model used can accurately capture the response of the measurement setup. For example, trying to fit a motionless skeleton model to measurements where the frame resonance is strong will lead to a set of parameters that gives a good mathematical fit, but which is not truly representative of the motionless

skeleton material. Similarly, a parameter can only be found accurately if the model is sensitive to this parameter. Since each parameter is expressed more or less in different frequency ranges, it is recommended to analyse a wide range of different frequencies. For example, the influence ranges of the JCAL and Biot parameters for different frequencies are shown for melamine foam in Figure 1.15. For more information on this subject, other sensitivity graphs are given in Appendix A.

To improve the sensitivity of the cost function to every parameter, Cuenca et al. [181] suggest minimizing over several measurement procedures, using an impedance tube with a rigid backing and with a resonant expansion chamber. Cuenca [182] also suggests combining audible frequency range and ultrasonic measurements to fit both low and high frequency parameters. In this case, when performing a fit on several curves at once, it is possible to weight each curve or different frequency ranges differently [148]. Further, some authors recommend a multistep minimization process [56, 183], in which some parameters are fit using simpler models first, then with progressively more advanced models involving more parameters.

4.2 | Micro-macro approaches

In what follows, an overview of the state of the art of the main categories of micro-macro characterization approaches with their pros and cons is given. Then, simple analytic micro-macro formulas are applied to polyurethane foams based on microstructural information gathered from microscopic images.

4.2.1 | General methodology

Micro-macro, also called multiscale or bottom-up, approaches rely on modelling a material's microstructure to compute its macroscopic properties. The microstructure is often assumed to have an ideal geometry, such as Kelvin cells for foams or a network of beams for fibrous materials, the dimensions of which can be obtained from microscopic images or 3D X-ray computer tomography. The first micro-macro approaches were mainly empirical relations relating microstructural features, such as cell size or fibre width, to macroscopic material properties. Empirical relations have been developed to predict the mechanical properties of compressed fibres [184, 185, 186, 187], and the transport properties of porous materials for acoustic applications [161, 188, 189, 190].

Nonetheless, numerical and analytic methods can be more accurate than empirical relations. These methods rely on analysing a Periodic Unit Cell (PUC) for foams, or building a Representative Volume Element (RVE) for fibrous networks, and performing a homogenization to obtain macroscopic properties. Many types of materials have been analysed with a micro-macro approach, and a benchmark of existing numerical methods is given by Zielinski et al. [106]. In regard to fibrous media, their transport parameters have been studied in [191, 192, 193, 194, 195, 196] and [197, 198, 199] for metallic fibres. Their mechanical parameters have also been analysed in [200, 201]. The biggest difficulty in modelling fibrous networks is finding an adequate RVE, which tends to be gigantic due to its structure [202, 203], making the creation of the microstructure geometry difficult and the computation time long.

In regard to polymer foams, their transport properties have been analysed for cubic cells [204], polyhedral cells [205], a full 3D scanned geometry [206], partially reticulated cells [30, 207, 208], and partially reticulated Kelvin cells for polyurethane foams [207, 209, 210, 211, 212]. The sensitivity of these models to microstructural parameters is studied by Doutres et al. [213]. Their mechanical parameters have also been studied numerically in [214, 215, 216]. Novel metamaterials have also been investigated using micro-macro approaches, such as double-porosity media which can improve low-frequency absorption [217, 218, 219, 220], and 3D-printed materials which allow the creation of an ideal material geometry [221, 222, 223, 224, 225]. All in all, micro-macro approaches can be

used in a feedback loop to improve material behaviour by controlling the microstructure through the manufacturing process, as explored in [226, 227, 228].

Overall, micro-macro approaches are powerful and can be used to obtain many material parameters, including the thermal permeability q_0' and the static tortuosities α_0 and α_0' of the Pride model which cannot be measured directly. Further, they are capable of predicting the impact of microscopic properties such as membranes blocking pore openings, which can help guide manufacturing processes. However, the biggest difficulty lies in finding an RVE that is representative of the homogenized material. Fibrous media RVEs can be very large [203], and polydisperse foams with variable cell dimensions require additional considerations [30]. Additionally, micro-macro methods require accurate knowledge of the microstructural geometry of the geometry, and deviations of the real material from the ideal modelled structure due to inhomogeneity, unreliable manufacturing process, damage or ageing are a large source of uncertainty.

4.2.2 | Application example

In this section, SEM images are used to measure the dimensions of the microstructural cells of the PU60 and PU250 polyurethane foams, and simple analytic formulas relating them to the transport parameters are applied. These formulas are applied to highly porous polyurethane foams composed of Kelvin cells by Doutres et al. [209], and the objective is to assess if they can be applied directly to the studied materials. The cell dimensions, notably the strut length l and strut edge width w, are measured from SEM images using ImageJ software, as shown in Figure 2.22.

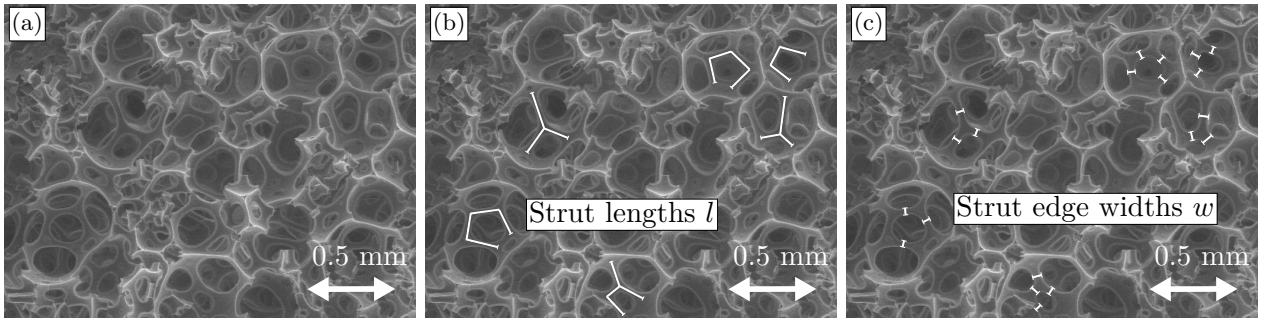

Figure 2.22. (a) SEM image of the PU60 microstructure. Measurement markings of (b) the strut lengths l, and (c) the strut edge widths w.

For fully reticulated materials, meaning that there are no membranes blocking the openings between the cells, which is the case of the studied foam, the porosity is given by [229]

$$\phi = 1 - \frac{\rho_1}{\rho_s} = 1 - \rho_r, \tag{2.15}$$

where ρ_r is the relative density which can be expressed as $\rho_r = C^\rho \left(\frac{t}{l}\right)^2$, with l the average strut length and t the average strut thickness. For materials with high porosity and low tortuosity, the resistivity is given by [230, 231]

$$\sigma = \frac{C^\sigma}{t^2}\rho_r^2 = C^\sigma \left(C^\rho \frac{t}{l^2}\right)^2, \tag{2.16}$$

where the parameter C^σ is given by $C^\sigma = 128\alpha_\infty \frac{\mu_0}{c_g^2}$, and c_g is a constant that depends on pore shape. The assumption of cylindrical pores can be made to obtain $c_g = 1$. The viscous characteristic length is given by [39]

$$\Lambda = \frac{t}{4\rho_r}, \tag{2.17}$$

and the thermal characteristic length by [232]

$$\Lambda' = D_1 \frac{l^2}{t} - D_2 t. \tag{2.18}$$

These formulas rely on the average strut length l and thickness t. For triangular strut cross-sections, the strut thickness t is related to the measured strut edge width w by $t = a\frac{\sqrt{3}}{2}$. As seen on the broken off struts in Figure 2.22, their cross-section is triangular and concave. C^ρ, D_1 and D_2 are constants that depends on the cell shape, and their values depending on strut cross-section shape are given in Table 2.7. Doutres et al. [209] find that concave triangular strut cross-sections give the best results for the highly porous polyurethane foams they studied.

Table 2.7. Kelvin cell constants C^ρ, D_1 and D_2 for triangular and concave triangular strut cross-sections [209].

Strut cross-section shape	Triangular ▲	Concave triangular ▲
C^ρ	$\sqrt{3}/2\sqrt{2}$	$(2\sqrt{3}-\pi)/\sqrt{2}$
D_1	$2\sqrt{2}/3\sqrt{3}$	$2\sqrt{6}/3\pi$
D_2	$1/3$	$(12-2\pi\sqrt{3})/3\pi$

Equation 2.15-2.18 are applied to the PU60 foam, using dimensions $t = 36.7$ µm (±27.2 %) and $l = 142.2$ µm (±41.3 %) computed from SEM images. The measured value of the tortuosity $\alpha_\infty = 1.25$ is used instead of the assumption $\alpha_\infty \approx 1$. The resulting values of the transport parameters are presented in Table 2.8.

Table 2.8. Results of the micro-macro analytic approach for Kelvin cells applied to the PU60 foam.

Micro-macro results	α_∞ (-)	ϕ (%)	σ (Nsm^{-4})	Λ (µm)	Λ' (µm)
Triangular struts ▲	-	95.9	3 634	225	300
Concave triangular struts ▲	-	98.5	504	604	287
Measured values	1.25	94.0	[redacted]	-	-

These results show that the concave triangular struts give better results than regular triangular struts, since the latter yield $\Lambda' < \Lambda$. The computed porosity overestimates the true measured porosity, which means that some additional parameters would be needed in these formulas to account for the lower porosity of the material. Further, the resistivity computed for concave triangular struts is $\sigma = 3\,634$ Nsm^{-4}, which is much lower than the measured resistivity $\sigma =$ [redacted] Nsm^{-4}. Overall, these results reveal that these analytic formulations are not adapted to the PU60 foam, which is understandable because the hypotheses of high porosity and low tortuosity are not valid. Therefore, micro-macro formulations specifically adapted to the studied materials would be required to predict their transport parameters accurately.

Furthermore, the dimensions of the pores obtained from SEM images can be used to grossly approximate the characteristic lengths. Indeed, Λ' is approximately the radius of the largest pores, and Λ is approximately the radius of the smallest pores. These dimensions are found from SEM images, as shown for PU60 in Figure 2.23. Many measurements on SEM images are performed to obtain average cell sizes. This approximation of the characteristic lengths is performed for PU60 and PU250 foams, with results shown in Table 2.9.

The results found seem consistent with expected values. The ratio Λ'/Λ is equal to 2.9 for PU60 and 4.7 for PU250, which is quite high, indicating that the pore openings are quite small compared to

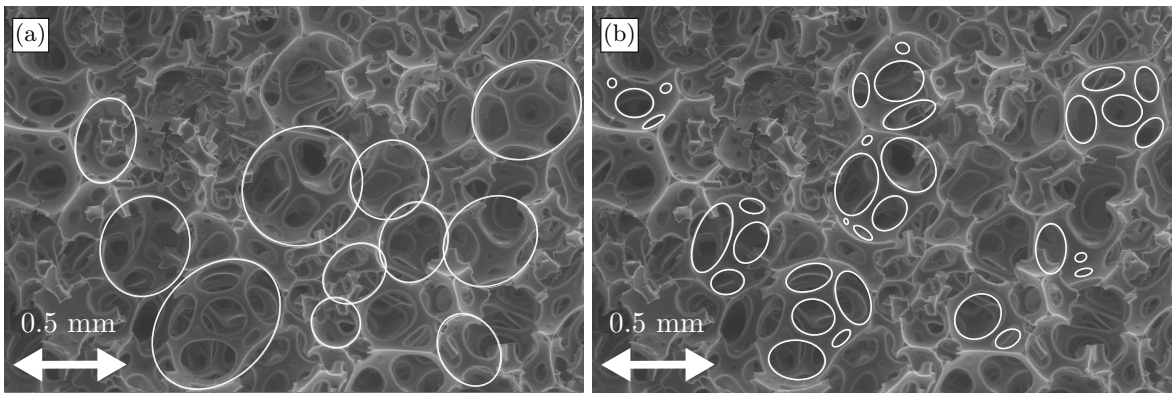

Figure 2.23. Measurement of microstructural cell dimensions from SEM images, for (a) the size of the largest pores, and (b) the size of the smallest pore openings.

Table 2.9. Approximated values of Λ and Λ' from the radii of the largest and of the smallest pore openings.

	Λ (µm)	CI (±%)	Λ' (µm)	CI (±%)	Λ'/Λ
PU60	60.5	69.9	175.7	98.6	2.9
PU250	20.5	95.4	96.0	125.1	4.7

cell size, which makes sense because the PU250 is a dense low-porosity material. The large confidence interval also indicates that there is a large dispersion of the pore sizes throughout the materials. All in all, this method is a gross approximation of Λ and Λ' and does not constitute a reliable evaluation of their values.

4.3 | Indirect method for transport parameters

The indirect characterization method relies on deducing the transport parameters by measuring the material's behaviour and analytically manipulating results to isolate the sought-after properties. Notably, the material density $\tilde{\rho}_{eq}$ and bulk modulus $\tilde{K}_{eq}$, obtained from 3-microphone impedance tube measurements for example, can be used to compute transport parameters. This method has the advantage of not requiring a specific bench for each material property, since only a common impedance tube is required. The method is presented in Section 4.3.1 and applied to the six studied materials in Section 4.3.2. Its practical limitations and the validity conditions are examined in Section 4.3.3.

4.3.1 | Principle of the indirect method

The indirect method is an analytic inversion of the equivalent density $\tilde{\rho}_{eq}$ and bulk modulus $\tilde{K}_{eq}$ of the material, which can be obtained from 3-microphone impedance tube measurements. It was first presented by Panneton and Olny [115] for viscous parameters (σ, Λ, α_∞), and by Olny and Panneton [116] for thermal parameters (Λ', q_0'). This method is especially helpful for computing parameters which can be difficult to measure directly, such as Λ, Λ', and q_0'. By knowing the porosity ϕ of the material, the other transport parameters are computed from

$$\sigma = -\frac{1}{\phi} \lim_{f \to 0} \mathrm{Im}(\omega \tilde{\rho}_{eq}), \tag{2.19}$$

$$\alpha_\infty = \frac{\phi}{\rho_0} \left(\mathrm{Re}(\tilde{\rho}_{eq}) - \sqrt{\mathrm{Im}(\tilde{\rho}_{eq})^2 - \left(\frac{\sigma}{\omega}\right)^2} \right), \tag{2.20}$$

$$\Lambda = \alpha_\infty \sqrt{\frac{2\rho_0\mu_0}{\omega\phi\,\mathrm{Im}(\tilde{\rho}_{eq})(\rho_0\alpha_\infty - \phi\,\mathrm{Re}(\tilde{\rho}_{eq}))}}\,, \tag{2.21}$$

$$\Lambda' = \delta'_0\sqrt{2}\left(-\mathrm{Im}\left(\left(\frac{1-\frac{\tilde{K}_{eq}}{K_0}}{1-\frac{\gamma\tilde{K}_{eq}}{K_0}}\right)^2\right)\right)^{-1/2}, \tag{2.22}$$

$$q'_0 = \frac{\phi\delta'_0}{2}\left(-\mathrm{Re}\left(\left(\frac{1-\frac{\tilde{K}_{eq}}{K_0}}{1-\frac{\gamma\tilde{K}_{eq}}{K_0}}\right)^2\right)\right)^{-1/2}. \tag{2.23}$$

The resistivity σ is computed from a low frequency asymptote extrapolation, whereas the other parameters are found from mid-frequency results. Alternatively, the tortuosity α_∞ and the viscous characteristic length Λ, which are high frequency parameters, can also be computed from a high frequency asymptote extrapolation. To do so, the high frequency asymptotic behaviour of Σ is approximated by a linear function of $\omega^{-3/2}$ as

$$\Sigma = \frac{\phi}{\rho_0}\left[\mathrm{Re}(\tilde{\rho}_{eq}) + \mathrm{Im}(\tilde{\rho}_{eq})\right] \simeq m\omega^{-3/2} + b, \tag{2.24}$$

where m is the slope and b is the y-intercept of the linear regression of Σ. These are related to the high frequency parameters by

$$\alpha_\infty = b, \tag{2.25}$$

$$\Lambda = -m\alpha_\infty\sqrt{\frac{8\mu_0\rho_0^3}{\sigma^4\phi^4}}. \tag{2.26}$$

This asymptotic approximation is only valid in high frequencies, when

$$\omega_{min} > \sqrt[3]{m^2}. \tag{2.27}$$

This inequality means that generally more resistive materials require information at higher frequencies to apply the indirect method. Additionally, the porosity can be obtained from low and high frequency asymptotes of the equivalent bulk modulus $\tilde{K}_{eq}$ [233]

$$\lim_{\omega\to 0}\mathrm{Re}\left(\tilde{K}_{eq}\right) = \frac{P_0}{\phi}, \tag{2.28}$$

$$\lim_{\omega\to\infty}\mathrm{Re}\left(\tilde{K}_{eq}\right) = \frac{\gamma_0 P_0}{\phi}. \tag{2.29}$$

Nevertheless, it can be difficult to obtain accurate low frequency information with an impedance tube due to measurement error. It can also be difficult to obtain the high frequency behaviour of materials, since this requires narrow tubes in which samples are no longer homogeneous and representative of the material.

Overall, since the indirect method is applied to impedance tube measurements, the results are strongly dependent on sample mounting conditions, leakages, and skeleton resonances within the impedance tube. Precautions must be taken when installing samples to ensure repeatability and reliability of results. Furthermore, the indirect method is applicable to materials behaving as motionless frame JCAL equivalent fluids, which means frame resonances can cause invalid results. The difference between motionless frame and limp frame behaviours can be assessed by $\lim_{f\to 0}\mathrm{Im}\left(\tilde{\rho}_{eq}\right)$, which tends $-\infty$ for a rigid frame and ρ_t for a limp frame, as shown in Figure 1.14. At last, the indirect method Equations 2.19-2.21 make use of previous parameter values to compute the next, which means that

any error on ϕ, σ and α_∞ has a trickle-down effect on the values of σ, α_∞ and Λ respectively. Consequently, to avoid accumulating error through the estimation of each parameter, it is preferable to use the reliably measured values of ϕ, σ and α_∞ where possible.

4.3.2 | Application and results

The indirect method is applied to the six materials studied in this work. Because the indirect method relies on a motionless frame hypothesis, Panneton and Olny [115] suggest introducing needles into samples to reduce the skeleton's displacement. To investigate this, melamine samples are characterized with and without needles, in order to evaluate the impact of the frame displacement on the results. The melamine sample with needles is shown in Figure 2.24(a). It can be seen on the absorption coefficient in Figure 2.24(b) that when more needles are added, the frame resonance magnitude is reduced and it is shifted to lower frequencies.

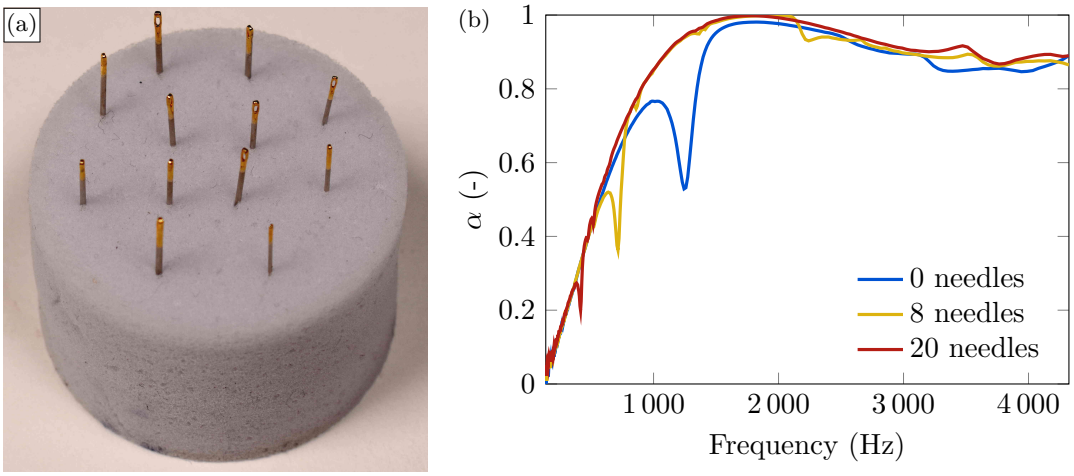

Figure 2.24. (a) Melamine sample with needles to reduce the effect of the frame. (b) Absorption coefficient of melamine sample with varying number of needles.

Determination of the porosity ϕ

First, the porosity is obtained from low frequency or high frequency asymptotic regression of the equivalent modulus Re $\left(\tilde{K}_{eq}\right)$. The low and high frequency regressions are shown in Figure 2.25. The shaded zone indicates the frequency range that the linear regression is computed on, chosen manually. It can be seen that this frequency range must be chosen wisely to obtain realistic porosity values, and the noisy low frequency information and the high frequency frame resonance must be excluded from the regression range. Results obtained from the indirect method are compared to directly measured values in Table 2.10. Overall, even though the indirect method yields results close to the measured values for the melamine foam, the results for the other materials are unreliable and even have non-physical values that do not respect $0 < \phi < 1$. Since the porosity is most often contained within the range 0.90-0.99, a small error on the linear regression can quickly lead to a value that is outside the plausible range. Errors on the linear regressions can be caused by noisy low frequency information for the low frequency asymptote, and from frame resonances at high frequencies.

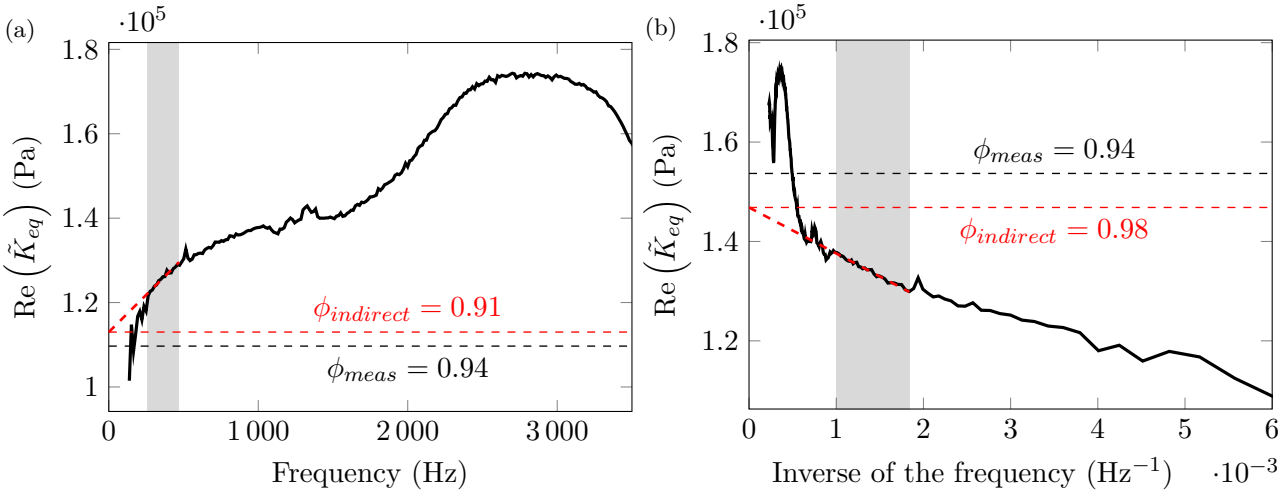

Figure 2.25. Application of the indirect method to obtain the porosity ϕ of a melamine sample, pierced by 20 needles and backed by an air gap, from the (a) low frequency and (b) high frequency asymptotes. The shaded zone represents the manually chosen frequency range used to compute the linear regression to find ϕ.

Determination of the resistivity σ

Next, the resistivity σ is computed from a linear regression at low frequencies, which is shown in Figure 2.26. It can be seen that the linear regression used to determine σ can be inaccurate at low frequencies due to measurement noise. The resistivity results for all materials are presented and compared to measured values in Table 2.11. The results show that the indirect method works quite well for low-resistivity materials, such as the melamine and the Greenflocks materials. The difference is larger for more resistive materials, which could be partly due to the difficulty in accurately measuring their resistivity due to air leaks in the measurement bench. Placing a cavity behind the material improves the results for the highly resistive and thin Polyfiber material, because the air gap allows more airflow through the material and allows the low-frequency behaviour and the resistivity to be expressed. Adding an air gap does not improve results so much for the melamine or the PU60. Furthermore, adding needles to the melamine foam does not seem to improve results consistently.

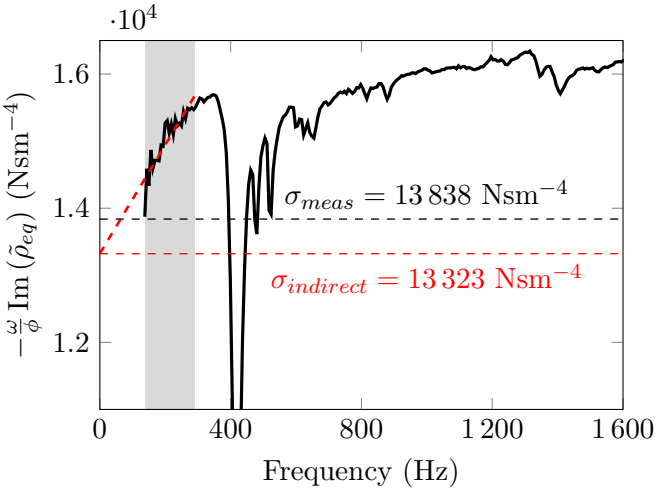

Figure 2.26. Curves used to obtain the resistivity with the indirect method for a melamine foam pierced by 20 needles. The shaded zone represents the manually chosen frequency range used to compute the linear regression to find σ.

Table 2.10. Comparison of porosity results ϕ (%) using the indirect method from the low frequency (LF) and high frequency (HF) asymptotes, and the measured value using a porosimeter. Results in italics indicate non-physical or unlikely values.

Porosity ϕ (%)	Air gap	Measurement	Indirect LF	Indirect HF
Melamine, no needles		94	*100*	94
Melamine, no needles	20 mm	94	163	99
Melamine, 12 needles	20 mm	94	99	95
Melamine, 20 needles	20 mm	94	91	98
PU60		94	*144*	*142*
PU60	20 mm	94	*106 400*	*-1 800*
PU250		79	*162*	*-251*
Polyfiber		99	*240*	*153*
Polyfiber	5 mm	99	*-26*	87
Greenflocks 20 mm		93	*135*	*118*
Greenflocks 25 mm		95	*57*	*103*

Table 2.11. Results obtained for resistivity σ (Nsm^{-4}), from direct measurement and from the indirect method. The relative difference between the indirect method and the direct measurement Δ is computed. Results in italics represent non-physical or unlikely values.

Resistivity σ (Nsm^{-4})	Air gap	Measurement	Indirect	Δ (%)
Melamine, no needles		13 838	15 802	14.2
Melamine, no needles	20 mm	13 838	10 267	25.8
Melamine, 12 needles	20 mm	13 838	9 054	34.6
Melamine, 20 needles	20 mm	13 838	13 323	3.7
PU60		[redacted]	[redacted]	50.0
PU60	20 mm	[redacted]	[redacted]	58.1
PU250		[redacted]	[redacted]	54.7
Polyfiber		228 728	*-105 885*	146.3
Polyfiber	5 mm	228 728	318 642	39.3
Greenflocks 20 mm		[redacted]	[redacted]	1.0
Greenflocks 25 mm		[redacted]	[redacted]	30.1

Determination of the tortuosity α_∞

The tortuosity α_∞ computed with Equation 2.20 yields a frequency dependant function, which is supposed to be constant, real, and physical ($\alpha_\infty \geq 1$) in the validity range of the motionless frame equivalent fluid model. However, the computed curve is actually complex and frequency dependant, so user input is required to select a frequency range of validity. This requires human expertise and introduces a bias in the results. It is also a sign that the measured equivalent density $\tilde{\rho}_{eq}$ is not representative of the motionless frame JCAL model. Moreover, the expected value of the tortuosity is often very close to 1 but can never be less than 1, which creates a tight tolerance of valid values for α_∞.

An example of the frequency dependant tortuosity for the melamine foam is given in Figure 2.27(a). A strong variation of the tortuosity with the frequency is visible, and the result is

not exploitable over a large frequency range, especially in low frequencies. The results of the tortuosity for all materials with the indirect method are reported in Table 2.12. The tortuosity obtained for the PU250 foam is $\alpha_\infty = 9.77$, which is an unrealistically high value, and the tortuosity for the Polyfiber with a cavity is $\alpha_\infty = -0.22$, which is not physical. Overall, the Polyfiber and the PU60 and PU250 foams indirect results are very different from the measured results, but the melamine and the Greenflocks materials, which have a tortuosity much closer to 1, give believable results. Increasing the number of needles in the melamine foam brings the indirect method value closer to the measured value, however it also increases the confidence interval, which means the results are less reliable. The tortuosity values computed from the high-frequency asymptote of Σ are also given, however this results in unrealistic and non-physical values, so the high frequency asymptote method is not recommended for the tortuosity.

Determination of the other parameters: Λ, Λ', and q'_0

The indirect method also gives frequency dependant curves for Λ, Λ', and q'_0. These results yield complex and frequency dependant curves, which should be constant and real in the frequency range of validity of the indirect method. As a consequence, their average is computed over a frequency range selected by the user. The results for Λ are shown in Table 2.13, and compared to simplified value computed for cylindrical pores and with the 3-parameter model given by Horoshenkov et al. [109] in Equation 1.102. This model assumes log-normally distributed pore sizes and expresses all transport parameters as a function of the porosity ϕ, the median pore size $\bar{s}$, and the pore size standard deviation σ_s. Consequently, the experimental knowledge of ϕ, σ and α_∞ can be used to compute Λ, Λ' and q'_0. It can be noted that there is a strong similarity between the values found with the cylindrical pores hypothesis and Horoshenkov's 3-parameter model, except for the highly resistive materials, the PU250 and the Polyfiber. The value of Λ is also computed from the high frequency asymptote of Σ, which gives very different results from the indirect method. Considering that the high-frequency asymptote method was found to be unreliable for the tortuosity, it can also be discarded for Λ. The value $\Lambda = 135.8$ µm obtained for the melamine without needles is coherent with values found in the literature, mostly found around 100 µm to 116 µm [146, 147, 148, 149].

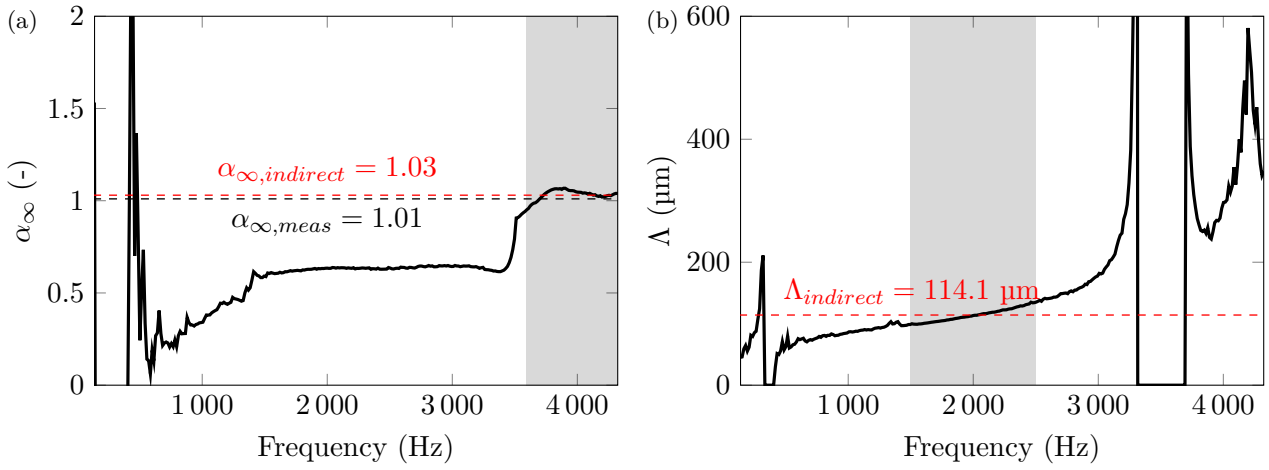

Figure 2.27. Application of the indirect method to obtain (a) the tortuosity α_∞ and (b) the viscous characteristic length Λ. The shaded zone represents the frequency range used to average α_∞ and Λ, chosen manually.

The frequency-dependant curve for Λ' is shown in Figure 2.28(a), and its values for all materials are in Table 2.14, along with the value computed from Horoshenkov's 3 parameter model. The frequency dependant curve shows that there is no frequency range which gives constant values for Λ',

Table 2.12. Results obtained for tortuosity α_∞ (-). The 95 % Confidence Interval (CI) indicates the dispersion of the value over the frequency range of computation. The relative difference between the indirect method and the direct measurement Δ is computed. Results in italics represent unlikely values.

Tortuosity α_∞ (-)	Air gap	Measurement	Indirect	CI (±%)	Δ (%)	Indirect HF
Melamine, no needles		1.01	1.18	2.1	16.8	1.06
Melamine, no needles	20 mm	1.01	1.11	2.8	9.5	*0.40*
Melamine, 12 needles	20 mm	1.01	1.11	2.6	10.3	*0.78*
Melamine, 20 needles	20 mm	1.01	1.03	5.1	2.3	*0.59*
PU60		1.25	2.36	19.7	89.0	2.82
PU60	20 mm	1.25	2.16	9.6	73.2	1.91
PU250		2.45	*9.77*	0.8	298.8	*6.44*
Polyfiber		1.49	2.39	19.1	60.5	*-1.44*
Polyfiber	5 mm	1.49	*-0.22*	51.6	115.0	*-2.01*
Greenflocks 20 mm		1.03	1.15	40.6	12.1	2.06
Greenflocks 25 mm		1.01	1.01	3.7	0.2	1.82

Table 2.13. Results obtained for viscous characteristic length Λ (µm). The simplifying assumption of nearly straight cylindrical pores gives $\Lambda \approx \sqrt{\frac{8\mu\alpha_\infty}{\phi\sigma}}$ [39]. The simplified 3-parameter model by Horoshenkov et al. [109], and the value is computed from the measured porosity, resistivity and tortuosity. Results in italics represent unlikely values.

Λ (µm)	Air gap	Indirect	CI (±%)	Cyl. pores	Horoshenkov	Indirect HF
Melamine, no needles		135.8	2.25	106.1	106.6	93.5
Melamine, no needles	20 mm	100.7	19.1	106.1	106.6	37.9
Melamine, 12 needles	20 mm	168.9	3.0	106.1	106.6	18.6
Melamine, 20 needles	20 mm	114.1	18.1	106.1	106.6	57
PU60		29.0	23.9	80.2	91.9	52.8
PU60	20 mm	36.0	14.9	80.2	91.9	34.9
PU250		7.8	26.1	19.4	45.2	*-8.4*
Polyfiber		22.7	16.6	25.4	33.6	7.9
Polyfiber	5 mm	12.5	7.0	25.4	33.6	5.6
Greenflocks 20 mm		48.5	4.7	121.9	123.7	*448.3*
Greenflocks 25 mm		65.6	3.0	139.2	139.9	*660*

Table 2.14. Results obtained for thermal characteristic length Λ' (µm). The simplified 3-parameter model by Horoshenkov et al. [109] is described by Equation 1.103, and the value is computed from the measured porosity, resistivity and tortuosity. Results in italics represent unlikely values.

Λ' (µm)	Air gap	Indirect	CI (±%)	Λ'/Λ	Horoshenkov
Melamine, no needles		277.4	33.5	2.04	106.7
Melamine, no needles	20 mm	179.5	64.6	1.78	106.7
Melamine, 12 needles	20 mm	223.4	55.8	1.32	106.7
Melamine, 20 needles	20 mm	181.9	33.8	1.59	106.7
PU60		258.0	72.0	8.9	112.2
PU60	20 mm	211.9	83.5	5.89	112.2
PU250		170.2	50.9	21.9	*1127.6*
Polyfiber		*22.3*	13.5	0.98	63.5
Polyfiber	5 mm	22.5	54.9	1.8	63.5
Greenflocks 20 mm		125.2	8.9	2.58	124.1
Greenflocks 25 mm		241.4	8.0	3.68	140.0

Table 2.15. Results obtained for thermal permeability q'_0 (10^{-9}m^2). The simplifying assumption of cylindrical pores is given by $q'_0 = \frac{\phi\Lambda'^2}{8}$. The simplified 3-parameter model by Horoshenkov et al. [109] is described by Equation 1.104, and the value is computed from the measured porosity, resistivity and tortuosity. Results in italics represent unlikely values.

q'_0 (10^{-9} m^2)	Air gap	Indirect	CI (±%)	Cyl. pores	Horoshenkov
Melamine, no needles		3.0	4.4	9.0	1.3
Melamine, no needles	20 mm	4.9	28.1	3.8	1.3
Melamine, 12 needles	20 mm	3.2	5.5	5.9	1.3
Melamine, 20 needles	20 mm	6.0	16.2	3.9	1.3
PU60		3.4	7.6	7.8	1.4
PU60	20 mm	11.4	9.3	5.3	1.4
PU250		16.2	59.3	2.9	*569.9*
Polyfiber		0.6	14.7	*0.06*	0.5
Polyfiber	5 mm	0.4	14.6	*0.06*	0.5
Greenflocks 20 mm		1.2	25.1	1.82	1.7
Greenflocks 25 mm		1.5	8.6	6.92	2.3

which is reflected in the large confidence interval computed, and indicates fairly unreliable results. The ratio Λ'/Λ is also computed, and it presents a high variability from material to material. Notably the fibrous Polyfiber material has Λ'/Λ close to 1, but the polyurethane PU60 and PU250 foams have a much higher ratio of 9 and 22. Consequently, it does not seem possible to select a general value of Λ'/Λ to predict Λ' from Λ for any material. The value $\Lambda' = 277.4$ µm obtained for the melamine without needles is slightly higher than values found in the literature, which are mostly around 200 µm to 256 µm [146, 147, 148, 149].

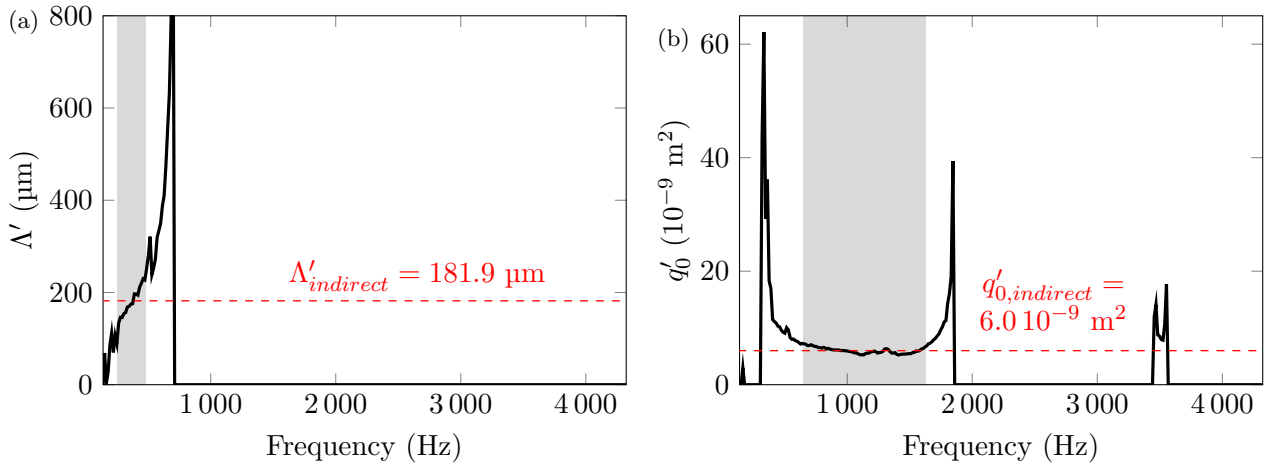

Figure 2.28. Application of the indirect method to obtain (b) the thermal characteristic length Λ' and (a) thermal permeability q'_0. The shaded zone represents the frequency range used to average Λ' and q'_0, chosen manually.

The frequency-dependant curve for q'_0 is shown in Figure 2.28(b), and its values for all materials are in Table 2.15, along with the value computed from Horoshenkov's 3 parameter model. The confidence interval for q'_0 is also quite large, indicating that it is difficult to compute it reliably using the inverse method. Furthermore, the value of q'_0 is computed from the simplified assumption of cylindrical pores, which gives results quite different from the indirect method. This highlights that the assumption of cylindrical pores does not work well with the studied materials. Additionally, the 3-parameter model by Horoshenkov et al. [109] finds unrealistic values of Λ' and q'_0 for the PU250, due in part to its high tortuosity of $\alpha_\infty = 2.45$, which indicates that this model is not applicable to all materials. The value $q'_0 = 3.0\ 10^{-9}$ m^2 obtained for the melamine without needles is coherent with values found of the literature between $2.8\ 10^{-9}$ m^2 to $4.0\ 10^{-9}$ m^2 [146, 148, 149].

4.3.3 | Validity of results and frequency range

The high frequency asymptote of Σ, which can be used to compute α_∞ and Λ, is only exploitable above a minimum frequency f_{min}. This frequency can be computed from the slope of Σ according to Equation 2.27. Nevertheless, the experimental regression on Σ is error-prone due to measurement error and frame resonances, so an ideal equivalent fluid model is created from each material's properties from Table 2.21 to compute their theoretical value of f_{min}. The values of f_{min} found experimentally and computed theoretically from a modelled JCAL behaviour using their parameters are presented in Table 2.16. Overall, there are large differences between the experimentally computed values of f_{min} and its theoretical values, so the latter are considered. For an impedance tube of diameter 44.5 mm which goes up to 4323 Hz, the high frequency asymptote method can be applied for all materials except the highly resistive Polyfiber and PU250. However, having sufficiently high frequency experimental data does not guarantee that the high frequency asymptote method is exploitable, due to frame resonances and measurement uncertainties.

Table 2.16. Minimum frequency required for exploiting the high-frequency asymptote of Σ, used to compute α_∞ and Λ, based on the criterion in Equation 2.27, for each material. The experimental value is computed from impedance tube measurements of $\tilde{\rho}_{eq}$, and the theoretical value is computed analytically from material properties.

Min. frequency f_{min} (Hz)	Air gap	Experimental	Theoretical
Melamine, no needles		1 553	1 864
Melamine, no needles	20 mm	850	1 864
Melamine, 12 needles	20 mm	530	1 864
Melamine, 20 needles	20 mm	1 117	1 864
PU60		1 942	1 301
PU60	20 mm	1 473	1 301
PU250		15 920	15 155
Polyfiber		10 402	16 876
Polyfiber	5 mm	8 246	16 876
Greenflocks 20 mm		3 012	684
Greenflocks 25 mm		8 246	594

Further, each transport parameter is expressed strongly in different frequency ranges. For example, σ is a low frequency viscous parameter, Λ is a high frequency viscous parameter, q_0' is a low frequency thermal parameter, and Λ' is a high frequency thermal parameter. Consequently, their zones of influence are separated by the viscous and thermal characteristic frequencies. These are computed from Equation 1.155, and their values for each material are presented in Table 2.17. This reveals that for the highly resistive PU250 and Polyfiber materials, the viscous transition frequency f_v is greater than the high frequency limit of the impedance tube (44.5 mm, 4 323 Hz). As a consequence, their high frequency viscous behaviour, defined by $f \gg f_v$, is not strongly expressed experimentally. This causes results to have a low sensitivity to Λ. Furthermore, the thermal frequency f_t for the PU250 foam is at 164 Hz, which is too low to be measured accurately in the impedance tube. Therefore, measurement results for the PU250 foam are not sensitive to q_0', which deteriorates its computation with the indirect method.

$$f_v = \frac{1}{2\pi}\frac{\phi\sigma}{\rho_0\alpha_\infty}, \quad f_t = \frac{1}{2\pi}\frac{\phi\mu_0}{q_0'\rho_0\mathrm{Pr}}. \tag{1.155}$$

Table 2.17. Viscous and thermal transition frequencies for each material. Material properties from Table 2.21 are used.

Transition frequency	f_v (Hz)	f_t (Hz)
Melamine	1 638	1 057
PU60	[redacted]	932
PU250	[redacted]	164
Polyfiber	19 869	5 564
Greenflocks 20 mm	[redacted]	2 136
Greenflocks 25 mm	[redacted]	2 613

In summary, the indirect method succeeds in retrieving the resistivity σ of a material, but the other parameters, which include the porosity ϕ, the tortuosity α_∞, the thermal permeability q_0', and

the characteristic lengths Λ' and Λ, are frequency dependant and require user input to choose an exploitable frequency range. The high frequency asymptote method for computing Λ and α_∞ has shown to be unreliable due to the difficulty of predicting the high frequency behaviour experimentally and due to frame resonances. Consequently, it is preferable to obtain ϕ, α_∞ and σ from direct measurements. Acceptable results are found with the indirect method for Λ, however there are large uncertainties for Λ' and q_0'. In short, even though the indirect method works in theory for an ideal material, it does not work as well with real experimental results, due to measurement error and low sensitivity to certain parameters in certain frequency ranges. Adding an air gap behind the thin and resistive Polyfiber samples slightly improves the determination of σ, although there is no clear improvement of results for the other parameters or for other materials. Further, adding needles into the melamine does not seem to eliminate frame resonances, but rather displace them due to their added inertia. A possible improvement would be to fix the needles to the rigid backing to reduce their movement further. The indirect method suffers from all the same uncertainties as impedance tube measurements. A sensitivity analysis could be performed to estimate the validity of the results obtained with the indirect method. Moreover, relying on user input to select a frequency range to compute average parameter values adds a subjective bias into the results.

5 | Mechanical parameters direct measurement

Predicting the acoustic behaviour of porous layers requires modelling the waves propagating inside their solid frame. The biphasic Biot model, which accounts for these solid-borne waves, requires the mechanical properties related to the material's solid phase. These notably include the storage modulus E', the loss factor η, and the Poisson ratio ν. An overview of mechanical characterization methods to obtain these properties is given in Section 5.1. A particular attention is then given to the quasistatic compression method, which has unique advantages over other methods. This quasistatic method is then applied to the six studied materials in Section 5.2. Its limits and sources of error are explored in detail.

5.1 | State of the art

5.1.1 | Overview of characterization methods

Many types of setups exist to measure the mechanical properties of porous materials, which involve different types of excitations. The general principle consists in exciting the material with a mechanical or an acoustic source, and measuring its response to identify a Young's modulus $\tilde{E}$, a shear modulus $\tilde{G}$, and/or a Poisson ratio ν. The storage modulus E' or G' and the loss factor η can be retrieved from the complex moduli $\tilde{E}$ or $\tilde{G}$. Even though ν is in fact complex and frequency dependent, characterization results often find real values, with very small variation with frequency [65, 234, 235], so the assumption of a constant real Poisson ratio is often made. An in-depth review of several mechanical characterization setups is given by Jaouen et al. [234]. The principal, strengths and limits of several methods are presented in this section.

A first category consists in exciting a material sample acoustically. Sellen [176] excites a material inside an impedance tube and fits $\tilde{E}$ and ν to match the skeleton resonance observed experimentally. This method is sensitive to mounting conditions which strongly shift resonance frequency. Allard et al. [236] induces a shear wave on a thin rigid-backed porous layer with an acoustic source at a near grazing angle to identify $\tilde{G}$. This method requires large samples and cannot identify ν. Generally, it can be more difficult to excite the material skeleton with an acoustic excitation, especially for low airflow resistivity materials.

Consequently, a second category of resonant methods rely on a direct mechanical excitation by contact with the skeleton. Pritz [237] describes a porous beam excited longitudinally to find its stiffness from the resonances, from which $\tilde{E}$ and ν must then be extracted. The method is applicable from 100-1000 Hz, and requires materials with very low or very high resistivity because the fluid phase is not accounted for. To reduce the viscous effects of the fluid, Sfaoui et al. [238, 239] apply this method in a vacuum, and uses the Time-Temperature Superposition (TTS) principle to extend the frequency range. Alternatively, a transverse displacement can be applied to a porous beam, known as the Oberst method, described in standard ASTM E 756 [240], and improved for porous materials by Wojtowicki et al. [241] by exciting the beam in its centre. The porous beam is usually glued to a metal beam, but it can also be sandwiched between two metal beams to increase the damping caused by shear, which improves results for materials with a low modulus. The beam properties are then obtained from an iterative global minimization inverse resolution with a numerical simulation, which allows for modelling the fluid phase of the medium. This method is very powerful, however it requires heavy numerical simulations and computations. This method does not work in very low frequencies where the induced damping is negligible.

Resonant methods also exist for mechanically excited plates. A setup with a clamped porous plate is described by Etchessahar et al. [65, 242], and its properties are obtained from an iterative global minimization process. Since applying a point force on a porous plate is difficult, Jaouen et al. [243] glue the porous plate onto a metal plate which is excited mechanically. In all methods where glue is used between a porous layer and another material, the impact of the glue on experimental results and how it should be modelled poses many questions. This method assumes material isotropy. Next, Allard et al. [244] determines $\tilde{G}$ from structure-borne surface Rayleigh waves (2000-4000 Hz), Boeckx et al. [245] uses the phase velocities computed from spatial Fourier Transforms of the surface waves to fit $\tilde{G}$ and ν as a function of frequency (200-1300 Hz), and Geslain et al. [246] analyses the spatial Laplace transform instead of the Fourier Transform, which is capable of separating the contribution of overlapping modes (200-4000 Hz). Bonfiglio et al. [247] excites a sample mechanically and uses a transfer matrix to compute the complex longitudinal wavenumbers and find $\tilde{E}$ in the range of around 100-1500 Hz.

Resonant characterization can be performed by exciting smaller cubic or a cylindrical sample. By placing a mass on a porous sample, the mass-spring resonance of the system can be used to compute the sample's stiffness. This method has the advantage of controlling the static preload applied to the material before characterization, which is very helpful for obtaining *in situ* material properties when a preload is required. However, this method only works at the resonance frequencies of the sample and mass system. As a consequence, it does not give access to low frequency information, and it can be unreliable when other resonances close to the target resonance are excited at the same time. Moreover, it is not possible to separate the preload from the frequency of characterization.

At last, to control the static preload and the characterization frequency independently, non-resonant quasistatic methods can be used. Quasistatic methods are distinguished by a much lower frequency range than resonant methods, since they work below the resonance frequencies of characterized samples. Quasistatic characterization can be done in torsion to obtain $\tilde{G}$ [248], which keeps the sample volume constant. This has the advantage of allowing the viscous effects of the air to be neglected, however it also means that ν cannot be determined. Quasistatic torsion measurements are quite quick and efficient, and measurement benches called rheometers already exist commonly in laboratories. Similarly to torsion, pure shear measurements can also be performed [69, 248] to obtain $\tilde{G}$. Torsion and shear measurements work well in very low frequencies, such as 0.01-10 Hz.

To obtain $\tilde{E}$ and ν from quasistatic measurements, a tension-compression measurement setup can be used [71, 249]. The method to obtain $\tilde{E}$ and ν from QMA measurements is explained in Section 5.1.2. This method is performed using a Quasistatic Mechanical Analyser (QMA), which is

equivalent to a Dynamic Mechanical Analyser (DMA), classically used for viscoelastic materials, that has been adapted to low frequencies and to soft materials. Quasistatic methods work over a range of frequencies with an upper bound limited by the first resonance frequency of the sample and the viscous effect of air which is neglected in the quasistatic regime. Consequently, the tension-compression method works best around 1-100 Hz. Furthermore, it can be noted that the frequency range of characterization can be extended with Time-Temperature Superposition. However, this should be done with care, because increasing the temperature decreases the modulus and therefore the resonance frequency of the material, which could end up inside the frequency range of measurement. In addition, the air's viscosity increases with temperature, so the viscous effects of the fluid phase become more important. Atalla [174] shows that the variation of air properties varies by less than 1 % between -20 °C and 80 °C, so this effect is only important at much higher temperatures.

Overall, despite the multitude of existing mechanical characterization methods, large uncertainties exist around the results they provide. As shown by round-robins studies on these methods [250, 251], different laboratories using various methods on the same materials find significantly different results. These uncertainties stem from the inhomogeneity and anisotropy of the samples, boundary conditions along the sample surfaces, imperfect sample shapes, and varying ambient temperature. In the absence of a greatly-needed standard for measuring viscoelastic properties of porous materials, all of these measurement conditions should be specified during measurements since they could strongly affect results.

5.1.2 | Description of the quasistatic tension-compression method

The quasistatic tension-compression method is done with a Quasistatic Mechanical Analyser (QMA) [71, 249]. It is performed at frequencies much lower than the first resonance frequency of the characterized sample in order to neglect its inertia. The viscous effects tied to the ambient air are also neglected. It also allows for easy control of the preload of the material to simulate *in situ* conditions. A uniaxial tension-compression QMA is shown in Figure 2.29. This method can be performed with cubic samples to characterize the sample in different directions and evaluate material anisotropy [252]. Cylindrical samples can also be used [253, 254], assuming material isotropy, as performed in this work due to their quick and repeatable cutting process using a hole saw.

The measurement process consists in placing a porous sample between two plates, and applying a very small dynamic displacement δ_d, chosen to ensure a linear material response. The reaction force $\tilde{F}$ of the sample is recorded at different angular frequencies ω. However, if the sample is not glued to the two plates, then there is a departure from contact at each cycle. To ensure constant contact, a static compression displacement δ_s is applied preemptively. Moreover, this static displacement serves to represent the initial loading condition of the material in real conditions. The total displacement can therefore be considered in the form $\delta(t) = \delta_s + \delta_d \sin \omega t$. The dynamic stiffness $\tilde{k}$, in the frequency domain, is obtained as

$$\tilde{k} = \frac{\tilde{F}}{\tilde{\delta}}. \tag{2.30}$$

The material mechanical parameters are computed from the stiffness $\tilde{k}$. First, the loss factor η is obtained from

$$\eta(\omega) = \frac{\mathrm{Im}(\tilde{k})}{\mathrm{Re}(\tilde{k})}. \tag{2.31}$$

Further, the stiffness contains the information about the Young's modulus $\tilde{E}$ and the bulging phenomenon of the Poisson effect with the Poisson ratio ν, shown in Figure 2.30(a). They are related

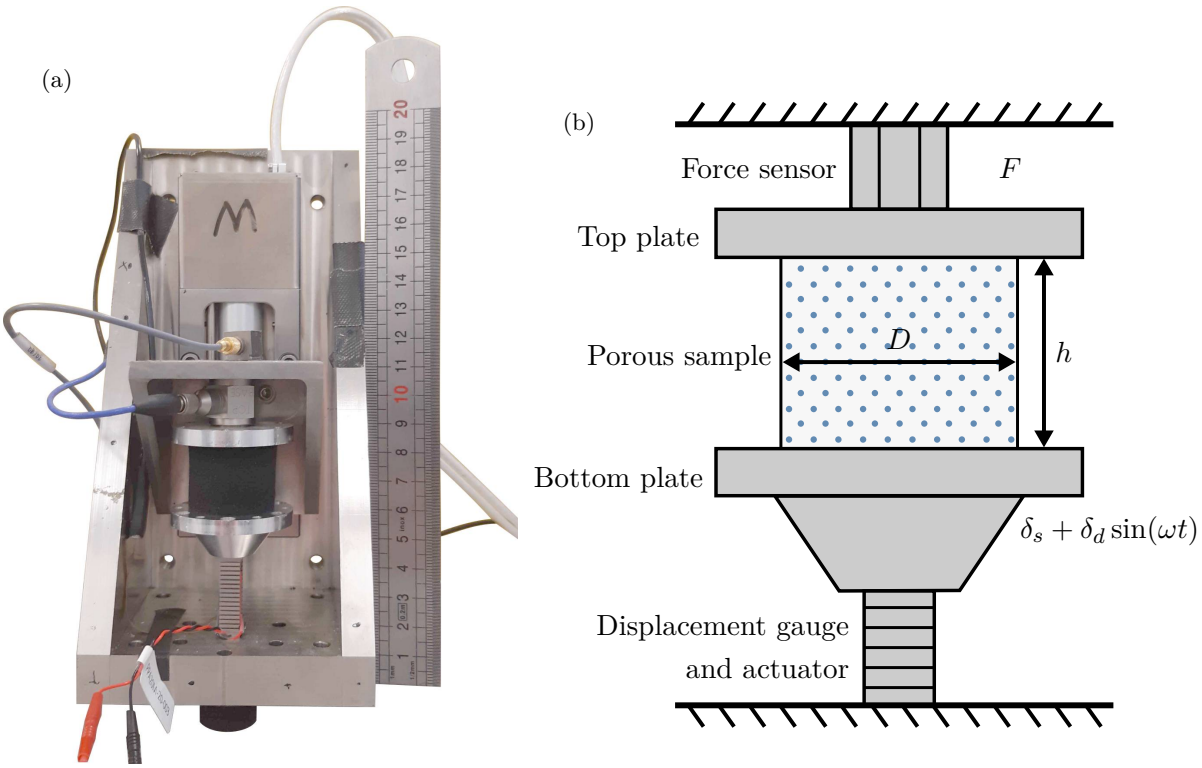

Figure 2.29. (a) Picture of the QMA, (b) elements of the QMA and measurement principle.

through

$$\tilde{k} = h\frac{\tilde{E}(1-\nu)}{H(\nu)}, \tag{2.32}$$

where h is the sample height, and $H(\nu)$ is the function relating the sample's shape and modulus to its stiffness, which can be computed numerically. To separate the contributions of $\tilde{E}$ and ν from the stiffness, Sim and Kim [255] suggest measuring two samples with a very small and very large shape factor and using an inverse numerical method to fit the parameters, and Langlois et al. [253] suggests using precomputed polynomial relations to predict the Poisson effect for different sample shape factors. Sahraoui et al. [252] suggest correlating the lateral displacement measured with a laser vibrometer with numerical simulations, and Sahraoui et al. [256] suggest stacking samples to compute a normalized stiffness ratio. The lateral displacement can also be measured using digital image correlation, which could work quite well on these porous materials. For glass wools, Tarnow [257] suggests neglecting the Poisson effect ($\nu = 0$) to compute $\tilde{E}$ from the stiffness. Examples of $H(\nu)$ for different sample shapes are given in Figure 2.30(b).

Since measuring the lateral displacement with a vibrometer can be difficult on porous materials, two samples with different shape factors are measured to isolate the contributions of $\tilde{E}$ and ν. Sahraoui et al. [256] define the sample shape factor s as $s = \frac{D}{h}$, where D is the diameter of the cylindrical sample. The stiffness $\tilde{k}_s$ of a sample of shape factor s can be normalized by its dimensions, yielding its normalized stiffness

$$\tilde{k}_{s,norm} = \frac{D}{s\tilde{E}S}\tilde{k}_s, \tag{2.33}$$

with S the cross-section area of the sample. The ratio of normalized stiffnesses $\frac{\tilde{k}_{s,norm}}{\tilde{k}_{2s,norm}} = \frac{2\tilde{k}_s}{\tilde{k}_{2s}}$ is Poisson ratio dependant and can be compared with numerical simulations to find the value of ν. Furthermore, this process can be generalized to any two shape factors s_1 and s_2 with

$$\frac{\tilde{k}_{s_1}}{\tilde{k}_{s_2}} = \frac{h_1 H_{s_2}(\nu)}{h_2 H_{s_1}(\nu)}. \tag{2.34}$$

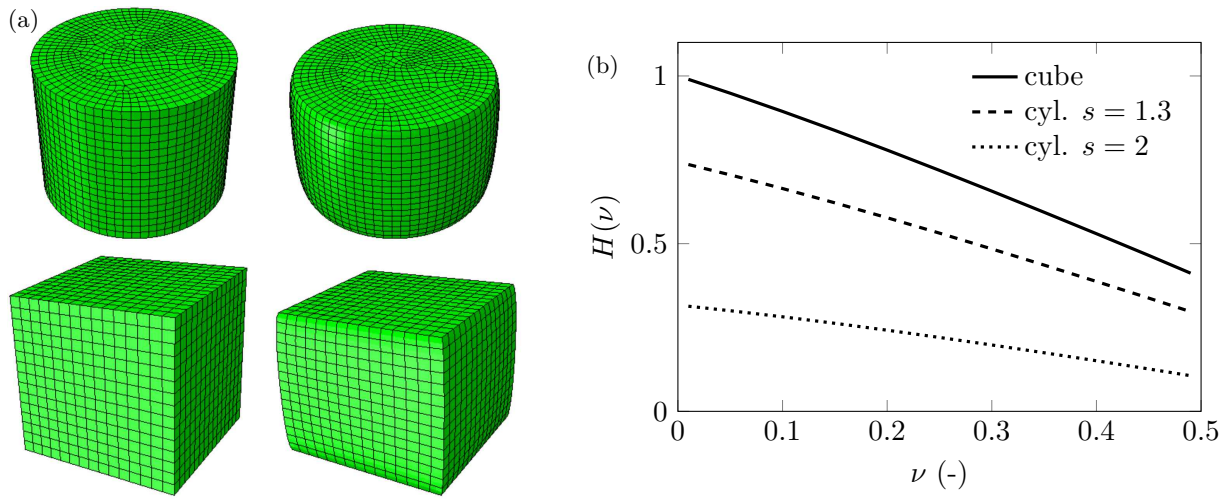

Figure 2.30. (a) Visualization of the Poisson effect on the compressed sample deformation for different sample geometries, (b) H as a function of ν for different sample geometries. The shape factor of a cylinder is $s = \frac{D}{h}$.

Once ν is known, $\tilde{E}$ can be computed from Equation 2.32. It can be noted that, with this method, the error on the Poisson ratio propagates into the estimation of the Young's modulus.

5.1.3 | Limits of the tension-compression QMA method

There are many sources of error with mechanical characterization methods, including material inhomogeneity and anisotropy, poorly controlled boundary conditions, imperfect sample shape and varying ambient temperature. With a QMA setup, material anisotropy can be estimated using cubic samples, although cylindrical samples are considered in this work. Further, the quasistatic hypothesis only holds before the sample's first resonance frequency. The quarter wavelength resonance frequency f_r of the six studied materials is computed in Table 2.18 using Equation 2.35 and their properties from Table 2.21.

$$f_r \approx \frac{1}{4h}\sqrt{\frac{E'\frac{1-\nu}{(1+\nu)(1-2\nu)}}{\rho_1}}. \tag{2.35}$$

Table 2.18. First quarter-wavelength resonance frequency of the frame for the studied materials.

First frame resonance frequency	f_r (Hz)
Melamine	1 613
PU60	494
PU250	711
Polyfiber	1 238
Greenflocks 20 mm	208
Greenflocks 25 mm	213

This reveals that the Greenflocks materials have resonance frequencies of 208 Hz and 213 Hz, which constitutes a restrictive upper limit for the measurements. Indeed, common practice consists in setting an upper frequency limit at about a third of the first resonance frequency. The PU60 has a resonance at 494 Hz and the PU250 at 711 Hz, which are also quite low. In practice, using

less thick samples increases the quarter wavelength resonance frequency, but it also increases the viscous effects of the air being pushed out of the sides of the sample when it is compressed, which constitutes yet another high-frequency limit. In addition, the resonance frequency of the QMA bench itself limits the high frequency measurement range. The QMA used in this work was designed to have high a resonance frequency, which is located above 400 Hz. Moreover, the low-frequency limit of the acquisition hardware is 0.5 Hz, giving a total exploitable range of around $0.5 - 400$ Hz. The actuator allows a dynamic amplitude of up to the order of magnitude of 15 µm at 400 Hz, measured using the displacement gauge.

5.2 | Application, results, and influencing factors

5.2.1 | Result example

An example of E' and η results obtained on the PU250 is shown in Figure 2.31. It can be seen that E' increases from 238 kPa at 1 Hz to 397 kPa at 300 Hz. η increases from 10 % at 1 Hz to 22 % at 300 Hz. At 400 Hz, a resonance appears and causes E' to rapidly increase and a peak for η. Beyond this resonance, the confidence interval increases, making the results unreliable at higher frequencies.

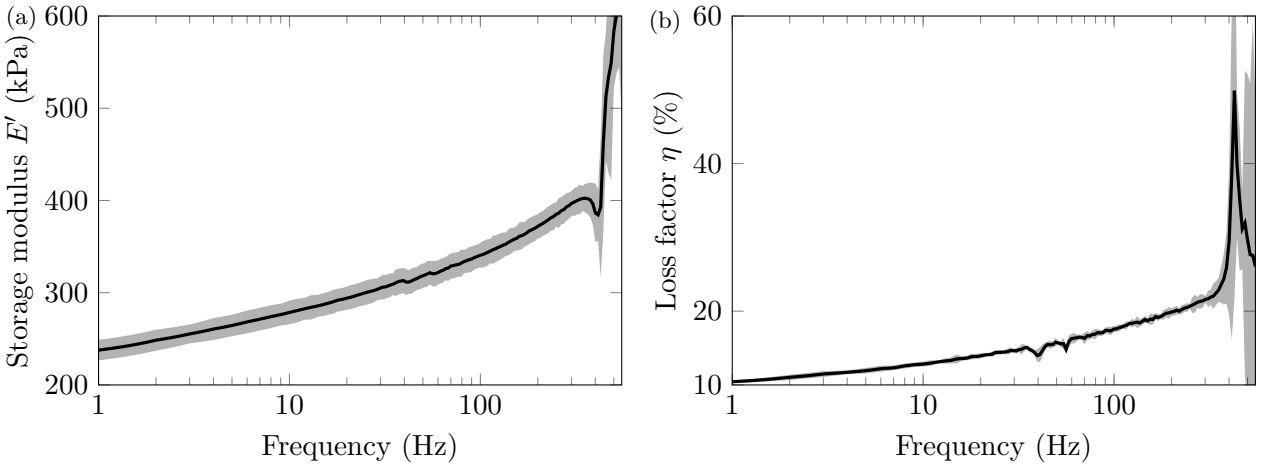

Figure 2.31. Typical QMA results of (a) the storage modulus E and (b) the loss factor η for a PU250 sample at $\varepsilon_s = -1$ % compressive strain, between 1 Hz and 550 Hz, with 95 % confidence interval.

Further, the Poisson ratio ν is computed by measuring the stiffness ratio of PU250 samples with different shape factors $s = 1.34$ and $s = 2.06$. Their stiffnesses are measured and averaged between 30 Hz and 100 Hz. The ratio of their stiffnesses is plotted in Figure 2.32, and the value of ν is obtained from where they intersect the numerically computed ratio of their $H(\nu)$ functions. The results show that ν depends on the static strain, as a static strain $\varepsilon_s = -0.3$ % gives $\nu = 0.24$, $\varepsilon_s = -0.5$ % gives $\nu = 0.30$, and $\varepsilon_s = -0.7$ % gives $\nu = 0.32$. These different Poisson ratios are found for stiffness ratios varying between 2.41 and 2.47, which means that a small error on the stiffness measurement can lead to a large difference in the estimation of ν. Using samples with very different shape factors can help improve the quality of this determination. As pointed out by Bonfiglio et al. [250], the estimation of the Poisson ratio depends strongly on the characterization method used and the preload applied. These experimental results shed light on the large uncertainties when trying to determine the Poisson ratio.

Additionally, Making an error on the estimation of ν propagates an error in the determination of E'. The values of E' computed from different values of ν are shown in Appendix B for cylindrical samples of diameter 29 mm. The variation of E' between $\nu = 0$ and $\nu = 0.44$ is around 20 % for the

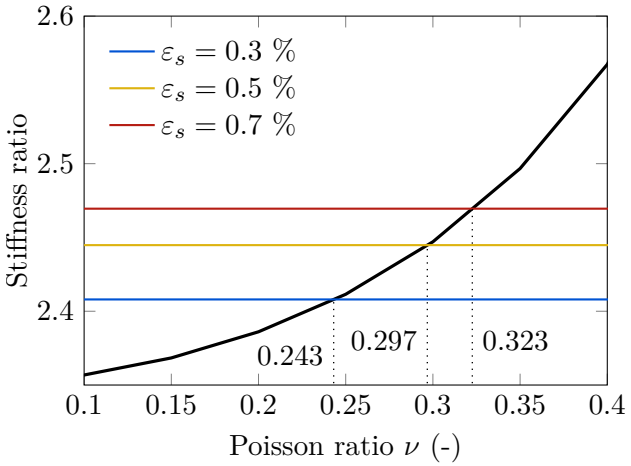

Figure 2.32. Ratio of $H(\nu)$ computed numerically for two sample shape factors in black. Horizontal lines correspond to the measured stiffness ratios for different static strains.

Greenflocks materials, with a height of around 20 mm. For the melamine and PU250 foam samples of height around 20 mm, E' varies by only 5 % and 10 % when ν varies between 0.30 and 0.44. However, the Polyfiber sample, which has a height of 4.6 mm and is much more sensitive to the Poisson effect, and exhibits a 77 % variation on E' between $\nu = 0$ and $\nu = 0.44$. As a consequence, for wide samples that are sensitive to the Poisson effect, the error on ν can have a big impact on the computed Young's modulus, but for more realistic differences of ν and samples with aspect ratios closer to $s \approx 1$, the variation of E' is much smaller.

Table 2.19. Difference on the estimation of E based on the value chosen for ν.

	ν (-)	E' (kPa)	ν (-)	E' (kPa)	Difference in E' (%)
Melamine	0.44	104	0.3	110	5
PU250	0.44	265	0.3	296	11
PU60	0.44	26	0.3	30	12
Polyfiber	0	144	0.44	64	77
Greenflocks 20 mm	0	19	0.44	16	20
Greenflocks 25 mm	0	25	0.44	21	16

The QMA characterization results of all six materials with a null prestrain $\varepsilon = 0$ % are shown in Figure 2.33 for E' and in Figure 2.34 for η. No confidence interval is presented on these results, however since a large part of the error comes from the compression of the samples due to relaxation and material nonlinearity, and these measurements are performed at null prestrain, the confidence interval can be considered quite small until 400 Hz at least, after which the confidence interval increases, similarly to Figure 2.31. Due to the difficulty to measure the Poisson ratio experimentally, it is given a typical value based on the material type (foam or fibrous). A value of 0.44 is chosen for melamine, due to the Kelvin-cell like microstructure. Langlois et al. [253] find $\nu = 0.45$ and Jaouen et al. [234] find $\nu = 0.44$ at 2 % strain for the melamine foam, which is coherent with the expected value for polymer foams with this microstructure. A value of 0.3 is chosen for the PU60 and PU250 foams, which are common values for these types of materials [250]. Fibrous materials are given a Poisson's ratio $\nu = 0$ due to horizontal fibre orientation.

The frequency dependence of E' is highest for the PU60, PU250, and Polyfiber materials, which have relatively high loss factors of 10 %, 12 %, and 38 % respectively. This supports the finding

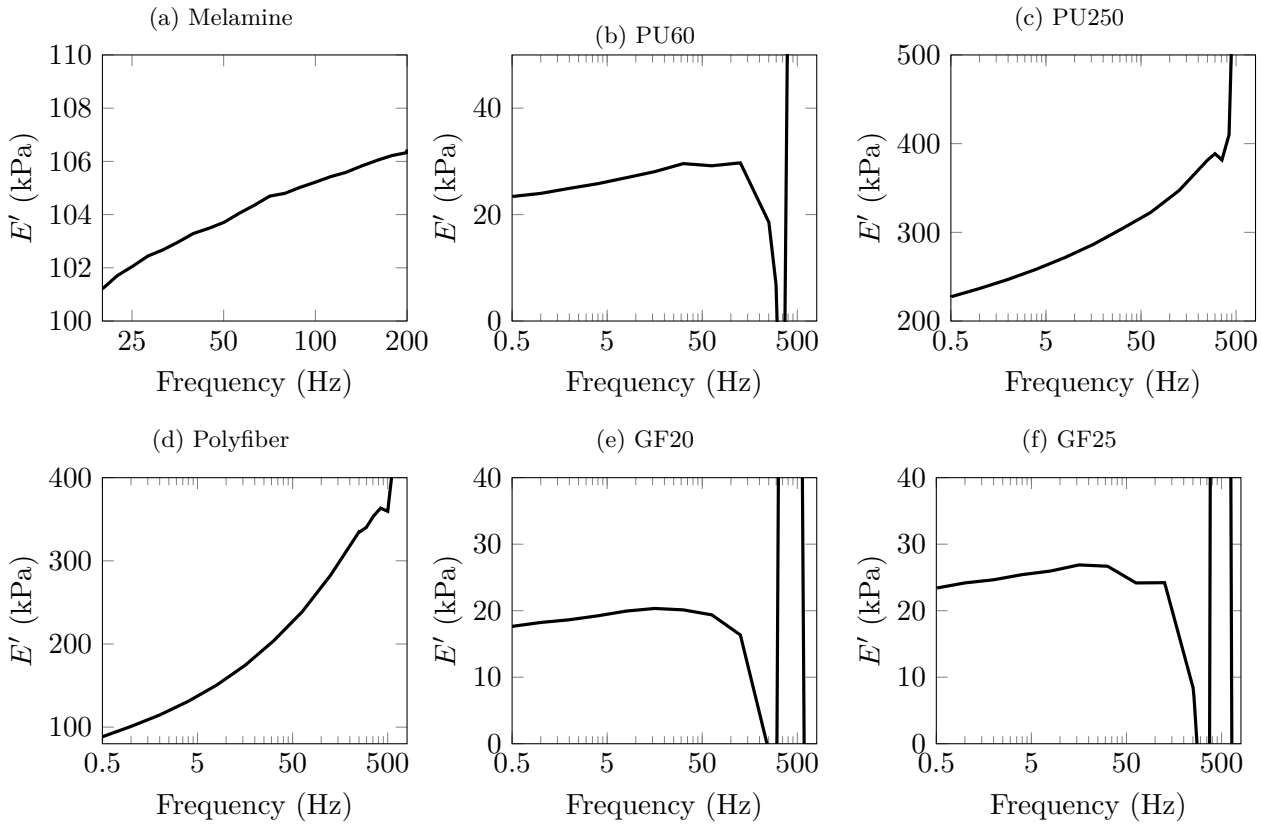

Figure 2.33. Storage modulus E' as a function of frequency measured for the six studied materials on a QMA, at zero prestrain $\varepsilon = 0$ %.

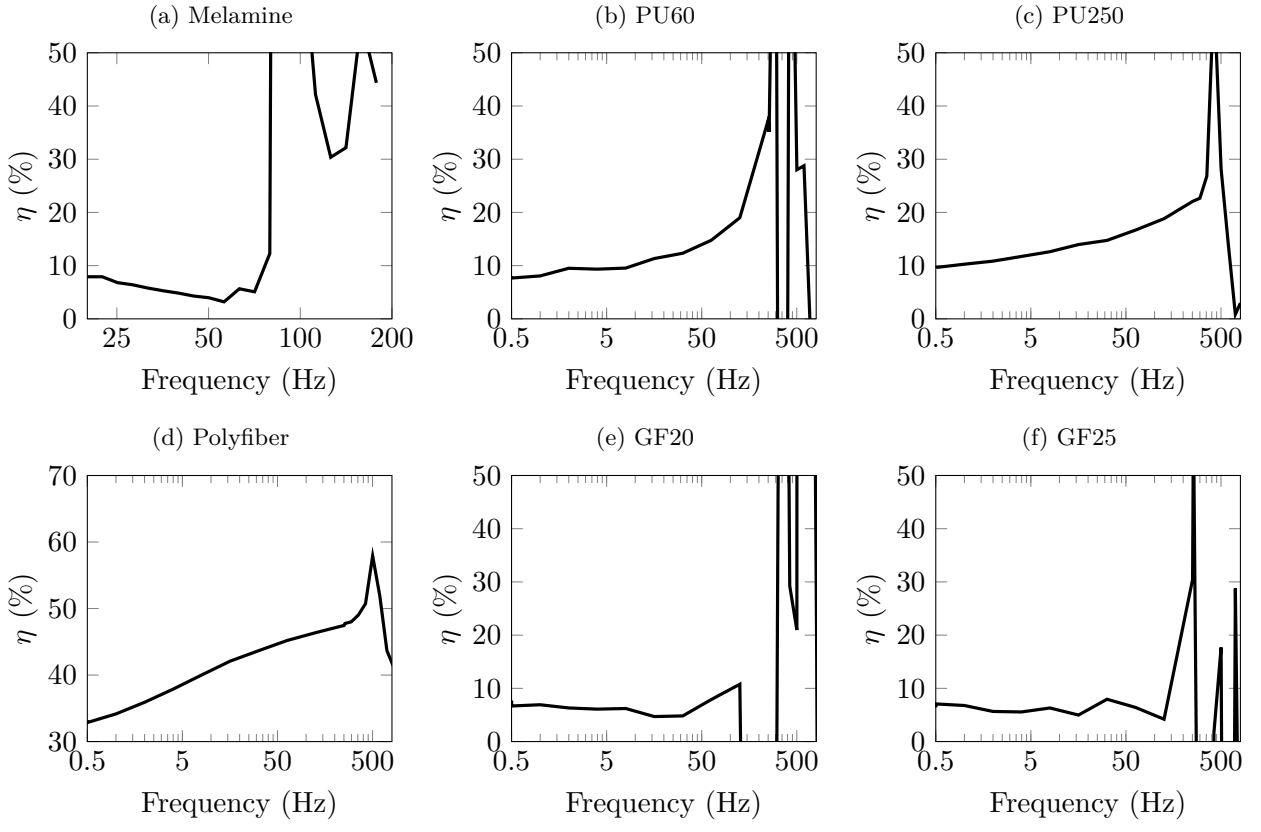

Figure 2.34. Loss factor η as a function of frequency measured for the six studied materials on a QMA, at zero prestrain $\varepsilon = 0$ %.

by Pritz [258] that the frequency variation of mechanical properties are highest for polymers with high loss factors. The studied materials are assumed to be isotropic in these results. Nevertheless, the anisotropy of melamine foam has been highlighted in the literature. For example, Guastavino [259] finds E' between 170 kPa and 300 kPa, and Jaouen et al. [234] finds E' between 180 kPa and 340 kPa, depending on the direction of anisotropy. From our measurements, E' is around 104 kPa for the melamine, which is in the same order of magnitude but slightly less than the results found in the literature. Jaouen et al. [234] also find η around 10 % ±6 % for a static strain of 2 %, which is slightly higher than the results found here of 4.6 %. Overall, the QMA results become unreliable after 100 Hz, possibly due to the resonance of the samples or the bench itself which causes non-physical values for the E' and η. The averaged storage modulus and loss factor results between 0.5 Hz and 100 Hz are reported in Table 2.21.

5.2.2 | Influence of the static preload

The static preload δ_s applied to a sample before characterization has an important effect on sample stiffness. The nonlinear nature of porous cellular materials and their strain-dependant stiffness is caused by their microstructure, which is historically well documented [60, 229, 234, 254, 260, 261, 262, 263]. When compressing a porous sample, several compression stiffness regions can be observed. They are schematized in Figure 2.35. First, for very small strains, the sample experiences partial contact. In this case, the cells or fibres near the surface are not yet fully in contact with the plate. The stiffness increases rapidly with the strain. Second, once all strands of the sample are in contact, there is a linear behaviour of the material for small strains. In practice, this region is very small or even inexistent, since the material quickly enters the buckling regime for foams, or the densification regime for fibrous materials. This is the ideal region to perform QMA measurements in. Third, the material cells or fibres buckle. In this region, the material stiffness decreases strongly, and the stress increases slowly with the strain. The buckling phenomenon can begin even for small strains. This large buckling zone is what grants porous materials high energy absorption characteristics during impacts [13]. For fibrous materials with horizontal fibres, the buckling region can be very small or inexistent, because their compression increases the number of contact points between fibres which causes a densification behaviour [201]. Fourth, the solid phase experiences densification. The cells and fibres of the skeleton come into contact with one another and cannot be compressed further, leading to a rapid increase of the stiffness.

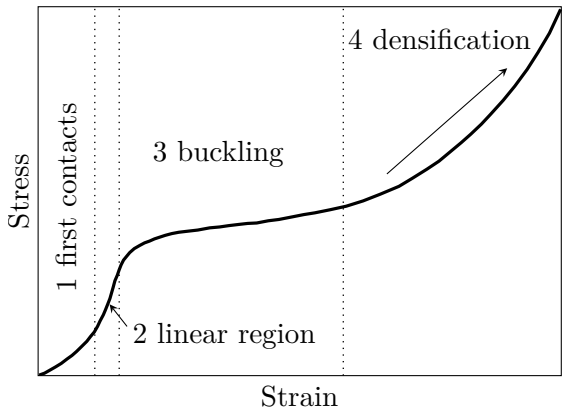

Figure 2.35. Regimes of a porous material subjected to compression.

For best results, the material should be characterized with the same preload as its final use. Chevillotte et al. [251] recommend that the static compression strain ε_s be less than 2 % for foams and 5 % for fibrous materials, and that the dynamic strain ε_d should be an order of magnitude lower

than the static strain of the material in its final use. The dynamic strain amplitude should be high enough to reduce measurement noise as much as possible, however it should be lower than about 0.1 % sample strain to stay in its linear regime [254]. When it is not possible to characterize the material for the same static strain as its final use, it is suggested to measure its properties for different static strains and extrapolate the results to the sought static strain [251, 264]. However, this can be time-consuming and inaccurate due to material nonlinearity. It is also difficult to identify the stress-free position when the sample has an uneven or non-flat surface.

On top of this, the material surface roughness and bonding conditions with the QMA's plates change the measured stiffness for small strains. Sample shape defects due to sample cutting, resulting in a material surface that is uneven (non-planar) and non-parallel to the opposite surface contribute to this error. Chevillotte et al. [251] recommend a static strain of at least 0.5 % to bypass surface irregularity effects. If the sample is glued, the error due to sample surface roughness can be reduced at small strains. However, it adds an extra parameter as a source of uncertainty to the measurement procedure, and destroys the samples when they are removed, making them unusable for further measurements. The boundary conditions that can be obtained for different preloads in Figure 2.36(a). If the sample is not glued, then the position of the top plate without preload, *i.e.* $\varepsilon = 0$ %, is chosen as the first contact of the tallest strands of the sample with the top plate. When the sample is glued to the top plate, full contact can be obtained for any strain, however this results in a non-uniform stress throughout the sample, meaning that part of the sample can be in compression and part of the sample in tension for example. All in all, the uneven surface of samples makes it difficult to identify the position where $\delta_s = 0$.

The effect of the uneven surface is shown in Figure 2.36(b), which plots the stiffness of a PU250 sample as a function of static strain. When the sample is simply placed without glue between the QMA plates, its stiffness gets close to zero when the strain varies from -2 % to 0 %, due to the reduction of the contact surface between the upper plate and the sample. For taped and glued samples, the stiffness instead keeps increasing as the compression strain approaches zero and becomes positive, *i.e.* when the sample is in tension. Overall, both glue and double-sided tape give similar results. For larger compressive strains, there is little difference between glueing the sample or leaving it simply installed. Delgado-Sánchez et al. [265] report that glueing is necessary to determine the elastic modulus for stiff and brittle foams, which is not the case for the studied materials.

Some authors consider that the material properties under no preload are found where the stiffness reaches a maximum as a function of preload [264], which corresponds to a static strain of $\varepsilon = -2$ % in Figure 2.36(b). This position likely corresponds to the smallest strain where there is full contact between the plate and the sample, after which the measured stiffness decreases due to buckling. However, the results in Figure 2.36(b) indicate that when full contact is maintained for a glued sample, the stiffness keeps increasing for strains between -2 % and 0 %. This suggests that the material begins to buckle for very small strains, even when the contact is partial, and that samples should be glued to accurately obtain its properties without preload.

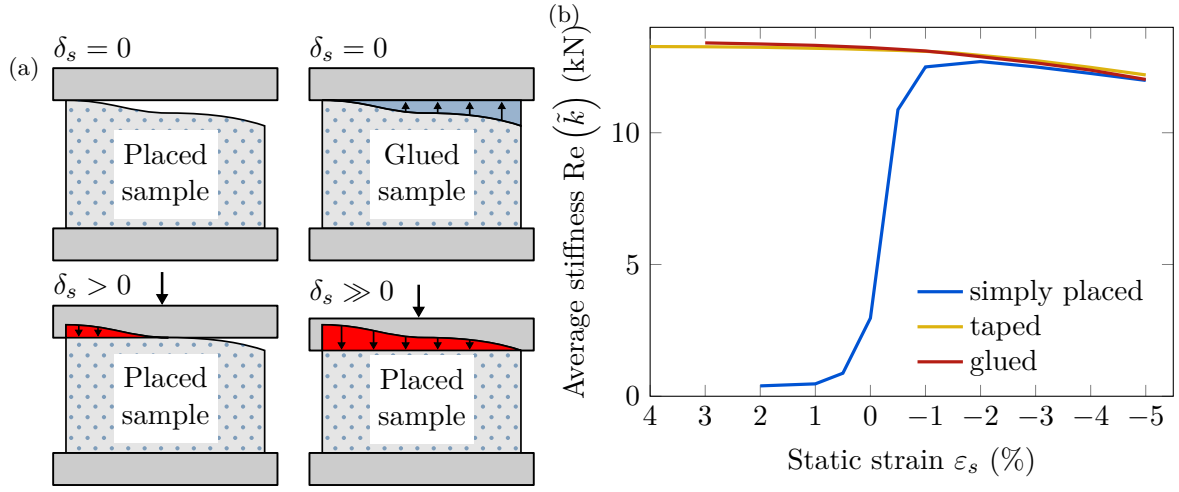

Figure 2.36. (a) Non-uniform contact between the porous material and the QMA plates, (b) Average stiffness between 100 Hz and 200 Hz for PU250 as a function of applied static strain.

5.2.3 | Influence of relaxation

When a sample is compressed to a given strain ε_s, its internal stress changes over time, due to the viscous relaxation within the material. As a consequence, the measured dynamic stiffness $\tilde{k}$ and loss factor η change over time, as shown in Figure 2.37. In these measurements, a melamine sample is compressed to $\varepsilon_s = -5$ % strain and its dynamic stiffness is measured multiple times over 4 days. In these results, the stiffness increases by 5 % after 30 minutes, by 10 % after 1 day, and by 13 % after 4 days. It is difficult to assess the effect of sample relaxation on QMA results, because the measurement process itself is not instantaneous, meaning that relaxation occurs within each measurement, and that it is impossible to measure the material's instantaneous response. Nonetheless, the effect of relaxation becomes significant at long durations, and accounting for it could help improve the accuracy of QMA measurements. Alternatively, performing measurements quickly after compressing the sample can help improve result repeatability. Recent results in the literature observe this phenomenon too, for instance in [266], although relaxation is not suggested as an explanation. The relaxation is observed in the dynamic regime here, however a more detailed analysis and prediction are proposed in Chapter 3 for the relaxation in the static regime.

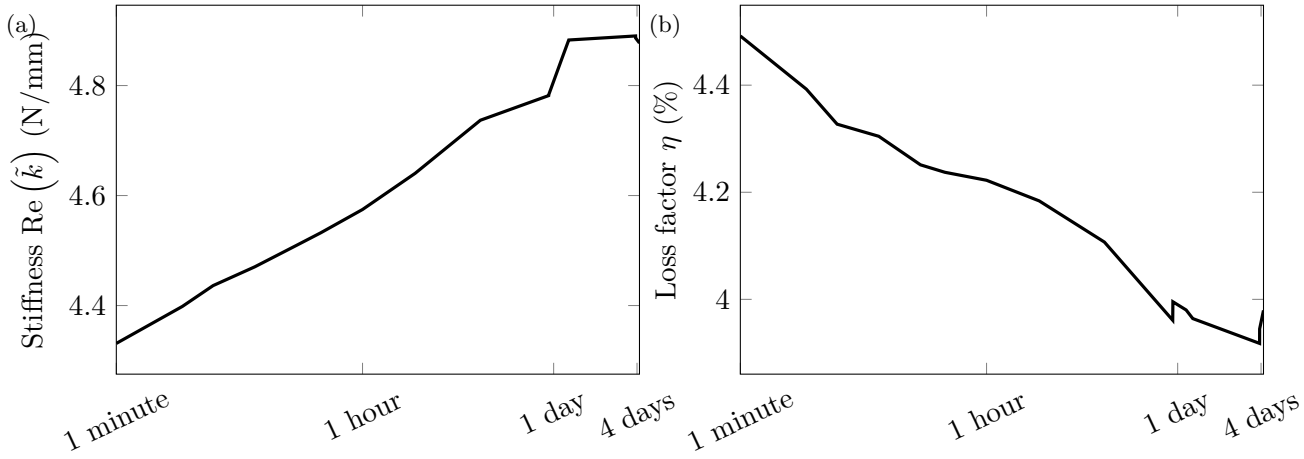

Figure 2.37. Variation of (a) stiffness and (b) loss factor η for QMA measurements of melamine foam with static strain $\varepsilon_s = -5$ % between 20 Hz and 100 Hz.

5.2.4 | Influence of the coupling with the surrounding air

The quasistatic hypothesis requires that the viscous coupling of the porous material with the surrounding air be negligible. However, for material samples which are highly resistive and have a wide aspect ratio $s = \frac{D}{h}$, the viscous effects of the air might not be negligible, even in relatively low frequencies [267]. Etchessahar [65] reports that, for a cubic sample of width 20 mm and modulus 100 kPa, the influence of air appears around 1 Hz for $\sigma = 10^7$ Nsm^{-4}, 10 Hz for $\sigma = 10^6$ Nsm^{-4}, and 100 Hz for $\sigma = 10^5$ Nsm^{-4}. The materials studied in this work are in the order of magnitude $\sigma = 10^4$ Nsm^{-4}, except for the Polyfiber and the PU250 which are in the order of magnitude $\sigma = 10^5$ Nsm^{-4}. For these two materials, especially the Polyfiber which is very thin ($h = 4.6$ mm), the viscous effect of air might not be completely negligible. To check if the effect of air is negligible on QMA measurements of the six studied materials, they were characterized at atmospheric pressure and in a vacuum chamber at 1 % of the atmospheric pressure. Results are not reported here directly, but are presented in Appendix B due potentially unreliable results, caused by a sensor which is not graded for the vacuum. However, these results show that there is no frequency dependence of the results between the atmospheric pressure and the vacuum, indicating that the viscous coupling with the surrounding air can likely be neglected for the studied materials.

6 | Characterization results summary

6.1 | Validity of each characterization method

The various characterization methods for porous materials, which can be categorized into direct and inverse approaches, have distinct advantages and disadvantages over each other. A summary of how well each characterization method works for the sought-after material properties for poroelastic modelling is shown in Table 2.20. Direct methods provide a directly measured value of parameters and can be highly effective when measurement conditions are well-controlled. Each measurement method has sources of error which must be controlled appropriately. For the transport parameters ϕ, σ, and α_∞, direct measurements give the most reliable and trustworthy results.

Inverse methods regroup iterative global minimization methods, micro-macro approaches, and analytic inverse methods. Iterative minimization methods are powerful because they can be used to obtain many parameters at once from a measurement. However, robust parameter adjustment requires a strong sensitivity to these parameters, and it provides no guarantee of finding the physical value of the parameters instead of a mathematical local minimum. Micro-macro methods can be used to relate macroscopic material properties by observing and modelling the material microstructure. These methods have a lot of potential because all material properties can be computed from its known microscopic geometry. However, this is also the weak point of this method, since material microstructure can be polydisperse or require very large RVE simulations. Overall, the microgeometry varies from material to material, which requires a tailored micro-macro methodology for each material. At last, analytic inverse methods can be used to analytically derive some parameters from acoustic measurements. They are helpful for easily measuring properties that cannot be measured directly otherwise, and are therefore commonly used for this purpose. However, they rely on motionless frame material behaviour which is a strong assumption and not always the case in practice.

For the mechanical parameters E', η, and ν, direct measurements are also recommended. The quasistatic method using a QMA has the advantage of giving access to material properties for all frequencies below the sample's first resonance frequency, as well as allowing easy control over the static preload applied to the material before characterization. There are many factors that influence QMA results which require precautions, notably the nonlinearity of the results with respect to the

static strain, the variation of properties over time due to relaxation, and the viscous effects of ambient air and its temperature. Moreover, the determination of the Poisson ratio ν can be unreliable, and can propagate a large error to the determination of the modulus E' for samples that are thin and wide.

Table 2.20. Characterization methods and their reliability for finding poroelastic material properties. ✓: reliable characterization method, ∼: method can be less reliable and requires expertise, ×: method that exists but gives unreliable results in practice.

		Transport parameters						Skeleton parameters			
		σ	ϕ	α_∞	Λ	Λ'	q_0'	ρ_1	E	η	ν
Direct methods	Porosimeter		✓					✓			
	Tortuosity meter			✓							
	Resistivity meter	✓									
	QMA								✓	✓	∼
Inverse methods	Indirect	✓	×	∼	✓	∼	∼				
	Minimization	∼	∼	∼	∼	∼	∼	×	×	×	×
	Micro-macro	∼	∼	∼	∼	∼	∼				∼
Simplifying assumptions			∼	∼	×	×	×				∼

The material properties obtained from a combination of the different characterization methods for the six studied materials are presented in Table 2.21. The most reliable method for each parameter is kept. Chevillotte et al. [251] explain that common practice in the industry consists in the direct measurement of the mechanical parameters, the porosity, and the resistivity, followed by the analytic or minimization inverse methods for the tortuosity, the characteristic lengths, and the thermal permeability. Their results show that the inverse computation of the tortuosity, the thermal characteristic length and the thermal permeability are not always reliable, which is in accordance with the results found in this chapter. Thus, resistivity σ, porosity ϕ, tortuosity α_∞, and density ρ_1 are obtained through direct measurements. Viscous and thermal characteristic lengths Λ and Λ', along with thermal permeability q_0', are obtained through an indirect method. Mechanical properties, which include the storage modulus E', the loss factor η are measured directly. E' and η values are averaged over the range [0.5 Hz, 100 Hz].

Table 2.21. Studied materials' properties.

Final results	h mm	ϕ %	α_∞ -	σ Nsm^{-4}	Λ μm	Λ' μm	q_0' 10^{-9}m^2	ρ_1 kg m^{-3}	E' kPa	η %	ν -
Melamine	29.07	94	1.01	13 838	135.8	277.4	3.0	9.58	104	4.6	0.44
PU60	19.85	94	1.25	[redacted]	29.0	258.0	3.4	54.8	30	10	0.3
PU250	20.93	79	2.45	[redacted]	7.8	170.2	16.2	242.5	296	12	0.3
Polyfiber	4.6	99	1.49	228 728	22.7	22.7	0.6	275.5	143	38	0
GF 20 mm	20.6	94	1.03	[redacted]	48.5	125.2	1.2	65.6	19	6	0
GF 25 mm	24.9	95	1.01	[redacted]	65.6	241.1	1.5	55.3	25	6	0

6.2 | Comparison between predictions from models and measurements

The absorption coefficient of these materials is computed using the transfer matrix method and compared to measurements in an impedance tube in Figure 2.38. It can be noted that absorption coefficients are compared instead of radiation efficiencies, which would better represent the use case of of these materials as acoustic screens. This is due to the experimental difficulties in accurately measuring the radiation efficiency of a porous layer for comparison with a one-dimensional Transfer Matrix model, as explained later in Chapter 4. Thus absorption coefficient measurements allow good control over the measured acoustic behaviour of the materials to validate models.

The agreement between measurements and simulations is quite good, which gives confidence in the validity of the obtained parameters. The prediction of the PU250 foam's absorption coefficient is not very accurate, which highlights the difficulty in properly characterizing this dense and resistive material. Moreover, a frame resonance is observed experimentally for the melamine and the Polyfiber backed by an air gap, but not predicted by the transfer matrix model, which suggests that this resonance originates from the sample mounting condition in the tube. Similarly, the large confidence interval on the PU60 measurements are due to the absorption coefficient being shifted to lower or higher frequencies depending on the sample mounting conditions.

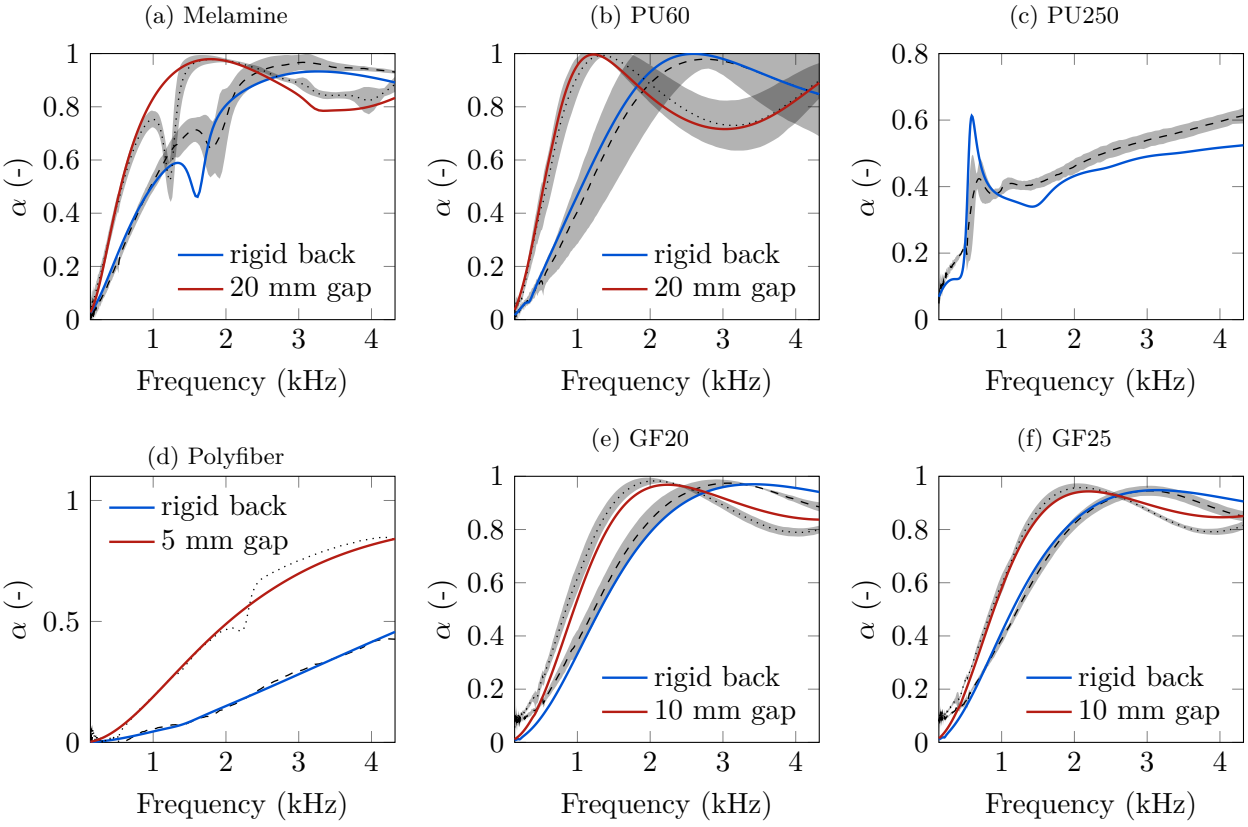

Figure 2.38. Absorption coefficient of the studied materials on a rigid background.

7 | Conclusion

There is a wide range of methods that can be used to characterize porous materials. The various characterization methods were applied in combination with each other to obtain material properties presented in Table 2.21. Their advantages and limits were showcased by applying them to real non-ideal materials. The material properties obtained can be used to model their acoustic behaviour for automotive applications within the SEMPAE project, and the recommendations provided to accurately characterize them can help improve the reliability of future characterization of transport and mechanical parameters.

Some of the transport parameters can be accurately measured through direct methods, however these are not applicable to every transport parameter and sometimes require expertise to minimize uncertainties. Inverse methods can therefore be used to obtain these missing transport parameters. Iterative global minimization methods can be used to find any number of material properties, however they make a strong assumption on the material's behaviour, and they are less likely to result in accurate physical material properties when prior knowledge about material properties is scarce. Micro-macro approaches are powerful but requires reliable knowledge about the material microstructure. The indirect approach, performed from the analytic inversion of impedance tube measurements, is useful to obtain properties that cannot be measured directly, however it requires user expertise to select valid frequency ranges and is unreliable for some of the transport parameters.

Furthermore, a particular effort was put into accurately characterizing the mechanical properties of the materials, and into identifying the sources of error. In particular, applying a preload to the material modifies its stiffness. For this reason, material mechanical properties at small or zero preload are often sought, which requires glueing samples to overcome the effect of surface irregularities. On top of this, the influence of material relaxation affects results increasingly over time, which means that measurements should be performed quickly after compression and within a short time frame to improve repeatability. Material nonlinearity and relaxation are studied in more detail in the static regime in Chapter 3. Relaxation seems to be a major source of uncertainty which is not accounted for in QMA measurements, and modelling it would significantly improve the characterization of compressed samples. The determination of the Poisson ratio is also difficult to perform reliably on porous materials, which is a promising direction to improve the mechanical characterization of porous materials.

Key findings

- Porosity ϕ, airflow resistivity σ, tortuosity α_∞ and density ρ_1 can be measured directly. Characteristic lengths Λ, Λ' and thermal permeability q_0' are computed from inverse acoustical measurements in duct. The analytic indirect method can be used on a restricted frequency range to compute σ and Λ, but is less reliable to compute α_∞, Λ' and q_0'.

- Making simplifying hypotheses to compute some transport parameters from other known transport parameters, such as assuming cylindrical pores or using a simplified 3-parameter model instead of the 6-parameter JCAL model, does not result in a reliable prediction for a wide range of materials, such as materials with high tortuosity, high resistivity and low porosity.

- The quasistatic method for the characterization of E', η and ν allows control over the static preload applied to the material and works in the low-frequency range (approximately 0.5 Hz to 100 Hz), as long as the ambient air's viscosity can be neglected.

- The storage modulus E' and the Poisson ratio ν need to be extracted from the stiffness measured with a QMA. Because ν is often real and frequency independent in practice, and determining it experimentally can be difficult, we can assume a simplified value, however care must be taken for thin and wide samples which are sensitive to the Poisson effect could propagate a large error to the determination of E'.

- Porous material behaviour is intrinsically nonlinear, as its stiffness changes with the static strain. Its experimental measurement is further affected by uneven sample surfaces. Determining the position where static strain is null is difficult, or impossible, when the characterized sample has a rough uneven surface. Samples should be glued to obtain properties under no preload.

- Material stiffness changes over time when it is compressed due to viscous relaxation. Measurements should be performed quickly to improve repeatability.

Chapter 3. Contact stiffness of a rough surface

This chapter studies the impact of macroscopic asperities on the contact stiffness of porous materials, and is derived from an article published in the International Journal of Solids and Structures [268]. This work is a continuation of the article by Hentati et al. [269], which studies the quasi-static stiffness of spherical asperities of melamine foam and found a good correlation with Hertz' law, which is normally applicable to continuous media. In this new work, larger static strains are applied to pyramidal asperities, and nonlinearity and relaxation are accounted for. Further, numerical simulations of the compressed asperities are performed, which require expertise and custom tools. For this reason, this work was performed in collaboration with Jean-Philippe Crété and Stéphane Job from the Quartz laboratory (ISAE Supméca, Saint-Ouen-sur-Seine, France). The numerical model of an indented asperity represented by a network of Kelvin cells in Section 3.3, and by a continuous medium in Section 4.2, was performed by Jean-Philippe Crété. The ageing model described in Section 2.4 and Section 2.5 was elaborated with the help of Stéphane Job.

The article published in the International Journal of Solids and Structures was adapted to this dissertation with additional work performed within the context of the SEMPAE project. Amongst the additions not in the original article submission, a comparison between discrete and continuous surface roughness descriptions is performed in Section 5.2. The application to a real Greenflocks material with a rough surface is added in Section 5.4. This chapter is also complemented by an experimental measurement of the relaxation of SEMPAE materials over time in Appendix C.

1 | Introduction

The surface of porous materials is often uneven. This causes difficulties in predicting the behaviour of the foam at small strains, since this relies on the accurate mechanical properties, and the uneven preload due to surface asperities is often ignored. This surface roughness can exist at different scales, and can result from uneven cutting in Figure 3.1(a) and Figure 3.1(b), manufacturing processes in Figure 3.1(c) or intentional design in Figure 3.1(d). The analysis of these surface asperities is a key to improve our understanding of the compression stiffness of porous materials.

The surface roughness found on the surface of many porous materials is a source of error and difficulty for their mechanical characterization, and probably contributes to the low reliability of these methods found by the round-robin study performed by Bonfiglio et al. [250], in which the characterized modulus can sometimes span several orders of magnitude depending on the laboratory and the method used. Further, material characterization without preload is often sought, but there is no widely accepted procedure to do so, and extrapolation methods suggested by [251, 264] can be difficult to implement because of material nonlinearity, surface roughness, and the difficulty of identifying the strain-free position when the sample has an uneven or non-flat surface. For these reasons, highly inhomogeneous materials such as the Greenflocks in Figure 3.1(c) are difficult to characterize using a Quasistatic Mechanical analyser (QMA) or a Dynamic Mechanical analyser (DMA), for example. Furthermore, the surface roughness influences the prediction of the mechanical behaviour of porous materials when they are installed against rigid walls, which is often the case. This is because the

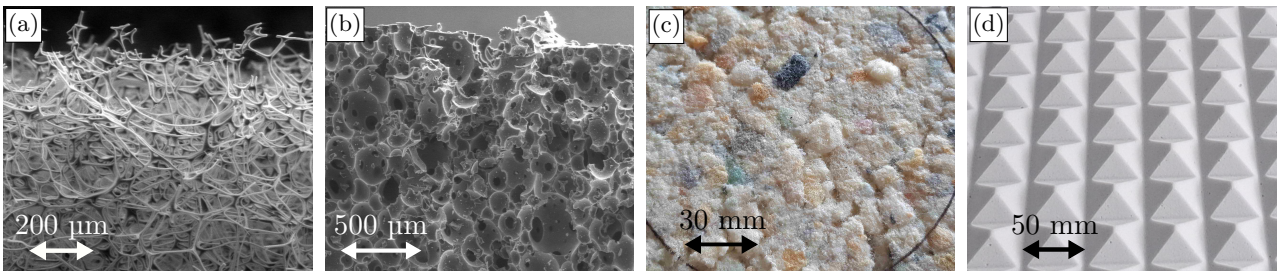

Figure 3.1. Examples of uneven porous material surfaces, due to (a) uneven cutting on an open-cell material (microscopic scale), (b) uneven cutting on a closed-cell material (microscopic scale), (c) industrial manufacturing process (mesoscopic scale) and (d) intentional design for acoustic absorption and aesthetic reasons (macroscopic scale).

inherently irregular surface of porous materials results in partial contact and inhomogeneous preload, which affect the material's effective stiffness in the contact region. Further, the partial contact can be caused by the surface that the materials are placed on, for instance the complex geometry of a car engine being encapsulated.

In short, the mechanical stiffness of a porous material at its contact boundary must be understood to improve its modelling. Guastavino and Göransson [270] observe a soft boundary layer at the contact boundaries of foam samples using 3D image correlation. Dauchez et al. [254] theorize that such a zone could be caused by damaged cells at the surface of the sample when it is cut into shape. Mao et al. [271] model this phenomenon by damaging the struts of the cells composing the material near the sample's boundaries by disconnecting their extremities, to mimic the damage experienced by the material sample when it is cut. However, this method does not account for intrinsic material surface roughness. Marchetti and Chevillotte [272] analyse the stiffness of uniaxially compressed corrugated foam, and observe that the presence of the bumps on the surface modifies the apparent Young's modulus, before transitioning to the bulk behaviour of the material once they are all compressed.

How can the prediction of the compression stiffness of porous materials at small strains be improved by accounting for their surface roughness? The aim of this work is to predict the compression stiffness of macroscopic surface asperities of a rough open-cell material's surface, by accounting for material nonlinearity, relaxation, and asperity geometry. The mesoscopic and macroscopic scales, shown in Figure 3.1(c) and Figure 3.1(d), are considered in this work, and not the microscopic irregularities due to lone strands.

The first step is to evaluate the material's nonlinearity and time dependence, to establish its constitutive laws in Section 2. The nonlinear behaviour can be modelled using a nonlinear constitutive behaviour model, such as a hyperelastic model. The stress relaxation undergone by porous materials over time while under constant strain leads to a significant error over a long duration, and can be modelled using an adapted viscoelastic or an ageing model. The creation of a hyperelastic and the fitting of a novel ageing model allows the determination of the conditions under which the material behaves following its instantaneous response. In this chapter, compression ramps are performed, in which the ramp response of the material is examined and not its dynamic mechanical behaviour. Further, isolated surface asperities are studied in order to disregard the transition to the bulk material behaviour below the asperities.

Then, the prediction of the stiffness of a single ideal pyramidal asperity of melamine foam is performed analytically and numerically and compared with experimental results in Section 3. The validity of a continuous description of the pyramidal geometry is verified. Next, the material nonlinearity is combined with the pyramidal geometry, to study how they interact in Section 4. A single equivalent modulus is found that can be used instead of the real strain-dependent modulus of the material to

obtain satisfying results. In the end, a surface of multiple pyramidal asperities of different heights and a real material with an uneven surface are modelled in Section 5, using a multi-asperity surface roughness model inspired by the Greenwood-Williamson model [273, 274]. The validity of this surface roughness model for an ideal surface composed of a discrete number of asperities is assessed. Its application at small strains to a real Greenflocks material reveals information about the distribution of the asperities on the surface.

2 | Material nonlinearity and relaxation

In this section, the material's constitutive behaviour is examined and modelled. A compression ramp is applied to a cylindrical sample of the studied material to obtain a force-displacement curve, which is turned into a stress-strain curve, in which the material's intrinsic nonlinear and viscous behaviour can be expressed. The stress-strain nonlinearity is modelled using a hyperfoam model. The time-dependant behaviour of the foam reveals a relaxation time that increases with time when the material is at rest. This is well described by an ageing model, which is combined with the hyperelastic behaviour to create an original hyperelastic ageing model. This model is exploited to show that under the right conditions, the material behaves according to its instantaneous response, and therefore its time dependence can be neglected.

2.1 | Compression experimental setup

Experimental compression measurements are performed on an Anton Paar MCR 502 rheometer. Cylindrical foam samples of melamine are placed between two plates, as pictured in Figure 3.2. The top plate compresses the sample, up to around 80 % strain of its initial height $h = 19.3$ mm. The top plate's position relative to the bottom plate and its compression force are measured over time. The temperature is also tracked to ensure stability with respect to thermal dilation and mechanical properties, for instance. The cylindrical sample is taped to the plate so that all the cells at the interface (about 42 000 cells within the 29 mm in diameter cross-section) are in contact with it. Taping the sample rules out effect of surface irregularities, allowing interpreting the deformation of the sample as an effect of its bulk properties only, and avoids any contact detection protocol to determine the reference deformation.

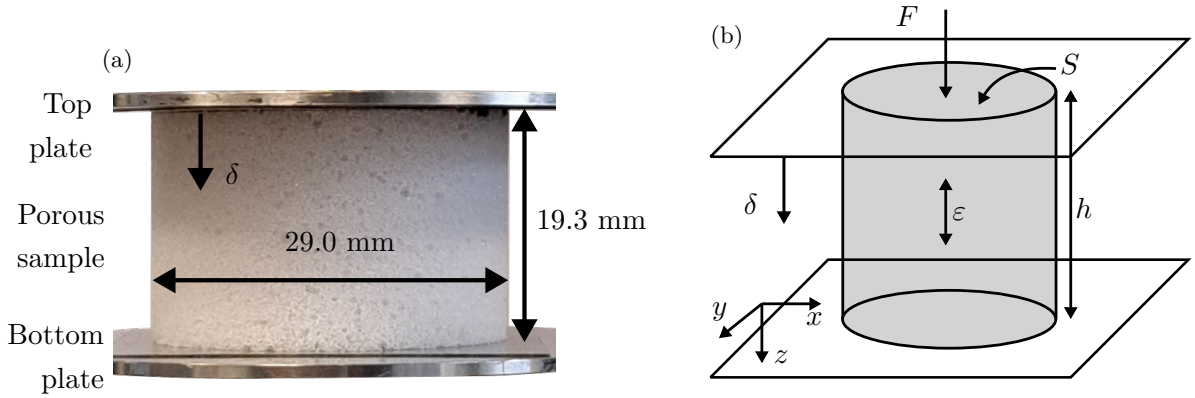

Figure 3.2. Experimental setup to measure the compression force and the compression distance over time. (a) Cylindrical melamine foam sample between the plates of the rheometer. (b) Diagram of a cylindrical sample being indented in uniaxial compression.

2.2 | Material nonlinearity

The relationship between stress and strain is obtained from the measurements to model the material's nonlinearity. The schematic of the uniaxial compression is presented in Figure 3.2(b). The strain is supposed uniform, and nominal stress and strain are used. The axial nominal strain is expressed as

$$\varepsilon = \frac{\delta}{h}, \tag{3.1}$$

and the axial nominal stress is expressed as

$$T_L = \frac{F}{S}. \tag{3.2}$$

δ is the compression distance, h is the height of the cylinder, F is the measured compression force and S is the original cross-section area of the cylinder. Stress-strain measurement results, averaged over 5 samples, are shown in Figure 3.3(a), revealing the nonlinearity between stress and strain. The usual compression regimes of porous materials, as reported by many authors [60, 229, 234, 254, 260, 261, 262, 263], can be identified: the linear bending of the surface strands between 0 % and 2 % strain, the buckling of the cell walls between 2 % and 20 % strain, and lastly the densification of the cell struts above 20 % strain, which becomes much more significant above 60 % strain. The inhomogeneous strain field caused by damaged struts found by Guastavino and Göransson [270] is not accounted for here. It is thus worth noting that defining an elastic modulus from the stress-strain relation relies on an effective feature at the scale of the sample itself.

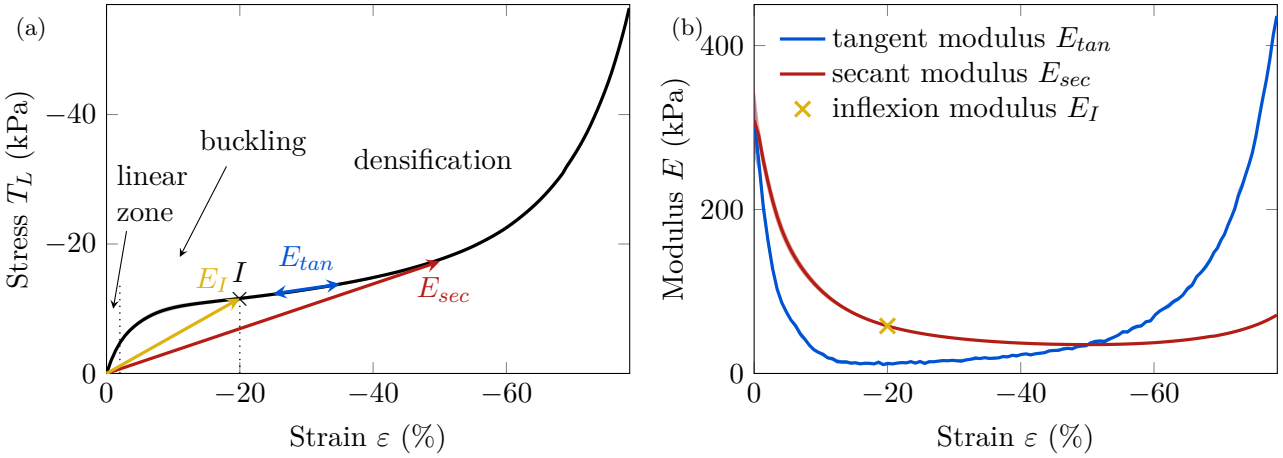

Figure 3.3. Nonlinear regimes of compressed foam averaged over five measurements. (a) Stress versus strain (b) Tangent modulus E_{tan} and secant modulus E_{sec} as a function of strain, and inflexion modulus E_I location.

From these results, several moduli can be identified. The tangent modulus of the material E_{tan} is the slope of the stress-strain curve at a given position, and is obtained as

$$E_{tan}\left(\varepsilon_x\right) = \left.\frac{\partial T_L}{\partial \varepsilon}\right|_{\varepsilon=\varepsilon_x}. \tag{3.3}$$

The secant modulus E_{sec} is defined as the ratio of the stress T_L over the strain ε:

$$E_{sec}\left(\varepsilon_x\right) = \frac{T_L}{\varepsilon_x} = \frac{1}{\varepsilon_x}\int_0^{\varepsilon_x} E_{tan}(\varepsilon)d\varepsilon. \tag{3.4}$$

The tangent modulus E_{tan} and the secant modulus E_{sec} are different, as shown in Figure 3.3(b). Indeed, between 0 % and 20 % strain, the tangent modulus E_{tan} decreases from 290 kPa to 12 kPa

due to cell buckling. It then climbs slowly to 35 kPa at 50 % strain, and then rises sharply to 436 kPa at 80 % strain due to cell densification. Meanwhile, the secant modulus E_{sec} is close to 290 kPa for strains less than 1 %, then drops to below 50 kPa at 25 % strain and 34.7 kPa at 50 % strain, as a consequence of buckling. Then, due to densification, it increases and reaches 72 kPa at 80 % strain.

It is worth noting that quasistatic compression ramps are performed here to obtain the tangent modulus E_{tan}, which can be different from the dynamic tangent modulus, obtained with a QMA for example. This has been shown by some authors [275, 276], as well as some of our measurements which are not presented in this work.

These moduli can help identify the different compression regimes of the material. The inflexion point I at strain $\varepsilon_I = 20$ % represents the minimum of the tangent modulus E_{tan}, *i.e.* $\frac{\partial E_{tan}}{\partial \epsilon} = 0$, and marks the end of buckling and the beginning of densification. It is sometimes called the crush strain in the literature [55, 277]. The secant modulus computed at the inflexion point is $E_I = E_{sec}(\varepsilon_I) = 58.0$ kPa, and will be used as an average equivalent modulus to model the material. Furthermore, the minimum of the secant modulus E_{sec}, *i.e.* $\frac{\partial E_{sec}}{\partial \epsilon} = 0$, indicates what is sometimes called the strain of densification [55, 278], though this strain of densification can have different definitions, as explained by Li et al. [55]. It is found at $\varepsilon = 50.2$ %, and corresponds to the point where the energy absorption efficiency E_s defined by Equation 3.5 [279] starts to increase.

$$E_s(\varepsilon_x) = \frac{1}{T_L(\varepsilon_x)} \int_0^{\varepsilon_x} T_L(\varepsilon) d\varepsilon, \tag{3.5}$$

The nonlinear behaviour of the material can be predicted with a hyperelastic model [280, 281, 282] that is adapted to polymer foams subject to large strains, called the hyperfoam model [283, 284, 285]. It is derived from Ogden's hyperelastic model [286], and it is adapted for these materials because, unlike other hyperelastic models, it predicts a Poisson ratio that stays constant at large strains [287]. It relates the stress and strain through

$$T_L = \frac{2}{\lambda} \sum_{i=1}^{N} \frac{\mu_i}{\alpha_i} (\lambda^{\alpha_i} - J_{el}^{-\alpha_i \beta_i}), \tag{3.6}$$

where N represents the number of terms of the model, $\beta_i = \frac{\nu_i}{1-2\nu_i}$ with ν_i the ith Poisson ratio, $\lambda = 1 + \varepsilon$ the stretch in the compression direction, and J_{el} the elastic volume ratio. For uniaxial strain and assuming a linear relationship between axial and lateral displacement, $J_{el} = \lambda(1 - \nu\varepsilon_1)^2$. Increasing the number of terms N in the hyperfoam model can help improve the fit over the measured data range. An example of fitting the hyperfoam model to a measurement is shown in Figure 3.4, for model orders $N = 1$ and $N = 2$. This shows that using an order $N = 2$ is better at predicting the overall nonlinear behaviour than an order $N = 1$. However, increasing N also increases the risk of failing the Drucker stability condition for different strain values and strain modes, such as uniaxial, equibiaxial, shear or volumetric strains [288]. Since only uniaxial compression is studied here, $N = 1$ is reliable.

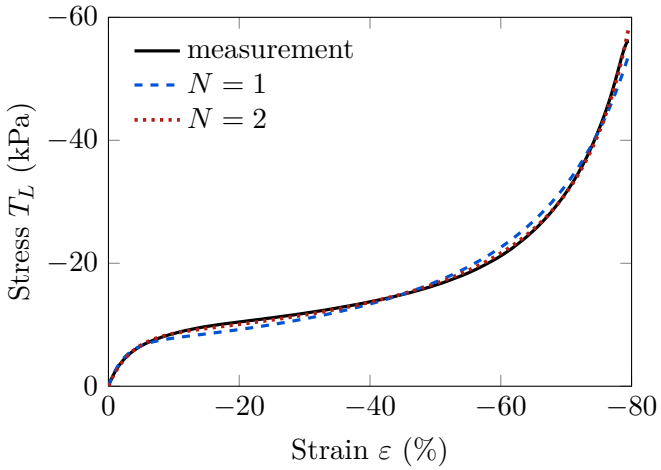

Figure 3.4. Fit of the hyperelastic model on the stress-strain response of a cylindrical sample of melamine, compressed from 0 % to 80 % strain over 26 s. Model orders $N = 1$ and $N = 2$ are compared.

2.3 | Material relaxation

The objective of this section is to predict the time dependence of the material, and find the right conditions to isolate its instantaneous response. When a foam sample is kept at a constant strain, its compression force drops over time. This decay is shown in Figure 3.5 for a sample compressed from 0 % strain to 30 % strain in 12 seconds, after which the strain is kept constant at 30 % strain. The compression force drops by 14.1 % after 1 minute, 20.0 % after 5 minutes, and 40.0 % after 24 hours. Ignoring material relaxation when performing measurements over time can therefore lead to a significant error.

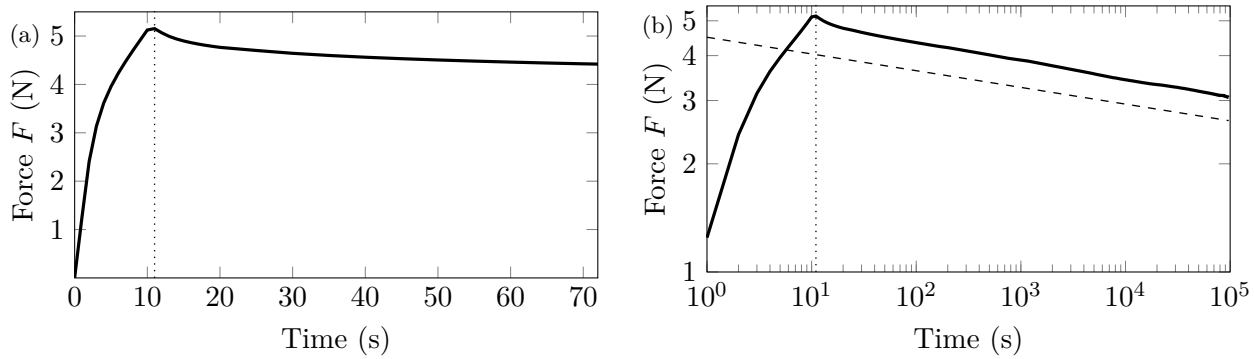

Figure 3.5. Stress relaxation of a compressed cylindrical melamine sample at 30 % strain during (a) the first minute and (b) 26 hours. The vertical dotted line indicates when the stress relaxation at constant strain begins.

Standard protocols to measure the compression stiffness of rubber [289], flexible cellular materials [290], and certain foams in the industry [291] define a sequence of compressions and decompression cycles before taking measurements, resulting in values that incorporate the material's hysteresis. In contrast, our interest lies obtaining material properties which are independent of its loading history. If measurements are performed quickly enough, the instantaneous time response of the material can be captured and its relaxation can be neglected. This is ideal because it is impractical to measure the long-term response of the material due to very long wait times.

However, the stress decay is fastest immediately following compression ramp, which can be seen in Figure 3.5, since the compression force varies as much during the first 5 minutes following the

compression than during the following 26 hours. This is also confirmed by the typical relaxation time of the material $\tau = -F/\dot{F}$ in the relaxation phase, shown in Figure 3.6(a)-(c), which is in the order of 60 s immediately after the compression ramp, and then increases up to 120 hours after 6 hours of relaxation. This suggests that during the compression ramps, the relaxation time might be very short, which makes it more difficult to assert whether the material's instantaneous response cannot be measured experimentally. Furthermore, this relaxation also occurs for different types of porous materials, as presented for the other SEMPAE project materials in Appendix C. It can also be noted that these other material also exhibit a relaxation time that increases with time at constant strain.

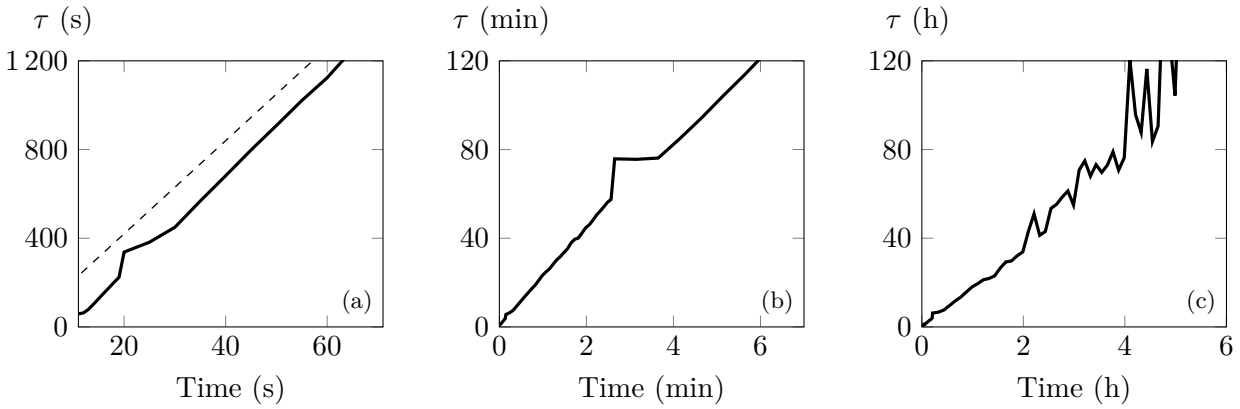

Figure 3.6. The relaxation time $\tau = -F/\dot{F}$ increases linearly with time with a constant slope $a = \dot{\tau}$ at (a) early, (b) intermediate, and (c) long-terms. The dashed guideline in (a), $\tau = at$ with arbitrary $a = 21$, relies on a power law dependency, $F(t) \propto t^{-1/a}$.

A first verification can be performed experimentally, by performing compression measurements at different time scales. When compression measurements are performed for different strain rates, a variation in the measured stress can be observed. This is shown in Figure 3.7, in which cylindrical samples are compressed experimentally for strain rates going from 3.0 $\%\,s^{-1}$ to 3.7×10^{-3} $\%\,s^{-1}$. This corresponds to compression ramps lasting between approximately 26 s and 6 hours (or 21 600 s). The variation in the results can be explained by the viscous relaxation of the material. These measurements reveal that the effect of relaxation on the measured stress can be observed for compression ramps longer than 106 s, whereas compression ramps shorter than 106 s are very similar. Consequently, from these experimental results it is concluded that the instantaneous response can be achieved for compression rates greater than or equal to 1.5 $\%\,s^{-1}$, and in these cases the effect of relaxation can be neglected. In the following, a model to predict the material relaxation is proposed to verify that the measurement conditions allow for it to be neglected.

2.4 | Material relaxation model

Several existing models have been proposed in the literature to encompass the nonlinear stress-strain relationship and the viscous effects of porous materials. Stress relaxation is usually represented using a viscoelastic model. Some authors consider the total stress as the sum of a viscous stress and a hyperelastic stress [292, 293], whereas others combine the two into a rheological model [294, 295]. The material nonlinearity is either represented using a hyperelastic [172, 295, 296, 297] or a polynomial [298] model. The relaxation is either represented on the basis of the generalized Maxwell model [295, 296, 298], a fractional derivative model [172], K-BKZ theory [299] or an empirical time-shift method [300].

However, a typical viscoelastic representation does not seem adapted to this material's observed behaviour. For example, despite an apparent convergence of the time response of the compressed

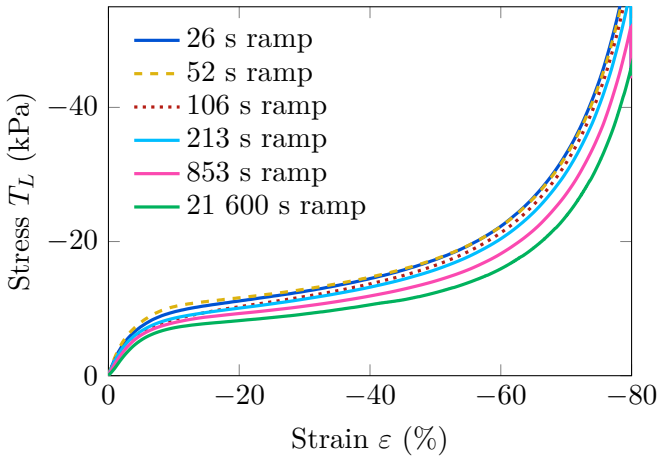

Figure 3.7. Cylindrical sample compression results at different strain rates, resulting in ramps of different durations.

melamine sample to an asymptotic behaviour within one minute of measurement in Figure 3.5(a), it does not reveal an asymptotic limit even over an entire day of measurement in Figure 3.5(b). Further, the typical relaxation time of the material $\tau = -F/\dot{F}$ in the relaxation phase, shown in Figure 3.6(a)-(c), differs noticeably from common viscoelastic models, since the relaxation time is not an intrinsic constant but time-dependent, as for ageing mechanisms [301]. The observed behaviour does not reveal a classical exponential decay as a function time, $F(t) \propto \mathrm{e}^{-t/\tau}$, but instead a power law $F(t) \propto t^n$ with some exponent n, as shown in Figure 3.5(b). Such a behaviour is characteristic of an ageing mechanism, which can be thought of as a linearly increasing relaxation time, $\tau \propto t$. The main concern with such mechanisms is determining the dynamics at short times, during which the material is fresh and highly reactive, that is to say $\tau \sim 0$ when $t \sim 0$.

A model adapted to the studied foam must be chosen, and these observations can be linked to ageing mechanisms that describe a continuously time varying decay rate. For instance, the ageing model described by Derec et al. [302] relates the stress rate $\dot{T}_L$ to the strain rate $\dot{\varepsilon}$ by introducing a history-dependent fluidity term f. Espíndola et al. [303] suggest a simplified expression of the fluidity f resulting in

$$\begin{cases} \dot{T}_L = -f T_L + E_0\,\dot{\varepsilon} \\ \dot{f} = -a f^2 + r\,\dot{\varepsilon}^2, \end{cases} \tag{3.7}$$

where E_0 is an elastic modulus, a is a parameter representing material ageing (decrease in f, or increase in relaxation time over time) and r is a parameter representing material rejuvenation (increase in f, or decrease of relaxation time over time). In the case where $f = \frac{E_0}{\eta_0} = \text{const}$, this model is equivalent to a Maxwell model with a constant relaxation time, where η_0 stands for the viscosity of the Maxwell model's dashpot. The second line of Equation 3.7 is the evolution equation of the fluidity f, which is the inverse of a relaxation time, $\tau = \frac{1}{f}$, and holds information related to the memory of the system. When the strain rate $\dot{\varepsilon}$ is null, the relaxation time increases linearly with time proportionally to the ageing parameter a, $\tau \propto at$, which is in close agreement with observations shown in Figure 3.5. When the material is being deformed, that is to say $\dot{\varepsilon} \neq 0$, the relaxation time τ decreases according to rejuvenation parameter r.

Considering the fact that the instantaneous response of the foam is hyperelastic, the hyperelastic component is integrated into the ageing model described by Espíndola et al. [303] by replacing the constant modulus E_0 with the strain-dependant secant modulus E_{sec}. This results in an ageing hyperelastic model, described by Equation 3.8, with a rheological representation sketched in Figure 3.8.

$$\begin{cases} \dot{T_L} = -fT_L + E_{sec}\,\dot{\varepsilon} \\ \dot{f} = -af^2 + r\,\dot{\varepsilon}^2, \end{cases} \tag{3.8}$$

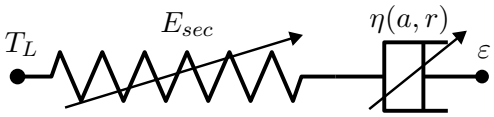

Figure 3.8. Schematic representation of the ageing model. The nonlinear dashpot represents the nonlinear time dependence of the ageing model, and the nonlinear spring represents the hyperelastic response of the material.

2.5 | Application of the ageing hyperelastic model

The new ageing hyperelastic model described by Equation 3.8 is applied in this section, and its parameters are determined from the experimental data. First, the parameter a can be obtained when the strain rate $\dot{\varepsilon}$ is null in Equation 3.7, in which case the relaxation time increases linearly with slope a:

$$\tau = \frac{1}{f} = at + \text{cste} = \frac{-T_L}{\dot{T_L}}, \tag{3.9}$$

where the constant is irrelevant at this stage and represents the initial relaxation time τ when the relaxation begins. In short, a is computed as the slope of $\frac{-T_L}{\dot{T_L}}$ when the strain rate is null, as shown in Figure 3.6(a)-(c) for instance.

Second, the hyperelastic parameters are obtained from the instantaneous response of the material, that is to say when the compression rate $\dot{\varepsilon}$ is high enough, for instance from the fastest ramp of 26 s, which is considered as an instantaneous response. The hyperelastic parameters (α_1, μ_1, ν_1) are obtained by a least squares curve fitting on the experimental stress-strain curve.

Third, the remaining parameter r can be found from compression ramps of different durations, as those shown in Figure 3.7. These compression ramps must last long enough for the effect of relaxation to be visible during the compression ramp. Compression ramps from 0 % to 80 % strain lasting between 26 s and 21 600 s were used to fit the parameter r. The parameters obtained for the hyperelastic ageing model are presented in Table 3.1. It is interesting to note that the Poisson ratio found is close to 0, indicating that the overall Poisson effect is small. Similar results for foams undergoing large strain can be found in the literature [57, 263, 292], even though the Poisson ratio is strain dependant in reality [304, 305].

Table 3.1. Parameter values obtained for the hyperelastic ageing model used to represent the studied material's behaviour, averaged over several measurements. The 95 % confidence intervals obtained from fitting the results on several measurements are given.

Hyperelastic parameters			Ageing parameters	
α_1	μ_1 (kPa)	ν_1	a	r
104.8	122.8	0.020	17.8	3.42
±36.6	±48.0	±0.009	±7.0	±3.39

The predictions from the hyperelastic ageing model are compared to a measurement in Figure 3.9, for the fastest ramp of 26 s. The strain ramp over time is shown in Figure 3.9(a), and the measured stress is shown in Figure 3.9(c), which displays a nonlinear behaviour during the loading and stress relaxation when the strain is held constant. The modelled stress response, shown in Figure 3.9(c),

exhibits a similar behaviour to the measured response. Notably, both the nonlinear behaviour and the time-dependent relaxation of the material are captured by the proposed hyperelastic ageing model. The difference between the measurement and the model can be due to the heterogeneity between samples, since the hyperelastic ageing model is fitted on the average behaviour of several samples and compared with the measurement on a single sample. It can also be explained by the difficulty to obtain a good fit of the hyperelastic behaviour on a wide strain range, since the fit yields a good average behaviour, but can be different from the measurement at the extremity at high strains. Overall, the goal of this model is to encompass the hyperelastic behaviour of the material as well as the continuously varying relaxation time observed experimentally, but not necessarily to predict the stress in response to a given strain over time quantitavely.

The instantaneous response computed from the ageing hyperelastic model is also plotted, which reveals that it is quite close to the predicted time-dependent for this 26 s compression ramp. The mechanical relaxation time (inverse of the fluidity f) of the material is plotted in Figure 3.9(b), which shows that the minimum value it reaches is around $\tau = 104$ s, which is greater than the duration of the ramp of 26 s. This indicates that the material relaxation has a weak effect during the compression phase at this strain rate. In conclusion, material relaxation can be safely neglected when the compression ramp is fast enough, which is the case for this 26 s long, or 3.2 % s^{-1}, strain ramp, which confirms experimental results shown in Figure 3.7.

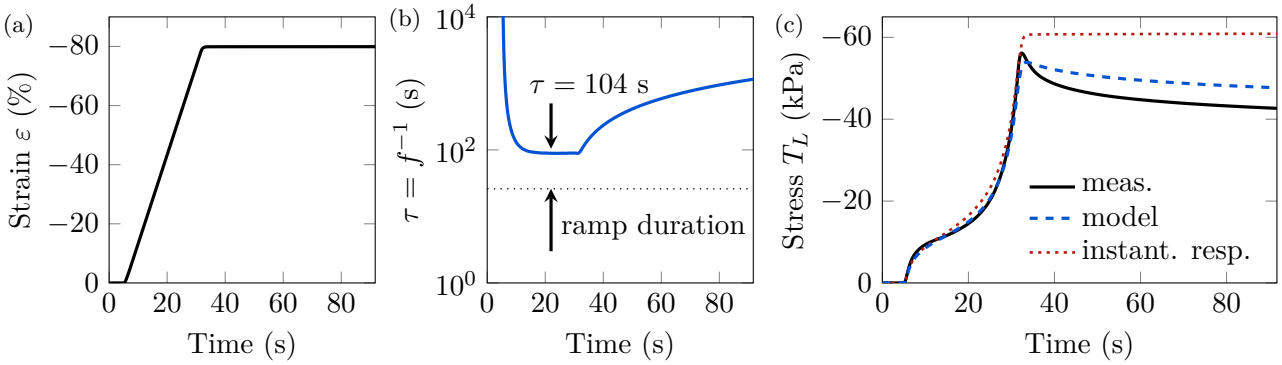

Figure 3.9. Comparison of the ageing model with measurements for a compression ramp of 0 % to 80 % strain over 26 seconds. (a) Strain applied over time. (b) Modelled material relaxation time over time, compared with the characteristic time of the compression ramp. (c) Measured and predicted stress over time. The modelled instant response is also shown. Average parameters from Table 3.1 are used, except for $r = 2.49$ which is obtained from a 26 s ramp measurement.

2.6 | Comparison with a hyperviscoelastic model

A classical viscoelastic model to predict the relaxation of the material is explored in this section. A Prony series is used in combination with the hyperfoam model to showcase its capabilities and its limits. A slightly different approach than before is used to fit a hyperfoam model. The Poisson ratio is enforced to be $\nu = 0$, due to its value close to 0 found above. Consequently, a higher number of terms $N = 3$ is used for the hyperfoam model, instead of $N = 1$, which improves the prediction of the stress-strain relationship when the value of the Poisson ratio is fixed, despite increasing the risk of obtaining a numerically unstable model.

Next, the hyperfoam model can be fit either from the instantaneous response of the material, meaning the sum of all springs $\sum_{i=1}^{N} E_i$ in the generalized Maxwell rheological model (see Figure 1.5(b)) is hyperelastic, or from the long term response of the material, meaning only the long term spring E_0 is hyperelastic. The difference between these two hypotheses is whether the viscoelastic time-dependant

part of the material depends on the hyperelasticity of the material (hyperelastic instantaneous response) or not (hyperelastic long term response). This distinction is not explored in detail in this work, and both hypotheses are tested.

2.6.1 | Viscohyperelastic prediction using the instantaneous material reponse

First, the hyperelastic model is fitted based on the instantaneous response of the material from a 26 s ramp. The result of this fit is shown in Figure 3.10(a). The hyperfoam fits the measurements much better for $N = 3$ than $N = 1$ or $N = 2$. The parameter values of this hyperfoam model are shown in Table 3.2. Next, a viscoelastic Prony series is fitted to measurements to predict the time-dependant behaviour of the material. The compression of a cylinder of melamine foam is modelled using finite elements, to match the experimental compression distance over time at different strain rates. A viscoelastic material described by a Prony series with $N = 5$ terms is applied to the cylinder, which is commonly used for porous media in the literature. The instantaneous time response of the material is characterized by the instantaneous modulus $G_{inst} = G_0 + \sum_{i=1}^{N} G_i$. The terms of the hyperfoam model obtained from the material's instantaneous response are shown in Table 3.2.

Table 3.2. Parameters used in the 3-term hyperfoam model obtained from the material's instantaneous response, and parameters of the 5-term Prony series obtained for a wide range of deformations.

Hyperfoam model			
α_i (-)	20.1	25.0	-5.2
μ_i (kPa)	-20.0	36.2	4.86×10^{-3}
ν_i (-)	0	0	0

Prony series terms					
G_{inst} (kPa)	160				
G_i (kPa)	0.288	15.729	18.561	0.073	14.208
τ_i (s)	0.0966	54.0	579.8	21.1	853.9

The compression force of the cylinder computed numerically is compared with experimental results in Figure 3.10(b), for compression ramps lasting between 26 s and 6 hours from 0 % to 80 % strain. The difference between the predicted and measured stresses is due in large part to the heterogeneity between samples. The results show that it is possible to predict both the time dependant and nonlinear behaviour of the compressed melamine material by combining a hyperfoam model with a viscoelastic Prony series.

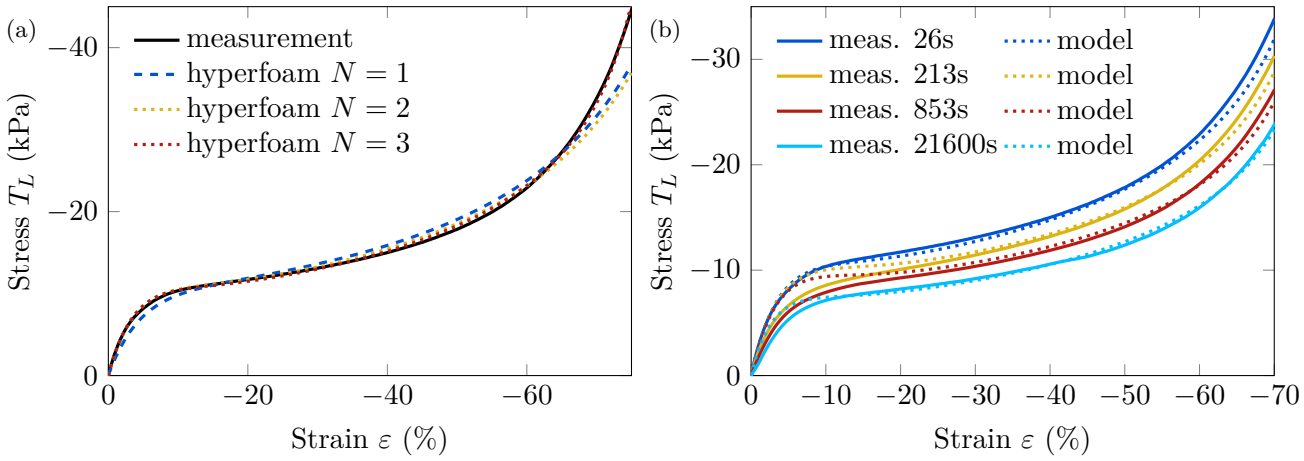

Figure 3.10. (a) Hyperfoam model fit to the measured instantaneous stress-strain relationship obtained for a 26 s long compression ramp, with $N = 1$ to $N = 3$ terms and $\nu = 0$. (b) Hyperfoam Prony series model which combines the nonlinear stress-strain relationship with the relaxation, fit between 0 % and 80 % strain.

2.6.2 | Comparison with QMA results using the long-term material reponse

The viscoelastic Prony series model is fitted on experimental results which give information on a restricted time or frequency range. It would be interesting to see if it is possible to extrapolate this data outside of the experimental time or frequency range. To evaluate this hypothesis, the Prony series is analysed in the frequency domain, in which it can be compared with QMA results on the same material. A focus on small strains ε less than 20 % is therefore made in this section. Consequently, the hyperfoam model is fitted from the long term response of the material for the 6-hour-long compression ramp, since this long term response gives a better prediction of the stress than the instantaneous response does in the small strain range $\varepsilon < 20$ %. The resulting hyperfoam and Prony series parameters are given in Table 3.3, and the comparison with experimental stress-strain relationships are shown in Figure 3.11.

Table 3.3. Parameters used in the 3-term hyperfoam model obtained from the material's long-term response, and parameters of the 5-term Prony series obtained for a small strains of less than 20 %.

Hyperfoam model			
α_i (-)	10.2	13.5	-2.9
μ_i (kPa)	-91.5	161.7	45.5
ν_i (-)	0	0	0

Prony series terms					
G_{inst} (kPa)	242.7				
G_i (kPa)	136.9	23.38	9.102	0.421	2.660
τ_i (s)	0.2307	9.194	291.5	120.4	1714.6

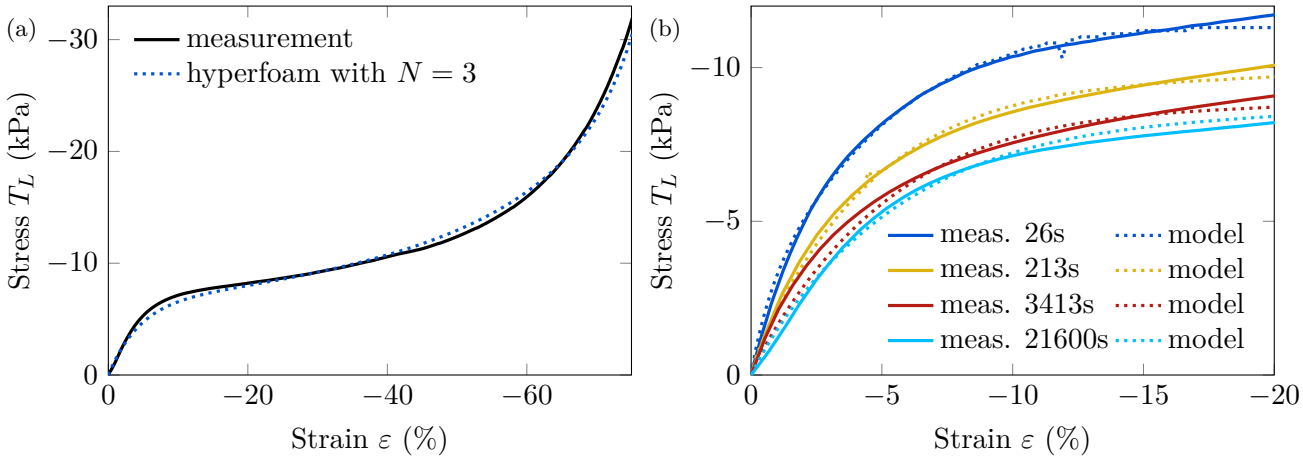

Figure 3.11. (a) 3-term hyperfoam model fit to the measured long-term stress-strain relationship obtained for a 6-hour-long compression ramp, with $\nu = 0$. (b) Hyperfoam Prony series model which combines the nonlinear stress-strain relationship with the relaxation, fit between 0 % and 20 % strain.

The frequency-dependant storage modulus E' and the loss factor η of the melamine foam are then computed as a function of frequency. This is done by computing the storage shear modulus G' and the loss shear modulus G'' from [288, 306]

$$G' = G_{inst} - \sum_{i=1}^{N} G_i \left(1 + \frac{\tau_i^2 \omega^2}{1 + \tau_i \omega^2}\right), \tag{3.10}$$

$$G'' = \sum_{i=1}^{N} \frac{G_i \tau_i \omega^2}{1 + \tau_i^2 \omega^2}. \tag{3.11}$$

The storage and loss moduli E' and E'' are computed from $\tilde{E} = 2\tilde{G}(1+\nu)$. The results are plotted in Figure 3.12.

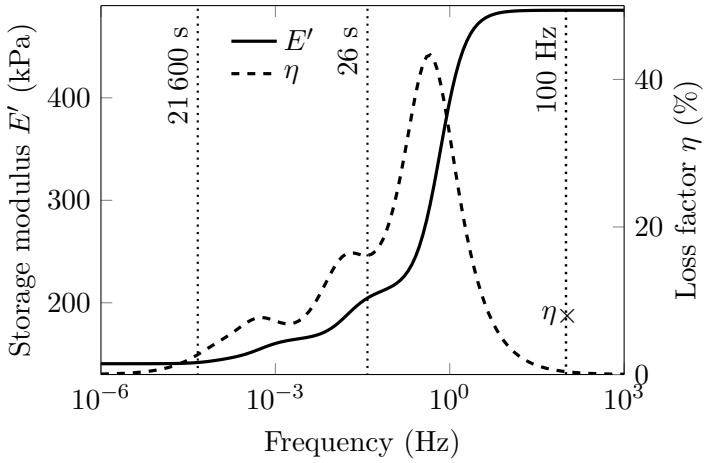

Figure 3.12. Storage modulus E' and loss factor η as a function of frequency computed from the hyperfoam Prony series.

At 100 Hz, the storage modulus computed from the Prony series is $E' = 485.5$ kPa, and the loss factor is $\eta = 0.39$ %. The storage modulus found this way overestimates the storage modulus found experimentally, which is in the order of $100-200$ kPa. Conversely, the Prony series underestimates the loss factor of the melamine foam, which is around $\eta = 5$ %. This can be understood by noticing that the damping peaks in Figure 3.12 are located for frequencies lower than the QMA frequency range around 100 Hz. This indicates that the relaxation times of the Prony series τ_i are too high, which makes sense because the Prony series was fitted on measurements lasting between 26 s and 21 600 hours, whereas the 100 Hz range corresponds to times of 10^{-2} s. This explains the overestimated storage modulus E' and underestimated loss factor η at 100 Hz.

In short, this illustrates how the viscoelastic behaviour computed by fitting a Prony series over the static compression ramps performed in this work, which are ramps of 0 % to 80 % strain within time range of 26 s to 6 hours, cannot be directly extrapolated to the dynamic regime, as characterized with a QMA. This is because they represent two very different time or frequency ranges.

3 | Compression stiffness of a pyramidal geometry

The behaviour of a single pyramidal asperity is analysed in this section. First, the open-cell microstructure of the porous material is modelled and compared with the expected analytic results for a pyramidal geometry. Then, the material hyperelasticity is combined with the pyramidal geometry to shed light on the interaction between the shape and the material nonlinearities.

3.1 | Description of the pyramids obtained experimentally

Pyramidal asperities are compressed experimentally to obtain the relation between force and compression distance for a single asperity. The same compression measurement setup is used as for the cylindrical samples described in Section 2.1. Square-base pyramidal asperities are used because they allow for easy and repeatable creation in high numbers from a sheet of melamine foam, whereas there are no practical methods to create several spherical asperities as studied by Hentati et al. [269]. Pyramid samples are compressed with strain rates high enough that the material's response is considered instantaneous, and can be represented with a hyperfoam model.

The pyramid tips are supposed to be pointy, however due to imperfections in the cutting process and the microstructure of the material, there is an uncertainty on the tip width w_0 in the same order of magnitude as the foam's cell size h_0 and ligament length l: $w_0 \sim h_0 \sim l$. Since this bias is at the edge of a continuous description of the pyramids, it is assumed to have a negligible effect at the macroscopic scale, such that $w_0 = 0$. The cell size h_0 for melamine foam is found between 0.10 mm and 0.15 mm by Kino and Ueno [147], and between 0.1 mm and 0.2 mm by Hentati et al. [269], both estimations being obtained from independent scanning electron microscopy measurements. In the frame of our study, we chose $h_0 = 0.125$ mm as a fair value lying in both intervals, to identify the effects related to the cell size of melamine foam in dimensionless quantities.

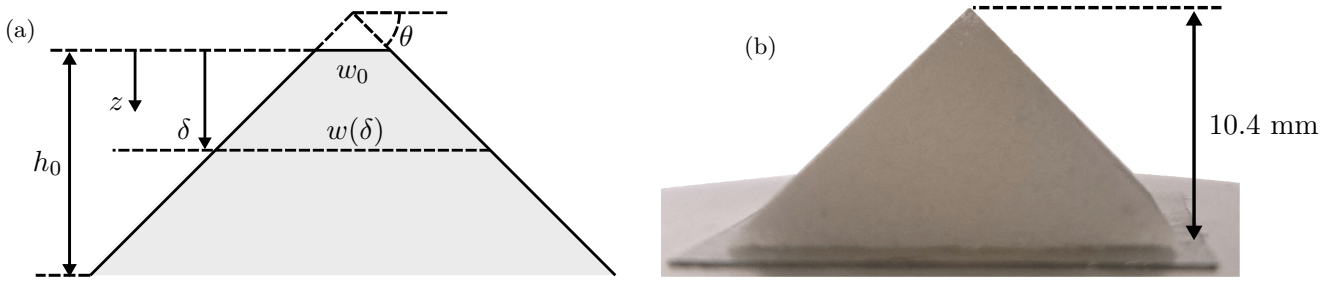

Figure 3.13. (a) Diagram of a truncated pyramid being indented. (b) Picture of a pyramid being tested.

3.2 | Analytic representation

The expected tendency of the compression force of an indented continuous pyramid can be approximated using geometrical considerations. Using geometrical arguments only, Hooke's law states that the pyramid's compression force F per unit of contact area $S_{pyr}(\delta)$, is proportional to an elastic modulus E and the strain $\varepsilon(\delta)$:

$$\frac{F(\delta)}{S_{pyr}(\delta)} \propto E\,\varepsilon(\delta). \tag{3.12}$$

The cross-section area $S_{pyr}(\delta)$ of the pyramid at compression distance δ is computed as

$$S_{pyr}(\delta) = w^2(\delta), \tag{3.13}$$

where $w(\delta)$ is the length of the sides of the cross-section :

$$w(\delta) = w_0 + \frac{2\delta}{\tan(\theta)}, \tag{3.14}$$

where w_0 is assumed negligible in our case. Further, the strain ε is proportional to the compression distance δ:

$$\varepsilon \propto \delta. \tag{3.15}$$

Therefore, combining Equation 3.12 to Equation 3.15 provides a tendency of the compression force for the pyramid as

$$F \propto \frac{E}{\tan\theta}\delta^2. \tag{3.16}$$

In this case, the force F increases quadratically with the compression distance δ, which confirms findings by several authors that pyramidal indenters behave similarly to cones in contact mechanics, which also behave as $F \propto \delta^2$, up to a small correction factor [307, 308]. This model is oversimplified since it only accounts for the geometry of the pyramid. Nonetheless, iterestingly, this naive geometric

model provided agrees with the exact prediction of the compression force F of a pyramid being indented by a rigid plane by an amount δ [309, 310]

$$F = \frac{4}{\pi\sqrt{\pi}} \frac{E^*}{\tan\theta} \delta^2, \tag{3.17}$$

where $E^* = \frac{E}{(1-\nu^2)}$ is the effective elastic modulus of the material and ν is its Poisson ratio. In other words, the resulting force is expected to evolve quadratically with the compression distance δ, and its magnitude is driven by a prefactor $\frac{E}{\tan\theta}$ which is proportional to a material modulus E and inversely proportional to the pyramid angle $\tan\theta$.

3.3 | Numerical open-cell microstructural model

A finite elements model is created to accurately represent the 3D stress and strain undergone by an indented pyramidal sample made from an open-cell material. This model represents the microstructure of the porous network using Kelvin cells. It attempts to capture the nonlinear phenomena of the material through its microgeometry, such as the initial contacts with an indenting plate, involving the progressive recruitment of a finite number of free ligaments and struts near the foam's surface and their buckling at large strains. The mesh of the microstructure for a pyramidal asperity is shown in Figure 3.14.

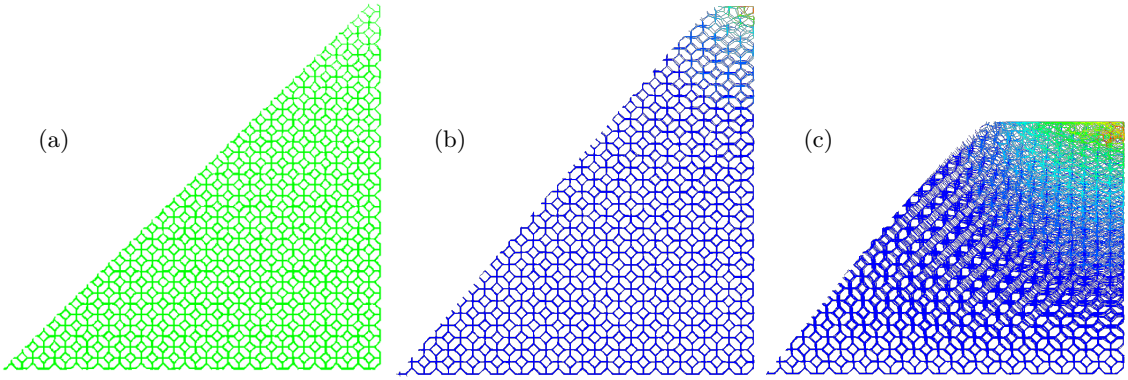

Figure 3.14. Meshes of the numerical model of the pyramid with a microstructure of Kelvin cells. Quarter-pyramids are modelled by exploiting the problem's symmetry. (a) Slice of the FEM model composed of approximately 1 185 Kelvin cells. (b) Deformation of the Kelvin cell FEM pyramid at $\delta = 1$ mm, *i.e.* $\delta/h_0 = 1.7$ and approximately 15 cells in contact, and (c) $\delta = 4$ mm, *i.e.* $\delta/h_0 = 7.0$ and approximately 247 cells in contact.

The open-cell microstructure is modelled using distorted Kelvin cells [229], composed of beam elements with circular sections, using the same modelling approach as Hentati et al. [269]. Material parameters and cell properties are presented in Table 3.4. The cell height is the same as the M7 polyurethane foam in reference [209] and the strut length and radius are from references [211, 311]. The aim of this numerical model is to be qualitative. Consequently, its specifications (cell size, elasticity) describe a typical open-cell foam but do not match the melamine foam used in this study quantitatively, and the results are examined as dimensionless relative to the cell size. Matching quantitatively the parameters of this model to the specifications of the sample is a matter of adjusting a prefactor, it thus brings less understanding than analysing the trends qualitatively.

Rayleigh damping $(\alpha_R, \beta_R) = (0, \tau_R)$ is introduced in the beams' response to improve computation convergence. A viscous relaxation time, $\tau_R = 10^{-4}$ s, relying on the beam material is imparted by adding a viscous-like damping stress tensor $\boldsymbol{\sigma_d} = \tau_R \boldsymbol{D}\dot{\boldsymbol{\varepsilon}}$ to the elastic tensor, with $\dot{\boldsymbol{\varepsilon}}$ the strain rate tensor and $\boldsymbol{D}$ the elastic constitutive tensor. The value of τ_R is chosen much smaller than the loading

duration of the sample ($\tau_L > 10$ s), such that the damping has no other effect than accelerating the numerical convergence, by filtering spurious and unphysical high-frequency artefacts (*e.g.* when light and stiff submillimetric edge ligaments go into resonance). Each strut is composed of two aligned B32 Timoshenko beam elements. A uniformly distributed random displacement, ranging within ±7.5 % of the strut lengths, *i.e.* ±15.2 µm, is applied to each node's position. No contact between beams is considered, meaning that the densification of the material is not represented at large strains. An implicit numerical time integration scheme is used.

Table 3.4. Parameters used in the microstructural Kelvin cell FEM model.

Avg. cell height	h_0	0.574 mm
Avg. beam length	l	0.203 mm
Beam radius	r_0	0.021 mm
Elastic modulus	E	3000 MPa
Poisson ratio	ν	0.38
Mass density	ρ	1300 kg m^{-3}
Mass damping	α_R	0
Stiffness damping	β_R	1.10^{-4}

The pyramidal shape is created by intersecting a wide parallelepipedic lattice of Kelvin cells with a pyramidal geometry of total height $h = 10.0$ mm and of side angle $\theta = 50$ ° using a Python routine. An angle $\theta = 50$ ° is used in the FEM model, instead of 45 ° for the pyramids created experimentally, to break up the symmetry stemming from the repetition of the Kelvin cells pattern along the side of the pyramid at 45 °. The resulting pyramid of Kelvin cells is indented against a rigid plane by an amount $\delta = 5$ mm. The frictionless contact between the cell struts and the rigid plane is handled by Abaqus software. Finally, only a quarter of the pyramid is created by exploiting the symmetry of the geometry and of the loading.

3.4 | Comparison between predictions and measurements

In this section, the results for the measurements, the analytic quadratic tendency predicted from Equation 3.16, and the Kelvin cell numerical simulation are compared to each other. The compression distance δ is normalized by the cell height h_0, in order to compare the qualitative features of the numerical model with the experiment. The magnitude of the numerical predictions are not compared quantitatively to the experimental results because the numerical Kelvin cells are not quantitatively equal to the cells of the melamine foam, so the attention is focused on the qualitative tendency. A key question is the validity of a continuum mechanics description in the context of an inherently inhomogeneous porous material made of finite-size cells.

The contact detection protocol to determine the accurate location of the tip of the undeformed pyramid is performed by translating the indenting plate by 0.1 mm increments until sensing at least a 0.01 N force, where 0.01 N is the reading threshold of the built-in sensor display. Then, extrapolating the force F - displacement δ relationship above 0.01 N with the behaviour determined in Equation 3.16, $F \propto (\delta - \delta_{err})^2$, allows determining the contact origin offset $\delta_{err} \simeq 0.23$ mm, with an error likely bound well below the cell size. In addition, the error δ_{err} on the pyramid heights causes a relative error which is larger at small deformations and becomes negligible at large deformations, due to the $F \propto (\delta - \delta_{err})^2$ nature of the force. This is visible in Figure 3.15(a).

The measured and predicted results are shown in Figure 3.15(b). As predicted analytically, both the measured pyramid and the numerical model forces seem to increase quadratically with the com-

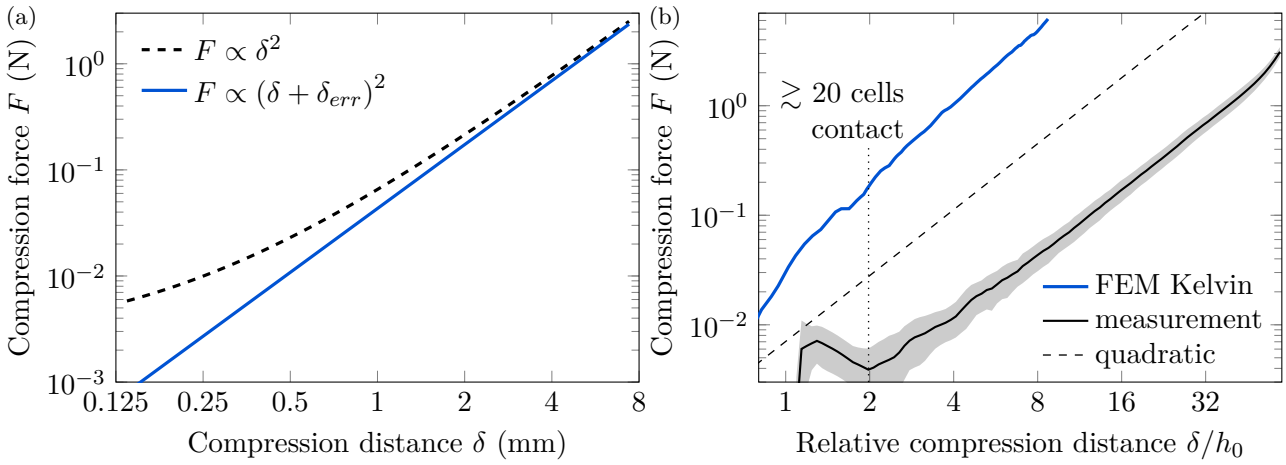

Figure 3.15. (a) Visualization of the error on the predicted force F when an error on the height of the pyramids $\delta_{err} = 0.23$ mm is performed. The relative error is larger for small deformations than large deformations. (b) Force and compression distance relationship for a single pyramid, obtained experimentally and with the Kelvin cell FEM model. The standard deviation measured over 5 repetitions is given. The expected quadratic tendency is plotted. The vertical line indicates the compression distance where the pyramid cross-section area S_{pyr} is equal to the surface area of 20 cells.

pression distance. This is shown by the black dashed line, which is without amplitude and represents the quadratic tendency between the compression force and the compression distance. Curves parallel to this dashed line on this log-log axis represent a quadratic relationship between compression force and compression distance. Nonetheless, for small strains (*i.e.* $\delta/h_0 \approx 2$, or fewer than 20 cells in contact with the indenting plane), the experimental stress does not follow the expected quadratic tendency with the compression distance. This can be explained by the imperfectly cut tip of the pyramid and by the fact that the material cannot be considered as a continuous medium at the scale of the cell size.

These phenomena are also exhibited by the Kelvin cell FEM model, which does not follow the quadratic tendency for small strains. This corroborates previous results by Hentati et al. [269] that material homogeneity is valid once enough material strands are in contact with the rigid indenting plane, which is a few tens of strands. As a reminder, the objective of the Kelvin cell numerical model is not to quantitatively predict the reaction force of the pyramid, but to capture the tendency of the reaction force due to the cellular structure of the material.

For large compression distances, around $\delta/h_0 \approx 50$, the measured force diverges from the expected quadratic tendency because the strain field inside the pyramid reaches the rigid plate below the pyramid. This phenomenon can be understood thanks to the numerical simulation: for small strains in Figure 3.14(b), the strain field does not extend much into the pyramid, whereas for larger strains in Figure 3.14(c), the strain field extends further and spherically into the pyramid, until it reaches the plate below the pyramid. This increases its apparent rigidity since the problem is not a single contact behaviour any more.

In summary, the analytic model of a pyramid works for the pyramids of melamine foam as long as more than approximately 10 cells of the material are in contact with the indenting plane, and if the compression distance is small enough that the strain field is contained within the finite dimension of the pyramid. Finally, in a non-trivial way, the nonlinearity of the material does not appear in the experimental compression results shown in Figure 3.15. This can be surprising because the modulus in Equation 3.17 is actually strongly strain-dependent modulus. In the following section,

the material nonlinearity is included in models of a pyramid to understand how it interacts with the shape nonlinearity.

4 | Integration of hyperelasticity into the pyramid models

In this section, the hyperelastic model is integrated with the pyramidal geometry, to understand how the material nonlinearity and the shape nonlinearity interact. This reveals how the shape nonlinearity takes precedence over the material nonlinearity, meaning that a constant modulus can be used instead of a hyperelastic strain-dependent modulus without deteriorating the predictions. Interestingly, the equivalent modulus is found to be different from the tangent modulus at small strains which would be use for acoustic applications.

4.1 | Slices model

An analytic model accounting for varying strain and modulus throughout the height of the pyramid is investigated. This model consists in studying horizontal slices throughout the height of the pyramid, in which the strain is considered constant. Considering a constant force F transmitted throughout the height of the pyramid, the local stress-strain relationship in a thin horizontal slice at distance z from the pyramid tip gives

$$F = S_{pyr}(z)\, E_{sec}(\varepsilon(z))\, \varepsilon(z), \tag{3.18}$$

where $S(z)$ is the local cross-section area computed from Equation 3.13, and where the Poisson effect is neglected because the Poisson ratio was found small in Table 3.5. The strain $\varepsilon(z)$ in each horizontal slice is computed from Equation 3.18, and then the total compression distance δ is

$$\delta = \int_0^h \varepsilon(z) dz, \tag{3.19}$$

which yields the relationship between the force F and the compression distance δ.

Using this model, the strain throughout the height of the pyramid can be estimated for a given force F, as shown in Figure 3.16(a). Near the tip of the pyramid, the local strain is close to 100 %, meaning that the material is completely crushed: its contribution to the apparent stiffness disappears. Beyond this region, in the centre of the pyramid, the strain and the modulus evolve quickly: this region mainly drives the relationship between applied force and the total compression distance of the pyramid. Near the base of the pyramid, the strain is close to 0 %, unless a very large force is applied to the pyramid (see for instance $F = 8$ N). In this zone, the pyramid has a high modulus and a high surface area: it hardly deforms and its contribution to the apparent stiffness is also small. Only the zone in the centre of the pyramid undergoes high strain and has a low modulus due to buckling, which could explain why the nonlinearity of the modulus is hidden for a pyramidal geometry.

4.2 | Solid FEM model

To obtain a more accurate 3D representation of the strain inside a pyramidal asperity made of a hyperelastic material, a pyramid made of a continuous solid hyperelastic material is simulated with FEM under the same conditions. The model mesh is shown in Figure 3.16(b). Linear tetrahedral elements (C3D4) of average size 0.2 mm are used, ensuring results which are independent of the element size. The material behaviour is described by a hyperfoam model using parameters from Table 3.1.

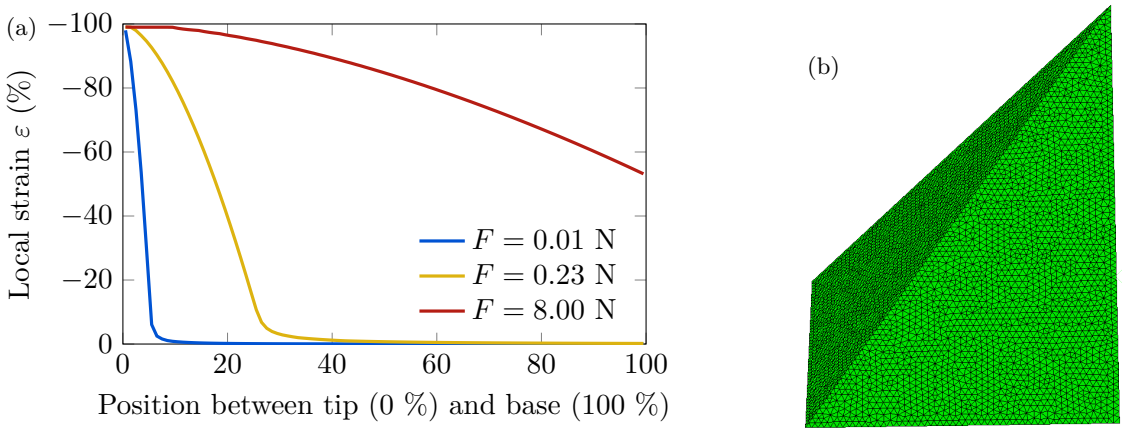

Figure 3.16. (a) Strain throughout the height of the pyramid obtained from the analytic slices model for different values of the compression force F applied. (b) Model of a quarter of a pyramid with continuous solid elements composed of approximately 353 553 elements.

Table 3.5. Parameter values obtained for the hyperelastic model to represent that material's instantaneous response. 95 % confidence intervals are given.

α_1 (-)	μ_1 (kPa)	ν_1 (-)
49.8	189.1	0.0047
±16.1	±55.5	±0.0037

4.3 | Results and interpretation

The hyperelastic FEM model and the analytic slices model are compared to measurements in Figure 3.17. The black dashed line once again represents the quadratic relationship between force and displacement, without amplitude. Both models follow the same tendency as a quadratic law, despite the hyperfoam material behaviour used. The slices model overestimates the compression force, which could be due to the hypothesis of constant strain within each horizontal slice, since Figure 3.14(c) shows that the strain field front in fact extends spherically into the pyramid. The force predicted by the hyperelastic FEM model matches the quadratic tendency of the experiment accurately once the experimental compression distance provides a few tens of cells of contact, to bypass surface effects and the error on the height determination of the pyramids.

Using Equation 3.17, the equivalent modulus fit to the hyperelastic FEM results is $E = 65.3$ kPa and the modulus fit to the experimental results is $E = 60.2$ kPa. These similar results validate the hyperfoam model in Table 3.5 for the pyramidal geometry. The constant prefactor modulus fit to experimental results is chosen to represent the quadratic tendency of a single pyramidal asperity, by simplifying the strain-dependent modulus with an equivalent value, providing a reasonable prediction of experimental results within the whole range of probed deformations past the effect of the surface cells. This raises the question of how to determine the value of an equivalent modulus to approximate the material's nonlinear behaviour.

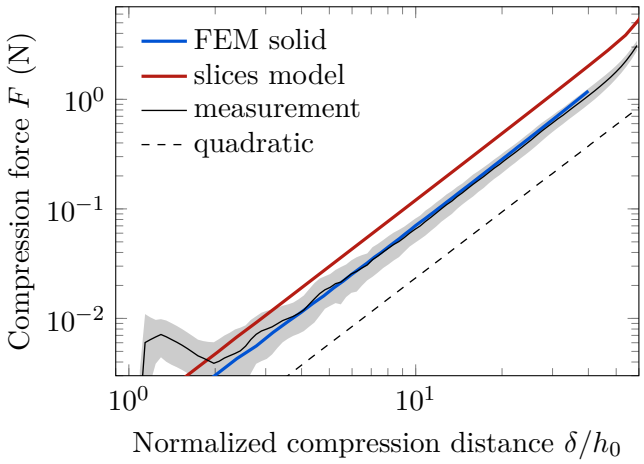

Figure 3.17. Measured and simulated compression force versus compression distance for the measured pyramid, the FEM model with solid elements and the analytic slices model. The quadratic slope is also represented.

4.4 | Estimation of an equivalent modulus

The aim of this section is to determine an appropriate constant modulus to approximate the hyperelastic law. This will shed light on which effective modulus drives the behaviour of the asperity amongst the multiple definitions and their strain dependence. Three hypotheses are proposed. A first option is to use the secant modulus at small strains, which is equal to the tangent modulus at small strains $E_{tan}(\varepsilon = 0) = 300$ kPa, as shown in Figure 3.3(b). A second option is to consider the pyramid as a sum of stiffnesses in series, in which case the overall stiffness is driven by the lowest stiffness. This means the overall stiffness can be approximated by the minimum value of the secant modulus $E_{min} = \min(E_{sec}) = 35$ kPa, found for $\varepsilon = -50$ %. As explained in Section 2.2, this corresponds to the strain of densification, where the material energy absorption efficiency (defined in Equation 3.5) starts increasing. A third option is to consider the secant modulus at the inflexion point $E_I = E_{sec}(I) = 58.0$ kPa, found for $\varepsilon = -20$ %, where the tangent modulus transitions from buckling to densification.

The compression force of a pyramid using the slices model and the hyperelastic law $E_{sec}(\varepsilon)$ is shown in Figure 3.18. It is compared to models using the three proposed hypotheses $E_{tan}(\varepsilon = 0)$, E_{min} and E_I. The small strain modulus $E_{tan}(\varepsilon = 0\ \%)$ overestimates the material stiffness, whereas the minimum of the secant modulus E_{min} underestimates the material stiffness. Using the secant modulus at the inflexion point E_I, shown in Figure 3.3(b), gives a prediction that is close to the full strain-dependent secant modulus $E_{sec}(\varepsilon)$. Indeed, $E_I = 58.0$ kPa is a good approximation of the prefactor found by the FEM hyperelastic model $E = 65.3$ kPa for a pyramidal geometry in Figure 3.17.

In summary, the analytic formula of a compressed pyramid predicts a reaction force that increases quadratically with the compression distance. Experiments and numerical simulations incorporating the microstructure find that this holds for more than a few tens of cells in contact with the indenting plane, and before the strain field reaches the other end of the pyramid. When the hyperelastic behaviour is implemented in a continuous pyramidal medium, a quadratic tendency is also found. This reveals that the shape nonlinearity that causes the quadratic evolution of the compression force is predominant over the material nonlinearity. Consequently, a constant modulus can be used instead of the strain dependant modulus to give satisfying results. This equivalent modulus is not equal to the tangent modulus at small strains, as measured by a QMA for instance, and which would be used to model a material for acoustic applications. The equivalent modulus found is largely surrounded by the tangent modulus at small strains $E_{tan}(\varepsilon = 0)$ and the minimum of the secant modulus caused by

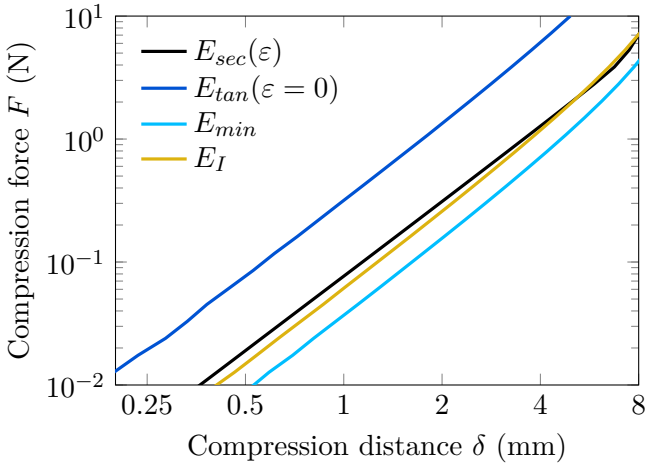

Figure 3.18. Comparison of the analytic slices model for different prefactors, using the strain dependent modulus $E_{sec}(\varepsilon)$, the small strain tangent modulus $E_{tan}(\varepsilon = 0)$, the minimum of the secant modulus E_{min}, and the secant modulus at the inflexion point E_I.

buckling $\min(E_{sec})$, but can be fairly well approximated by the secant buckling modulus $E_{sec}(I)$.

5 | Application to a multi-asperity rough surface

After analysing a single asperity, a real rough surface of multiple asperities is now studied through a surface roughness model. A Greenwood-Williamson-like surface roughness model is applied to an ideal surface of pyramids of varying heights. The equivalence between the continuous Greenwood-Williamson model description and a finite surface created from a finite number of asperities is verified. Then, the surface of a Greenflocks material, made from shredded polyurethane flocks, is analysed. The surface roughness model is applied and compared with experimental compression results.

5.1 | Description of the Greenwood-Williamson model

The first major surface roughness model is the Greenwood-Williamson and Williamson model [273, 274] which assumes that a rough surface is made up of spherical asperities of radius of curvature R_{asp}, and with tip heights that follow a probability density function $\phi(z)$. The stiffness of the spherical asperities is based on the mechanics of sphere-to-plane contact described by Hertz [312], valid for linear elasticity in small deformation, for a size of the contact region and an overlap between bodies much smaller than the dimensions of the bodies themselves, for spherical shapes, and by neglecting contact surface friction and adhesion. The medium is assumed to be isotropic and bulk behaviour is neglected, since each asperity behaves independently of the others. Strain hardening, yielding, and thermal effects are neglected.

Asperity height distribution $\phi(z)$ often follows a Gaussian distribution in practice [274, 313], though any probability density function can be used. Furthermore, the Greenwood-Williamson model uses spherical asperities, although asperities can be of different geometries. For example, Hisakado [314] takes into account asperity radius of curvature distribution, Bush [315] approximates the summits of the rough surface by paraboloids to obtain curvature radius and Persson et al. [316] consider the case of self-affine fractal rough surfaces. Ultimately, the Greenwood-Williamson model predicts the load F required to compress a rough surface with a rigid plane by an amount δ as

$$F(\delta) = N_{asp}\frac{4}{3}R_{asp}^{\frac{1}{2}}E^*\int_{-\infty}^{\delta}(z-\delta)^{\frac{3}{2}}\phi(z)dz, \tag{3.20}$$

where N_{asp} is the total number of asperities on the rough surface. The prefactor $\frac{4}{3}R_{asp}^{\frac{1}{2}}E^*$, and the force that increases as $\delta^{\frac{3}{2}}$, result from using hemispherical asperities, although asperities can be of different shapes.

When using pyramidal asperities, with compression force given by Equation 3.17, the Greenwood-Williamson model becomes

$$F(\delta) = N_{asp}\frac{4}{\pi\sqrt{\pi}}\frac{E^*}{\tan\theta}\int_{-\infty}^{\delta}(z-\delta)^2\phi(z)dz. \tag{3.21}$$

In this case the prefactor is $\frac{4}{\pi\sqrt{\pi}}\frac{E^*}{\tan\theta}$ and the force increases as δ^2.

The Greenwood-Williamson model relies on a continuous description of the statistical distribution of the asperity heights $\phi(z)$, and it is equivalent to summing the individual reaction forces of a discrete number of N_{asp} asperities of known heights. The sketch of the surface roughness model composed of pyramids and the corresponding experiment are shown in Figure 3.19. The reference plane is chosen at the tip of the tallest pyramid, which means that the tallest pyramid is expected to contribute to the force quadratically with the total compression distance.

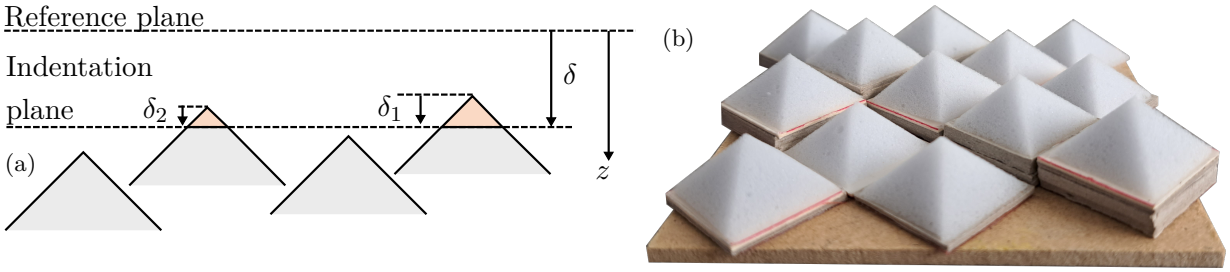

Figure 3.19. Rough surface represented by pyramidal asperities coming into contact with a rigid plane. (a) Greenwood-Williamson surface roughness model representation. (b) Experimental setup representing a rough surface made up of pyramidal asperities of varying heights.

5.2 | Similarity between discrete and continuous descriptions

The similarity between a continuous statistical description of asperity heights $\phi(z)$ and a discrete description of N_{asp} asperities of known heights is studied in this section. The error generated by considering only N_{asp} pyramidal asperities in a surface roughness model is shown in Figure 3.20, and is computed for a uniform distribution and a normal distribution of the tip heights $\phi(z)$. The statistical distributions are bounded by $z = 0$ and $z = h$, where $z = 0$ is the position of the tallest pyramid, and the normal law is centred around the middle of the interval $z = 0.5h$ with a standard deviation of 3 mm.

The results reveal that the error decreases as the number of asperities N_{asp} increases, which is expected. For instance, for a normal distribution, a relative error of 10.5 % is obtained for $N_{asp} = 10$ asperities, which drops to 5.1 % for $N_{asp} = 25$ asperities. The results also show that using a discrete number of asperities gives results closer to the continuous distribution for a uniform distribution than for a normal distribution. For a uniform distribution of $N_{asp} = 13$ pyramids, which is the configuration studied here, the error relative to a continuous statistical Greenwood-Williamson model is about 3.9 %. Therefore, we can consider with a minimal error that the results obtained for a rough surface of 13 asperities can be considered representative of a statistically continuous model.

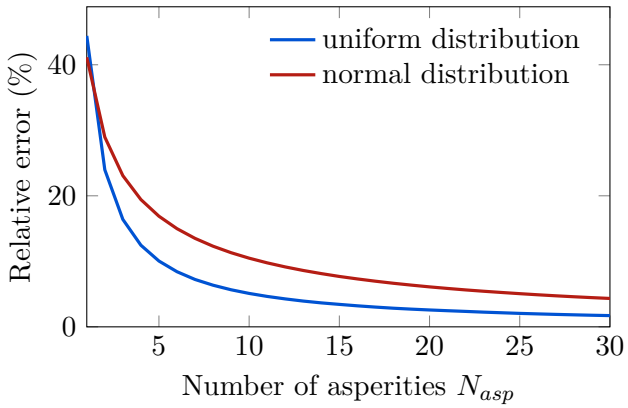

Figure 3.20. Mean relative error (%) on the estimated force for a discrete number of N_{asp} pyramidal asperities compared to a continuous statistical model.

5.3 | Application to a surface of multiple pyramids

An ideal surface of 13 pyramidal asperities is created, each with a different height, as shown on Figure 3.19(b), and the Greenwood-Williamson surface roughness model is applied to it. The pyramids are placed on supports to obtain different heights, and the height of each pyramid is measured individually. The asperity tip heights are uniformly distributed over a range of 6 mm, meaning that the average height difference between two neighbouring pyramid tips is 0.5 mm for 13 pyramids. A uniform distribution was chosen because, compared to a normal distribution for example, it is more feasible to create experimentally and allows for more accurate control over the asperity heights relative to each other. The pyramids are compressed by up to 8.7 mm from the position of the highest pyramid, such that it is compressed by 83.6 % of its initial height. A single set of pyramids is characterized this way, considering the averaging effect of compressing 13 pyramids at once and the good measurement repeatability found for single pyramids.

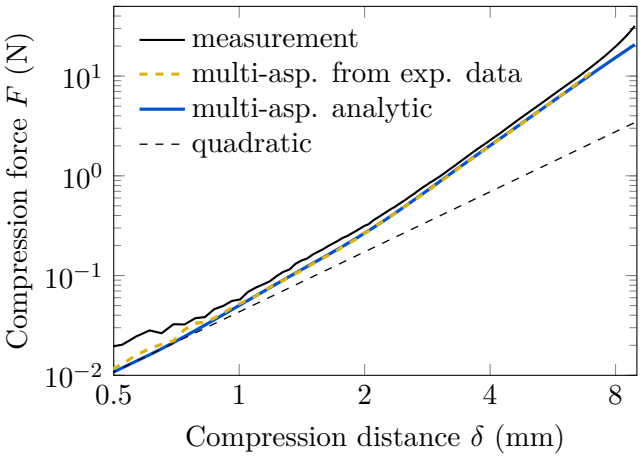

Figure 3.21. Compression force and compression distance relationship for an ideal surface of 13 pyramids of different heights. Experimental results and predictions using a Greenwood-Williamson like multi-asperity description are plotted. The quadratic tendency expected for a single pyramid is also represented.

The compression force and the compression distance are measured and compared to predictions in Figure 3.21. It can be seen that the force resulting from the compression of several pyramids of different heights diverges from the quadratic slope which represents the behaviour of a single pyramid. The reaction force is predicted by using the experimental force and displacement relationship from Figure 3.15(b). This relationship provides a robust prediction of the compression force of the multi-

asperity surface, from small to large deformations. The analytic prediction is obtained by applying the modulus of $E = 60.2$ kPa, found experimentally in Section 4.3, to Equation 3.17. The analytic solution converges to the prediction from the experimental force and displacement relationship, because of the good fit it provides for a single pyramid.

For very large compression distances $\delta > 7.5$ mm, the analytic model does not predict the force increase caused by the finite size of the pyramids, as observed for a single pyramid in Section 4.3. Nonetheless, for intermediary compression distances, this Greenwood-Williamson-like model is adapted to predicting the compression force of this ideal surface of asperities.

In short, extrapolating the behaviour of a single pyramid to a surface of several pyramids of varying heights is reliable to predict the compression stiffness of this surface. This prediction is performed on a surface with a finite number of asperities, and can be extended equivalently to a continuous distribution of asperities as described by the Greenwood-Williamson model. This is promising for predicting the compression stiffness of a rough porous material characterized statistically by a 3D surface scan, for example. The ideal surface of pyramids studied is composed solely of asperities, so the transition to the bulk stiffness of the material underneath the asperities does not appear, though this would be the case for a real material undergoing large compression distances relative to the asperity size.

5.4 | Application to a material with macroscopic asperities

In this section, a real material with a rough surface is analysed using a 3D surface scan, and the Greenwood-Williamson surface model is applied to it. Applying the Greenwood-Williamson model to a real material raises two difficulties. The first is that the real material smoothly transitions to its bulk behaviour when the compression distance is large enough that the asperities are strongly compressed. The second is that the geometrical shape and height distribution of the asperities is unknown. These issues are addressed in this section.

The first issue lies with the transition to the bulk stiffness of the material once the asperities are strongly compressed. Samples of Greenflocks of nominal heights 20 mm and 25 mm are compressed to observe this transition, and their compression force is shown in Figure 3.22. The results reveal the regions of partial contacts, buckling zone, and densification. The transition from the partial contacts to the bulk behaviour appears at 7.85 % strain for the Greenflocks 20 mm and 7.86 % strain for the Greenflocks 25 mm, marked by the first inflexion point in the force-compression distance curve. Consequently, it is assumed that the hypothesis of partial contact is valid below this strain. The transition to the bulk behaviour beyond is not modelled here. Note that because the material has a rough surface on both sides (top and bottom), the partial contact identified here corresponds to the contribution of the roughness of both of the sample's sides.

The second issue lies in obtaining the statistical properties of the asperities. The Greenflocks of nominal height 20 mm is analysed in the following. Its surface, pictured in Figure 3.1(c), was scanned to obtain a 3D point scatter of the surface, shown in Figure 3.23(a). This scan reveals the roughness on the surface material at a mesoscopic scale. The distribution in the elevation of the material surface is plotted in Figure 3.23(b), which resembles a Gaussian distribution with a standard deviation of 0.48 mm, and a skewness and a kurtosis. The distribution of the radii of curvature is plotted in Figure 3.23(c), which is inversely proportional to the radius.

The information from the 3D surface scan could be analysed to compute statistical information about the distribution of the asperity heights and their geometry. However, care must be taken because the distribution of the height of the entire profile in Figure 3.23(b) is not equal to the distribution of the asperity tip heights. To access the statistical information of the asperity tip heights, further processing of the surface scan would be required, which is not performed in this work. Instead, two distributions are tested and compared, which are a uniform distribution which distributes the asperity

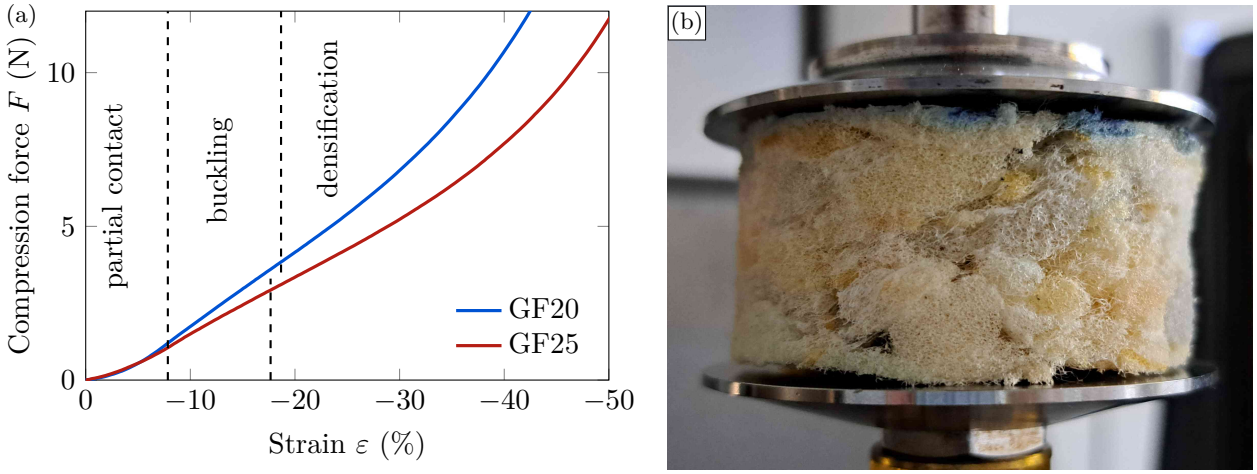

Figure 3.22. Compression of a Greenflocks material sample. (a) compression force versus compression distance for samples of nominal heights 20 mm and 25 mm. (b) Image of the experimental setup.

tips evenly across different heights, and a Dirac distributions which places all asperity tips at the same height. The uniform distribution spans the entire range of the partial contact, that is to say between 0 % strain and 7.85 % strain, and the Dirac distribution places all asperity tips at $z = 0$ mm. Similarly, lacking the prior knowledge of the shapes of the asperities, both spherical and pyramidal geometries are tested. Additionally, the number of asperities N_{asp} distributed over the surface is not known, so the prefactor of the Greenwood-Williamson compression force cannot be determined. Therefore, the predicted force is normalized by the measured compression force at the inflexion point at 7.85 % strain.

The tendency of the force over the partial contact zone can be compared with the tendency of the measurement, when using uniform or Dirac distributions, and for pyramidal or spherical asperities, is shown in Figure 3.24. The vertical line represents to the transition to the bulk behaviour at the inflexion point at 7.85 % strain, *i.e.* at $\delta = 1.72$ mm. The results show that the Dirac distribution fits the tendency of the measured force better than the uniform distribution, for both the spheres and the pyramids. This suggests that most asperity tips are probably located at the surface of the material, and do not have different heights. This would make sense considering the manufacturing process of this material, which is calendared and thermoformed [132, 133], leading to a uniform height of the asperities. Further, the measured force is between the force predicted for pyramids and for spheres, suggesting the real geometry of the asperities has an average power law contained between $F \propto \delta^{\frac{3}{2}}$ and $F \propto \delta^2$.

To improve results, the surface scan could be analysed further to determine the shape and the distribution in height and geometry of the asperities. Additionally, a model accounting for the transition to the bulk behaviour of the material once all the asperities are compressed could provide the full prediction of the compression stiffness of a material, from small to large deformations.

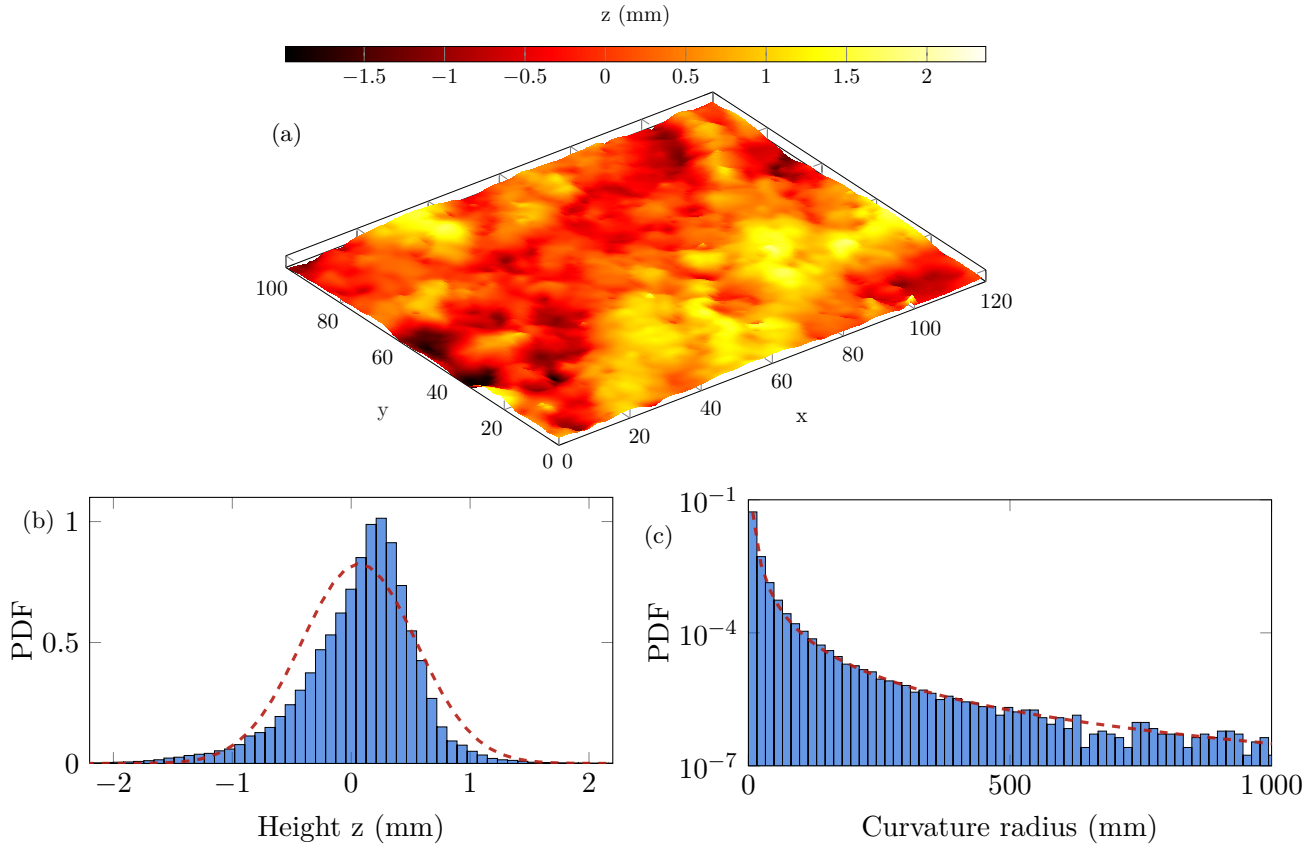

Figure 3.23. Surface scan of a Greenflocks material. (a) surface point scatter, (b) height distribution with normal distribution with the same standard deviation overlaid, and (c) radius curvature distribution with power law overlaid.

6 | Conclusion

The compression stiffness of macroscopic asperities of porous materials has been studied. The influence of material nonlinearity and relaxation have been evaluated in the context of the macroscopic asperities, allowing for a simple prediction of the compression stiffness of a multi-pyramidal surface of a cellular material.

To begin with, the nonlinearity was accounted for with a hyperfoam model. The material relaxation was estimated using an ageing relaxation model. This model predicts how the melamine foam studied continues to relax at very long time scales, which is also the case for other porous materials, as shown in Appendix C. This long term relaxation is often not taken into consideration when modelling their behaviour, and raises concerns about the validity of QMA characterization results when the relaxation is not taken into account. It was shown that this relaxation can be neglected when the loading time is short compared to the material relaxation time, that is to say at compression rates higher than 1.5 % per second.

Then, the effect of the pyramidal geometry was studied using models of varying complexity. The prediction from a simple continuous elastic model is satisfactory over several orders of magnitude, except for very small strains, typically below a few tens of cells in contact, and very large strains, typically above 90 % of the total pyramid height. Overall, numerical and analytic models find the same quadratic evolution of the force with the compression distance as experimental results, despite the intrinsic material nonlinearity. This signifies that the combination of the material hyperelasticity with the pyramidal shape nonlinearity results in force that is mostly driven by the pyramidal shape. Moreover, this means that the strain-dependant modulus can be approximated by an equivalent con-

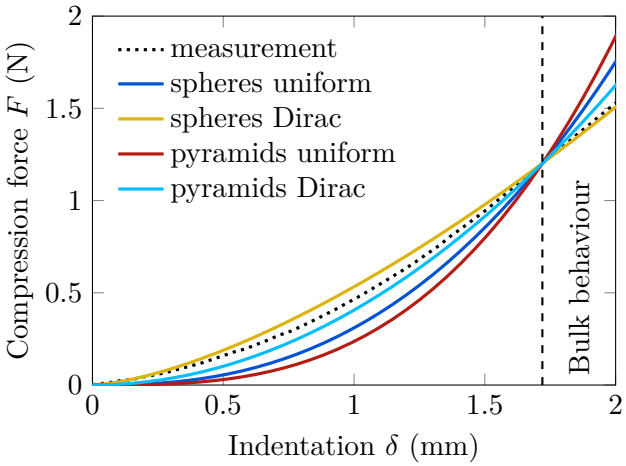

Figure 3.24. Comparison of the compression force of a compressed surface of Greenflocks material for a measurement and for the Greenwood-Williamson model. Spherical and pyramidal asperities, and uniform and Dirac distributions, are compared. The vertical line represents the inflexion point that marks the transition from partial contacts to the bulk behaviour.

stant modulus. The equivalent modulus is different from the tangent modulus at small strains, which would be used for acoustical applications, and is found close to the secant modulus at the inflexion point located between the buckling and densification zones.

Finally, the proposed surface roughness model has shown good agreement with experimental results for an ideal multi-pyramidal material. This surface roughness model was applied to a real inhomogeneous Greenflocks material, on which the zone of partial contact was identified. The statistical height and geometry of the asperities is not known, however tested configurations reveal that the variability of the asperity heights is quite limited.

Key findings

- The studied melamine's stress-strain relationship is strongly nonlinear, which is modelled with a hyperfoam model.
- It is also time-dependant, with a relaxation time which increases with time and spans several orders of magnitude. A custom ageing hyperfoam model predicts both nonlinearity and time-dependance, showing that the instantaneous response is approached for strain rates greater than 1.5 % per second.
- Macroscopic pyramidal asperities of melamine are found to have a compression force that increases quadratically with the compression distance, which is validated experimentally and numerically once the indenting plane is in contact with more than a few tens of cells of the material. This tendency is caused by the shape effect of the pyramid, which overrides the material nonlinearity.
- A Greenwood-Williamson-like surface model applied to a Greenflocks material suggests that asperity tips are all located at approximately the same height on the material surface.

Chapter 4. Reduction of the acoustic radiation of a source by exploiting partial contact

1 | Introduction

The objective of the SEMPAE project is to predict the effectiveness of acoustic screens at reducing the noise radiated by car engine, by placing the porous screens in direct contact with the engine. Due to the complex engine geometry and the rough surface of the screens, the contact between the two is partial, and air gaps occupy the zones without contact. This partial contact has an important effect on the acoustic behaviour of the system, and can be exploited to improve the effectiveness of the screens. No simple modelling approaches to estimate the acoustic behaviour of partial contact are suggested in the literature. In this chapter, the improvement of the Transmission Loss achieved by introducing partial contact surface area between a radiating plate and a porous screen is examined. The partial contact is created experimentally by architecting a porous layer of melamine foam by cutting triangular grooves into it, and it is modelled using the Parallel Transfer Matrix Method (PTMM).

2 | Description of the measurement setup

2.1 | Measurement principle

A measurement setup is devised to examine how much a porous screen placed in contact with a radiating surface reduces its radiated noise level. The setup involves measuring the acoustic power radiated by a plate into a reception semi-anechoic chamber, using a sound intensity probe. The reduction in acoustic power level radiated by a plate when it is covered by a screen can be evaluated by its Insertion Loss (IL). The IL is the difference between the radiated acoustic power level of the bare plate Π_{rad}^{bare} and that of the covered plate $\Pi_{rad}^{covered}$:

$$IL = 10 \log \left(\frac{\Pi_{rad}^{bare}}{\Pi_{rad}^{covered}} \right). \tag{4.1}$$

The plate is placed at the boundary between two decoupled rooms, and is excited from the emission room on the other side. It can be excited acoustically using an air-borne noise, which requires the emission room to be a reverberant chamber. In this case, the injected acoustic power can be measured with a microphone. The plate can also be excited mechanically using a shaker, in which case the injected power is measured using an impedance head. The vibrational power of the plate can also be measured using a laser vibrometer which measures the velocity along a mesh of points on the surface of the plate. Since the radiated acoustic power depends on the power injected into the plate, the IL has to be normalized by a reference power. This can be the airborne injected power Π_{inj}^{ac}, which gives access to the Air-Borne Transmission Loss (ABIL), or the solid-borne injected power Π_{inj}^{mech}, which

gives access to the Solid-Borne Insertion Loss (SBIL) [39, 317].

$$ABIL = 10\log\left(\frac{\Pi_{inj,ac}^{covered}}{\Pi_{rad}^{covered}}\right) - 10\log\left(\frac{\Pi_{inj,ac}^{bare}}{\Pi_{rad}^{bare}}\right), \tag{4.2}$$

$$SBIL = 10\log\left(\frac{\Pi_{inj,mech}^{covered}}{\Pi_{rad}^{covered}}\right) - 10\log\left(\frac{\Pi_{inj,mech}^{bare}}{\Pi_{rad}^{bare}}\right). \tag{4.3}$$

Alternatively, instead of normalizing the radiated power by the power injected into the plate, it can be normalized by its vibrational power Π_{vib}, which can be measured with a laser vibrometer:

$$vibIL = 10\log\left(\frac{\Pi_{vib}^{covered}}{\Pi_{rad}^{covered}}\right) - 10\log\left(\frac{\Pi_{vib}^{bare}}{\Pi_{rad}^{bare}}\right). \tag{4.4}$$

Several standards describe measurement procedures to estimate the sound insulation of building partition elements from airborne excitation, such as ISO 15186-1, ISO 140.3 ASTM E90-09, and ISO 140-5 [318, 319, 320, 321]. Weber et al. [322] compares some of these standard protocols with each other, and find that they give similar results within a ±2 dB range. Using an airborne excitation has the advantage of exciting the plate homogeneously on its entire surface with a diffuse field. Moreover, it normalizes the radiated power by the incident acoustic power, and not on the injected acoustic power, which makes it independant of the structural damping. However, an airborne excitation requires a large reverberant chamber to access low frequencies, and it can be difficult to obtain grazing angles. It can also require high sound pressure levels to create a sufficient signal amplitude. This is why in the following, a shaker is used to inject mechanical energy into the system.

Bertolini and Ruggeri [323] compare SBIL and ABIL, and find that the SBIL can be averaged over several excitation points to find similar results as the ABIL, except around the frequency range of the mass-spring resonance. They also find a strong dependence of the SBIL on the structural damping. As a consequence, Bertolini et al. [323, 324] propose a method to excite the entire plate boundary, which is closer to the types of excitations that automotive panels are subjected to. Nevertheless, this method requires a specific mounting chassis to excite the plate boundaries. The objective of this chapter is to use an experimental Insertion Loss criterion which is comparable to the radiation efficiency σ_r computed theoretically, which is defined at constant vibrational power:

$$\sigma_r = \frac{\Pi_{rad}}{\Pi_{vib}}. \tag{4.5}$$

Therefore, the $vibIL$ definition given in Equation 4.4 seems to be the most adapted criterion to compare the measurement results with the predictions.

2.2 | Experimental setup

The diagram of the measurement setup is shown in Figure 4.1, and images of the real setup are shown in Figure 4.2 and Figure 4.3. A shaker is connected to the metal plate with cyanoacrylate glue, in a position that avoids nodes and antinodes. Sweep signals lasting 1 s between 20 Hz and 1600 Hz are sent. A single measurement position is tested, although for improved results, measurements should be performed at several excitation points. The plate connecting the two rooms has dimensions 673 mm × 970 mm, and is made of 4 mm thick aluminium. It is held in place inside a tunnel, and placed on top of soft window sealing strips to avoid direct contact with the tunnel. Further, the plate edges are sealed with aluminium tape to prevent acoustic leaks.

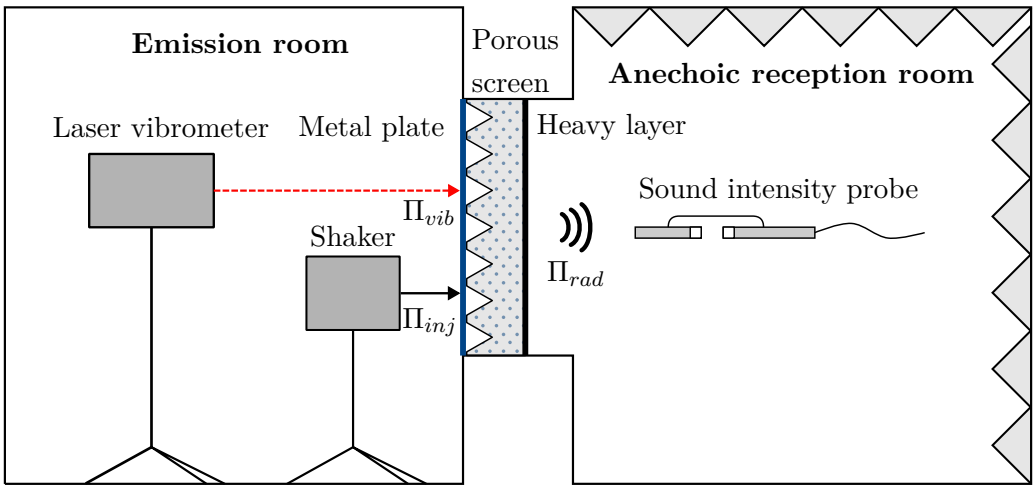

Figure 4.1. Diagram of the measurement setup.

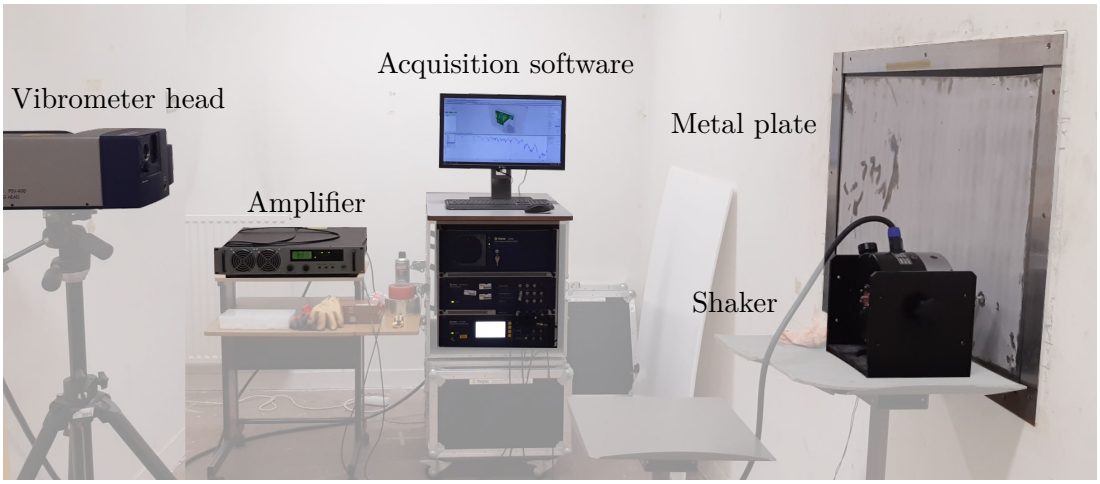

Figure 4.2. Measurement setup in the emission room.

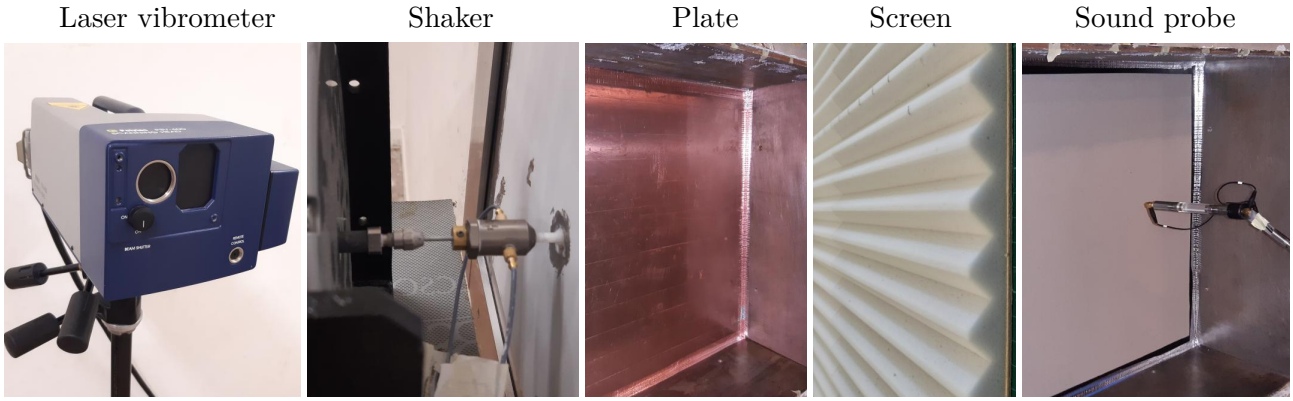

Figure 4.3. Close-up images of the elements involved in the experimental setup.

The porous screens are covered with a heavy layer to induce a mass-spring-like behaviour of the system, which is a configuration often exploited in acoustic insulation applications. The heavy layer used is a dense cardboard material of thickness 3 mm and surface density 1.86 kg m^2. The layer of cardboard is glued on the plane side of the melamine sheets.

Melamine sheets of thickness 19.0 mm are used for the porous layer, because it is easy to cut using cutter blades for example. This allows the sheets to be easily cut and shaped to enforce the amount of sought-after partial contact with the metal plate. To do so, grooves are cut into the porous

sheets, such that only a small percentage of the surface is in contact with the plate. The grooves were cut using cutter blades at a 45° angle. This results in triangular or pyramidal shapes with a flat surface. By cutting grooves in one direction, 16.7 % contact is achieved, and by cutting grooves in both directions, 2.8 % contact is achieved. The cut samples are shown in Figure 4.4. The melamine sheets with partial contact are glued to the metal plate with neoprene glue. As little preload as possible is applied to the melamine sheets while the glue dries to avoid artificially increasing the contact area by compressing the surface asperities. The glue ensures continuity of the displacement between the plate and the porous layer.

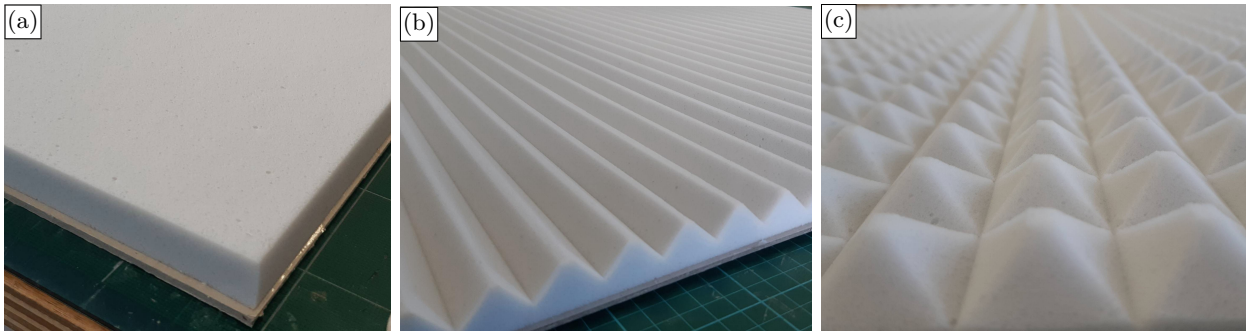

Figure 4.4. Melamine sheets with partial contact. (a) Original melamine plate. (b) Grooves in one direction give 16 % contact. (c) Grooves in two directions give 2.8 % contact.

3 | Modelling of the Insertion Loss and of the partial contact

3.1 | Insertion Loss computation from TMM

Some examples of Insertion Losses computed using TMM are presented in this section. The Insertion Loss (dB) is computed from the radiation efficiency as $IL = -10\log_{10}(\sigma_r)$. This corresponds to how much the radiated acoustic power level of a piston is reduced by adding a covering compared to a bare piston, at constant vibrational power.

The IL of a single layer of melamine foam of thickness $h = 19.0$ mm covered by a heavy layer of surface density $m_s = 1.86\ \mathrm{kg\,m^2}$ is shown in Figure 4.5. The modulus E of the melamine foam is multiplied and divided by 2 to showcase the effect of the stiffness on the insertion loss. Full contact between the melamine sheet and the vibrating surface is enforced in Figure 4.5(a), whereas a shallow 1 mm air gap is enforced in Figure 4.5(b).

In low frequencies, the IL is close to 0 dB meaning that the covered plate radiates as much as the bare plate. A decrease in the IL caused by a resonance inside the system can be observed, which causes the covered system to radiate better than the bare plate with a negative IL. When there is full contact between the porous layer and the vibrating surface, this resonance frequency is driven by the modulus of the porous layer. However, when a shallow 1 mm air gap of thickness is introduced, the boundary conditions are changed, and the modulus has no effect on the location of this resonance frequency. This provides insight into how strongly the solid-borne waves affect the acoustic radiation when contact between the radiating surface and the porous screen is ensured.

Moreover, after the resonance frequency, the IL increases with the frequency. As a consequence, the lower the resonance frequency is located, the higher the IL is at higher frequencies. When an air gap is added behind the porous layer, the resonance is moved to lower frequencies, since it is found at 558 Hz without an air gap and 260 Hz with an air gap. In short, the IL can be improved by reducing the resonance frequency of the system, which can be achieved by reducing the modulus of the porous screen and by adding an air gap between the porous screen and the vibrating surface. This raises the question of how partial air gaps can be exploited to improve the IL of acoustic coverings.

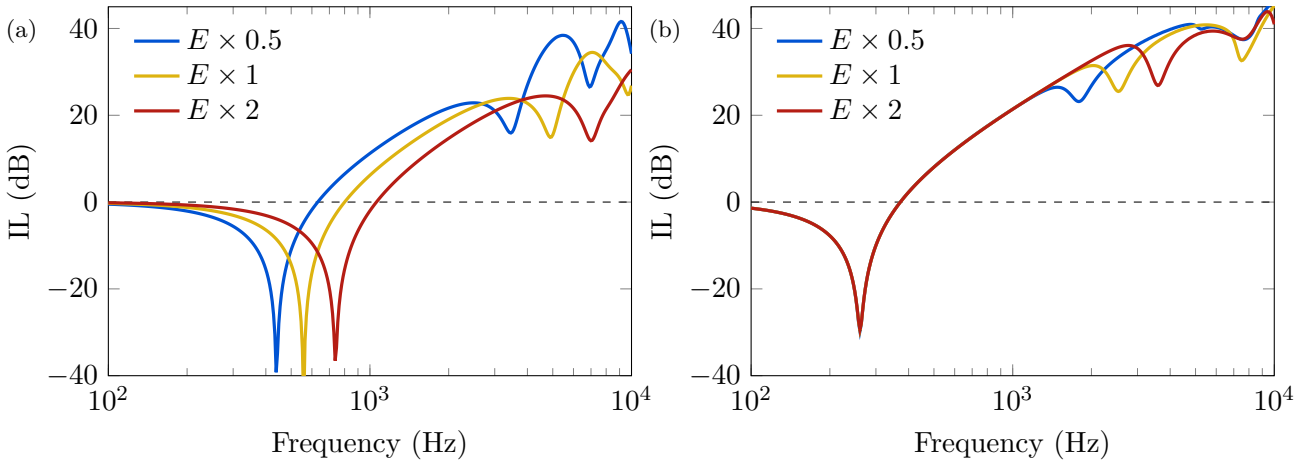

Figure 4.5. IL computed from TMM for melamine foam covered by a heavy layer. Its sensitivity to the foam's modulus E is evaluated by disturbing the value of E. (a) Full contact between the foam and backing is ensured, and (b) the foam is backed by a 1 mm air gap.

3.2 | Description of the Parallel Transfer Matrix Method

A simple model is sought to account for the partial contact between the melamine sheets and the metal plate within the Transfer Matrix Method. Chevillotte et al. [325] propose mixing laws to homogenize equivalent fluids occupying a volume, each with a ratio $\phi_{M,i}$. These are given for equivalent fluids, and not poroelastic media:

$$\tilde{\rho}_{eq} = \left(\sum_{i=1}^{N} \frac{\phi_{M,i}}{\tilde{\rho}_{eq,i}} \right)^{-1}, \tag{4.6}$$

$$\tilde{K}_{eq} = \left(\sum_{i=1}^{N} \frac{\phi_{M,i}}{\tilde{K}_{eq,i}} \right)^{-1}. \tag{4.7}$$

Alternatively, the Parallel Transfer Matrix Method (PTMM) can be used to represent layers of different nature in parallel, such as air layers and porous layers side by side. The width of the layers placed in parallel can be changed to control the amount of partial contact in the model. The PTMM is described by Verdière et al. [326]. It is similar to the Admittance Sum Method (ASM), which states that the total admittance at the surface of parallel media is the sum of their admittances. Nevertheless, the PTMM is capable of simulating more complex configurations than the ASM, notably by reconnecting parallel layers after they have been split, and by giving access to a layer's Transmission Loss [327]. However, these methods cannot take into account the pressure diffusion from one parallel layer to another, since they are considered independent of each other, which is problematic for oblique incidence on thick layers. Further, they rely on the hypothesis that the elementary layers in parallel are much smaller than the wavelength, in order to apply homogenization.

The PTMM relies on the coupling equations at the boundaries of the parallel media to construct an equivalent transfer matrix. Verdière et al. [326] provide the coupling equations for two by two transfer matrices of fluid media. The coupling equations are extended to biphasic porous layers in this section. Let's consider a porous medium of state vector V_0 and porosity ϕ_0, placed in contact with N parallel porous media of state vectors V_i and porosity ϕ_i, where $i = 1$ to N, with

$$V_0 = \begin{pmatrix} v^s_{y,0} & v^s_{x,0} & v^f_{x,0} & \sigma^s_{x,0} & \sigma^s_{xy,0} & \sigma^f_{x,0} \end{pmatrix}^T, \; V_i = \begin{pmatrix} v^s_{y,i} & v^s_{x,i} & v^f_{x,i} & \sigma^s_{x,i} & \sigma^s_{xy,i} & \sigma^f_{x,i} \end{pmatrix}^T. \tag{4.8}$$

Each parallel layer takes up a ratio $\phi_{M,i}$ of the total parallel assembly, as shown in Figure 4.6(a).

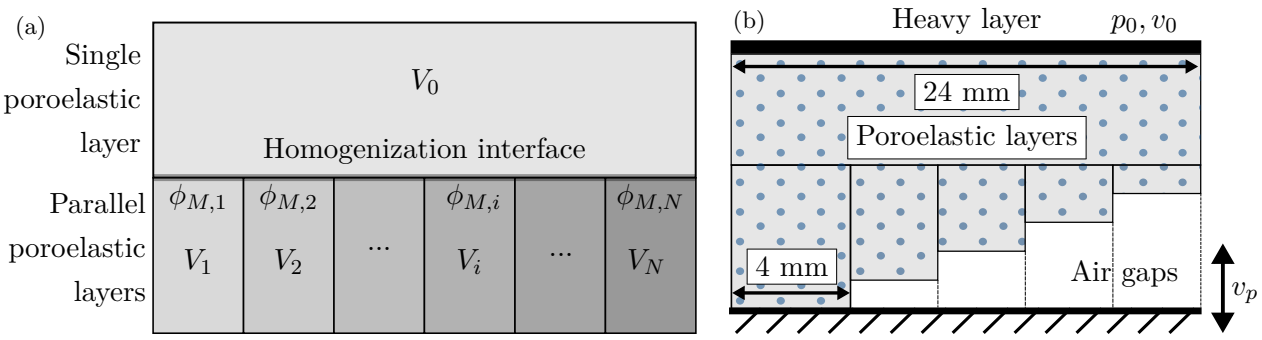

Figure 4.6. (a) Representation of the parallel layers used for PTMM, (b) schematic representation of the partial contact.

The interface conditions between all the layers provide the equality of velocities in the solid phases:

$$v^s_{x,0} = v^s_{x,i}, \tag{4.9}$$

$$v^s_{y,0} = v^s_{y,i}. \tag{4.10}$$

The continuity of pressure in the fluid gives:

$$\frac{\sigma^f_{x,0}}{\phi} = \frac{\sigma^f_{x,i}}{\phi_i \phi_{M,i}}, \tag{4.11}$$

and the continuity of stresses gives:

$$\sigma^s_{x,0} + \sigma^f_{x,0} = \sum_i \phi_{M,i}(\sigma^s_{x,i} + \sigma^f_{x,i}), \tag{4.12}$$

$$\sigma^s_{xy,0} = \sum_i \phi_{M,i}\sigma^s_{xy,i}. \tag{4.13}$$

Finally, the continuity of total flow gives:

$$\phi(v^f_x - v^s_x) = \sum_i \phi_{M,i}\,\phi_i \left(v^f_{x,i} - v^s_{x,i}\right). \tag{4.14}$$

Equations 4.9 to 4.14 can be integrated into the transfer matrix system to solve the whole problem, for example by adding them to the matrix D defined in Equation 1.139.

This model with parallel layers can be applied to the architected sheets of melamine foam obtained experimentally. The partial contact is achieved by creating triangular grooves in the melamine sheets, as shown in Figure 4.4(b), which can be represented in PTMM using the configuration shown in Figure 4.6(b). A porous layer represents the contact of the porous screen with the vibrating plate, and is placed in parallel with porous layers backed by and air gap of different depths. The PTMM relies on the hypothesis that the parallel media have a small size relative to the smallest wavelength. In this case, at 1600 Hz which is the highest frequency of interest for this experiment, the wavelength of acoustic waves in the air is around 212.5 mm, and the shortest solid-borne compression wavelength in the melamine foam is 81.9 mm. The pyramids have a base of width 24 mm, and a contact with the vibrating plate of width 4 mm, so the hypothesis that the parallel media are homogenizeable compared to the wavelengths is valid. The compression of the surface geometries of the porous sheet in contact with the metal plate is not considered in this chapter, and the nominal flat contact surface area is

considered.

4 | Comparison with experimental results

A structure-borne excitation of the plate is performed using a shaker. The injected mechanical power level is measured via an impedance head as $20\log_{10}\left(\frac{\Pi_{inj,mech}}{\Pi_0}\right)$, where $\Pi_0 = 10^{-12}$ W and $\Pi_{inj,mech} = \frac{1}{2}\mathrm{Re}\,(F^* v)$. The * notation denotes the complex conjugate. In practice, this is computed using the cross-power spectrum between the force F and acceleration spectra, measured by the impedance head. The velocity spectrum v is obtained by time integrating the acceleration by dividing it by $j\omega$. The injected mechanical power is plotted in Figure 4.7 for the different contact ratio coverings. This reveals that the injected power varies slightly depending on the covering. Further, less energy is injected into the system as the frequency increases.

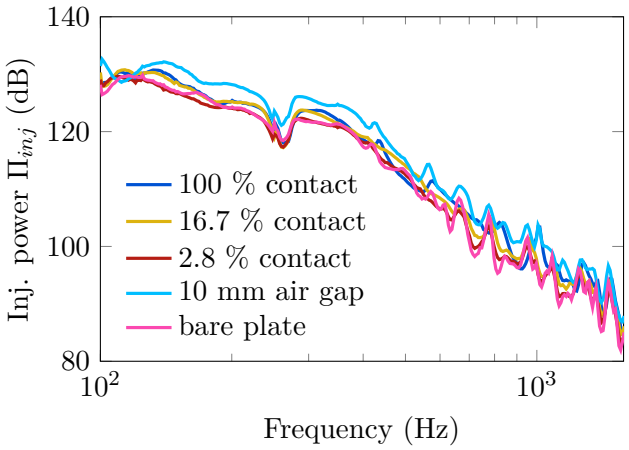

Figure 4.7. Injected mechanical power into the metal plate via the shaker.

The vibrational power level of the plate is computed as $20\log_{10}\left(\frac{\Pi_{vib}}{\Pi_0}\right)$, with $\Pi_{vib} = \frac{1}{2}\rho_0 c_0 S_p |v_p|^2$ and S_p the surface area of the plate. The average velocity spectrum of the plate v_p is measured via a laser vibrometer. The vibrational power level of the plate is shown in Figure 4.8(a). Similarly to the injected power, the vibrational power decreases with the frequency. Peaks of vibrational power can be found on the vibration power spectrum which are not on the injected power spectrum, due to the vibration modes of the plate. The frequency and amplitude of these modes are affected by the covering, as exemplified by the strong decrease in vibrational energy at 566 Hz in the case of 100 % contact between the screen and the plate. Moreover, the laser vibrometer measures the velocity at several locations along the plate, which allows us to see the vibration shapes of the plate, such as the first mode of the plate found at $f = 30$ Hz in Figure 4.8(b).

The radiated acoustical intensity is measured via a sound intensity probe. The radiated acoustic power level is computed as $10\log_{10}\left(\frac{\Pi_{rad}}{\Pi_0}\right)$, where Π_{rad} is the radiated power computed by integrating the radiated intensity over the radiation surface area. The radiated acoustic power level for the different configurations are shown in Figure 4.9.

The experimental IL is obtained experimentally from the $vibIL$ defined in Equation 4.4 and computed using PTMM. No estimator could be used between the injected power and the output acoustic intensity, due to acquisition setup limitations, however using a statistical estimator might give better results. The results are plotted in Figure 4.10. It can be seen that for 100 % contact, the resonance frequency is at 570 Hz. This frequency drops to around 422 HZ for 16.7 % contact and 408 Hz for 2.8 % contact. When there is a full air gap (0 % contact), the resonance drops to 202 Hz. The resonance frequencies predicted by PTMM are found at 620 Hz for 100 % contact, 579 Hz for

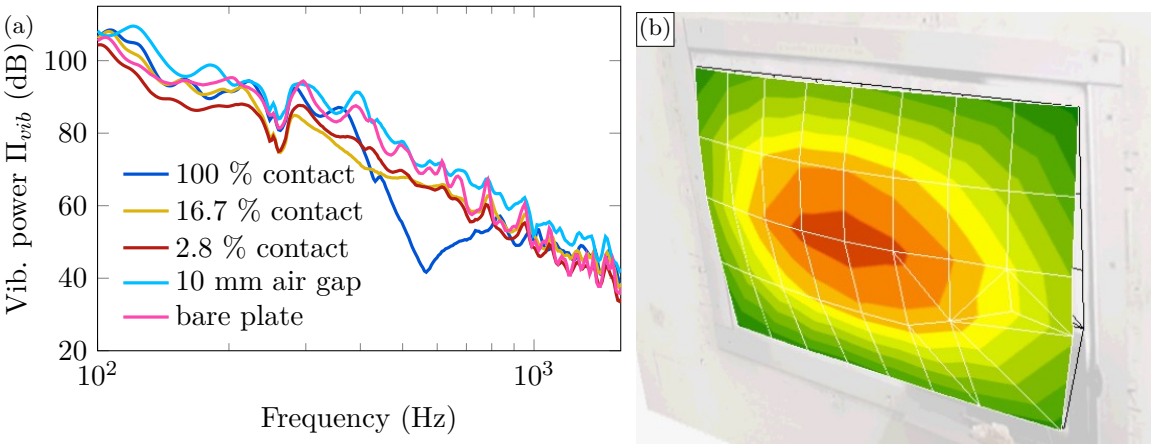

Figure 4.8. (a) Vibrational power spectra of the plate for different covering configurations. (b) First vibration mode of the plate at 30 Hz obtained from laser vibrometer measurements.

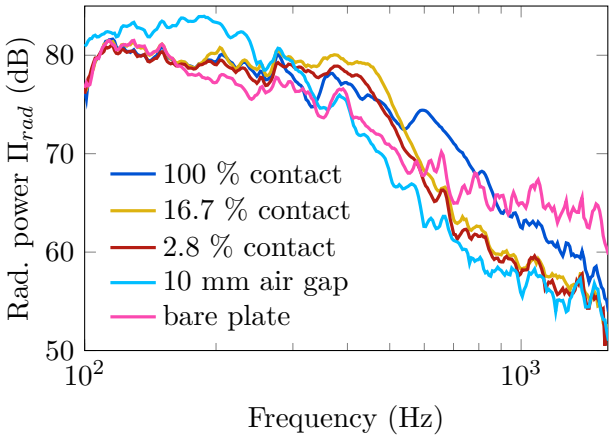

Figure 4.9. Radiated acoustic power level spectra for the different configurations.

16.7 % contact, 449 Hz for 2.8 % contact, and 225 Hz for a 10 mm air gap. These resonance frequencies are summarized in Table 4.1. Overall, this results confirm that as the amount of contact decreases, so does the resonance frequency, and consequently the decoupling occurs earlier which is advantageous for increasing the IL of the screens.

Table 4.1. Frequencies of the first peak of resonance in the measurement and in the models.

First resonance freq.	Measurement (Hz)	Model (Hz)	Difference (%)
100 % contact	570	557	2.3
16.7 % contact	422	418	1.0
2.8 % contact	408	316	33.6
0 % contact	202	225	10.8

When analysing the results in more detail, for full contact and for a 10 mm air gap, there is a fairly good correlation between the experimental and the modelled resonance frequencies. Furthermore, the resonance frequency with partial contact at However, the resonance frequency found experimentally for 2.8 % contact is very close to the resonance frequency for 16.7 % contact. This causes a large relative difference between the prediction and the measurement for the case of 2.8 % contact. Indeed, PTMM predicts a clear separation between these two configurations, which is a logical result.

There are several possible reasons why the result found experimentally for 2.8 % contact does

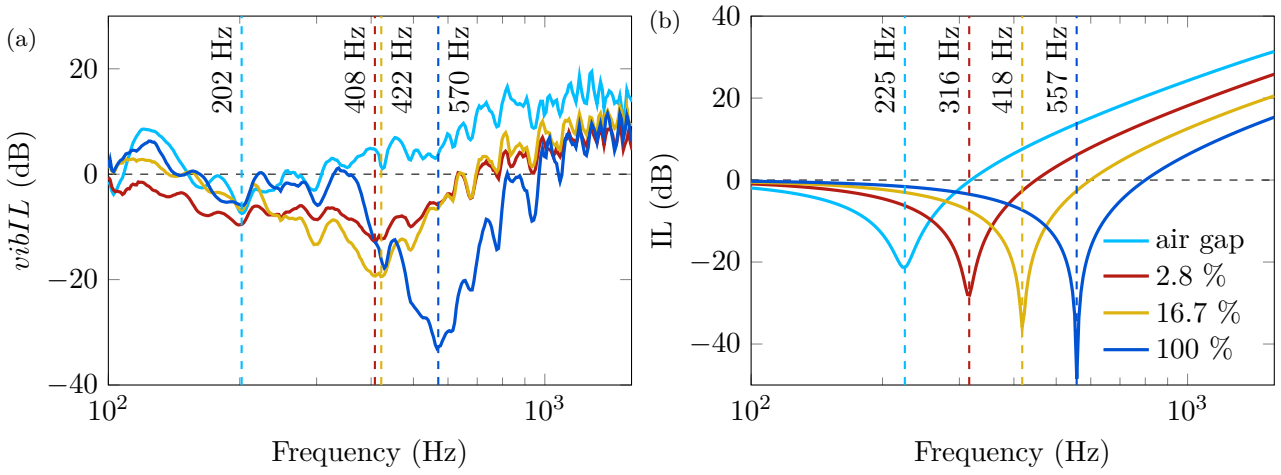

Figure 4.10. Insertion Losses of the acoustic screen for different contact ratios, indicated in the legend. (a) Experimental results, (b) predictions from PTMM.

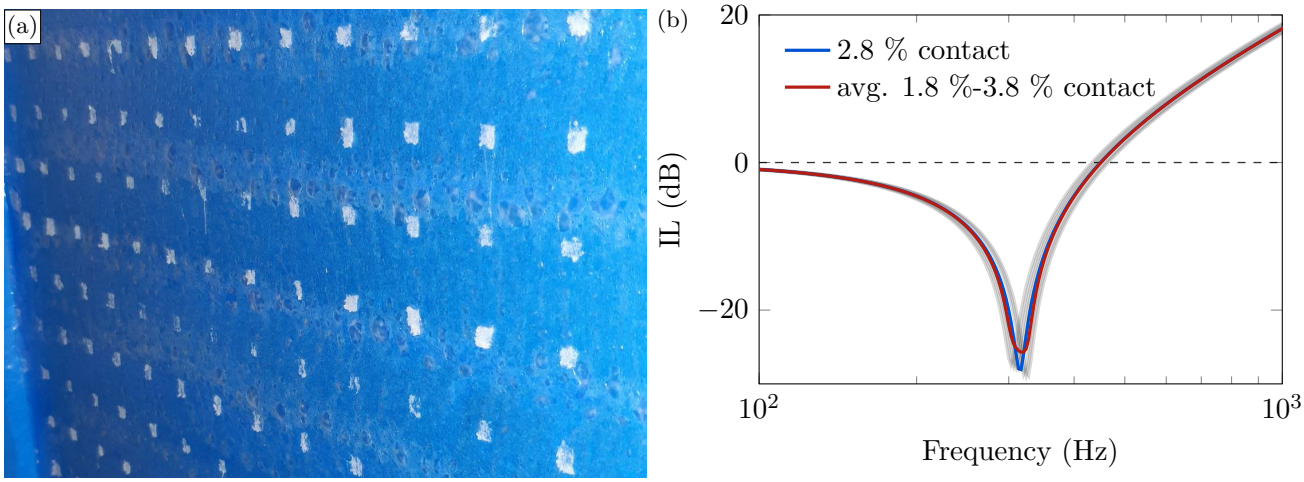

Figure 4.11. (a) Surface of the metal plate on which the porous sheet with 2.8 % contact was glued. The leftover pieces of foam are indicative of where displacement continuity was ensured. (b) Effect of an uncertainty of ±1 % of the partial contact on the average computed IL using PTMM.

not match expectations exactly. We can observe that damping found experimentally is much higher than the damping found in the prediction, where the resonance peaks are much more pronounced. To begin with, this could be due to a contact surface area that is greater than intended, due to preload during the glueing process. Moreover, the contact area of the individual truncated pyramids contains an experimental variation, as shown in Figure 4.11(a). The averaging effect of asperities with a different amount of contact results in a smoothed resonance peak as shown in Figure 4.11(b). Further, the small contact area of the pyramidal geometry for the 2.8 % contact case could give rise to larger displacements of the porous layer, and unforeseen nonlinear effects might appear. At last, the geometry is different between the 16 % contact case, which is composed of one-dimensional triangular grooves, and the 2.8 % contact case, which is composed of truncated pyramids. Consequently, their behaviour might be different due the Poisson effect for example, since in the 2.8 % contact case, the pyramids are free to deform in lateral directions without being constrained as in the 16 % contact case.

Further, the predictions performed with TMM and PTMM suppose the uniform displacement

of a piston-like surface, whereas the measurements are performed on a finite two-dimensional plate. As a consequence, the modal behaviour of the plate, its boundary conditions, and the lateral wave propagation effects are not modelled. To fully capture the behaviour of the studied configurations, a more complete model should be created, for instance using FEM to recreate the shape of the grooves and to model the lateral diffusion that occurs between layers that are considered parallel and independent in PTMM. Additionally, several excitation positions should be tested and averaged, and a statistical estimator could be used to compute the radiation efficiency to obtain more reliable results.

In summary, it was found that adding an air gap, even a partial one, helped decrease the first resonance frequency of the porous screen and heavy layer system, which is advantageous for improving the IL at low frequencies. This was found experimentally and numerically, by modelling the partial contact using PTMM. A good agreement is found for a partial contact of 16 %, achieved with 45° grooves. The configuration with 2.8 % contact, obtained by creating truncated pyramids on the surface of the porous screen, resulted in a resonance frequency that did not match the PTMM prediction exactly. A more accurate 3D representation of this configuration might help encompass the more complex phenomena occurring in this case.

5 | Conclusion

In this chapter, the Insertion Loss indicator of a porous multilayer was explored in different configurations, in order to evaluate how efficient the covering is at reducing the radiated acoustic power of a vibrating surface. An experiment measuring the IL efficiency of screens with different contact ratios was performed and compared to predictions computed using the Transfer Matrix Method. The experiment and the models showed that the less contact there is between the porous screen and the vibrating and radiating surface, the more effective the screen is at reducing the radiated noise level. This includes partial contact, which can often be found in real configurations, and which was created by cutting grooves into the porous screens.

The partial contact was modelled using Parallel Transfer Matrices, which is capable of predicting the continuous transition between 100 % to 0 % contact, and gives a good agreement with experimental results for a 16 % contact ratio. However, a disparity between experimental results and predictions was found for 2.8 % contact, which corresponds to a configuration with truncated pyramids, and which can be explained by the finiteness of the plate in the experimental setup and the lateral wave propagations which are not accounted for in the PTMM model. To improve the modelling of the partial contact in this configuration, a 3D model could be created using FEM for example. Despite this, the Parallel Transfer Matrix Method has been proposed as a method to quickly estimate the effect of partial contact surface area of a multilayer. This configuration has not been considered in the literature.

Additionally, indicators about the damping induced by the porous screen on the plate could be computed to further characterize the effects of the covering on the radiating surface. The induced damping can be estimated using Statistical Energy Analysis methods such as the Power Input Method (PIM) [328], the Decay Rate Method (DRM) [329] or Inhomogeneous Wave Correlation (IWC) [330]. This can also be done using the Force Analysis Technique (FAT) [331, 332] for example.

Key findings

- When a porous screen covered by a heavy layer is placed on a radiating surface, the decoupling that occurs after the resonance frequency of the system significantly reduces the radiated acoustic power. The resonance frequency can be lowered by reducing the modulus of the porous layer or by adding an air gap between the porous screen and the vibrating surface.
- Partial contact between the porous screen and the radiating surface results in a behaviour that is intermediary between full contact and no contact at all. This behaviour is obtained experimentally by cutting grooves in the porous screen, and is modelled using the Parallel Transfer Matrices approach.
- The Transfer Matrix approach is able to predict the configurations with 100 %, 16.7 % and 0 % contact fairly well.

General conclusions and perspectives

In this work, the modelling and the characterization of porous screens placed in contact with a radiating surface was studied. This work was performed within the context of the SEMPAE industrial project studying the encapsulation of car engines, in which the porous screens are placed directly in contact with the engine. Predicting the behaviour of this configuration requires accurate knowledge of the material properties, and especially of their mechanical properties, due to the strong contribution of solid-borne waves. Further, material surface roughness and its effect on the apparent stiffness of a porous layer is an important parameter to take into account to improve models. Material ageing and how it affects the material properties over time when pressed against a rigid surface is another important aspect in understanding encapsulation material effectiveness over long durations. At last, the screens' surface roughness and the engine's complex geometry cause partial contact between the two, which has a significant effect on their acoustic behaviour. These three subjects were studied in detail within this work.

The characterization of porous materials was performed in Chapter 2. Material transport properties can be measured directly for good accuracy, whereas properties obtained from inverse methods require more expertise and precaution to be applied effectively. Currently, it is difficult or impossible to directly measure certain material parameters, such as the thermal permeability q_0' for example. In the future, it could be helpful to have cheap, easy and reliable methods to directly measure all missing parameters.

The measurement of the mechanical properties is crucial for accurately modelling the encapsulation materials, and yet existing characterization methods contain many uncertainties. The influence of the temperature, the ambient air viscosity, the preload, and the relaxation were highlighted. The effect of the static strain applied to samples was explored, and the interpretation of mechanical characterization results for samples with uneven surface was clarified. Furthermore, the effect of material relaxation on the measured dynamic stiffness of a porous sample has been observed but is poorly understood. It has a significant effect and should be accounted for when samples are compressed. This problem is encountered but rarely explained in the literature. It would be useful to predict how the dynamic stiffness varies when a sample is compressed over a long duration, to improve the accuracy of characterization results as well as material long-term behaviour *in situ*. On top of this, the measurement of the Poisson ratio is difficult to perform accurately, since it is sensitive to many factors, and has significant effect on the determination of the elastic modulus. Thus, it would be useful to investigate a more thorough technique to characterize its value. All in all, melamine foam and five SEMPAE materials were characterized using the proposed methods, providing accurate predictions of the measured absorption coefficient.

The surface roughness of porous materials was studied in Chapter 3. The constitutive behaviour of melamine foam was studied, and its nonlinear stress-strain relationship was modelled with a hyperfoam model. Moreover, the stress of the material varies over time when kept at constant strain, and this was described with an ageing model predicting a relaxation time that increases linearly with time, indicating that the material relaxation occurs over very long durations.

Next, a rough surface was represented by a sum of macroscopic pyramidal asperities of foam.

Compressing these asperities reveal that they behave similarly to continuous elastic pyramidal geometries. This reveals that porous material asperities can be considered as continuous media once a few tens of cells are compressed. Further, the nonlinear strain-dependant modulus was masked by the shape geometry of the pyramid, suggesting that a constant equivalent modulus can be used for simplicity's sake. Notably, this equivalent modulus was different from the tangent modulus at small strains, which is the modulus sought after for acoustic applications. It would be interesting to develop a method to determine the equivalent modulus of a nonlinear material based on its strain dependant modulus and its geometry.

A surface roughness model was compared to compression measurements of a Greenflocks material, which is highly inhomogeneous due to its composition and manufacturing process. The resulting tendency suggests that the asperities on the Greenflocks' surface all have approximately the same height. To push the analysis of the Greenflocks' surface roughness further, the 3D scan of the material's surface could be exploited to extrapolate the geometry and height distribution of its asperities. Additionally, the surface roughness model developed is valid for isolated asperities, without any transition to the bulk behaviour of the material once all the asperities are compressed. Modelling the transition between the behaviour of the asperities and the bulk behaviour of the material would be useful to relate the dynamic stiffness of a sample to its modulus, as a function of compression amount. Furthermore, it would be interesting to establish a satisfying link between the modulus obtained from a static compression ramp and quasistatic QMA measurements. This might require adapting the strain rate of the compression ramp to get close to the strain rates obtained with the QMA, though this is not guaranteed to succeed due to the different natures of the static compression and quasistatic oscillatory modes.

The radiation of a plate covered by a porous screen with partial contact was studied in Chapter 4. The porous sheet is covered by a heavy layer, causing a strong resonance which increases the radiated acoustic power, and which is followed by a decoupling causing the radiated noise to decrease strongly with frequency. Partial contact between the porous screen and the radiating metal plate was controlled to simulate real configurations. The partial contact was obtained experimentally by cutting triangular grooves into sheets of melamine foam one or both directions. A simple implementation using the Parallel Transfer Matrix Method allows a rapid prediction of the effect of partial contact behaviour. Overall, both experiments and predictions find that the less contact there is between the screen and the radiating plate, the lower the resonance frequency is found, and the more the covering is efficient at reducing the radiated noise.

To improve the similarity between the configurations with 16 % contact and 2.8 % contact, the grooves should be cut the same way in both configurations, that is to say the grooves should all be made in only one direction or in two dimensions in both cases. Additionally, to facilitate the integration of partial contact into established FEM codes, it would be helpful to formulate an equivalent transfer matrix of the homogenized poroelastic medium instead of representing it with parallel transfer matrices. To improve the accuracy of the model's predictions of the resonance frequencies, a more complete three-dimensional representation of the partial contact should be explored. Finally, the contact area between the porous sheet and the radiating surface was controlled, but the materials are also compressed in real configurations. It would be interesting to create an interface layer, between the porous sheet and the radiating surface, that takes into consideration the compression of the material near the interface with a varying modulus and with a varying contact surface area.

Overall, the observations highlighted in this work can help improve the reliable characterization and the accurate modelling of porous engine encapsulation screens. Moreover, the work performed by the industrial partners within the SEMPAE project also resulted in fruitful outcomes. For example, PBN noise measurements were performed and analysed by Renault Group. Furthermore, the radiated power of a bare and covered real engine casing part were measured by Trèves Group, and were

correlated with a complete numerical model of the experimental setup.

Appendix A: Sensitivity of measured quantities to material parameters

The sensitivity of a porous medium's acoustic behaviour is influenced more or less by different parameters as a function of frequency. Knowing the influence range of each parameter can help guide inverse minimization procedures, by knowing in which frequency range each parameter is strongly expressed. This appendix shows examples of the sensitivity of several indicators to porous material properties. As a reminder, the sensitivity Δ and the normalized sensitivity Δ_n of the absorption coefficient α to a material parameter β are computed from

$$\Delta\alpha\left(\beta\right) = \frac{\partial\alpha}{\partial\beta},\ \ \Delta_n\alpha\left(\beta\right) = \frac{\beta}{\alpha}\frac{\partial\alpha}{\partial\beta}. \tag{A.1}$$

The normalized sensitivity of the melamine foam using an equivalent fluid JCAL model is shown in Figure A.1.

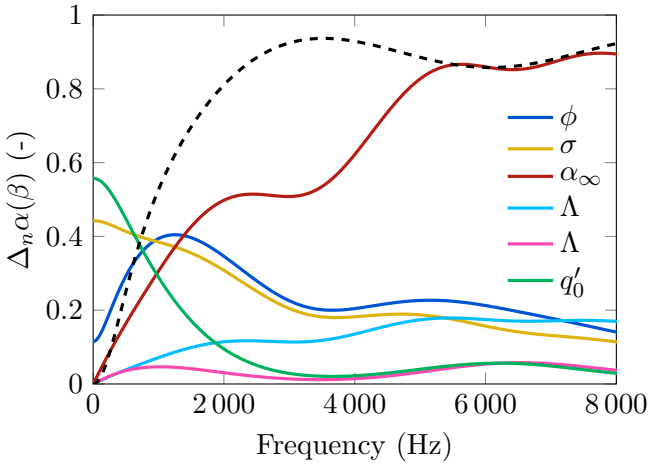

Figure A.1. Normalized sensitivity $\Delta_n\alpha$ of the absorption coefficient α for melamine foam with an equivalent fluid JCAL model to transport parameters. The black dashed line represents the value of α.

The sensitivity to material parameters can also be computed on the transfer function $\tilde{H}_{12}$ between the two microphones upstream from the characterized sample in impedance tube measurements. In this case, the sensitivity Δ of the transfer function $\tilde{H}_{12}$ to a parameter β is only normalized by the magnitude of β

$$\beta\Delta\,\tilde{H}_{12}\left(\beta\right) = \beta\frac{\partial\tilde{H}_{12}}{\partial\beta}. \tag{A.2}$$

The sensitivity $\beta\Delta\,\tilde{H}_{12}\left(\beta\right)$ of the real and imaginary parts of $\tilde{H}_{12}$ are plotted in Figure A.2.

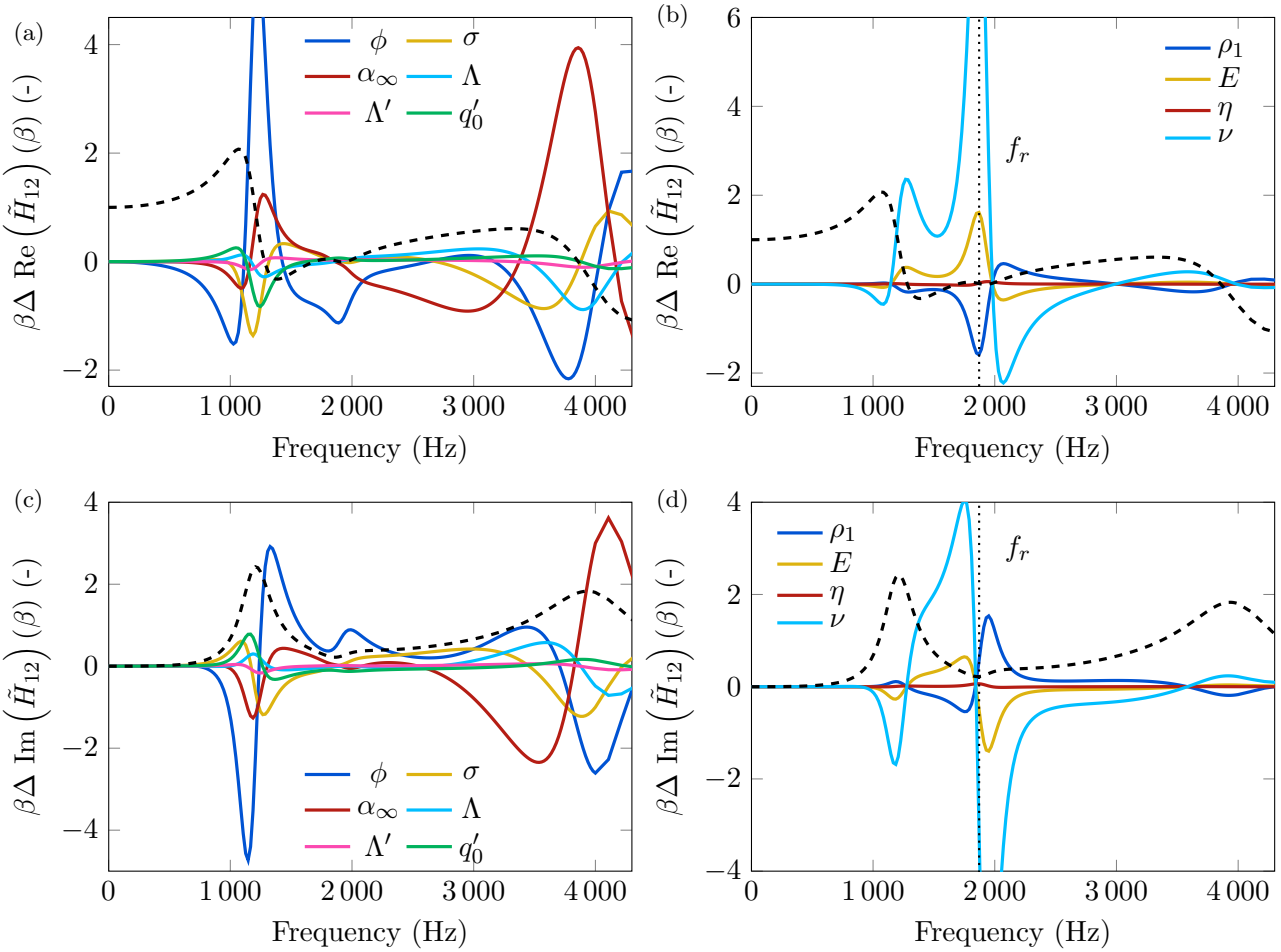

Figure A.2. Sensitivity of the real and imaginary parts of the microphone transfer function $\tilde{H}_{12}$ to material parameters β, normalized by the value of the parameter β: $\beta\Delta\,\tilde{H}_{12}\,(\beta)$. The sensitivity is computed for a melamine sample using the Biot model, and with the real microphone positions from the impedance tube shown in Figure 1.18. The black dashed line represents the value of $\tilde{H}_{12}$. The sensitivity is computed for the real part of $\tilde{H}_{12}$ to (a) transport parameters, and (b) mechanical parameters, and for the imaginary part of $\tilde{H}_{12}$ to (c) transport parameters, and (d) mechanical parameters.

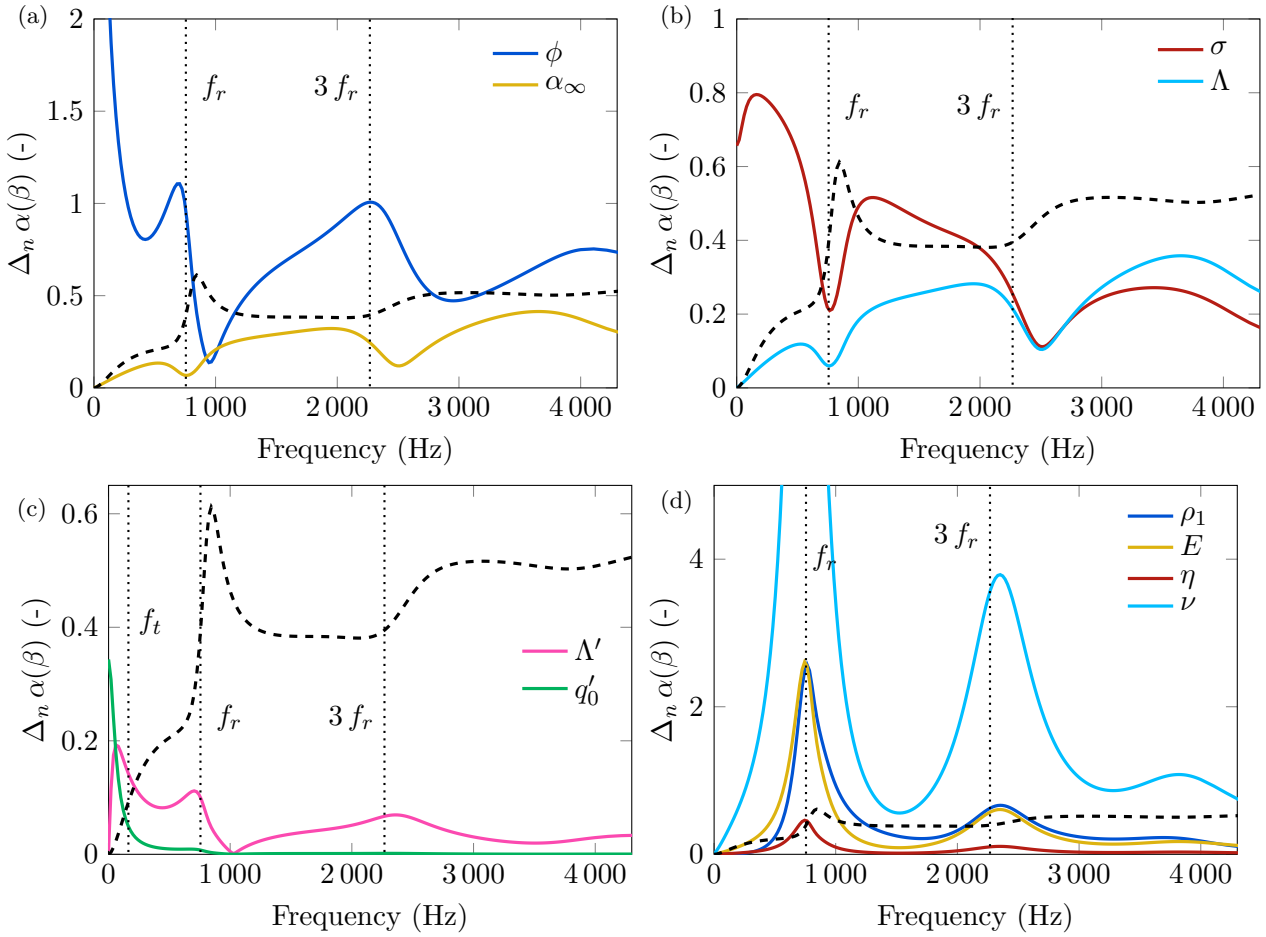

Figure A.3. Normalized sensitivity Δ_n of the absorption coefficient α to material parameters β. The sensitivity is computed for a PU250 foam using the Biot model. The black dashed line represents the value of α. Sensitivity is computed for (a) ϕ and α_∞, (b) viscous transport parameters σ and Λ, (c) thermal transport parameters Λ' and q_0', and (d) mechanical material parameters using a Biot JCAL model.

Appendix B: QMA measurements *in vacuo*

The quasistatic characterization of the mechanical properties of a porous material is done using a QMA device and assumes the hypothesis that the viscous effects of the air saturating the porous material has a negligible impact on measured stiffness. To verify this hypothesis, six studied materials are characterized on a QMA bench at atmospheric pressure and under vacuum. To do so, the QMA bench was placed inside a vacuum chamber, shown in Figure B.1.

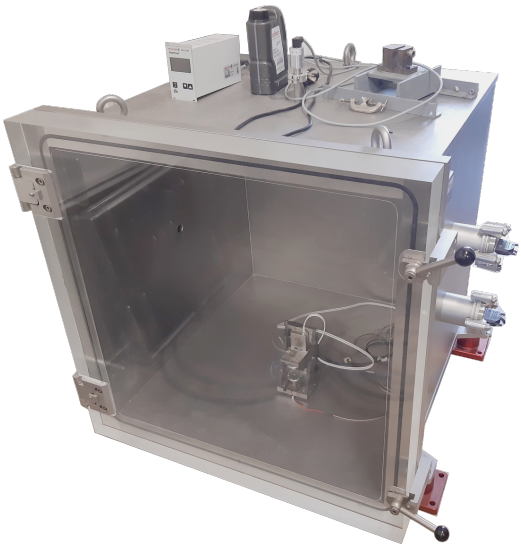

Figure B.1. QMA placed in the vacuum chamber.

The measured storage modulus E' at atmospheric pressure and *in vacuo* are shown in Figure B.2, and the measured loss factor η is shown in Figure B.3. The results show that the measured modulus increases and the loss factor decreases inside a vacuum. This can be attributed to two additional factors other than the vacuum. First, the relaxation can account for a variation of measurement results over time. Second, the strain gauge used to measure the displacement of the sample is not rated for low pressures. These two factors make it more difficult to conclude decisively on the effect of the surrounding air on the QMA results. Since there does not seem to be a strong frequency dependence of the variation of E' and η at atmospheric pressure and *in vacuo*, it can be assumed conservatively that material characterization can be performed with a QMA for these materials at atmospheric pressure with a negligible bias due to ambient air pressure.

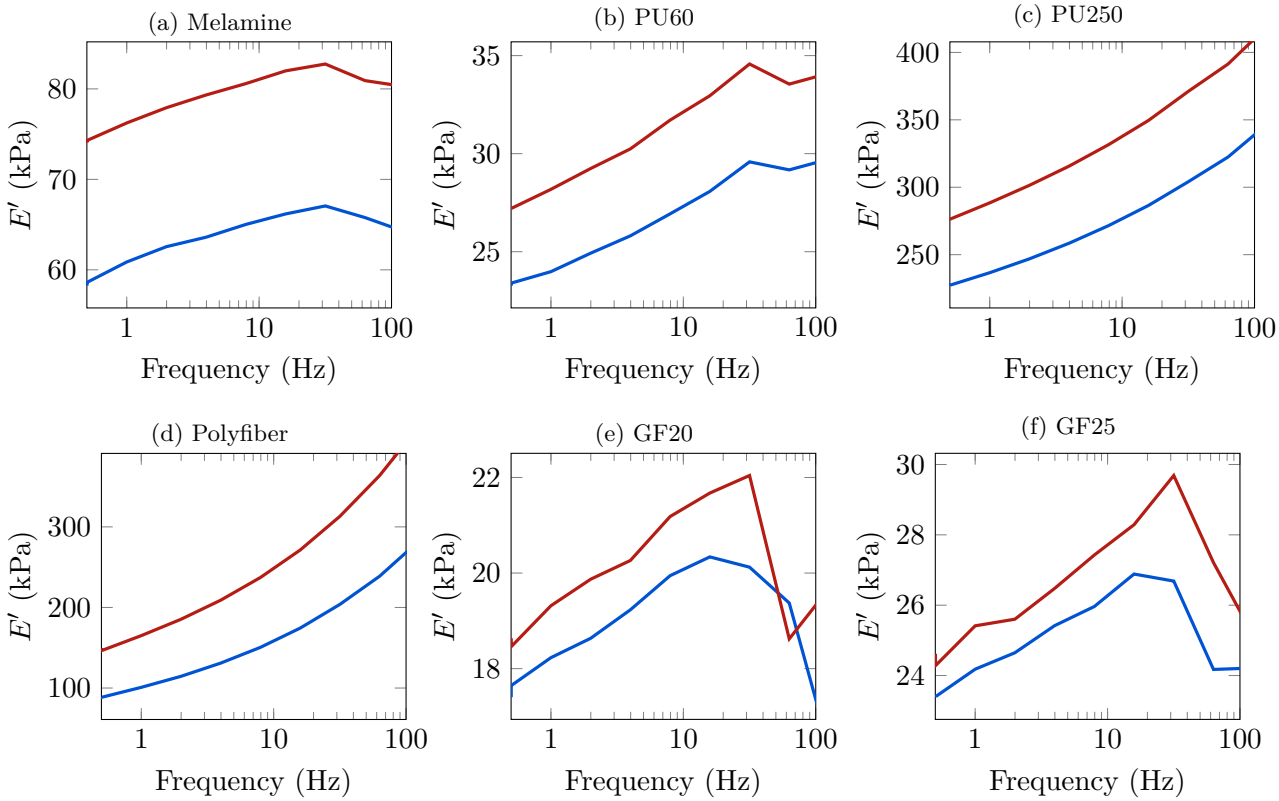

Figure B.2. Storage modulus E' measured on a QMA at atmospheric pressure (blue) and in a vacuum (red) for each material at 0 % strain.

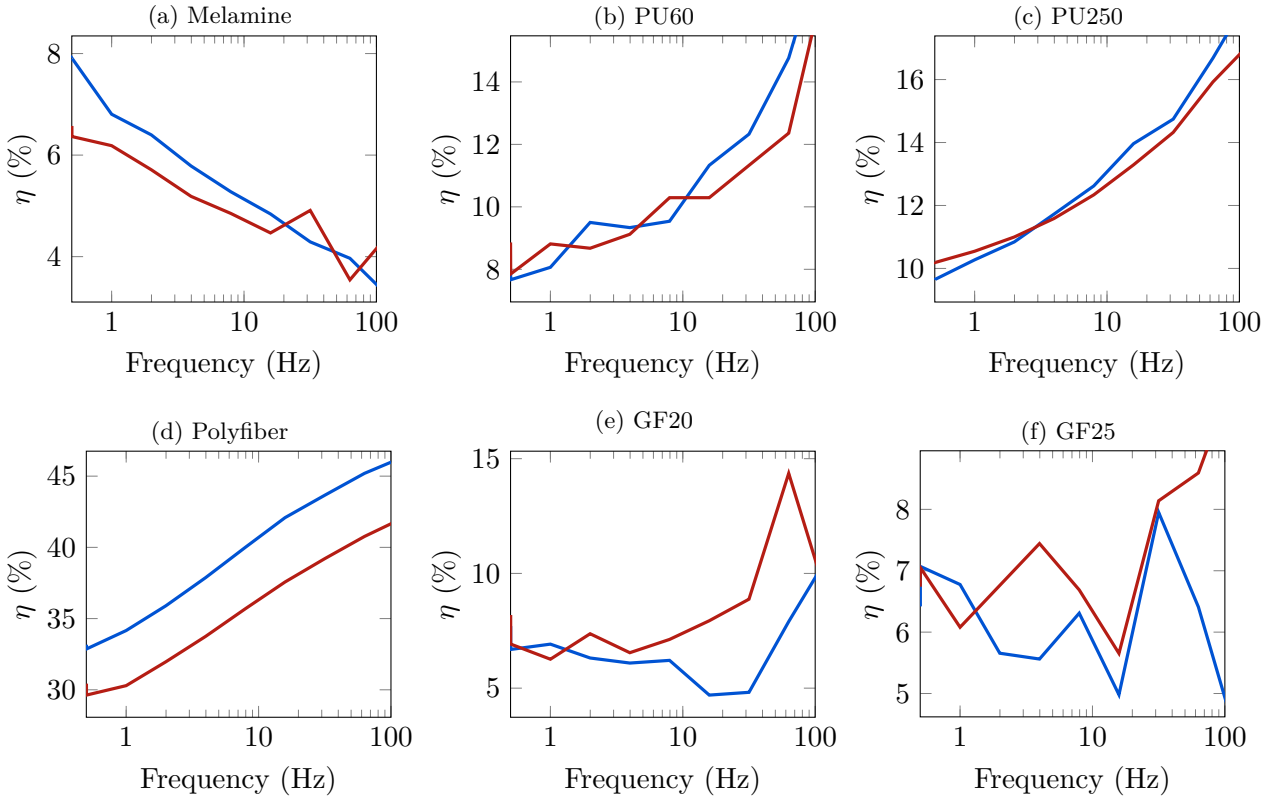

Figure B.3. eta measured on a QMA at atmospheric pressure (blue) and in a vacuum (red).

Appendix C: Relaxation and nonlinearity of different materials

The nonlinearity and the relaxation of a melamine foam is studied in Chapter 3. The behaviour that is found for the melamine foam also applies to different materials, as demonstrated here. The nonlinear stress-strain response of the PU60, PU250, and Greenflocks of nominal thicknesses 20 mm and 25 mm are shown in Figure C.1. This reveals that the typical nonlinearity of porous materials can be found for materials with different compositions and different microstructures.

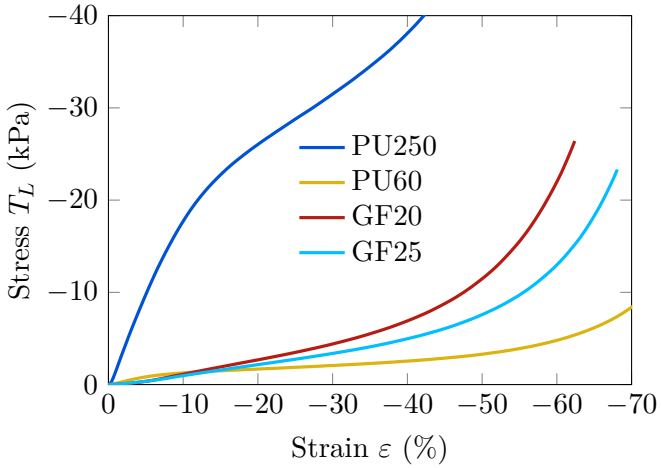

Figure C.1. Nonlinear stress-strain curve obtained for different materials being compressed.

Further, the stress relaxation of these foams behaves similarly to that for melamine foam, in that the stress continues to evolve at very long time scales with a relaxation time that increases. This is shown in Figure C.2, which plots the variation of the stress over time relative to the stress immediately following the compression ramp. The different materials are compressed at different strains ε. After 10 hours, the stress for the PU250 has varied by 19.2 %, by 33.8 % for the PU60, by 33.0 % for the Greenflocks 20 mm, and by 27.5 % for the Greenflocks 25 mm. Additionally, the PU60 was compressed to 15 % strain for 16.8 days, after which the stress had decreased by 46.9 %. These results strengthen the argument that taking into account the time relaxation of these materials when performing measurements at long durations is necessary.

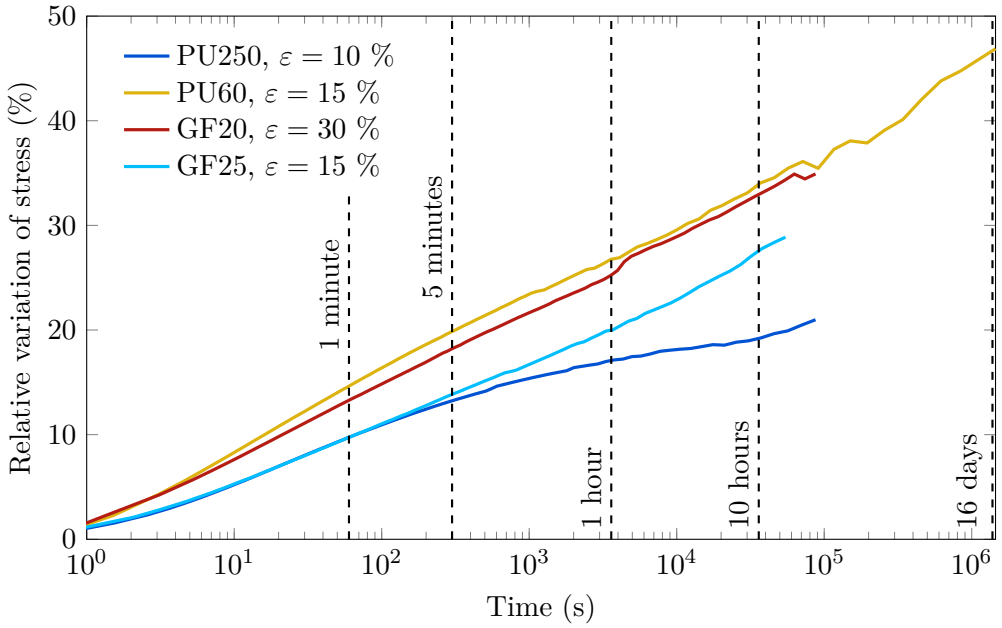

Figure C.2. Relative variation of the stress over time for different materials when the strain is kept constant.

References

[1] CRÉDOC and Bruitparif, "Perception du bruit en Ile-de-France fin 2021 Quelle situation après près de deux ans de pandémie ? Quelles évolutions en 5 ans ?" Tech. Rep., 2021. [Online]. Available: https://www.bruitparif.fr/pages/Focus/995PerceptiondubruitparlesFranciliens/RÃľsultatscompletsdel'ÃľtudeBruitparifCrÃľdocsurlaperceptiondubruitparlesFranciliens.pdf (Cited on page 1.)

[2] Bruitparif, "Bilan d'activité 2016," 2016. [Online]. Available: https://www.bruitparif.fr/pages/Actualites/2017-06-01Bruitparifpubliesonrapportd'activitÃľ2016/2017-06-01Rapportd'activitÃľ2016.pdf (Cited on page 1.)

[3] European Environment Agency, "Health risks caused by environmental noise in Europe," 2020. [Online]. Available: https://www.eea.europa.eu/publications/health-risks-caused-by-environmental (Cited on page 1.)

[4] ADEME, I CARE CONSULT, ÉNERGIES DEMAIN, M. Douillet, G. Sipos, L. Delugin, B. Bulliot, L. Remontet, and E. Bidault, "Estimation du coût social du bruit en France et analyse de mesures d'évitement simultané du bruit et de la pollution de l'air," Tech. Rep., 2021. [Online]. Available: https://librairie.ademe.fr/https://librairie.ademe.fr/air-et-bruit/4815-cout-social-du-bruit-en-france.html (Cited on pages 1 and 2.)

[5] J. Wayman and SIEMENS, "Simcenter Testlab Pass-by Noise Testing," 2022. [Online]. Available: https://community.sw.siemens.com/s/article/Simcenter-Testlab-Pass-by-Noise-Testing (Cited on page 1.)

[6] O. Journal, E. Union, S. D. Application, A. Specifications, T. Services, T. Approval, and A. Appendix, "Regulation No 51 of the Economic Commission for Europe of the United Nations (UNECE) - Uniform provisions concerning the approval of motor vehicles having at least four wheels with regard to their sound emissions," 2018. [Online]. Available: https://eur-lex.europa.eu/legal-content/EN/TXT/PDF/?uri=CELEX:42018X0798{&}rid=8 (Cited on page 1.)

[7] L. Jeroen, "Simcenter Testlab 2019.1: Answering trends in Pass-by Noise Engineering," 2019. [Online]. Available: https://blogs.sw.siemens.com/simcenter/simcenter-testlab-2019-1-answering-trends-in-pass-by-noise-engineering/ (Cited on page 1.)

[8] D. Ragot and F. Carta, "Contribution to the definition of acoustic performanes characterization cycles for electrical and hybrid motorizations," in *Congrès SIA Confort Automob. Ferrov.*, Le Mans, France, 2006. (Cited on page 4.)

[9] N. Jiménez, J.-P. Groby, and O. Umnova, *Acoustic Waves in Periodic Structures, Metamaterials, and Porous Media: From Fundamentals to Industrial Applications*, 2021. [Online]. Available: https://link.springer.com/book/10.1007{%}2F978-3-030-84300-7{#}about (Cited on page 4.)

[10] Y. Wang and K. H. Low, "Damped response analysis of nonlinear cushion systems by a linearization method," *Comput. Struct.*, vol. 83, no. 19-20, pp. 1584–1594, 2005. http://doi.org/10.1016/j.compstruc.2005.02.004 (Cited on page 2.)

[11] C. Ge and B. Rice, "Impact damping ratio of a nonlinear viscoelastic foam," *Polym. Test.*, vol. 72, no. August, pp. 187–195, 2018. http://doi.org/10.1016/j.polymertesting.2018.10.023. [Online]. Available: https://doi.org/10.1016/j.polymertesting.2018.10.023 (Cited on page 2.)

[12] J. H. Oh, J. S. Kim, V. H. Nguyen, and I. K. Oh, "Auxetic graphene oxide-porous foam for acoustic wave and shock energy dissipation," *Compos. Part B Eng.*, vol. 186, no. January, p. 107817, 2020. http://doi.org/10.1016/j.compositesb.2020.107817. [Online]. Available: https://doi.org/10.1016/j.compositesb.2020.107817 (Cited on page 2.)

[13] G. Belingardi, R. Montanini, and M. Avalle, "Characterization of polymeric structural foams under compressive impact loading by means of energy-absorption diagram," *Int. J. Impact Eng.*, vol. 25, no. 5, pp. 455–472, 2001. (Cited on pages 2 and 83.)

[14] F. Yang, Z. Li, Z. Liu, and Z. Zhuang, "Shock Loading Mitigation Performance and Mechanism of the PE/Wood/PU/Foam Structures," *Int. J. Impact Eng.*, vol. 155, no. January, p. 103904, 2021. http://doi.org/10.1016/j.ijimpeng.2021.103904. [Online]. Available: https://doi.org/10.1016/j.ijimpeng.2021.103904 (Cited on page 2.)

[15] H. M. Lee, D. H. Kim, D. Y. Kim, M. S. Kim, J. Park, and G. H. Yoon, "Enhancement of vibration attenuation and shock absorption in composite sandwich structures with porous foams and surface patterns," *Compos. Struct.*, vol. 295, no. December 2021, p. 115755, 2022. http://doi.org/10.1016/j.compstruct.2022.115755. [Online]. Available: https://doi.org/10.1016/j.compstruct.2022.115755 (Cited on page 2.)

[16] J. S. Chen and C. T. Sun, "Reducing vibration of sandwich structures using antiresonance frequencies," *Compos. Struct.*, vol. 94, no. 9, pp. 2819–2826, 2012. http://doi.org/10.1016/j.compstruct.2012.03.041. [Online]. Available: http://dx.doi.org/10.1016/j.compstruct.2012.03.041 (Cited on page 2.)

[17] R. A. Novak, "Sound insulation of lightweight double walls," *Appl. Acoust.*, vol. 37, no. 4, pp. 281–303, 1992. http://doi.org/10.1016/0003-682X(92)90016-L (Cited on page 3.)

[18] J. S. Bolton, N. M. Shiau, and Y. J. Kang, "Sound transmission through multi-panel structures lined with elastic porous materials," *J. Sound Vib.*, vol. 191, no. 3, pp. 317–347, 1996. http://doi.org/10.1006/jsvi.1996.0125 (Cited on page 3.)

[19] R. Panneton and N. Atalla, "Numerical prediction of sound transmission through finite multilayer systems with poroelastic materials," *J. Acoust. Soc. Am.*, vol. 100, no. 1, pp. 346–354, 1996. http://doi.org/10.1121/1.415956 (Cited on pages 3 and 12.)

[20] C. Lagarrigue, J. P. Groby, V. Tournat, O. Dazel, and O. Umnova, "Absorption of sound by porous layers with embedded periodic arrays of resonant inclusions," *J. Acoust. Soc. Am.*, vol. 134, no. 6, pp. 4670–4680, 2013. http://doi.org/10.1121/1.4824843 (Cited on page 3.)

[21] S. Luo and Q. Huang, "Resonance variation of double-layer structure composed of porous material and air layer based on biot theory," *Acta Acust. united with Acust.*, vol. 100, no. 3, pp. 477–484, 2014. http://doi.org/10.3813/AAA.918728 (Cited on page 3.)

[22] C. K. Amédin, A. Berry, and Y. Champoux, "Sound field of a baffled piston source covered by a porous medium layer," *J Acoust Soc Am*, vol. 1766, pp. 1757–1766, 1995. http://doi.org/https://doi.org/10.1121/1.413440. [Online]. Available: https://doi.org/10.1121/1.413440 (Cited on page 3.)

[23] A. Cummings, H. J. Rice, and R. Wilson, "Radiation damping in plates, induced by porous media," *J. Sound Vib.*, vol. 221, no. 1, pp. 143–167, 1999. http://doi.org/10.1006/jsvi.1998.1987 (Cited on page 3.)

[24] O. Doutres, N. Dauchez, and J.-M. Génevaux, "Porous layer impedance applied to a moving wall: Application to the radiation of a covered piston," *J. Acoust. Soc. Am.*, vol. 121, no. 1, pp. 206–213, 2007. http://doi.org/10.1121/1.2359233 (Cited on pages 3 and 29.)

[25] B. Campolina, N. Dauchez, N. Atalla, and O. Doutres, "Effect of porous material compression on the sound transmission of a covered single leaf panel," *Appl. Acoust.*, vol. 73, no. 8, pp. 791–797, 2012. http://doi.org/https://doi.org/10.1016/j.apacoust.2012.02.013 (Cited on page 3.)

[26] L. Lei, "Étude des matériaux poreux thermocompressés pour la modélisation des écrans acoustiques automobiles," Ph.D. dissertation, Laboratoire Roberval, Université de technologie de Compiègne, 2018. (Cited on pages 3 and 4.)

[27] A. Duval, M. Goret, N. Dauchez, A. Wilkinson, L. Polac, L. Lei, and G. Crignon, "Efficient Engine Encapsulation Strategy Using Poroelastic Finite Element Simulation," in *24SNVH*, Graz, 2024. (Cited on page 3.)

[28] Trèves Group, "Trèves Group website." [Online]. Available: https://www.treves-group.com/fr/expertises-produits (Cited on page 5.)

[29] O. Dazel, F. Sgard, F.-X. Becot, and N. Atalla, "Expressions of dissipated powers and stored energies in poroelastic media modeled by {u,U} and {u,P} formulations," *J. Acoust. Soc. Am.*, vol. 123, no. 4, pp. 2054–2063, 2008. http://doi.org/10.1121/1.2874520 (Cited on page 7.)

[30] C. T. Nguyen, V. Langlois, J. Guilleminot, F. Detrez, A. Duval, M. Bornert, P. Aimedieu, and C. Perrot, "Polydisperse solid foams: Multiscale modeling and simulations of elasto-acoustic properties including thin membrane effects," *Int. J. Solids Struct.*, vol. 249, no. April, p. 111684, 2022. http://doi.org/10.1016/j.ijsolstr.2022.111684. [Online]. Available: https://doi.org/10.1016/j.ijsolstr.2022.111684 (Cited on pages 8, 62, and 63.)

[31] L. L. Beranek, "Acoustical properties of homogeneous, isotropic rigid tiles and flexible blankets," *JASA*, vol. 19, no. 4, pp. 556–568, 1947. (Cited on pages 8 and 14.)

[32] C. Zwikker and C. W. Kosten, *Sound absorbing materials*. New York: Elsevier Pub. Co., 1949. [Online]. Available: https://babel.hathitrust.org/cgi/pt?id=mdp.39015002118456{&}seq=78{&}q1=decoupling (Cited on pages 8, 19, 28, and 50.)

[33] M. A. Biot, "Theory of Propagation of Elastic Waves in a Fluid-Saturated Porous Solid (low frequency range)," *J. Acoust. Soc. Am.*, vol. 28, no. 2, pp. 168–178, 1956. http://doi.org/10.1121/1.1908239 (Cited on page 8.)

[34] M. A. Biot, "Theory of Propagation of Elastic Waves in a Fluid-Saturated Porous Solid II. Higher Frequency Range," *J. Acoust. Soc. Am.*, vol. 28, no. 2, pp. 179–191, 1956. http://doi.org/10.1121/1.1908241 (Cited on page 8.)

[35] M. A. Biot and D. G. Willis, "The elastic coefficients of the theory of Consolidation," *J. Appl. Mech.*, pp. 594–601, 1957. http://doi.org/10.1002/9780470172766.ch13 (Cited on page 8.)

[36] R. Burridge and J. B. Keller, "Poroelasticity Equations Derived From Microstructure." vol. 1146, p. 226, 1981. (Cited on page 8.)

[37] L. Jaouen, "Biot's theory of poroelasticity." [Online]. Available: https://apmr.matelys.com/PropagationModels/BiotTheory/index.html (Cited on page 8.)

[38] R. S. Lakes, "Experimental microelasticity of two porous solids," *Int. J. Solids Struct.*, vol. 22, no. 1, pp. 55–63, 1986. http://doi.org/10.1016/0020-7683(86)90103-4. [Online]. Available: http://dx.doi.org/10.1016/0020-7683(86)90103-4 (Cited on page 8.)

[39] J. F. Allard and N. Atalla, *Propagation of sound in porous media*, Wiley, Ed., 2009. (Cited on pages 8, 14, 21, 23, 24, 25, 27, 29, 30, 33, 59, 63, 71, and 120.)

[40] D. L. Johnson, J. Koplik, and R. Dashen, "Theory of dynamic permeability and tortuosity in fluid saturated porous media," *J. Fluid Mech.*, vol. 176, pp. 379–402, 1987. http://doi.org/10.1017/S0022112087000727 (Cited on pages 8, 21, 23, 25, and 26.)

[41] Y. Champoux and J. F. Allard, "Dynamic tortuosity and bulk modulus in air-saturated porous media," *J. Appl. Phys.*, vol. 70, no. 4, pp. 1975–1979, 1991. http://doi.org/10.1063/1.349482 (Cited on pages 8, 23, and 25.)

[42] D. Lafarge, "Propagation du son dans les matériaux poreux à structure rigide saturés par un fluide viscothermique: définition de paramètres géométriques, analogie électromagnétique, temps de relaxation," Ph.D. dissertation, Uiversité du Maine, 1993. (Cited on pages 8, 26, and 35.)

[43] S. R. Pride and J. G. Berryman, "Connecting theory to experiment in poroelasticity," *J. Mech. Phys. Solids*, vol. 46, no. 4, pp. 719–747, 1998. http://doi.org/10.1016/S0022-5096(97)00043-4 (Cited on page 8.)

[44] L. L. Beranek, "Acoustic Impedance of Porous Materials," *J. Acoust. Soc. Am.*, vol. 13, no. 3, pp. 248–260, 1942. http://doi.org/10.1121/1.1916172 (Cited on pages 9, 50, and 51.)

[45] M. A. Biot, "Mechanics of deformation and acoustic propagation in porous media," *J. Appl. Phys.*, vol. 33, no. 4, pp. 1482–1498, 1962. http://doi.org/10.1063/1.1728759 (Cited on page 12.)

[46] O. Dazel, B. Brouard, C. Depollier, and S. Griffiths, "An alternative Biot's displacement formulation for porous materials," *J. Acoust. Soc. Am.*, vol. 121, no. 6, pp. 3509–3516, 2007. http://doi.org/10.1121/1.2734482 (Cited on pages 12 and 34.)

[47] P. Göransson, "A weighted residual formulation of the acoustic wave propagation through a flexible porous material and a comparison with a limp material model," *J. Sound Vib.*, vol. 182, no. 3, pp. 479–494, 1995. (Cited on pages 12 and 15.)

[48] N. Atalla, R. Panneton, and P. Debergue, "A mixed displacement-pressure formulation for poroelastic materials," *J. Acoust. Soc. Am.*, vol. 104, no. 3, pp. 1444–1452, 1998. http://doi.org/10.1121/1.424355 (Cited on page 12.)

[49] N. Dauchez, "Etude vibroacoustique des matériaux poroélastiques par éléments finis," Mécanique, acoustique, Université du Maine, Université de Sherbrooke, 1999. (Cited on page 12.)

[50] N. Dauchez, S. Sahraoui, and N. Atalla, "Convergence of poroelastic finite elements based on Biot displacement formulation," *J. Acoust. Soc. Am.*, vol. 109, no. 1, pp. 33–40, 2001. http://doi.org/10.1121/1.1289924 (Cited on page 12.)

[51] S. Rigobert, N. Atalla, and F. C. Sgard, "Investigation of the convergence of the mixed displacement-pressure formulation for three-dimensional poroelastic materials using hierarchical elements," *J. Acoust. Soc. Am.*, vol. 114, no. 5, pp. 2607–2617, 2003. http://doi.org/10.1121/1.1616579 (Cited on page 12.)

[52] N.-E. Hörlin, "Hierarchical finite element modelling of Biot ' s equations for vibro-acoustic modelling of layered poroelastic media," 2004. (Cited on page 12.)

[53] B. Brouard, D. Lafarge, and J. F. Allard, "A general method of modelling sound propagation in layered media," *J. Sound Vib.*, vol. 183, no. 1, pp. 129–142, 1995. http://doi.org/10.1006/jsvi.1995.0243 (Cited on pages 12 and 30.)

[54] A. P. Roberts and E. J. Garboczi, "Elastic properties of model random three-dimensional open-cell solids," *J. Mech. Phys. Solids*, vol. 50, no. 1, pp. 33–55, 2002. http://doi.org/10.1016/S0022-5096(01)00056-4 (Cited on page 13.)

[55] Q. M. Li, I. Magkiriadis, and J. J. Harrigan, "Compressive strain at the onset of densification of cellular solids," *J. Cell. Plast.*, vol. 42, no. 5, pp. 371–392, 2006. http://doi.org/10.1177/0021955X06063519 (Cited on pages 13 and 95.)

[56] T. Hentati, L. Bouazizi, M. Taktak, H. Trabelsi, and M. Haddar, "Multi-levels inverse identification of physical parameters of porous materials," *Appl. Acoust.*, vol. 108, pp. 26–30, 2016. http://doi.org/10.1016/j.apacoust.2015.09.013. [Online]. Available: http://dx.doi.org/10.1016/j.apacoust.2015.09.013 (Cited on pages 13 and 62.)

[57] J. A. Rinde, "Poisson's Ratio for Rigid Plastic Foams," *J. Appl. Polym. Sci.*, vol. 14, no. 1, pp. 1913–1926, 1970. (Cited on pages 13 and 99.)

[58] P. H. Mott and C. M. Roland, "Limits to Poisson's ratio in isotropic materials," *Phys. Rev. B - Condens. Matter Mater. Phys.*, vol. 80, no. 13, pp. 1–4, 2009. http://doi.org/10.1103/PhysRevB.80.132104 (Cited on page 13.)

[59] R. Lakes, "Foam Structures with a Negative Poisson's Ratio," *Am. Assoc. Adv. Sci.*, vol. 235, no. 4792, pp. 1038–1040, 1987. (Cited on page 13.)

[60] L. J. Gibson, "Modelling the mechanical behavior of cellular materials," *Mater. Sci. Eng. A*, vol. 110, no. C, pp. 1–36, 1989. http://doi.org/10.1016/0921-5093(89)90154-8 (Cited on pages 13, 83, and 94.)

[61] K. E. Evans and M. A. Nkansah, "Molecular network design," *Nature*, vol. 353, no. September 1991, p. 124, 1991. (Cited on page 13.)

[62] K. E. Evans and A. Alderson, "Auxetic materials: Functional materials and structures from lateral thinking!" *Adv. Mater.*, vol. 12, no. 9, pp. 617–628, 2000. http://doi.org/10.1002/(SICI)1521-4095(200005)12:9<617::AID-ADMA617>3.0.CO;2-3 (Cited on page 13.)

[63] R. Guastavino, "Elastic and acoustic characterisation of anisotropic porous materials," The Marcus Wallenberg Laboratory for Sound and Vibration Research Postal, KTH, 2008. (Cited on page 13.)

[64] A. Geslain, "Anisotropie naturelle et induite des matériaux poreux : étude expérimentale et modélisation," Acoustique, Université du Maine, 2011. (Cited on page 13.)

[65] M. Etchessahar, "Caractérisation mécanique en basses fréquences des matériaux acoustiques," Ph.D. dissertation, 2002. (Cited on pages 13, 75, 76, and 86.)

[66] K. Attenborough, "The prediction of oblique-incidence behaviour of fibrous absorbents," *J. Sound Vib.*, vol. 14, no. 2, pp. 183–191, 1971. http://doi.org/10.1016/0022-460X(71)90383-X (Cited on page 13.)

[67] S. Burke, "The absorption of sound by anisotropic porous layers," *J. Acoust. Soc. Am.*, vol. 74, no. S1, pp. S58–S58, 1983. http://doi.org/10.1121/1.2021041 (Cited on page 13.)

[68] V. Tarnow, "Measurements of anisotropic sound propagation in glass wool," *J. Acoust. Soc. Am.*, vol. 108, no. 5, pp. 2243–2247, 2000. http://doi.org/10.1121/1.1318900 (Cited on page 13.)

[69] V. Tarnow, "Dynamic measurements of the elastic constants of glass wool," *J. Acoust. Soc. Am.*, vol. 118, no. 6, pp. 3672–3678, 2005. http://doi.org/10.1121/1.2118267 (Cited on pages 13 and 76.)

[70] O. Doutres, N. Dauchez, J.-M. Génevaux, and O. Dazel, "Validity of the limp model for porous materials: A criterion based on the Biot theory," *J. Acoust. Soc. Am.*, vol. 122, no. 4, pp. 2038–2048, 2007. http://doi.org/10.1121/1.2769824 (Cited on pages 13 and 14.)

[71] M. Melon, E. Mariez, C. Ayrault, and S. Sahraoui, "Acoustical and mechanical characterization of anisotropic open-cell foams," *J. Acoust. Soc. Am.*, vol. 104, no. 5, pp. 2622–2627, 1998. http://doi.org/10.1121/1.423897 (Cited on pages 13, 76, and 77.)

[72] P. Göransson and N. E. Hörlin, "Vibro-acoustic modelling of anisotropic porous elastic materials: A preliminary study of the influence of anisotropy on the predicted performance in a multi-layer arrangement," *Acta Acust. united with Acust.*, vol. 96, no. 2, pp. 258–265, 2010. http://doi.org/10.3813/AAA.918275 (Cited on page 13.)

[73] N.-E. Hörlin and P. Göransson, "Weak, anisotropic symmetric formulations of Biot's equations for vibro-acoustic modelling of porous elastic materials," *Int. J. Numer. Methods Eng.*, vol. 84, pp. 1519–1540, 2010. http://doi.org/http://dx.doi.org/10.1002/nme.2955 (Cited on page 13.)

[74] T. Cavalieri, J. Boulvert, L. Schwan, G. Gabard, V. Romero-Garcìa, J.-P. Groby, M. Escouflaire, and J. Mardjono, "Acoustic wave propagation in effective graded fully anisotropic fluid layers," *J. Acoust. Soc. Am.*, vol. 146, no. 5, pp. 3400–3408, 2019. http://doi.org/10.1121/1.5131653 (Cited on page 13.)

[75] K. U. Ingard, "Locally and Nonlocally Reacting Flexible Porous Layers; a Comparison of Acoustical Properties." *Am. Soc. Mech. Eng.*, vol. 103, no. 80 -WA/NC-14, 1981. (Cited on page 14.)

[76] K. U. Ingard, *Notes on Sound Absorption Technology*, ser. Notebook. Noise Control Foundation, 1994. [Online]. Available: https://books.google.fr/books?id=FTnvAAAACAAJ (Cited on pages 14 and 15.)

[77] S. Katragadda, H.-Y. Lai, and J. S. Bolton, "A model for sound absorption by and sound transmission through limp fibrous layers," *J. Acoust. Soc. Am.*, vol. 98, no. 5_Supplement, pp. 2977–2977, 1995. http://doi.org/10.1121/1.413937 (Cited on page 14.)

[78] R. Panneton, "Comments on the limp frame equivalent fluid model for porous media," *J. Acoust. Soc. Am.*, vol. 122, no. 6, pp. EL217–EL222, 2007. http://doi.org/10.1121/1.2800895 (Cited on page 14.)

[79] O. Doutres, N. Dauchez, J. M. Génevaux, and O. Dazel, "A frequency independent criterion for describing sound absorbing materials by a limp frame model," *Acta Acust. united with Acust.*, vol. 95, no. 1, pp. 178–181, 2009. http://doi.org/10.3813/AAA.918139 (Cited on page 14.)

[80] P. Göransson, "Acoustic finite element formulation of a flexible porous material-a correction for inertial effects," *J. Sound Vib.*, vol. 185, no. 4, pp. 559–580, 1995. http://doi.org/10.1006/jsvi.1995.0401 (Cited on page 15.)

[81] R. M. Christensen, *Theory of Viscoelasticity*, 2nd ed. Livermore: Academic Press, 1982. (Cited on pages 15 and 17.)

[82] W. N. Findley, J. S. Lai, K. Onaran, and R. M. Christensen, *Creep and Relaxation of Nonlinear Viscoelastic Materials With an Introduction to Linear Viscoelasticity.* Dover publications, inc., New York, 1976. http://doi.org/10.1115/1.3424077 (Cited on page 15.)

[83] N. W. Tschoegl, *The phenomenological theory of linear viscoelastic behavior*, 1st ed., S.-V. B. Heidelberg, Ed., Berlin, 1989. (Cited on pages 15 and 16.)

[84] J. Salençon, *Viscoélasticité pour le Calcul des structures*, 2009th ed., Les presses des Ponts et Chaussées and Les éditions de l'école Polytechnique, Eds., Palaiseau, 2009. (Cited on page 15.)

[85] M. Le Deunf, "Caractérisation par problème inverse de l'amortissement présent dans une structure sandwich mousse - plaque avec différents types de contact à l'interface," Ph.D. dissertation. (Cited on pages 16 and 60.)

[86] J. C. Maxwell, "On the Dynamical Theory of Gases," *Philos. Trans. R. Soc. London*, vol. 157, pp. 49–88, 1867. [Online]. Available: http://www.jstor.org/stable/108968 (Cited on page 16.)

[87] E. Wiechert, *Ueber elastische Nachwirkung.* Hartungsche buchdr., 1889. [Online]. Available: https://books.google.fr/books?id=wCWhAQAACAAJ (Cited on page 17.)

[88] E. Wiechert, "Gesetze der elastischen Nachwirkung für constante Temperatur," *Ann. Phys.*, vol. 286, no. 10, pp. 335–348, 1893. http://doi.org/https://doi.org/10.1002/andp.18932861110 (Cited on page 17.)

[89] L. H. Sperling, "Sound and Vibration Damping with Polymers," pp. 5–22, 1990. http://doi.org/10.1021/bk-1990-0424.ch001 (Cited on page 18.)

[90] S. Arrhenius, "Über die Reaktionsgeschwindigkeit bei der Inversion von Rohrzucker durch Säuren," *Zeitschrift für Phys. Chemie*, vol. 4U, no. 1, pp. 226–248, 1889. http://doi.org/10.1515/zpch-1889-0416 (Cited on page 18.)

[91] S. Arrhenius, "Über die Dissociationswärme und den Einfluss der Temperatur auf den Dissociationsgrad der Elektrolyte," *Zeitschrift für Phys. Chemie*, vol. 4U, no. 1, pp. 96–116, 1889. http://doi.org/10.1515/zpch-1889-0408 (Cited on page 18.)

[92] M. L. Williams, R. F. Landel, and J. D. Ferry, "The Temperature Dependence of Relaxation Mechanisms in Amorphous Polymers and Other Glass-forming Liquids," *J. Am. Chem. Soc.*, vol. 77, no. 14, pp. 3701–3707, 1955. http://doi.org/10.1016/j.jnoncrysol.2017.12.029 (Cited on page 19.)

[93] H. Darcy, *Les fontaines publiques de la ville de Dijon.* Paris: Victor Dalmont, 1856. (Cited on page 20.)

[94] O. Umnova, K. Attenborough, and K.-m. Li, "A cell model for the acoustical properties of fibrous absorbents," in *29th Int. Convress Exhib. Noise Control Eng.*, Nice, 2000. (Cited on page 22.)

[95] D. L. Johnson, J. Koplik, and L. M. Schwartz, "New pore-size parameter characterizing transport in porous media," *Phys. Rev. Lett.*, vol. 57, no. 20, pp. 2564–2567, 1986. http://doi.org/10.1103/PhysRevLett.57.2564 (Cited on page 23.)

[96] M. E. Delany and E. N. Bazley, "Acoustical properties of fibrous absorbent materials," *Appl. Acoust.*, vol. 3, no. 2, pp. 105–116, 1970. http://doi.org/10.1016/0003-682X(70)90031-9 (Cited on page 24.)

[97] I. Dunn and W. A. Davern, "Calculation of Acoustic Impedance of multi-layer Absorbers," *Appl. Acoust.*, vol. 19, pp. 321–334, 1986. (Cited on page 24.)

[98] Y. Miki, "Acoustical properties of porous materials - Modifications of Delany-Bazley models," *J. Acoust. Soc. Jpn.*, vol. 1, pp. 19–24, 1990. (Cited on pages 24 and 54.)

[99] D. Lafarge, P. Lemarinier, J. F. Allard, and V. Tarnow, "Dynamic compressibility of air in porous structures at audible frequencies," *J. Acoust. Soc. Am.*, vol. 102, no. 4, pp. 1995–2006, 1997. http://doi.org/10.1121/1.419690 (Cited on pages 25 and 26.)

[100] S. R. Pride, F. D. Morgan, and A. F. Gangi, "Drag forces of porous-medium acoustics," *Phys. Rev. B*, vol. 47, no. 9, pp. 4964–4978, 1993. http://doi.org/10.1103/PhysRevB.47.4964 (Cited on page 26.)

[101] Lafarge, *Matériaux et acoustique 1 propagation des ondes acoustiques*, M. Bruneau and C. Potel, Eds. Lavoisier, 2006. (Cited on page 27.)

[102] Y. Salissou, *Caractérisation des propriétés acoustiques des matériaux poreux*, L. Canada and Archives, Eds., 2009. (Cited on pages 27 and 39.)

[103] K. C. Opiela, T. G. Zielinski, T. Dvorák, and S. Kúdela, "Perforated closed-cell aluminium foam for acoustic absorption," *Appl. Acoust.*, vol. 174, no. 2015, 2021. http://doi.org/10.1016/j.apacoust.2020.107706 (Cited on page 27.)

[104] T. G. Zielinski, "Microstructure-based calculations and experimental results for sound absorbing porous layers of randomly packed rigid spherical beads," *J. Appl. Phys.*, vol. 116, no. 3, 2014. http://doi.org/10.1063/1.4890218 (Cited on page 27.)

[105] T. G. Zielinski, F. Chevillotte, and E. Deckers, "Sound absorption of plates with micro-slits backed with air cavities: Analytical estimations, numerical calculations and experimental validations," *Appl. Acoust.*, vol. 146, pp. 261–279, 2019. http://doi.org/10.1016/j.apacoust.2018.11.026 (Cited on page 27.)

[106] T. G. Zielinski, R. Venegas, C. Perrot, M. Cervenka, F. Chevillotte, and K. Attenborough, "Benchmarks for microstructure-based modelling of sound absorbing rigid-frame porous media," *J. Sound Vib.*, vol. 483, 2020. http://doi.org/10.1016/j.jsv.2020.115441 (Cited on pages 27 and 62.)

[107] L. Jaouen, "Johnson-Champoux- Allard-Pride-Lafarge (JCAPL) model." [Online]. Available: https://apmr.matelys.com/PropagationModels/MotionlessSkeleton/JohnsonChampouxAllardPrideLafargeModel.html (Cited on page 27.)

[108] K. V. Horoshenkov, J.-P. Groby, and O. Dazel, "Asymptotic limits of some models for sound propagation in porous media and the assignment of the pore characteristic lengths," *J. Acoust. Soc. Am.*, vol. 139, no. 5, pp. 2463–2474, 2016. http://doi.org/10.1121/1.4947540. [Online]. Available: http://dx.doi.org/10.1121/1.4947540 (Cited on page 27.)

[109] K. V. Horoshenkov, A. Hurrell, and J.-P. Groby, "A three-parameter analytical model for the acoustical properties of porous media," *J. Acoust. Soc. Am.*, vol. 145, no. 4, pp. 2512–2517, 2019. http://doi.org/10.1121/1.5098778. [Online]. Available: http://dx.doi.org/10.1121/1.5098778 (Cited on pages 27, 70, 71, 72, and 73.)

[110] K. V. Horoshenkov, A. Hurrell, and J.-P. Groby, " Erratum: A three-parameter analytical model for the acoustical properties of porous media [J. Acoust. Soc. Am. 145 (4), 2512–2517 (2019)] ," *J. Acoust. Soc. Am.*, vol. 147, no. 1, pp. 146–146, 2020. http://doi.org/10.1121/10.0000560 (Cited on page 27.)

[111] N. Dauchez, "Acoustic radiation of a vibrating wall covered by a porous layer," in *158th Meet. Acoust. Soc. Am.*, San Antonio, 2009. (Cited on page 29.)

[112] J. F. Allard, Y. Champoux, and C. Depollier, "Modelization of layered sound absorbing materials with transfer matrices," *J. Acoust. Soc. Am.*, vol. 82, no. 5, pp. 1792–1796, 1987. http://doi.org/10.1121/1.395796 (Cited on page 30.)

[113] O. Dazel and G. Gabard, "Discontinuous Galerkin Methods for poroelastic materials," *Proc. Meet. Acoust.*, vol. 19, no. 2013, 2013. http://doi.org/10.1121/1.4799714 (Cited on page 34.)

[114] N. Atalla, "An overview of hte numerical modeling of poroelastic materials," in *Symp. Acoust. Poro-elastic Mater.*, Bradford (UK, 2005, pp. 133–142. (Cited on page 34.)

[115] R. Panneton and X. Olny, "Acoustical determination of the parameters governing viscous dissipation in porous media," *J. Acoust. Soc. Am.*, vol. 119, no. 4, pp. 2027–2040, 2006. http://doi.org/10.1121/1.2169923 (Cited on pages 36, 65, and 67.)

[116] X. Olny and R. Panneton, "Acoustical determination of the parameters governing thermal dissipation in porous media," *J. Acoust. Soc. Am.*, vol. 123, no. 2, pp. 814–824, 2008. http://doi.org/10.1121/1.2828066 (Cited on pages 36 and 65.)

[117] Afnor, "NF EN ISO 10534-2 : Acoustics-Determination of Sound Absorption Coefficient and Impedance in Impedance Tube Part 2: Transfer Function Method," 2003. (Cited on pages 37 and 41.)

[118] ASTM, "ASTM E 1050 : Standard test method for impedance and absorption of acoustical materials using a tube, two microphones and a digital frequency analysis system," New York, NY, pp. 1–12, 1998. (Cited on pages 37 and 38.)

[119] ISO, "ISO 10534-2:2023 Acoustics — Determination of acoustic properties in impedance tubes — Part 2: Two-microphone technique for normal sound absorption coefficient and normal surface impedance," 2023. [Online]. Available: https://www.iso.org/standard/81294.html (Cited on page 38.)

[120] M. Wolkesson, "Evaluation of impedance tube methods - A two microphone in-situ method for road surfaces and the three microphone transfer function method for porous materials," Master's thesis, Chalmers University of technology, 2013. (Cited on page 38.)

[121] A. F. Seybert, "Notes on Absorption and Impedance Measurements." [Online]. Available: http://www.angelofarina.it/Public/Standing-Wave/Absorption{_}Meas.pdf (Cited on page 38.)

[122] H. Utsuno, T. Tanaka, T. Fujikawa, and A. F. Seybert, "Transfer function method for measuring characteristic impedance and propagation constant of porous materials," *J. Acoust. Soc. Am.*, vol. 86, no. 2, pp. 637–643, 1989. http://doi.org/10.1121/1.398241 (Cited on page 39.)

[123] T. Iwase, Y. Izumi, and R. Kawabata, "A new measuring method for sound propagation constant by using sound tube without any air spaces back of a test material," in *Internoise 98*. Christchurch, New Zealand: Institute of Noise Control Engineering, 1998, pp. 888–1338. (Cited on page 39.)

[124] B. H. Song and J. S. Bolton, "A transfer-matrix approach for estimating the characteristic impedance and wave numbers of limp and rigid porous materials," *J. Acoust. Soc. Am.*, vol. 107, no. 3, pp. 1131–1152, 2000. http://doi.org/10.1121/1.428404 (Cited on page 39.)

[125] ANSI, "ASTM E2611-19 : Standard Test Method for Normal Incidence Determination of Porous Material Acoustical Properties Based on the Transfer Matrix Method," p. 1. (Cited on pages 39 and 41.)

[126] O. Doutres, R. Panneton, and Y. Salissou, "An additional configuration to standard ASTM E2611-09 for measuring the normal incidence sound transmission loss in a modified impedance tube," *Proc. Acoust. 2012 Nantes Conf.*, no. April, pp. 2029–2033, 2012. [Online]. Available: http://hal.archives-ouvertes.fr/hal-00810671/ (Cited on page 39.)

[127] Y. Salissou, R. Panneton, and O. Doutres, "Complement to standard method for measuring normal incidence sound transmission loss with three microphones," *J. Acoust. Soc. Am.*, vol. 131, no. 3, pp. EL216–EL222, 2012. http://doi.org/10.1121/1.3681016 (Cited on page 39.)

[128] T. Dupont, P. Leclaire, R. Panneton, K. Verdière, and S. Elkoun, "A method for measuring the acoustic properties of a porous sample mounted in a rigid ring in acoustic tubes," *Proc. Meet. Acoust.*, vol. 19, pp. 0–8, 2013. http://doi.org/10.1121/1.4799701 (Cited on page 41.)

[129] K. V. Horoshenkov, A. Khan, F.-X. Bécot, L. Jaouen, F. Sgard, A. Renault, N. Amirouche, F. Pompoli, N. Prodi, P. Bonfiglio, G. Pispola, F. Asdrubali, J. Hübelt, N. Atalla, C. K. Amédin, W. Lauriks, and L. Boeckx, "Reproducibility experiments on measuring acoustical properties of rigid-frame porous media (round-robin tests)," *J. Acoust. Soc. Am.*, vol. 122, no. 1, pp. 345–353, 2007. http://doi.org/10.1121/1.2739806 (Cited on page 41.)

[130] F. Pompoli, P. Bonfiglio, K. V. Horoshenkov, A. Khan, L. Jaouen, F.-X. Bécot, F. Sgard, F. Asdrubali, F. D'Alessandro, J. Hübelt, N. Atalla, C. K. Amédin, W. Lauriks, and L. Boeckx, "How reproducible is the acoustical characterization of porous media?" *J. Acoust. Soc. Am.*, vol. 141, no. 2, pp. 945–955, 2017. http://doi.org/10.1121/1.4976087. [Online]. Available: http://dx.doi.org/10.1121/1.4976087 (Cited on page 41.)

[131] L. J. Gibson, "by Lorna Jane Gibson A dissertation submitted to the University of Cambridge for the Degree of Dbctor of Philosophy Churchill College Augus t 1981," 1981. (Cited on page 45.)

[132] A. Duval, G. Crignon, M. Roux, and D. Lemaire, "Green chips urethane based poroelastic materials: an opportunity for up to 80 % recycled and 100 % recyclable content coming from recycled PU mattresses," in *Resour. Effic. Veh. Conf.*, no. June, 2021. (Cited on pages 46 and 115.)

[133] A. Duval, G. Crignon, D. Lemaire, and M. R. Treves, "Arnaud Duval, Guillaume Crignon, Dominique Lemaire, and Maxime Roux Treves," pp. 1–10, 2022. http://doi.org/10.4271/2022-01-0961.Received (Cited on pages 46 and 115.)

[134] ASTM, "ASTM D2856-94 : Standard Test Method for Open-Cell Content of Rigid Cellular Plastics by the Air Pycnometer," 1998. (Cited on page 49.)

[135] S. Lowell and J. E. Shields, "Pore spectra from continuous scan mercury porosimetry," *Powder Technol.*, vol. 28, no. 2, pp. 201–204, 1981. http://doi.org/10.1016/0032-5910(81)87044-1 (Cited on page 49.)

[136] R. Dawson and E. K. Duursma, "Mercury Porosimetry : State of the Art," *Elsevier Oceanogr. Ser.*, vol. 31, no. C, pp. 497–512, 1981. http://doi.org/10.1016/S0422-9894(08)70338-6 (Cited on page 49.)

[137] H. Giesche, *Mercury Porosimetry*, F. Schüth, K. S. W. Sing, and J. Weitkamp, Eds., Weinheim, Federal Republic of Germany, 2002, vol. 1. http://doi.org/10.1002/9783527618286.ch9 (Cited on page 49.)

[138] R. Panneton and E. Gros, "A Missing Mass Method to Measure the Open Porosity of Porous Solids," *Acta Acust.*, vol. 91, no. 2, pp. 342–348, 2005. (Cited on page 49.)

[139] J.-P. Groby, E. Ogam, L. De Ryck, N. Sebaa, and W. Lauriks, "Analytical method for the ultrasonic characterization of homogeneous rigid porous materials from transmitted and reflected coefficients," *J. Acoust. Soc. Am.*, vol. 127, no. 2, pp. 764–772, 2010. http://doi.org/10.1121/1.3283043 (Cited on pages 50, 53, and 58.)

[140] D. Parmentier, B. Castagnede, O. Dazel, F. Fohr, N. Poulain, D. Parmentier, B. Castagnede, O. Dazel, F. Fohr, B. Brouard, F. Fohr, B. Brouard, and N. Poulain, "Mesure directe de la porosité des matériaux insonorisants

par réflexion d'ondes ultrasonores basse fréquence," in *10ème Congrès Français d'Acoustique*, Lyon, France, 2010. (Cited on page 50.)

[141] L. Jaouen and F.-X. Bécot, "Acoustical characterization of perforated facings," *J. Acoust. Soc. Am.*, vol. 129, no. 3, pp. 1400–1406, 2011. http://doi.org/10.1121/1.3552887 (Cited on page 50.)

[142] J. V. D. Eijk and C. Zwikker, "Absorption of sound by porous materials I," *Physica*, vol. 8, no. 2, pp. 149–158, 1941. (Cited on page 50.)

[143] Y. Champoux, M. R. Stinson, and G. A. Daigle, "Air-based system for the measurement of porosity," vol. 916, pp. 910–916, 1991. http://doi.org/https://doi.org/10.1121/1.1894653 (Cited on page 50.)

[144] P. Leclaire, O. Umnova, K. V. Horoshenkov, and L. Maillet, "Porosity measurement by comparison of air volumes," *Rev. Sci. Instrum.*, vol. 74, no. 3 I, pp. 1366–1370, 2003. http://doi.org/10.1063/1.1542666 (Cited on page 50.)

[145] Y. Salissou and R. Panneton, "Pressure/mass method to measure open porosity of porous solids," *Appl. Phys.*, vol. 101, no. 12, 2007. http://doi.org/10.1063/1.2749486 (Cited on pages 51 and 52.)

[146] E. Gourdon and M. Seppi, "On the use of porous inclusions to improve the acoustical response of porous materials: Analytical model and experimental verification," *Appl. Acoust.*, vol. 71, no. 4, pp. 283–298, 2010. http://doi.org/10.1016/j.apacoust.2009.11.004. [Online]. Available: http://dx.doi.org/10.1016/j.apacoust.2009.11.004 (Cited on pages 52, 55, 57, 70, and 73.)

[147] N. Kino and T. Ueno, "Comparisons between characteristic lengths and fibre equivalent diameters in glass fibre and melamine foam materials of similar flow resistivity," *Appl. Acoust.*, vol. 69, no. 4, pp. 325–331, 2008. http://doi.org/10.1016/j.apacoust.2006.11.008 (Cited on pages 52, 55, 57, 70, 73, and 104.)

[148] M. Niskanen, J.-P. Groby, A. Duclos, O. Dazel, J. C. Le Roux, N. Poulain, T. Huttunen, and T. Lähivaara, "Deterministic and statistical characterization of rigid frame porous materials from impedance tube measurements," *J. Acoust. Soc. Am.*, vol. 142, no. 4, pp. 2407–2418, 2017. http://doi.org/10.1121/1.5008742 (Cited on pages 52, 55, 57, 61, 62, 70, and 73.)

[149] L. Lei, N. Dauchez, and J. D. Chazot, "Prediction of the six parameters of an equivalent fluid model for thermocompressed glass wools and melamine foam," *Appl. Acoust.*, vol. 139, no. June 2017, pp. 44–56, 2018. http://doi.org/10.1016/j.apacoust.2018.04.010. [Online]. Available: https://doi.org/10.1016/j.apacoust.2018.04.010 (Cited on pages 52, 55, 57, 60, 70, and 73.)

[150] R. J. Brown, "Connection between formation factor for electrical resistivity and fluid-solid coupling factor in Biot's equations for acoustic waves in fluid-filled porous media." *Geophysics*, vol. 45, no. 8, pp. 1269–1275, 1980. http://doi.org/10.1190/1.1441123 (Cited on page 53.)

[151] B. Brouard, "Validation Par Holographie Acoustique De Nouveaux Modèles Pour La Propagation Des Ondes Dans Les Matériaux Poreux Stratifiés," 1994. (Cited on page 53.)

[152] J. F. Allard, B. Castagnede, M. Henry, and W. Lauriks, "Evaluation of tortuosity in acoustic porous materials saturated by air," vol. 65, no. 9, pp. 754–755, 1994. (Cited on pages 53 and 59.)

[153] P. Leclaire, L. Kelders, W. Lauriks, C. Glorieux, and J. Thoen, "Determination of the viscous characteristic length in air-filled porous materials by ultrasonic attenuation measurements," *J. Acoust. Soc. Am.*, vol. 99, no. 4, pp. 1944–1948, 1996. http://doi.org/10.1121/1.415378 (Cited on pages 53 and 59.)

[154] P. Leclaire, L. Kelders, W. Lauriks, M. Melon, N. Brown, and B. Castagnède, "Determination of the viscous and thermal characteristic lengths of plastic foams by ultrasonic measurements in helium and air," *J. Appl. Phys.*, vol. 80, no. 4, pp. 2009–2012, 1996. http://doi.org/10.1063/1.363817 (Cited on pages 53 and 59.)

[155] Mecanum, "Manuel d'utilisation : Tortuosity Meter Model : TOR Transmission method Installation and Instruction Manual." (Cited on page 53.)

[156] Z. E. A. Fellah, S. Berger, W. Lauriks, C. Depollier, C. Aristégui, and J.-Y. Chapelon, "Measuring the porosity and the tortuosity of porous materials via reflected waves at oblique incidence," *J. Acoust. Soc. Am.*, vol. 113, no. 5, pp. 2424–2433, 2003. http://doi.org/10.1121/1.1567275 (Cited on page 54.)

[157] Mecanum, "Manuel d'utilisation : Tortuosity Meter Model : TOR Reflection method Installation and Instruction Manual." (Cited on page 54.)

[158] ISO, "ISO 9053-1 Determination of airflow resistance — Part 1 : Static airflow method," 2018. (Cited on page 56.)

[159] ISO, "ISO 9053-1 Determination of airflow resistance — Part 2 : Alternating airflow method," 2020. (Cited on page 56.)

[160] ASTM, "ASTM C522-03 Standard Test Method for Airflow Resistance of Acoustical Materials," 2016. (Cited on page 56.)

[161] D. A. Bies and C. H. Hansen, "Flow resistance information for acoustical design," *Appl. Acoust.*, vol. 13, no. 5, pp. 357–391, 1980. http://doi.org/10.1016/0003-682X(80)90002-X (Cited on pages 57 and 62.)

[162] M. R. Stinson and G. A. Daigle, "Electronic system for the measurement of flow resistance," *J. Acoust. Soc. Am.*, vol. 83, no. 6, pp. 2422–2428, 1988. http://doi.org/10.1121/1.396321 (Cited on page 57.)

[163] W. Sutherland, "The viscosity of gases and molecular force," *London, Edinburgh, Dublin Philos. Mag. J. Sci.*, vol. 36, no. 223, pp. 507–531, 1893. http://doi.org/10.1080/14786449308620508 (Cited on page 57.)

[164] I. L. Vér and L. L. Beranek, *Noise and Vibration Control Engineering: Principles and Applications*. Wiley, 2006. (Cited on page 57.)

[165] A. Schiavi, P. Miglietta, and C. Guglielmone, "Considerations on the airflow resistivity measurement of porous and fibrous materials as function of temperature," *8th Eur. Conf. Noise Control 2009, EURONOISE 2009 - Proc. Inst. Acoust.*, vol. 31, no. PART 3, 2009. (Cited on page 57.)

[166] T. Samarasinghe, C. Hopkins, G. Seiffert, and J. Knox, "Airflow resistance measurement of fibrous materials at high temperatures for acoustical applications," *Appl. Acoust.*, vol. 164, p. 107255, 2020. http://doi.org/10.1016/j.apacoust.2020.107255. [Online]. Available: https://doi.org/10.1016/j.apacoust.2020.107255 (Cited on page 57.)

[167] P. Lemarinier, M. Henry, J. F. Allard, J. L. Bonardet, and A. Gedeon, "Connection between the dynamic bulk modulus of air in a porous medium and the specific surface," *J. Acoust. Soc. Am.*, vol. 97, no. 6, pp. 3478–3482, 1995. http://doi.org/10.1121/1.412434 (Cited on page 58.)

[168] N. Brown, M. Melon, V. Montembault, B. Castagnède, W. Lauriks, and P. Leclaire, "Evaluation of the viscous characteristic length of air-saturated porous materials from the ultrasonic dispersion curve," *Comptes rendus l'Académie des Sci.*, vol. Série IIb, no. 322 (2), pp. 122–127, 1996. (Cited on page 59.)

[169] P. Bonfiglio and F. Pompoli, "Inversion problems for determining physical parameters of porous materials: Overview and comparison between different methods," *Acta Acust. united with Acust.*, vol. 99, no. 3, pp. 341–351, 2013. http://doi.org/10.3813/AAA.918616 (Cited on page 60.)

[170] L. Jaouen, N. Atalla, and B. Brouard, "A method for the inverse characterization of poroelastic mechanical properties," *Can. Acoust. - Acoust. Can.*, vol. 30, no. 3, pp. 66–67, 2002. (Cited on page 60.)

[171] C. Van Der Kelen, J. Cuenca, and P. Göransson, "A method for the inverse estimation of the static elastic compressional moduli of anisotropic poroelastic foams-With application to a melamine foam," *Polym. Test.*, vol. 43, pp. 123–130, 2015. http://doi.org/10.1016/j.polymertesting.2015.03.006 (Cited on page 60.)

[172] I. R. Henriques, L. Rouleau, D. A. Castello, L. A. Borges, and J. F. Deü, "Viscoelastic behavior of polymeric foams: Experiments and modeling," *Mech. Mater.*, vol. 148, no. 2019, 2020. http://doi.org/10.1016/j.mechmat.2020.103506 (Cited on pages 60 and 97.)

[173] A. Terroir, L. Schwan, T. Cavalieri, V. Romero-García, G. Gabard, and J. P. Groby, "General method to retrieve all effective acoustic properties of fully-anisotropic fluid materials in three dimensional space," *J. Appl. Phys.*, vol. 125, no. 2, pp. 1–8, 2019. http://doi.org/10.1063/1.5066608 (Cited on page 60.)

[174] Y. Atalla, "Développement d'une technique inverse de caractérisation acoustique des matériaux poreux," Ph.D. dissertation, Université de Sherbrooke, 2002. (Cited on pages 60, 61, and 77.)

[175] Y. Atalla and R. Panneton, "Inverse acoustical characterization of open cell porous media using impedance tube measurements," *Can. Acoust. - Acoust. Can.*, vol. 33, no. 1, pp. 11–24, 2005. (Cited on page 60.)

[176] N. Sellen, "Modification de l'impédance de surface d'un matériau par contrôle actif : Application à la caractérisation et à l'optimisation d'un absorbant acoustique," Ph.D. dissertation, École Centrale Lyon, 2003. (Cited on pages 60 and 75.)

[177] J. C. Lagarias, J. A. Reeds, M. H. Wright, and P. E. Wright, "Convergence properties of the Nelder-Mead simplex method in low dimensions," *SIAM J. Optim.*, vol. 9, no. 1, pp. 112–147, 1998. http://doi.org/10.1137/S1052623496303470 (Cited on page 61.)

[178] N. Karmarkar, "A new polynomial-time algorithm for linear programming," *Combinatorica*, vol. 4, no. 4, pp. 373–395, 1984. http://doi.org/10.1007/BF02579150 (Cited on page 61.)

[179] J.-D. Chazot, E. Zhang, and J. Antoni, "Acoustical and mechanical characterization of poroelastic materials using a Bayesian approach," *J. Acoust. Soc. Am.*, vol. 131, no. 6, pp. 4584–4595, 2012. http://doi.org/10.1121/1.3699236 (Cited on page 61.)

[180] J.-d. Chazot, J. Antoni, E. Zhang, J.-d. Chazot, J. Antoni, E. Zhang, and J.-d. Chazot, "Characterization of poroelastic materials with a bayesian approach," in *10ème Congrès Français d'Acoustique*, Lyon, France, 2011. [Online]. Available: https://hal.archives-ouvertes.fr/hal-00554439 (Cited on page 61.)

[181] J. Cuenca, P. Göransson, L. De Ryck, and T. Lähivaara, "Deterministic and statistical methods for the characterisation of poroelastic media from multi-observation sound absorption measurements," *Mech. Syst. Signal Process.*, vol. 163, no. November 2020, 2022. http://doi.org/10.1016/j.ymssp.2021.108186 (Cited on page 62.)

[182] J. Cuenca, "Statistical characterisation of porous media from sound absorption and ultrasound transmission," in *SAPEM 2023*, 2023. (Cited on page 62.)

[183] F. S. Egner, "Investigation on inverse estimation of 9 poroelastic material parameters based on absorption coefficient," in *FA2020*, 2020, pp. 2759–2764. (Cited on page 62.)

[184] C. M. Van Wyk, "A study of the compressibility of wool, with special reference to South African merino wool," *Onderstepoort J. Vet. Sci. Anim. Ind.*, vol. 21, pp. 99–226, 1946. (Cited on page 62.)

[185] S. Toll, "Packing mechanics of fiber reinforcements," *Polym. Eng. Sci.*, vol. 38, no. 8, pp. 1337–1350, 1998. http://doi.org/10.1002/pen.10304 (Cited on page 62.)

[186] O. Bouaziz, J. P. Massea, and Y. Bréchetc, "An analytical description of the mechanical hysteresis of entangled materials during loading-unloading in uniaxial compression," *Scr. Mater.*, vol. 64, no. 2, pp. 107–109, 2011. http://doi.org/10.1016/j.scriptamat.2010.09.007 (Cited on page 62.)

[187] M. Baudequin, G. Ryschenkow, and S. Roux, "Non-linear elastic behavior of light fibrous materials," *Eur. Phys. J. B*, vol. 12, no. 1, pp. 157–162, 1999. http://doi.org/10.1007/s100510050990 (Cited on page 62.)

[188] M. Garai and F. Pompoli, "A simple empirical model of polyester fibre materials for acoustical applications," *Appl. Acoust.*, vol. 66, no. 12, pp. 1383–1398, 2005. http://doi.org/10.1016/j.apacoust.2005.04.008 (Cited on page 62.)

[189] N. Kino and T. Ueno, "Experimental determination of the micro- and macrostructural parameters influencing the acoustical performance of fibrous media," *Appl. Acoust.*, vol. 68, no. 11-12, pp. 1439–1458, 2007. http://doi.org/10.1016/j.apacoust.2006.07.008 (Cited on page 62.)

[190] N. Kino and T. Ueno, "Evaluation of acoustical and non-acoustical properties of sound absorbing materials made of polyester fibres of various cross-sectional shapes," *Appl. Acoust.*, vol. 69, no. 7, pp. 575–582, 2008. http://doi.org/10.1016/j.apacoust.2007.02.003 (Cited on page 62.)

[191] C. Peyrega and D. Jeulin, "Estimation of acoustic properties and of the representative volume element of random fibrous media," *J. Appl. Phys.*, vol. 113, no. 10, 2013. http://doi.org/10.1063/1.4794501 (Cited on page 62.)

[192] H. T. Luu, C. Perrot, and R. Panneton, "Influence of porosity, fiber radius and fiber orientation on the transport and acoustic properties of random fiber structures," *Acta Acust. united with Acust.*, vol. 103, no. 6, pp. 1050–1063, 2017. http://doi.org/10.3813/AAA.919134 (Cited on page 62.)

[193] H. T. Luu, R. Panneton, and C. Perrot, "Effective fiber diameter for modeling the acoustic properties of polydisperse fiber networks," *J. Acoust. Soc. Am.*, vol. 141, no. 2, pp. EL96–EL101, 2017. http://doi.org/10.1121/1.4976114. [Online]. Available: http://dx.doi.org/10.1121/1.4976114 (Cited on page 62.)

[194] H. T. Luu, C. Perrot, V. Monchiet, and R. Panneton, "Three-dimensional reconstruction of a random fibrous medium: Geometry, transport, and sound absorbing properties," *J. Acoust. Soc. Am.*, vol. 141, no. 6, pp. 4768–4780, 2017. http://doi.org/10.1121/1.4989373. [Online]. Available: http://dx.doi.org/10.1121/1.4989373 (Cited on page 62.)

[195] M. He, C. Perrot, J. Guilleminot, P. Leroy, and G. Jacqus, "Multiscale prediction of acoustic properties for glass wools: Computational study and experimental validation," *INTER-NOISE 2017 - 46th Int. Congr. Expo. Noise Control Eng. Taming Noise Mov. Quiet*, vol. 2017-Janua, pp. 3283–3299, 2017. http://doi.org/10.1121/1.5040479 (Cited on page 62.)

[196] C. Perrot, F. Chevillotte, and R. Panneton, "Bottom-up approach for microstructure optimization of sound absorbing materials," *J. Acoust. Soc. Am.*, vol. 124, no. 2, pp. 940–948, 2008. http://doi.org/10.1121/1.2945115 (Cited on page 62.)

[197] C. Perrot, F. Chevillotte, and R. Panneton, "Dynamic viscous permeability of an open-cell aluminum foam: Computations versus experiments," *J. Appl. Phys.*, vol. 103, no. 2, pp. 1–8, 2008. http://doi.org/10.1063/1.2829774 (Cited on page 62.)

[198] F. Chevillotte, R. Panneton, and C. Perrot, "Microstructure based model for sound absorption predictions of perforated closedcell metallic foams," *17th Int. Congr. Sound Vib. 2010, ICSV 2010*, vol. 4, pp. 2909–2916, 2010. http://doi.org/10.1121/1.3473696 (Cited on page 62.)

[199] T. G. Zielinski, "Microstructure representations for sound absorbing fibrous media: 3D and 2D multiscale modelling and experiments," *J. Sound Vib.*, vol. 409, pp. 112–130, 2017. http://doi.org/10.1016/j.jsv.2017.07.047 (Cited on page 62.)

[200] Y. Lee and I. Jasiuk, "Apparent elastic properties of random fiber networks," *Comput. Mater. Sci.*, vol. 79, pp. 715–723, 2013. http://doi.org/10.1016/j.commatsci.2013.07.037. [Online]. Available: http://dx.doi.org/10.1016/j.commatsci.2013.07.037 (Cited on page 62.)

[201] M. R. Islam and R. C. Picu, "Effect of network architecture on the mechanical behavior of random fiber networks,"

J. Appl. Mech. Trans. ASME, vol. 85, no. 8, pp. 1–8, 2018. http://doi.org/10.1115/1.4040245 (Cited on pages 62 and 83.)

[202] T. Kanit, S. Forest, I. Galliet, V. Mounoury, and D. Jeulin, "Determination of the size of the representative volume element for random composites: Statistical and numerical approach," *Int. J. Solids Struct.*, vol. 40, no. 13-14, pp. 3647–3679, 2003. http://doi.org/10.1016/S0020-7683(03)00143-4 (Cited on page 62.)

[203] J. Dirrenberger, S. Forest, and D. Jeulin, "Towards gigantic RVE sizes for 3D stochastic fibrous networks," *Int. J. Solids Struct.*, vol. 51, no. 2, pp. 359–376, 2014. http://doi.org/10.1016/j.ijsolstr.2013.10.011. [Online]. Available: http://dx.doi.org/10.1016/j.ijsolstr.2013.10.011 (Cited on pages 62 and 63.)

[204] X. H. Yang, S. W. Ren, W. B. Wang, X. Liu, F. X. Xin, and T. J. Lu, "A simplistic unit cell model for sound absorption of cellular foams with fully/semi-open cells," *Compos. Sci. Technol.*, vol. 118, pp. 276–283, 2015. http://doi.org/10.1016/j.compscitech.2015.09.009 (Cited on page 62.)

[205] C. Perrot, F. Chevillotte, M. Tan Hoang, G. Bonnet, F. X. Bécot, L. Gautron, and A. Duval, "Microstructure, transport, and acoustic properties of open-cell foam samples: Experiments and three-dimensional numerical simulations," *J. Appl. Phys.*, vol. 111, no. 1, 2012. http://doi.org/10.1063/1.3673523 (Cited on page 62.)

[206] L. Boeckx, M. Brennan, K. Verniers, and J. Vandenbroeck, "A numerical scheme for investigating the influence of the three dimensional geometrical features of porous polymeric foam on its sound absorbing behavior," *Acta Acust. united with Acust.*, vol. 96, no. 2, pp. 239–246, 2010. http://doi.org/10.3813/AAA.918273 (Cited on page 62.)

[207] K. Gao, J. A. van Dommelen, and M. G. Geers, "Investigation of the effects of the microstructure on the sound absorption performance of polymer foams using a computational homogenization approach," *Eur. J. Mech. A/Solids*, vol. 61, pp. 330–344, 2017. http://doi.org/10.1016/j.euromechsol.2016.10.011. [Online]. Available: http://dx.doi.org/10.1016/j.euromechsol.2016.10.011 (Cited on page 62.)

[208] V. H. Trinh, V. Langlois, J. Guilleminot, C. Perrot, Y. Khidas, and O. Pitois, "Tuning membrane content of sound absorbing cellular foams: Fabrication, experimental evidence and multiscale numerical simulations," *Mater. Des.*, vol. 162, pp. 345–361, 2019. http://doi.org/10.1016/j.matdes.2018.11.023. [Online]. Available: https://doi.org/10.1016/j.matdes.2018.11.023 (Cited on page 62.)

[209] O. Doutres, N. Atalla, and K. Dong, "Effect of the microstructure closed pore content on the acoustic behavior of polyurethane foams," *J. Appl. Phys.*, vol. 110, no. 6, 2011. http://doi.org/10.1063/1.3631021 (Cited on pages 62, 63, 64, and 105.)

[210] O. Doutres, N. Atalla, and K. Dong, "A semi-phenomenological model to predict the acoustic behavior of fully and partially reticulated polyurethane foams," *J. Appl. Phys.*, vol. 113, no. 5, pp. 1–13, 2013. http://doi.org/10.1063/1.4789595 (Cited on page 62.)

[211] M. Tan Hoang and C. Perrot, "Solid films and transports in cellular foams," *J. Appl. Phys.*, vol. 112, no. 5, 2012. http://doi.org/10.1063/1.4751345 (Cited on pages 62 and 105.)

[212] M. Tan Hoang and C. Perrot, "Identifying local characteristic lengths governing sound wave properties in solid foams," *J. Appl. Phys.*, vol. 113, no. 8, 2013. http://doi.org/10.1063/1.4793492 (Cited on page 62.)

[213] O. Doutres, M. Ouisse, N. Atalla, and M. Ichchou, "Impact of the irregular microgeometry of polyurethane foam on the macroscopic acoustic behavior predicted by a unit-cell model," *J. Acoust. Soc. Am.*, vol. 136, no. 4, pp. 1666–1681, 2014. http://doi.org/10.1121/1.4895695. [Online]. Available: http://dx.doi.org/10.1121/1.4895695 (Cited on page 62.)

[214] K. Gao, J. A. van Dommelen, and M. G. Geers, "Microstructure characterization and homogenization of acoustic polyurethane foams: Measurements and simulations," *Int. J. Solids Struct.*, vol. 100-101, no. 2016, pp. 536–546, 2016. http://doi.org/10.1016/j.ijsolstr.2016.09.024 (Cited on page 62.)

[215] M. S. Gholami, O. Doutres, and N. Atalla, "Effect of microstructure closed-pore content on the mechanical properties of flexible polyurethane foam," *Int. J. Solids Struct.*, vol. 112, pp. 97–105, 2017. http://doi.org/10.1016/j.ijsolstr.2017.02.016. [Online]. Available: http://dx.doi.org/10.1016/j.ijsolstr.2017.02.016 (Cited on page 62.)

[216] H. Mao, R. Rumpler, M. Gaborit, P. Göransson, J. Kennedy, D. O'Connor, D. Trimble, and H. Rice, "Twist, tilt and stretch: From isometric Kelvin cells to anisotropic cellular materials," *Mater. Des.*, vol. 193, p. 108855, 2020. http://doi.org/10.1016/j.matdes.2020.108855. [Online]. Available: https://doi.org/10.1016/j.matdes.2020.108855 (Cited on page 62.)

[217] R. Venegas and O. Umnova, "Numerical Modelling of Sound Absorptive Properties of Double Porosity Granular Materials," in *COMSOL Conf.*, 2010. (Cited on page 62.)

[218] R. Venegas and O. Umnova, "Acoustical properties of double porosity granular materials," *J. Acoust. Soc. Am.*, vol. 130, no. 5, pp. 2765–2776, 2011. http://doi.org/10.1121/1.3644915 (Cited on page 62.)

[219] R. Venegas and C. Boutin, "Enhancing sound attenuation in permeable heterogeneous materials via diffusion processes," *Acta Acust. united with Acust.*, vol. 104, no. 4, pp. 623–635, 2018. http://doi.org/10.3813/AAA.919202 (Cited on page 62.)

[220] F. Chevillotte, C. Perrot, and E. Guillon, "A direct link between microstructure and acoustical macro-behavior of real double porosity foams," *J. Acoust. Soc. Am.*, vol. 134, no. 6, pp. 4681–4690, 2013. http://doi.org/10.1121/1.4824842 (Cited on page 62.)

[221] H. J. Rice, J. Kennedy, P. Göransson, L. Dowling, and D. Trimble, "Design of a Kelvin cell acoustic metamaterial," *J. Sound Vib.*, vol. 472, p. 115167, 2020. http://doi.org/10.1016/j.jsv.2019.115167. [Online]. Available: https://doi.org/10.1016/j.jsv.2019.115167 (Cited on page 62.)

[222] T. G. Zielinski, "Pore-size effects in sound absorbing foams with periodic microstructure: Modelling and experimental verification using 3D printed specimens," *Proc. ISMA 2016 - Int. Conf. Noise Vib. Eng. USD2016 - Int. Conf. Uncertain. Struct. Dyn.*, pp. 95–104, 2016. (Cited on page 62.)

[223] S. Ren, Q. Ao, H. Meng, F. Xin, L. Huang, C. Zhang, and T. J. Lu, "A semi-analytical model for sound propagation in sintered fiber metals," *Compos. Part B Eng.*, vol. 126, pp. 17–26, 2017. http://doi.org/10.1016/j.compositesb.2017.05.083. [Online]. Available: http://dx.doi.org/10.1016/j.compositesb.2017.05.083 (Cited on page 62.)

[224] T. G. Zielinski, N. Dauchez, T. Boutin, M. Leturia, A. Wilkinson, F. Chevillotte, F. X. Bécot, and R. Venegas, "Taking advantage of a 3D printing imperfection in the development of sound-absorbing materials," *Appl. Acoust.*, vol. 197, 2022. http://doi.org/10.1016/j.apacoust.2022.108941 (Cited on page 62.)

[225] T. G. Zielinski, K. C. Opiela, N. Dauchez, T. Boutin, M.-A. Galland, and K. Attenborough, "Extremely tortuous sound absorbers with labyrinthine channels in non-porous and microporous solid skeletons," *Appl. Acoust.*, vol. 217, no. August 2023, p. 109816, 2024. http://doi.org/10.1016/j.apacoust.2023.109816 (Cited on page 62.)

[226] A. R. Park, J. S. Kim, S. W. Jang, Y. G. Park, B. S. Koo, and H. C. Lee, "Rational modification of substrate binding site by structure-based engineering of a cellobiose 2-epimerase in Caldicellulosiruptor saccharolyticus," *Microb. Cell Fact.*, vol. 16, no. 1, pp. 9–11, 2017. http://doi.org/10.1186/s12934-017-0841-3. [Online]. Available: https://doi.org/10.1186/s12934-017-0841-3 (Cited on page 63.)

[227] J. Boulvert, T. Cavalieri, J. Costa-Baptista, L. Schwan, V. Romero-García, G. Gabard, E. R. Fotsing, A. Ross, J. Mardjono, and J. P. Groby, "Optimally graded porous material for broadband perfect absorption of sound," *J. Appl. Phys.*, vol. 126, no. 17, 2019. http://doi.org/10.1063/1.5119715 (Cited on page 63.)

[228] F. Chevillotte and C. Perrot, "Effect of the three-dimensional microstructure on the sound absorption of foams: A parametric study," *J. Acoust. Soc. Am.*, vol. 142, no. 2, pp. 1130–1140, 2017. http://doi.org/10.1121/1.4999058. [Online]. Available: http://dx.doi.org/10.1121/1.4999058 (Cited on page 63.)

[229] L. J. Gibson and Ashby F, *Cellular Solids: Structure and Properties*, 2nd ed., Cambridge University Press, Ed. Cambridge: Cambridge University Press, 1997. http://doi.org/10.1017/CBO9781139878326. [Online]. Available: https://doi.org/10.1017/CBO9781139878326 (Cited on pages 63, 83, 94, and 105.)

[230] P. Göransson, "Acoustic and vibrational damping in porous solids," *Philos. Trans. R. Soc. A Math. Phys. Eng. Sci.*, vol. 364, no. 1838, pp. 89–108, 2006. http://doi.org/10.1098/rsta.2005.1688 (Cited on page 63.)

[231] E. Lind-Nordgren and P. Göransson, "Optimising open porous foam for acoustical and vibrational performance," *J. Sound Vib.*, vol. 329, no. 7, pp. 753–767, 2010. http://doi.org/10.1016/j.jsv.2009.10.009 (Cited on page 63.)

[232] C. Perrot, R. Panneton, and X. Olny, "Periodic unit cell reconstruction of porous media: Application to open-cell aluminum foams," *J. Appl. Phys.*, vol. 101, no. 11, 2007. http://doi.org/10.1063/1.2745095 (Cited on page 64.)

[233] L. Jaouen, E. Gourdon, and P. Glé, "Estimation of all six parameters of Johnson-Champoux-Allard-Lafarge model for acoustical porous materials from impedance tube measurements," *J. Acoust. Soc. Am.*, vol. 148, no. 4, pp. 1998–2005, 2020. http://doi.org/10.1121/10.0002162 (Cited on page 66.)

[234] L. Jaouen, A. Renault, and M. Deverge, "Elastic and damping characterizations of acoustical porous materials: Available experimental methods and applications to a melamine foam," *Appl. Acoust.*, vol. 69, no. 12, pp. 1129–1140, 2008. http://doi.org/10.1016/j.apacoust.2007.11.008 (Cited on pages 75, 81, 83, and 94.)

[235] M. Giovagnoni, "On the direct measurement of the dynamic Poisson's ratio," *Mech. Mater.*, vol. 17, no. 1, pp. 33–46, 1994. http://doi.org/10.1016/0167-6636(94)90012-4 (Cited on page 75.)

[236] J. F. Allard, M. Henry, L. Boeckx, P. Leclaire, and W. Lauriks, "Acoustical measurement of the shear modulus for thin porous layers," *J. Acoust. Soc. Am.*, vol. 117, no. 4, pp. 1737–1743, 2005. http://doi.org/10.1121/1.1868392 (Cited on page 75.)

[237] T. Pritz, "Dynamic young's modulus and loss factor of plastic foams for impact sound isolation," pp. 315–322, 1994. http://doi.org/10.1006/jsvi.1994.1488 (Cited on page 76.)

[238] A. Sfaoui, "On the viscoelasticity of the polyurethane foam," *J. Acoust. Soc. Am.*, vol. 97, no. 2, pp. 1046–1052, 1995. http://doi.org/10.1121/1.412987 (Cited on page 76.)

[239] A. Sfaoui, "Erratum: On the viscoelasticity of the polyurethane foam [J. Acoust. Soc. Am. 97, 1046-1052 (1995)]," *J. Acoust. Soc. Am.*, vol. 98, no. 1, p. 665, 1995. http://doi.org/10.1121/1.414443 (Cited on page 76.)

[240] ASTM, "ASTM E 756 - 98 : Standard Test Method for Measuring Vibration-Damping Properties of Materials," 1998. (Cited on page 76.)

[241] J. L. Wojtowicki, L. Jaouen, and R. Panneton, "New approach for the measurement of damping properties of materials using the Oberst beam," *Rev. Sci. Instrum.*, vol. 75, no. 8, pp. 2569–2574, 2004. http://doi.org/10.1063/1.1777382 (Cited on page 76.)

[242] M. Etchessahar, S. Sahraoui, and B. Brouard, "Vibrations of poroelastic plates: mixed displacement-pressure modelisation and Experiments," *Acta Acust. united with Acust.*, vol. 95, no. 5, pp. 857–865, 2009. http://doi.org/10.3813/AAA.918217 (Cited on page 76.)

[243] L. Jaouen, B. Brouard, N. Atalla, and C. Langlois, "A simplified numerical model for a plate backed by a thin foam layer in the low frequency range," *J. Sound Vib.*, vol. 280, no. 3-5, pp. 681–698, 2005. http://doi.org/10.1016/j.jsv.2003.12.038 (Cited on page 76.)

[244] J. F. Allard, G. Jansens, G. Vermeir, and W. Lauriks, "Frame-borne surface waves in air-saturated porous media," *J. Acoust. Soc. Am.*, vol. 111, no. 2, pp. 690–696, 2002. http://doi.org/10.1121/1.1427361 (Cited on page 76.)

[245] L. Boeckx, P. Leclaire, P. Khurana, C. Glorieux, W. Lauriks, and J. F. Allard, "Investigation of the phase velocities of guided acoustic waves in soft porous layers," *J. Acoust. Soc. Am.*, vol. 117, no. 2, pp. 545–554, 2005. http://doi.org/10.1121/1.1847848 (Cited on page 76.)

[246] A. Geslain, S. Raetz, M. Hiraiwa, M. Abi Ghanem, S. P. Wallen, A. Khanolkar, N. Boechler, J. Laurent, C. Prada, A. Duclos, P. Leclaire, and J. P. Groby, "Spatial Laplace transform for complex wavenumber recovery and its application to the analysis of attenuation in acoustic systems," *J. Appl. Phys.*, vol. 120, no. 13, 2016. http://doi.org/10.1063/1.4963827 (Cited on page 76.)

[247] P. Bonfiglio, F. Pompoli, K. V. Horoshenkov, and M. I. B. A. Rahim, "A simplified transfer matrix approach for the determination of the complex modulus of viscoelastic materials," *Polym. Test.*, vol. 53, pp. 180–187, 2016. http://doi.org/10.1016/j.polymertesting.2016.05.006 (Cited on page 76.)

[248] M. Etchessahar, S. Sahraoui, L. Benyahia, and J. F. Tassin, "Frequency dependence of elastic properties of acoustic foams," *J. Acoust. Soc. Am.*, vol. 117, no. 3, pp. 1114–1121, 2005. http://doi.org/10.1121/1.1857527 (Cited on page 76.)

[249] E. Mariez, S. Sahraoui, and J. F. Allard, "Elastic constants of polyurethane foam's skeleton for Biot model," in *Internoise Noisecon Congr. Conf. Proc.* Liverpool, England: Institute of Noise Control Engineering, 1996, pp. 950–954. (Cited on pages 76 and 77.)

[250] P. Bonfiglio, F. Pompoli, K. V. Horoshenkov, M. I. B. A. Rahim, L. Jaouen, J. Rodenas, F. X. Bécot, E. Gourdon, D. Jaeger, V. Kursch, M. Tarello, N. B. Roozen, C. Glorieux, F. Ferrian, P. Leroy, F. B. Vangosa, N. Dauchez, F. Foucart, L. Lei, K. Carillo, O. Doutres, F. Sgard, R. Panneton, K. Verdiere, C. Bertolini, R. Bär, J. P. Groby, A. Geslain, N. Poulain, L. Rouleau, A. Guinault, H. Ahmadi, and C. Forge, "How reproducible are methods to measure the dynamic viscoelastic properties of poroelastic media?" *J. Sound Vib.*, vol. 428, pp. 26–43, 2018. http://doi.org/10.1016/j.jsv.2018.05.006 (Cited on pages 77, 80, 81, and 91.)

[251] F. Chevillotte, F. Ronzio, C. Bertolini, M. T. Hoang, L. Dejaeger, L. Lei, A. Duval, and P. Mordillat, "Inter-Laboratory Characterization of Biot Parameters of Poro-Elastic Materials for Automotive Applications," *SAE Tech. Pap.*, no. 2020, pp. 1–9, 2020. http://doi.org/10.4271/2020-01-1523 (Cited on pages 77, 83, 84, 87, and 91.)

[252] S. Sahraoui, E. Mariez, and M. Etchessahar, "Mechanical testing of polymeric foams at low frequency," *Polym. Test.*, vol. 20, no. 1, pp. 93–96, 2000. http://doi.org/10.1016/S0142-9418(00)00006-4 (Cited on pages 77 and 78.)

[253] C. Langlois, R. Panneton, and N. Atalla, "Polynomial relations for quasi-static mechanical characterization of isotropic poroelastic materials," *J. Acoust. Soc. Am.*, vol. 110, no. 6, pp. 3032–3040, 2001. http://doi.org/10.1121/1.1419091 (Cited on pages 77, 78, and 81.)

[254] N. Dauchez, M. Etchessahar, and S. Sahraoui, "On measurement of mechanical properties of sound absorbing materials," in *2nd Biot Conf. poromechanics*, 2002, pp. 1–4. [Online]. Available: http://hal.archives-ouvertes.fr/hal-00331372/ (Cited on pages 77, 83, 84, 92, and 94.)

[255] S. Sim and K. J. Kim, "A method to determine the complex modulus and poisson's ratio of viscoelastic materials for FEM applications," *J. Sound Vib.*, vol. 141, no. 1, pp. 71–82, 1990. http://doi.org/10.1016/0022-460X(90)90513-Y (Cited on page 78.)

[256] S. Sahraoui, B. Brouard, L. Benyahia, D. Parmentier, and A. Geslain, "Normalized stiffness ratios for mechanical characterization of isotropic acoustic foams," *J. Acoust. Soc. Am.*, vol. 134, no. 6, pp. 4624–4629, 2013. http://doi.org/10.1121/1.4824833 (Cited on page 78.)

[257] V. Tarnow, "Dynamic measurements of the elastic constants of glass wool," *J. Acoust. Soc. Am.*, vol. 118, no. 6, pp. 3672–3678, 2005. http://doi.org/10.1121/1.2118267 (Cited on page 78.)

[258] T. Pritz, "Frequency dependences of complex moduli and complex poisson's ratio of real solid materials," *J. Sound Vib.*, vol. 214, no. 1, pp. 83–104, 1998. http://doi.org/10.1006/jsvi.1998.1534 (Cited on page 83.)

[259] R. Guastavino, "Elastic and acoustic characterisation of anisotropic porous materials," pp. —-, 2006. (Cited on page 83.)

[260] M. F. Ashby, "Mechanical Properties of Cellular Solids." *Metall. Trans. A, Phys. Metall. Mater. Sci.*, vol. 14 A, no. 9, pp. 1755–1769, 1983. http://doi.org/10.1007/BF02645546 (Cited on pages 83 and 94.)

[261] L. Gong, S. Kyriakides, and N. Triantafyllidis, "On the stability of Kelvin cell foams under compressive loads," *J. Mech. Phys. Solids*, vol. 53, no. 4, pp. 771–794, 2005. http://doi.org/10.1016/j.jmps.2004.10.007 (Cited on pages 83 and 94.)

[262] A. Geslain, O. Dazel, J.-P. Groby, S. Sahraoui, and W. Lauriks, "Influence of static compression on mechanical parameters of acoustic foams," *J. Acoust. Soc. Am.*, vol. 130, no. 2, pp. 818–825, 2011. http://doi.org/10.1121/1.3605535 (Cited on pages 83 and 94.)

[263] A. Schiffer, D. Lee, E. Kim, and T. Y. Kim, "Interaction of highly nonlinear solitary waves with rigid polyurethane foams," *Int. J. Solids Struct.*, vol. 152-153, pp. 39–50, 2018. http://doi.org/10.1016/j.ijsolstr.2018.05.010 (Cited on pages 83, 94, and 99.)

[264] N. Dauchez, "Effect of static preload on Young modulus," in *SAPEM 2014*, Stockholm, Sweden, 2014, pp. 1–13. [Online]. Available: https://sapem2014.matelys.com/ (Cited on pages 84 and 91.)

[265] C. Delgado-Sánchez, F. J. Santiago-Medina, V. Fierro, A. Pizzi, and A. Celzard, "Destructive vs. non-destructive methods for the mechanical characterisation of tannin-based thermoset foams," *Polym. Test.*, vol. 69, no. April, pp. 332–339, 2018. http://doi.org/10.1016/j.polymertesting.2018.05.046. [Online]. Available: https://doi.org/10.1016/j.polymertesting.2018.05.046 (Cited on page 84.)

[266] A. Schweighardt, B. Vehovszky, and D. Feszty, "The effect of the preload determination process on dynamic mechanical properties," *J. Phys. Conf. Ser.*, vol. 2677, no. 1, p. 012007, 2023. http://doi.org/10.1088/1742-6596/2677/1/012007 (Cited on page 85.)

[267] O. Danilov, F. Sgard, and X. Olny, "On the limits of an "in vacuum" model to determine the mechanical parameters of isotropic poroelastic materials," *J. Sound Vib.*, vol. 276, no. 3-5, pp. 729–754, 2004. http://doi.org/10.1016/j.jsv.2003.08.036 (Cited on page 86.)

[268] A. Wilkinson, J. Crété, S. Job, M. Rachik, and N. Dauchez, "Contact mechanics of open-cell foams with macroscopic asperities," *Int. J. Solids Struct.* (Cited on page 91.)

[269] C. Hentati, S. Job, J. P. Crété, M. Taktak, M. Haddar, and N. Dauchez, "On the contact law of open-cell poro-granular materials," *Int. J. Solids Struct.*, vol. 208-209, pp. 83–92, 2020. http://doi.org/10.1016/j.ijsolstr.2020.10.023. [Online]. Available: https://doi.org/10.1016/j.ijsolstr.2020.10.023 (Cited on pages 91, 103, 104, 105, and 107.)

[270] R. Guastavino and P. Göransson, "A 3D displacement measurement methodology for anisotropic porous cellular foam materials," *Polym. Test.*, vol. 26, no. 6, pp. 711–719, 2007. http://doi.org/10.1016/j.polymertesting.2007.02.008 (Cited on pages 92 and 94.)

[271] H. Mao, R. Rumpler, and P. Göransson, "A note on the linear deformations close to the boundaries of a cellular material," *Mech. Res. Commun.*, vol. 111, 2021. http://doi.org/10.1016/j.mechrescom.2021.103657 (Cited on page 92.)

[272] F. Marchetti and F. Chevillotte, "Characterization of the elastic properties of corrugated foams," in *Forum Acusticum 2023, 10th Conv. Eur. Acoust. Assocation*, no. September, Torino, 2023. (Cited on page 92.)

[273] J. A. Greenwood and J. B. P. Williamson, "Contact of nominally flat surfaces," *Proc. R. Soc. Lond. A.*, vol. 295, pp. 300–319, 1966. http://doi.org/10.1098/rspa.1966.0242 (Cited on pages 93 and 111.)

[274] J. A. Greenwood and J. H. Tripp, "The elastic contact of rough spheres," *J. Appl. Mech. Trans. ASME*, vol. 34, no. 1, pp. 153–159, 1967. http://doi.org/10.1115/1.3607616 (Cited on pages 93 and 111.)

[275] K. D. Cavender and M. R. Kinkelaar, "Real time dynamic comfort and performance factors of polyurethane foam in automotive seating," *SAE Tech. Pap.*, p. 18, 1996. http://doi.org/10.4271/960509 (Cited on page 95.)

[276] S. W. White, S. K. Kim, A. K. Bajaj, P. Davies, D. K. Showers, and P. E. Liedtke, "Experimental techniques

and identification of nonlinear and viscoelastic properties of flexible polyurethane foam," *Nonlinear Dyn.*, vol. 22, no. 3, pp. 281–313, 2000. http://doi.org/10.1023/A:1008302208269 (Cited on page 95.)

[277] P. J. Tan, J. J. Harrigan, and S. R. Reid, "Inertia effects in uniaxial dynamic compression of a closed cell aluminium alloy foam," *Mater. Sci. Technol.*, vol. 18, no. 5, pp. 480–488, 2002. http://doi.org/10.1179/026708302225002092 (Cited on page 95.)

[278] Y. Xing, D. Sun, M. Zhang, and G. Shu, "Crushing Responses of Expanded Polypropylene Foam," *Polymers (Basel).*, vol. 15, no. 9, 2023. http://doi.org/10.3390/polym15092059 (Cited on page 95.)

[279] J. Miltz and G. Gruenbaum, "Evaluation of cushioning properties of plastic foams from compressive measurements," *Polym. Eng. Sci.*, vol. 21, no. 15, pp. 1010–1014, 1981. http://doi.org/10.1002/pen.760211505 (Cited on page 95.)

[280] M. Mooney, "A theory of large elastic deformation," *J. Appl. Phys.*, vol. 11, pp. 582–592, 1940. http://doi.org/10.1063/1.1712836 (Cited on page 95.)

[281] R.S.Rivlin, "Large elastic deformations of isotropic materials. I. Fundamental concepts," *Br. Rubber Prod. Res. Assoc.*, pp. 459–490, 1947. (Cited on page 95.)

[282] R. S. Rivlin, D. W. Saunders, and B. Y. R. S. Rivlin, "large elastic deformations of isotropic materials VII . Experiments on the deformation of rubbBritish Rubber Producers' Research Association," *Philos. Trans. R. Soc.*, vol. 243, no. 865, pp. 251–288, 1951. http://doi.org/https://doi.org/10.1098/rsta.1951.0004 (Cited on page 95.)

[283] Abaqus Inc., "Abaqus documentation version 6.6-1: Hyperelastic behavior in elastomeric foams," 2006. [Online]. Available: https://classes.engineering.wustl.edu/2009/spring/mase5513/abaqus/docs/v6.6/books/key/default.htm?startat=ch08abk07.html{#}usb-kws-mhyperfoam (Cited on page 95.)

[284] R. Hill, *Aspects of Invariance in Solid Mechanics*, 1979, vol. 18. http://doi.org/10.1016/S0065-2156(08)70264-3 (Cited on page 95.)

[285] B. Storaakers, "On material representation and constitutive branching in finite compressible elasticity," *J. Mech. Phys. Solids*, vol. 34, no. 2, pp. 125–145, 1986. http://doi.org/10.1016/0022-5096(86)90033-5 (Cited on page 95.)

[286] R. W. Ogden, "Large Deformation Isotropic Elasticity - on the Correlation of Theory and Experiment for Incompressible Rubberlike Solids," in *Proc. R. Soc. Long. A.*, vol. 326, 1972, pp. 565–584. http://doi.org/10.5254/1.3542910 (Cited on page 95.)

[287] J. Bergstrom, "Hyperfoam Modeling of Soft Foams," 2021. [Online]. Available: https://polymerfem.com/hyperfoam-modeling-of-soft-foams/ (Cited on page 95.)

[288] Abaqus Inc., "Abaqus documentation version 6.6-1: Fitting of hyperelastic and hyperfoam constants," 2006. [Online]. Available: https://classes.engineering.wustl.edu/2009/spring/mase5513/abaqus/docs/v6.6/books/stm/default.htm?startat=ch04s06ath124.html (Cited on pages 95 and 102.)

[289] ASTM International, "D 575-91 - Standard Test Methods for Rubber Properties in Compression," West Conshohocken, 2001. (Cited on page 96.)

[290] ASTM International, "D 3574-03 - Standard Test Methods for Flexible Cellular Materials - Slab, Bonded, and Molded Urethane Foams," West Conshohocken, 2002. (Cited on page 96.)

[291] Renault, "D41 1003 - Matériaux alvéolaires souples de garnissage - Résistance à la compression (portance)," 2014. (Cited on page 96.)

[292] L. M. Yang and V. P. Shim, "A visco-hyperelastic constitutive description of elastomeric foam," *Int. J. Impact Eng.*, vol. 30, no. 8-9, pp. 1099–1110, 2004. http://doi.org/10.1016/j.ijimpeng.2004.03.011 (Cited on pages 97 and 99.)

[293] M. L. Ju, H. Jmal, R. Dupuis, and E. Aubry, "Visco-hyperelastic constitutive model for modeling the quasi-static behavior of polyurethane foam in large deformation," *Polym. Eng. Sci.*, vol. 55, no. 8, pp. 1795–1804, 2015. http://doi.org/10.1002/pen.24018 (Cited on page 97.)

[294] Y. Anani and Y. Alizadeh, "Visco-hyperelastic constitutive law for modeling of foam's behavior," *Mater. Des.*, vol. 32, no. 5, pp. 2940–2948, 2011. http://doi.org/10.1016/j.matdes.2010.11.010. [Online]. Available: http://dx.doi.org/10.1016/j.matdes.2010.11.010 (Cited on page 97.)

[295] C. Briody, B. Duignan, S. Jerrams, and J. Tiernan, "The implementation of a visco-hyperelastic numerical material model for simulating the behaviour of polymer foam materials," *Comput. Mater. Sci.*, vol. 64, pp. 47–51, 2012. http://doi.org/10.1016/j.commatsci.2012.04.012. [Online]. Available: http://dx.doi.org/10.1016/j.commatsci.2012.04.012 (Cited on page 97.)

[296] B. Markert, "Porous media viscoelasticity with application to polymeric foams," Ph.D. dissertation, Universität Stuttgart, 2005. [Online]. Available: http://elib.uni-stuttgart.de/opus/volltexte/2005/2338/ (Cited on page 97.)

[297] J. D. E. Dalisay, L. Liu, M. Eriten, L. A. Bergman, and A. F. Vakakis, "Characterization of visco-hyperelastic behavior of open cell polyurethane foam through transient shear testing," *Int. J. Solids Struct.*, vol.

241, no. January 2021, p. 111482, 2022. http://doi.org/10.1016/j.ijsolstr.2022.111482. [Online]. Available: https://doi.org/10.1016/j.ijsolstr.2022.111482 (Cited on page 97.)

[298] G. S. Batt, J. M. Gibert, and M. Daqaq, "Small strain vibration of a continuous, linearized viscoelastic rod of expanded polymer cushion material," *J. Sound Vib.*, vol. 349, pp. 330–347, 2015. http://doi.org/10.1016/j.jsv.2015.03.039. [Online]. Available: http://dx.doi.org/10.1016/j.jsv.2015.03.039 (Cited on page 97.)

[299] A. Jaishankar and G. H. McKinley, "A Fractional K-BKZ Constitutive Formulation for Describing the Nonlinear Rheology of Multiscale Complex Fluids," *J. Rheol. (N. Y. N. Y).*, vol. 25, pp. 1751–1788, 2014. http://doi.org/https://doi.org/10.1122/1.4892114 (Cited on page 97.)

[300] Z. C. Grasley and D. A. Lange, "Constitutive modeling of the aging viscoelastic properties of portland cement paste," *Mech. Time-Dependent Mater.*, vol. 11, no. 3-4, pp. 175–198, 2007. http://doi.org/10.1007/s11043-007-9043-4 (Cited on page 97.)

[301] L. Struik, "Physical aging in amorphous polymers and other materials," Ph.D. dissertation, T.U. Delft, 1977. http://doi.org/10.1016/0040-6031(82)85085-5. [Online]. Available: http://resolver.tudelft.nl/uuid:941d2af6-903a-4260-9953-2efb4cb38d2e (Cited on page 98.)

[302] C. Derec, A. Ajdari, and F. Lequeux, "Rheology and aging: A simple approach," *Eur. Phys. J. E*, vol. 4, no. 3, pp. 355–361, 2001. http://doi.org/10.1007/s101890170118 (Cited on page 98.)

[303] D. Espíndola, B. Galaz, and F. Melo, "Ultrasound induces aging in granular materials," *Phys. Rev. Lett.*, vol. 109, no. 15, 2012. http://doi.org/10.1103/PhysRevLett.109.158301 (Cited on page 98.)

[304] P. Pastorino, F. Scarpa, S. Patsias, J. R. Yates, S. J. Haake, and M. Ruzzene, "Strain rate dependence of stiffness and Poisson's ratio of auxetic open cell PU foams," *Phys. Status Solidi Basic Res.*, vol. 244, no. 3, pp. 955–965, 2007. http://doi.org/10.1002/pssb.200572714 (Cited on page 99.)

[305] B. Sanborn and B. Song, "Poisson's ratio of a hyperelastic foam under quasi-static and dynamic loading," *Int. J. Impact Eng.*, vol. 123, no. May 2018, pp. 48–55, 2019. http://doi.org/10.1016/j.ijimpeng.2018.06.001 (Cited on page 99.)

[306] Abaqus Inc., "Time domain viscoelasticity," 2006. [Online]. Available: https://classes.engineering.wustl.edu/2009/spring/mase5513/abaqus/docs/v6.6/books/usb/default.htm?startat=pt05ch17s07abm11.html (Cited on page 102.)

[307] J. M. Antunes, L. F. Menezes, and J. V. Fernandes, "Three-dimensional numerical simulation of Vickers indentation tests," *Int. J. Solids Struct.*, vol. 43, no. 3-4, pp. 784–806, 2006. http://doi.org/10.1016/j.ijsolstr.2005.02.048 (Cited on page 104.)

[308] R. B. King, "Elastic analysis of some punch problems for a layered medium," *Int. J. Solids Struct.*, vol. 23, no. 12, pp. 1657–1664, 1987. http://doi.org/10.1016/0020-7683(87)90116-8. [Online]. Available: http://dx.doi.org/10.1016/0020-7683(87)90116-8 (Cited on page 104.)

[309] L. Sirghi, J. Ponti, F. Broggi, and F. Rossi, "Probing elasticity and adhesion of live cells by atomic force microscopy indentation," *Eur. Biophys. J.*, vol. 37, no. 6, pp. 935–945, 2008. http://doi.org/10.1007/s00249-008-0311-2 (Cited on page 105.)

[310] I. N. Sneddon, "The relation between load and penetration in the axisymmetric boussinesq problem for a punch of arbitrary profile," *Int. J. Eng. Sci.*, vol. 3, no. 1, pp. 47–57, 1965. http://doi.org/10.1016/0020-7225(65)90019-4 (Cited on page 105.)

[311] M. T. Hoang, "Modélisation et simulation multi-échelle et multi-physique du comportement acoustique de milieux poroélastiques : application aux mousses de faible densité," Ph.D. dissertation, Universite Paris-Est, 2012. [Online]. Available: https://theses.hal.science/tel-00799779v3 (Cited on page 105.)

[312] H. Hertz, "On the contact of elastic solids," *J. für die reine und Angew. Math.*, vol. 92, pp. 156–171, 1881. (Cited on page 111.)

[313] E. Bickel, "Some Fundamental Problems in the Measurement of Surface Roughness," in *Proc. Int. Prod. Eng. Res. Conf.*, Pittsburgh, Pa., 1963, pp. 667–674. (Cited on page 111.)

[314] T. Hisakado, "Effect of surface roughness on contact between solid surfaces," *Wear*, vol. 28, no. 2, pp. 217–234, 1974. http://doi.org/10.1016/0043-1648(74)90163-X (Cited on page 111.)

[315] A. W. Bush, R. D. Gibson, and T. R. Thomas, "The elastic contact of a rough surface," *Wear*, vol. 35, no. 1, pp. 87–111, 1975. http://doi.org/10.1016/0043-1648(75)90145-3 (Cited on page 111.)

[316] B. N. Persson, O. Albohr, U. Tartaglino, A. I. Volokitin, and E. Tosatti, "On the nature of surface roughness with application to contact mechanics, sealing, rubber friction and adhesion," *J. Phys. Condens. Matter*, vol. 17, no. 1, pp. 0–62, 2004. http://doi.org/10.1088/0953-8984/17/1/R01 (Cited on page 111.)

[317] H. Nelisse, T. Onsay, and N. Atalla, "Structure borne insertion loss of sound package components," *SAE Tech. Pap.*, no. 724, 2003. http://doi.org/10.4271/2003-01-1549 (Cited on page 120.)

[318] International Standardization Organization, "ISO 15186-1 - Measurement of sound insulation in buildings and of building elements using sound intensity - Part 1: Laboratory measurements," 2000. (Cited on page 120.)

[319] ISO, "ISO 140-3: Measurement of sound elements - Part 3: Laboratory measurements of airborne sound insulation of building elements," 2004. (Cited on page 120.)

[320] ASTM, "ASTM E90-09 - Standard Test Method for Laboratory Measurement of Airborne Sound Transmission Loss of Building Partitions and Elements," 2016. http://doi.org/10.1520/E0090-09R16.2 (Cited on page 120.)

[321] International Standardization Organization, "ISO 140-5 - Measurement of sound insulation in buildings and of building elements - Part 5: Field measurements of airborne sound insulation of façade elements and façades," 1998. (Cited on page 120.)

[322] L. Weber, H. Schreier, and K.-d. Brandstetter, "Measurement of sound insulation in laboratory - comparison of different methods," in *NAG/DAGA 2009*, Rotterdam, 2009, pp. 701–704. (Cited on page 120.)

[323] C. Bertolini and G. Ruggeri, "Numerical investigations about Structure-Borne Insertion Loss as applied in the automotive field and a measurement system for its assessment," in *Forum Acusticum 2023, 10th Conv. Eur. Acoust. Assocation*, 2023. (Cited on page 120.)

[324] C. Bertolini, G. Ruggeri, and M. Galante, "A measurement system for the assessment of the effectiveness of sound-insulating multilayers against structure-borne excitation: design, prototyping and validation," *INTER-NOISE NOISE-CON Congr. Conf. Proc.*, vol. 268, no. 4, pp. 4763–4774, 2023. (Cited on page 120.)

[325] F. Chevillotte, L. Jaouen, and F.-X. Bécot, "On the modeling of visco-thermal dissipations in heterogeneous porous media," *J. Acoust. Soc. Am.*, vol. 138, no. 6, pp. 3922–3929, 2015. http://doi.org/10.1121/1.4937773. [Online]. Available: http://dx.doi.org/10.1121/1.4937773 (Cited on page 123.)

[326] K. Verdière, R. Panneton, S. Elkoun, T. Dupont, and P. Leclaire, "Transfer matrix method applied to the parallel assembly of sound absorbing materials," *J. Acoust. Soc. Am.*, vol. 134, no. 6, pp. 4648–4658, 2013. http://doi.org/10.1121/1.4824839 (Cited on page 123.)

[327] K. Verdière, R. Panneton, S. Elkoun, T. Dupont, and P. Leclaire, "Comparison between parallel transfer matrix method and admittance sum method," *J. Acoust. Soc. Am.*, vol. 136, no. 2, pp. EL90–EL95, 2014. http://doi.org/10.1121/1.4885481. [Online]. Available: http://dx.doi.org/10.1121/1.4885481 (Cited on page 123.)

[328] M. Bolduc and N. Atalla, "Measurement of SEA damping loss factor for complex structures," *JASA*, vol. 123, 2008. http://doi.org/10.4271/2005-01-2327 (Cited on page 128.)

[329] B. Bloss and M. D. Rao, "Measurement of damping in structures by the Power Input Method," *Exp. Tech.*, vol. 26, pp. 30–32, 2017. http://doi.org/10.1016/b978-0-323-91186-3.00001-0 (Cited on page 128.)

[330] M. N. Bin Fazail, "Caractérisation de l'amortissement des structures complexes par la méthode de corrélation," Ph.D. dissertation, Université de Technologie de Compègne, France, Université de Sherbrooke, Canada, 2023. (Cited on page 128.)

[331] C. Pezerat and J. Guyader, "Two inverse methods for localization of external sources excting a beam," *Acta Acust.*, vol. 3, no. May, pp. 1–10, 1995. (Cited on page 128.)

[332] C. Pezerat and J. L. Guyader, "Identification of vibration sources," *Appl. Acoust.*, vol. 61, no. 3, pp. 309–324, 2000. http://doi.org/10.1016/S0003-682X(00)00036-0 (Cited on page 128.)

Characterization and modelling of porous automotive engine encapsulation materials for external acoustics

Alexandre Wilkinson

Thesis submitted for the degree of Doctor of Philosophy in Vibration and Acoustics

---

The encapsulation of car engines by porous screens is a technology that reduces the noise they radiate into their environment. Currently, their use relies mostly on their ability to absorb sound when placed inside the engine compartment, at a distance from the engine, but a new configuration that positions them directly in contact with the engine offers several advantages. Notably, this allows a reduction in mass and raw materials needed, but significantly alters their acoustic behaviour. In particular, the engine temperature, applied preload, and the amount of contact between the engine and the screen influence the acoustic behaviour of the system. This thesis aims to characterize the porous encapsulation materials and study their acoustic behaviour in their new configuration, in contact with a radiating surface representing the engine. This work is part of an industrial project called SEMPAE (Simulation of engine encapsulation for external acoustics, from 2020 to 2024), which is a collaboration between Trèves Group, an automotive equipment supplier, Renault Group, an automotive manufacturer, ESI Group, a software publisher, and the Roberval research laboratory at UTC.

First, various encapsulation materials, including polymer foams and fibrous materials, are characterized to obtain their properties that serve as input for poroelastic models. Various characterization methods are compared and applied. Special attention is given to the characterization of mechanical properties, for which there are still many uncertainties.

Next, the stiffness of melamine foam compressed against a rigid surface is studied. Its relaxation over time is observed and modelled, highlighting the complex rheology of porous materials. Its nonlinearity as a function of strain is accounted for, revealing the interaction between the intrinsic nonlinearity of the material and the shape nonlinearity of a sample with a pyramidal geometry. Since the compression stiffness of an asperity made from a porous material can be modelled, the contact stiffness of a porous material with a rough surface can be predicted.

Finally, the reduction of the acoustic power radiated by a plate covered with a screen consisting of a porous layer and a heavy sheet is studied. The mass-spring behaviour of the screen significantly reduces the radiated power beyond the resonance of the system. Experimental results reveal that by reducing the contact ratio between the screen and the plate, the resonance is shifted towards lower frequencies, which improves the acoustic insulation of the covering. Partial contact is created experimentally by cutting grooves into the screens, and is modelled using the parallel transfer matrix method.